

**Developing contacting solutions for Mg₂(Si,Sn)-based thermoelectric generators:
Evaluating Cu and Ni₄₅Cu₅₅ as candidates for contacting electrodes, and
establishing the importance of charged point defects in the contacting process**

Von der Fakultät für Ingenieurwissenschaften
Abteilung Elektrotechnik und Informationstechnik
der Universität Duisburg-Essen

zur Erlangung des akademischen Grades

Doktor der Naturwissenschaften (Doctor rerum naturalium)

genehmigte Dissertation

von

Sahar Ayachi, M. Sc.

aus

Tunis, Tunesien

Gutachter: Prof. Dr. Johannes de Boor
Gutachter: Prof. Dr. Hyo Jae Yoon
Tag der mündlichen Prüfung: 27.08.2021

لجدّيا سعد و محمد، لجدّنايا فاطمة و شهية

لروح الملاك اسراء

To my grand-fathers Saad and Mohammad, to my grandmothers Fatma and Ch`hiba

To the soul of our angel Israa,

Acknowledgements

I would like to express my sincere gratitude to my supervisors Jun.-Prof. Johannes de Boor and Prof. Eckhard Müller for giving me the opportunity to join their group as a PhD candidate. I would like to thank them for their continuous support during my time in DLR and in Germany, for their patience and continuous advice, and for sharing their knowledge and expertise with me.

Jun.-Prof. Johannes de Boor was my direct supervisor during my PhD study. He made the mood in the group comfortable, so I could easily concentrate on my work. From him, I learnt to doubt myself when needed, but also to stand up for myself when necessary. I also learnt the dos and don'ts of group leading and supervision, as someone who aspires to be a supervisor one day. Thank you very much, Johannes, for being open and transparent with me, and for allowing me to be the same with you!

I would like to thank Przemyslaw Blaschkewitz for his continuing support with the thermoelectric measurements, and Pawel Ziolkowski for his constant support and advice for the PSM measurements.

I am also eternally grateful to my officemate Prasanna Ponnusamy for being the best work-partner ever. We shared an office together since day one, and you were welcoming and supportive. You helped me unconditionally, both at work and outside, you supported me each and every step of the way, even on a very personal level. I believe you may be one of the few people who might have actually met some parts of “*Lola*” in real life. Thank you, Prasanna, always!

I would also like to thank my amazing colleagues Gustavo, Julia, Mila, Aryan, Mohammad, Nader, Ngan, Nhi, Radhika, Kunal, Silvana, Nacho, Laura, Venkatesh, Antoine, Gregor, Klaus, Severin, Matthias, Vidushi, Adina, and Christian for their support, and for the enjoyable working environment. I would like to particularly thank Gustavo for always supporting and helping me. Thank you for the fruitful discussions that were very valuable to my work. I learnt a lot from you. Another particular thank goes to Radhika as she gave me the opportunity to supervise. You were my first intern; I am sure I wasn't the best supervisor all the time, that I was figuring it out as things went. But, you gave me this chance to learn, and I did learn a lot. I truly hope I managed to teach you at least one thing in return.

I would like to thank our collaborators Byungki Ryu, Sungjin Park and Sudong Park as well as everyone else in their team in the Korea Electrotechnology Research Institute (KERI) in Changwon, South Korea. Thank you for providing us with all the hybrid-DFT calculations that allowed me to take my research towards an interesting and novel path. I hope our collaboration can lead to even more fruitful works and publications.

I would like to thank my German family. You gave me so much love and support, and took me in as one of yours. You helped me unconditionally when the world exploded with a pandemic. You opened your doors as much as you opened your hearts. You helped me cope with all the stress from work and thesis writing, when I was alone and far from my family, and for that I am eternally grateful. No matter what my next step in life is, you will have the exact same huge spot in my heart. Sabrina, Anja, Sandra, Daniel, Liv, Mumin, and each and every single member of the Rudolph family. I love you.

I would also like to thank my dearest friend Abir Abdelli for being an amazing PhD hotline support. We both had our last year of PhD going in parallel, we synchronized stress from data analysis, thesis writing, revisions, supervisors, etc. You kept me company, despite the thousands of kilometers between us, and you gave me the motivation and the mental support I needed to keep going. Thank you for all of that, I will see you very soon! A special thanks goes also to baby Soha who always managed to change my mood and make me laugh no matter how angry, stressed or sad I was.

A special thanks also goes to my dear friend and colleague Peter-Philip Bauer. You helped me so much in my daily life in Germany, and we shared many good memories that I will always carry with me.

Last but not least, I would like to thank my family: my parents Fakhreddine and Saida, my brothers Skander and Rayan and my grandparents for always supporting my random ideas. Whether it's moving around the world or following crazy dreams, you never stopped me from taking my own path. I wouldn't be where I am today if it wasn't for you. I owe it all to you.

Declaration of Independence

(Versicherung & Selbständigkeitserklärung)

I hereby affirm that I have prepared the submitted thesis independently and without unauthorized outside support. All provided help and supervision are specified in the thesis and/or the acknowledgement, and all data taken from published work is marked as such. Utilized methods, instruments and experimental setups are also all indicated in the corresponding chapter. Results and data resulting from collaborative work are specified as such, and were utilized with full agreement of the collaborators.

The three papers included in this cumulative thesis as Chapters 3, 4 and 5 were added after knowledge and agreement of all co-authors. An exhaustive list of all co-authors, as well as task distribution, is provided at the end of this manuscript.

Sahar Ayachi

Date: 06.09.2021

Signature

This cumulative thesis contains the following publications:

1. **Paper 1: Sahar Ayachi**, Gustavo Castillo Hernandez, Ngan Hoang Pham, Nader Farahi, Eckhard Müller and Johannes de Boor, “*Developing Contacting Solutions for $Mg_2Si_{1-x}Sn_x$ -based Thermoelectric Generators: Cu and $Ni_{45}Cu_{55}$ as Potential Contacting Electrodes*”, ACS Applied Materials & Interfaces, 11, 43, 40769, 2019.
2. **Paper 2: Sahar Ayachi**, Gustavo Castillo Hernandez, Eckhard Müller and Johannes de Boor, “*Contacting Cu Electrodes to $Mg_2Si_{0.3}Sn_{0.7}$: Direct vs Indirect Resistive Heating*”, Semiconductors, 53, 13, 1825, 2019.
3. **Paper 3: Sahar Ayachi**, Radhika Deshpande, Prasanna Ponnusamy, Sungjin Park, Jaywan Chung, Sudong Park, Byungki Ryu, Eckhard Müller and Johannes de Boor, “*On the Relevance of Point Defects for the Selection of Contacting Electrodes: Ag as an example for $Mg_2(Si,Sn)$ -based Thermoelectric Generators*”, Materials Today Physics, 16, 100309, 2021.

Each of these papers are provided as a separate chapter in the “Paper Catalogue” of the manuscript (p. 41), respectively as Chapter 3, Chapter 4 and Chapter 5. A synopsis divided into an Introduction chapter (Chapter 1) and a Methods chapter (Chapter 2) is given before the Paper Catalogue, and a general discussion chapter of the published results as well as a Conclusion & Outlook chapter are provided after the Paper Catalogue in Chapters 6 and 7, respectively. Before each paper, an introductory page is provided to summarize its content.

Each paper is added to the manuscript as the final revised submitted version following the target journal template, including its references and Supplementary Material (in the case of Chapter 5/Paper 3).

Table of Contents

List of Figures	xi
List of Symbols and Abbreviations	xv
Thesis Abstract	xix
1. Introduction	1
1.1. Thermoelectric Effects	2
1.2. Thermoelectric Devices	3
1.3. Thermoelectric Materials: Mg_2X ($X = Si, Sn$)	6
1.4. Contacting and Electrode Selection	10
1.5. Electrical contact resistance	12
1.6. Point defects	15
1.7. Research Summary	19
1.7.1. Research Question	19
1.7.2. Thesis Overview	19
2. Methods	21
2.1. Powder synthesis and hot pressing	21
2.1.1. Induction melting	21
2.1.2. High energy ball milling (HEBM)	23
2.1.3. Sample compaction	24
2.2. Joining by sintering	26
2.3. Sample preparation (cutting, grinding, embedding, polishing)	28
2.4. Sample characterization	29
2.4.1. Scanning electron microscopy (SEM)	29
2.4.2. Potential & Seebeck Microprobe (PSM)	30
2.5. Annealing for thermal stability evaluation	34
2.6. Hybrid-Density Functional Theory	35
2.6.1. Background on Density Functional Theory	35
2.6.2. Hybrid Density Functional Theory	38
Paper Catalogue	41
3. Developing Contacting Solutions for $Mg_2Si_{1-x}Sn_x$ -based Thermoelectric Generators: Cu and $Ni_{45}Cu_{55}$ as Potential Contacting Electrodes	43
4. Contacting Cu Electrodes to $Mg_2Si_{0.3}Sn_{0.7}$: Direct vs Indirect Resistive Heating	71
5. On the Relevance of Point Defects for the Selection of Contacting Electrodes: Ag as an Example for $Mg_2(Si,Sn)$ -based Thermoelectric Generators	85
6. Discussion	125

6.1.	Effects of the preparation conditions on the contacting results	126
6.1.1.	Effect of the synthesis method of the TE material	126
6.1.2.	Effect of electrode treatment	131
6.1.1	Effect of the sintering current on the contacting results	136
6.1.2	Summary of Chapter 6.1	142
6.2	On the relevance of electrode-induced charged point defects in the contacting of Mg ₂ (Si,Sn) 144	
6.2.1	Cu defects in Li and Bi-doped Mg ₂ Si and Mg ₂ Sn	147
6.2.2	Ni defects in Li and Bi-doped Mg ₂ Si and Mg ₂ Sn	156
6.2.3	Summary and Conclusions	163
6.2.4	Limitations of the calculations as an electrode selection tool	165
7.	Conclusions and Outlook	167
7.1	Suggestions for Cu contacting on Mg ₂ (Si,Sn)	169
7.2	Suggestions for the <i>indirect resistive heating</i> method	171
7.3	Suggestions for the contacting of Mg ₂ (Si,Sn)	172
7.4	Expanding the hybrid-DFT calculation to further electrodes: Ti as an example	173
	Bibliography	175
	Appendix	183
A.1	Effect of the sintering current on the contacting results of Ni ₄₅ Cu ₅₅	183
A.1.1	Microstructure and SEM investigations	183
A.1.2	Favorable current paths	188
A.2	Hybrid-DFT calculations for the combined defect case of Ni ₄₅ Cu ₅₅	191
	Co-Authorship Statement	195

List of Figures

Figure 1.1: Visualization of the Seebeck effect as the movement of the dominant charge carriers (electrons in this case) in a material (n-type semiconductor in this case) under temperature gradient (T_h is the hot side and T_c is the cold side) generating an open-circuit voltage V	2
Figure 1.2: Refrigeration (left) and power generation (right) modes for thermoelectric devices.	4
Figure 1.3: a) Sample curves of simulation results of the impact of the total electrical contact resistance R_c on a) ZT of modules using different Bi_2Te_3 leg lengths (taken from [23]). b) Efficiency of a Zn_4Sb_3 -based TE device as R_c is varied between 0 and 1000 $\mu\Omega \text{ cm}^2$. The direction of the increase of R_c is displayed by the arrow. The points represent the calculated values and the solid lines represent polynomial fits. (taken from [24]).	6
Figure 1.4: State-of-the-art comparison of ZT in different n-type materials (taken from Zhu <i>et al.</i> [47])	7
Figure 1.5: Dependence of the dimensionless figure of merit zT on the charge carrier concentration (taken from [63]).	8
Figure 1.6: Optimized zT of p- (Li doped) and n- (Sb doped) type $\text{Mg}_2\text{Si}_{0.4}\text{Sn}_{0.6}$ composition. Data was taken from [28] and [29] respectively.	9
Figure 1.7: Configuration of a functional TE module containing a set of TE legs joined by a conducting multi-layer (Taken from [18]).	10
Figure 1.8: Schematic of the efficiency of a TE device as a function of the specific contact resistance.	11
Figure 1.9: Schematic diagram of the energy bands at the interface between a metal and a heavily-doped n-type semiconductor (a) before contacting and (b) after contacting. As soon as a contact is established, the electrons flow from the metal to the semiconductor because $\Phi_M < \Phi_S$ (electron movement shown by the green arrow in (a)). This movement results in an accumulation of positive charge at the edge of the metal and negative charge at the edge of the semiconductor. As the Fermi levels equalize, the transfer of charge from the metal to the semiconductor continues without having an added potential barrier to cross. The symbols utilized in this figure are explained in the text above. Eventually, when an external voltage is applied to the shown junction, electrons will be able to easily flow between both materials in both directions (electron movement shown by the green and orange arrows in (b)). As this is a characteristic of ohmic materials, such contacts are called ohmic contacts [77, 82].	13
Figure 1.10: Schematic diagram of the current flow lines across an interface with restricted crossing points. (taken from [83]). The labels M1, M2, P1 and P2, indicating respectively Material 1, Material 2, Point 1 and Point 2, were added in this work for the sake of the in-text discussion.	14
Figure 1.11: Calculated formation energies for intrinsic point defects in Mg_2X ($\text{X} = \text{Si}, \text{Ge}, \text{Sn}$) as functions of the Fermi energy. For each material type, the calculations are done under Mg-rich chemical potential conditions, as well as X-rich chemical potential conditions. The figure is taken from [41]. .	18
Figure 2.1: Diagram representing the third and last melting cycle of the induction melting route for n- (in blue) and p- (in red) type powder samples, reaching the final temperature of 900 °C.	22
Figure 2.2: Schematic representation of the graphite crucible fixed inside the Direct Sintering Press DSP chamber. The zoomed-in section shows the thermocouple that just remains inside the wall of the crucible, very close to the inner edge, but without actually going inside the crucible.....	23
Figure 2.3: Synthesis method for p-type $\text{Mg}_2\text{Si}_{1-x}\text{Sn}_x$ (The same method is used for n-type with Bi as dopant). The method is divided into three steps until the final pellet is obtained: a melting of the precursors following a route explained above (Chapter 2.1.1), high energy ball milling of the ingot obtained from melting (Chapter 2.1.2), and pressing in the direct sinter press (Chapter 2.1.3). The synthesis parameters depend on the desired composition.	26

Figure 2.4: Different joining methods of pressed pellets with Cu foil as an example. The first joining method referred to as <i>direct resistive heating</i> method, is a procedure during which the current from the direct sinter press (DSP) runs freely through the sample. The second joining method, called <i>indirect resistive heating</i> , is a procedure where layers of a boron nitride solution are added on top and bottom of the sample arrangement. By doing so, the current from the DSP is hindered from passing vertically through the sample and, instead, has to go through the graphite die around.....	28
Figure 2.5: Schematic of the a) Seebeck coefficient microprobe measurement, b) the potential drop measurement in the PSM facility (taken from [105])......	31
Figure 2.6: Representative line scan of the Seebeck profile (in black) and the potential profile (in blue) for an annealed n-type $\text{Mg}_2\text{Si}_{0.3}\text{Sn}_{0.7}$ sample contacted with Cu foil. The orange rectangles delimit the thickness of the Cu electrodes, and the green and red circles indicate the region where $V_{\text{elec}} - V_{\text{TE}}$ is read in order to calculate the electrical contact resistance. In this example, the left hand-side marked by the green circle shows a very smooth transition from the electrode region to the TE material region. Therefore, the specific electrical resistance r_c is expected to be low. However, on the right-hand side marked with the red circle, the passage from the TE material to the electrode exhibits a large drop in the potential line. Here, r_c is expected to be high. ΔV_{TE} would be the difference between the voltage value at the left-hand side (at $x = 0.15$ mm) and the voltage value at the right-hand side of the TE sample (at $x = 1.05$ mm).	33
Figure 2.7: Pictures of a) coated cut sample before annealing, b) ampoules after annealing. The darker areas of the ampoules indicate evaporated Mg that deposited on the inner walls.	35
Figure 6.1: SEM images of the cross section of non-contacted p-type $\text{Mg}_{1.97}\text{Li}_{0.03}\text{Si}_{0.3}\text{Sn}_{0.7}$ obtained through a) induction melting and through b) ball milling.	127
Figure 6.2: XRD spectra for the high energy ball milled (BM) and induction melted (IM) pressed p-type $\text{Mg}_{1.97}\text{Li}_{0.03}\text{Si}_{0.3}\text{Sn}_{0.7}$ powders, compared with an XRD pattern of a pure undoped $\text{Mg}_2\text{Si}_{0.3}\text{Sn}_{0.7}$ sample reported in [97]. The black star symbols pinpoint shoulder peaks in the BM sample indicating phase separation (Mg_2Sn phase).....	128
Figure 6.3: Graphs of normalized counts showing composition distribution of the a) induction melted (IM) sample and b) the ball milled (BM) sample as a function of the Sn content in $\text{Mg}_2\text{Si}_{1-x}\text{Sn}_x$ composition range. These counts are obtained from a <i>Gray scale analysis calibrated using EDX data</i> [156]. The IM sample shows a narrower range of composition distribution (FWHM = 0.136) centered around the main desired composition $\text{Mg}_2\text{Si}_{0.3}\text{Sn}_{0.7}$, while the BM sample shows a wider distribution range (FWHM = 0.186), indicating a sample with a less homogeneous matrix and more secondary phases.	128
Figure 6.4: SEM images of the cross section of Cu-contacted p-type $\text{Mg}_{1.97}\text{Li}_{0.03}\text{Si}_{0.3}\text{Sn}_{0.7}$ once obtained through a) induction melting and once through b) ball milling. Images c) and d) represent local high magnifications of the interfaces of the contacted induction melted and ball milled pellets, respectively.	130
Figure 6.5: Thick (250 μm) and thin (50 μm) Cu disk foils, exhibiting the difference in surface flatness and the presence of wrinkles between them.	132
Figure 6.6: SEM images of the cross section of a) n-type $\text{Mg}_{2.06}\text{Si}_{0.3}\text{Sn}_{0.665}\text{Bi}_{0.035}$ and b) p-type $\text{Mg}_{1.97}\text{Li}_{0.03}\text{Si}_{0.3}\text{Sn}_{0.7}$ contacted with thick treated Cu foil. Figures c) and d) represent magnified images of the resulting reaction layers after reaction and diffusion between the treated Cu foil and n- and p-type samples, respectively. The reaction layers are very similar in microstructure and detected phases to the samples for which untreated foils were employed, reported in Chapter 3.	133
Figure 6.7: PSM line scans of a) n-type $\text{Mg}_{2.06}\text{Si}_{0.3}\text{Sn}_{0.665}\text{Bi}_{0.035}$ and b) p-type $\text{Mg}_{1.97}\text{Li}_{0.03}\text{Si}_{0.3}\text{Sn}_{0.7}$ contacted with thick pre-treated Cu foil. The Seebeck profile lines are shown with the black lines, while the potential across the samples are shown with the blue lines. The green dashed line marks the Seebeck value of the TE materials before contacting.	135

Figure 6.8: Schematic figure to show the idealized current trajectories (colored arrows) across the graphite system and the sample inside it under a) “direct resistive heating” and b) “indirect resistive heating” joining conditions. The red arrows show the main path of the current under each joining condition. In a), the blue arrows show a secondary potential current path, but with a smaller current fraction than the main path (red arrow. In b), boron nitride (BN) layers are added above and below the sample to block the current from running through it.....	137
Figure 6.9: SEM images of Ni ₄₅ Cu ₅₅ -contacted n- and p-type Mg ₂ Si _{0.3} Sn _{0.7} a) and b) under direct resistive heating respectively, and c) and d) under indirect resistive heating, respectively.	139
Figure 6.10: PSM line scans of n- and p-type Mg ₂ Si _{0.3} Sn _{0.7} contacted with Ni ₄₅ Cu ₅₅ under a) and b) direct, c) and d) indirect resistive heating. The black lines represent the Seebeck profiles of the samples and the blue lines represent the potential across the samples. The green dashed lined mark the Seebeck value of the TE material before contacting.	140
Figure 6.11: Charged defect formation energies of Cu in: a) Li-doped and b) Bi-doped Mg ₂ Si under Mg-poor conditions c) Bi-doped Mg ₂ Si under Mg-rich conditions, d) Li-doped and e) Bi-doped Mg ₂ Sn under Mg-poor conditions f) Bi-doped Mg ₂ Sn under Mg-rich conditions. For simplicity, the Li-doped Mg ₂ Si and Mg ₂ Sn are only represented in the Fermi level region around the VBM while the Bi-doped samples are represented in the Fermi level region around the CBM. The labeling X _Y of the defects (where X and Y are chemical elements) on the figure correspond to the X _Y labeling in the text. X _{int} and X _{vac} correspond respectively to I _X and V _X	148
Figure 6.12: Charged defect formation energies of Ag (dashed lines) and Cu (full lines) in Bi-doped Mg ₂ Si a) under Mg-poor and b) Mg-rich conditions and in Bi-doped Mg ₂ Sn, c) under Mg-poor and d) under Mg-rich conditions. The intrinsic and dopant defects are also presented in full lines, and only the relevant defects with formation energies < 1 eV are plotted. The labeling X _Y of the defects (where X and Y are chemical elements) on the figure correspond to the X _Y labeling in the text. X _{int} and X _{vac} correspond respectively to I _X and V _X	156
Figure 6.13: Charged defect formation energies of Ni in: a) Li-doped and b) Bi-doped Mg ₂ Si under Mg-poor conditions c) Bi-doped Mg ₂ Si under Mg-rich conditions, d) Li-doped and e) Bi-doped Mg ₂ Sn under Mg-poor conditions f) Bi-doped Mg ₂ Sn under Mg-rich conditions. For simplicity, the Li-doped Mg ₂ Si and Mg ₂ Sn are only represented in the Fermi level region around VBM while the Bi-doped samples are represented in the Fermi level region around CBM. The labeling X _Y of the defects (where X and Y are chemical elements) on the figure correspond to the X _Y labeling in the text. X _{int} and X _{vac} correspond respectively to I _X and V _X	158
Figure 6.14: Average Seebeck profile line scan (with error bars) on the surfaces of as-sintered a) p-type Mg _{1.97} Li _{0.03} Si _{0.8} Sn _{0.2} , b) n-type Mg _{2.06} Si _{0.8} Sn _{0.17} Bi _{0.03} , and representative Seebeck profile lines of c) p-type Mg _{1.97} Li _{0.03} Si _{0.8} Sn _{0.2} contacted with Ni and d) n-type Mg _{2.06} Si _{0.8} Sn _{0.17} Bi _{0.03} contacted with Ni. The green dashed lines on c) and d) indicate the Seebeck coefficient values of the TE material before contacting.	161
Figure 6.15: Most stable native defects (in dashed lines) and Li (dopant)-related defects (in full lines) in Mg-poor Mg ₂ Si, showing the pinning of the Fermi level inside the band gap. The labeling X _Y of the defects (where X and Y are chemical elements) on the figure correspond to the X _Y labeling in the text. X _{int} and X _{vac} correspond respectively to I _X and V _X	163
Figure 7.1: Schematics of charged defect formation energies for Ti defects in: a) Li-doped and b) Bi-doped Mg ₂ Si, c) Li-doped and d) Bi-doped Mg ₂ Sn, all under Mg-poor conditions. The labeling X _Y of the defects (where X and Y are chemical elements) on the figure correspond to the X _Y labeling in the text. X _{int} and X _{vac} correspond respectively to I _X and V _X	173

List of Symbols and Abbreviations

Fundamental Constants

Quantity	Symbol	Value
Fundamental electron charge	e	$1.6 \times 10^{-19} \text{ C}$
Planck's constant	h	$6.62 \times 10^{-34} \text{ m}^2 \text{ kg s}^{-1}$
Electron mass	m_0	$9.1 \times 10^{-31} \text{ kg}$
Boltzmann's constant	k_B	$8.61 \times 10^{-5} \text{ eV K}^{-1}$

Physical Quantities

Quantity	Symbol	Unit
Temperature	T	K
Pressure	p	MPa
Time	t	min
Area	A	cm^2
Electrical current	I	A
Electrical current density	j	A mm^{-2}
Voltage	V	V
Resistance	R	Ω
Density	ρ	g cm^{-3}
Power output	P	W
Heat flow	Q	W

Thermoelectric Properties

Quantity	Symbol	Unit
Seebeck coefficient	S	V K^{-1}
Electrical conductivity	σ	S m^{-1}
Thermoelectric power factor	$S^2 \sigma$	$\text{W m}^{-1} \text{K}^{-2}$
Total thermal conductivity	κ	$\text{W m}^{-1} \text{K}^{-1}$
Electronic thermal conductivity	κ_e	$\text{W m}^{-1} \text{K}^{-1}$
Lattice thermal conductivity	κ_L	$\text{W m}^{-1} \text{K}^{-1}$
Bipolar thermal conductivity	κ_{bi}	$\text{W m}^{-1} \text{K}^{-1}$
Figure of merit of devices	ZT	-
Figure of merit of materials	zT	-
Electrical contact resistance	R_c	Ω
Specific electrical contact resistance	r_c	$\Omega \text{ cm}^2$
Thermal conductance	K	W K^{-1}
Peltier coefficient	Π	V
Thomson coefficient	τ_T	V K^{-1}
Maximum efficiency	η_{\max}	%

Lorenz number	L	V^2K^{-2}
Carrier concentration of electrons	n	cm^{-3}
Charge mobility	μ	$m^2 V^{-1} s^{-1}$
Density of state effective mass	m_D^*	m_0
Fermi level	E_F	eV
Energy	E	eV
Electron affinity	χ	$kJ mol^{-1}$
Work function of material X	Φ_X	eV
Hamiltonian operator	\hat{H}	J
Band gap	E_g	eV
Reduced chemical potential	η	-

Synthesis and Characterization

- IM: Induction melting
- HEBM/BM: High energy ball milling/Ball milling
- SEM: Scanning Electron Microscopy
- BSE: Back Scattered Electrons
- EDX: Energy Dispersive X-ray Spectroscopy
- WDS: Wavelength Dispersive Spectroscopy
- PSM: Potential Seebeck Microprobe
- XRD: X-ray Diffraction

Lattice Point Defects

- V_X : X vacancy: atom X missing from its lattice site
- I_X : X interstitial: atom X sitting on an interstitial site in the lattice
- X_Y : X atom on Y site: atom X sitting on Y atom's lattice site
- q : defect charge [-2, -1, 0, 1, 2]

Abbreviations

- TE: Thermoelectric
- TEG: Thermoelectric generator
- CTE: Coefficient of thermal expansion
- HIP: Hot isostatic pressing
- BN: Boron nitride
- HMS: Higher manganese silicides
- FWHM: Full width at half maximum
- DFT: Density functional theory

- GGA: Generalized Gradient Approximation
- PBE: Perdew-Burke-Ernzerhof
- LDA: Local-density approximation
- HSE: Heyd-Scuseria-Ernzerhof
- CB: Conduction band
- CBM: Conduction band minimum
- VB: Valence band
- VBM: Valence band maximum

Thesis Abstract

Solid solutions of Mg_2Si and Mg_2Sn ($\text{Mg}_2(\text{Si},\text{Sn})$) are some of the most attractive thermoelectric materials by virtue of several properties of their constituents such as being abundant, light-weight, non-toxic and environmentally friendly. They also have attractive thermoelectric properties, particularly for the n-type counterparts [1-3]. In order to implement these materials in technological applications, several n- and p-type legs need to be assembled as thermoelectric generators, for which they need to be contacted electrically in series through metallic electrodes. This contacting step of the thermoelectric legs with the metallic electrode is vital in the development of the generators. Yet, only a small portion of the research in thermoelectricity has been focusing towards it. In fact, the criteria of selection for a suitable electrode are not very well established, which complicates experimental investigations and thermoelectric generator development.

This thesis tackles the topic of contacting $\text{Mg}_2(\text{Si},\text{Sn})$ thermoelectric materials by evaluating several candidate materials for electrodes and providing a path towards a more exhaustive list of requirements for electrode selection, based on both experimental testing and *ab-initio* calculations.

In a first study, Cu and $\text{Ni}_{45}\text{Cu}_{55}$ electrodes were tested with n- (Bi-doped) and p- (Li-doped) type $\text{Mg}_2\text{Si}_{0.3}\text{Sn}_{0.7}$ materials, selected based on their fitting coefficients of thermal expansion (CTE). Our obtained results report successful joining with the p-type counterpart for both electrodes, and annealing experiments with Cu also confirm the stability of the contacts. Low electrical contact resistance values ($\leq 15 \mu\Omega \text{ cm}^2$) were obtained for both material types using both electrodes, and these values remained relatively low with Cu after annealing. An unexpected behavior was, however, observed where the Seebeck coefficient S changed by $\sim 50\%$ in the n-type materials after joining with both electrodes, while no such change occurred with the p-type samples. A further change in S was also observed after the Cu-joined n-type sample was annealed.

Following this work, experiments to understand the role and implication of the electrical current of the direct sinter press during the joining process were processed. For this purpose, an *indirect resistive heating* method was proposed and tested, where an electrically insulating layer was added on both sides of the sample system in an attempt to block the current from running through the sample. On the other hand, the samples contacted in the initial study were done following a *direct resistive heating* method where no insulating layer was included, and the sintering current was free to run through the sample. Comparing the results of both methods with Cu joining showed that the change in S still occurred, independently of the used method.

As a previous study also reported such change in S in n-type $\text{Mg}_2\text{Si}_{1-x}\text{Sn}_x$ but not in p-type after joining with Ag [4], it became clear that this behavior was not a one-time occurrence related to a particular

electrode; instead it was a general tendency in the behavior of our used TE materials with various electrodes. As the change in S was constantly observed with only one material type, a dependence of the behavior on the charge carrier concentration was concluded. As charge carrier concentrations are determined by the material's defects, the focus of this thesis widened to include materials' charged point defects. Here, we looked into the formation energies, therefore stabilities, of the intrinsic and extrinsic defects of the material system (doped thermoelectric material + electrode), and their relevance in the chemical potential windows of interest. To obtain these formation energies, hybrid-DFT calculations were conducted by our collaborators in the Korea Electrotechnology Research Institute (KERI), and comparisons with experimental data was processed.

To facilitate this first study involving defects, Ag was experimentally contacted with n-type (also Bi-doped) Mg_2Si and Mg_2Sn , as the hybrid-DFT calculations were done for the binary systems. The results of the experimental tests reported Ag defect diffusion in both binaries, causing, in fact, a change in the Seebeck value, which fits with the literature report on the ternary composition. Defect calculations predicted that the Ag substitutional defect on the Mg lattice site (Ag_{Mg}) would be the most stable defect in the Bi-doped $\text{Mg}_2(\text{Si},\text{Sn})$ systems. As Ag_{Mg} is an electron-acceptor defect with a low enough formation energy, it would trap the conduction electrons donated by the Bi atom on the Si/Sn site defect ($\text{Bi}_{\text{Si/Sn}}$), which is the main electron donor defect in the materials. This trapping of the conduction electrons results in a compensation of the charge carriers, which would experimentally translate into a change in the thermoelectric properties.

As this study reached a good match between the experimental data and the calculation predictions, the method where hybrid-DFT is used to predict the behavior of the joining electrode defects on the $\text{Mg}_2(\text{Si},\text{Sn})$ system was established and further tested. Hybrid-DFT calculations of Cu and Ni defects in Bi- and Li-doped Mg_2Si and Mg_2Sn systems were then processed, and the results were compared with the experimental findings of the Cu joining from this work and the Ni joining from previous literature [5], as well as new experiments introduced in this thesis. Upon these comparisons, we could establish good matches between hybrid-DFT predictions for defect stability and contacting experiment results, which in turn established the importance of considering defect formation energy calculations in the contacting electrode selection procedure.

As necessary as it may be, the step of contacting thermoelectric materials to build thermoelectric generators is rather challenging. No clear guidelines have been established yet, and fulfilling the available requirements (matching coefficients of thermal expansion, low electrical contact resistance, good mechanical adhesion, long term stability) is already laborious. In fact, all these requirements need experimental testing, but the pool of electrode candidate materials to select from and investigate is very large, which makes experimental investigations costly. Therefore, more pre-selection criteria are needed, to narrow down the available options. Through this thesis, we succeeded in establishing such a pre-selection requirement based on the defect formation energies of the materials' charged point defect.

Such calculations are highly automatable and provide predictions of the behavior of the thermoelectric material and the electrode of choice, which then tells if a certain electrode has potential to be a successful solution or not, before going through experimental investigations. With this newly established method, we believe that this work can make the electrode selection process simpler and can pave the way towards clearer guidelines for the $\text{Mg}_2(\text{Si},\text{Sn})$ system in particular, and for other thermoelectric systems in general.

Chapter 1

1. Introduction

The topic of energy is one of the most discussed topics of the decade. Between running out of the traditional energy sources, and a climate change crisis that is getting more serious by the day, finding new energy alternatives that are renewable and not harmful to the planet has gained priority in research, industry and even on the political scene all over the world.

As technologies progress, and as the world shifts further towards a more electronic and numeric platform, the need for electricity increases constantly. To fulfill these demands, countries are using too much oil and fossil fuels, which are having a negative impact on the environment. For this reason, other energy alternatives like solar and wind have been studied for a long time, to eventually lighten the load on oil and fossil fuels. However, these technologies still cannot be used independently due to limitations such as storage and capacity. Therefore, several other renewable energy sources are needed to support solar and wind energies, and research for new environment-friendly sources is constantly growing. Among these technologies, thermoelectricity has proved itself to be an efficient useful alternative [6]. Thermoelectricity can be used in converting (waste) heat into electricity, in small scale refrigeration and temperature control, as well as in thermal sensors. It has already been used since World War II by the Russians for military purposes, and since the 70s by NASA and the Russian spaceflight in several space missions like Voyager, Curiosity, as well as numerous others missions equipped with radioisotope thermoelectric generators (RTGs). Since then, research focuses on implementing more thermoelectric energy sources, not only for space, but also for terrestrial applications.

Our work at the German Aerospace Center (DLR) aims at providing reliable and efficient thermoelectric materials and devices for industrial and technological applications. Thermoelectric devices, being the final product of the research cycle, are self-sufficient modules that are highly reliable and have no movable parts. Therefore, once a device is built and functioning, it should be able to continue functioning for its entire planned lifetime. Thermoelectric devices are composed of optimized thermoelectric materials which are n- and p-type doped semiconductors called legs, that are electrically connected using metallic electrodes to guarantee a flow of the electric current with minimum contact resistances.

Therefore, in order to guarantee an efficient functional thermoelectric device, not only do the thermoelectric legs have to be efficient, but also the metallic connections between them have to be optimized and not hinder the current flow along the device, which would cause losses and decrease the performance.

The following sections will start with a brief history of thermoelectricity, followed by an overview on thermoelectric devices, then a few criteria to take into consideration while arranging the thermoelectric legs together using metallic electrodes.

1.1. Thermoelectric Effects

Thermoelectricity can be used for several applications, among which is the conversion of waste heat directly into electricity. It encompasses three different effects which are physically closely interlinked with each other: the Seebeck effect, the Peltier effect and the Thomson effect. The origin of these effects, usually observed in metals and semiconductors, is the motion of the charge carriers.

The Seebeck effect is the generation of voltage (difference of electrical potential) as a temperature difference is applied to a thermoelectric material in open-circuit voltage (no current flow) [7]. It was first observed in 1821 by Thomas J. Seebeck, and it occurs when charge carriers move inside a metal or a semiconductor, creating a redistribution of charge from one end to the other. These charge carriers are mainly electrons in n-type materials and holes in p-type materials. The Seebeck coefficient S is defined as the constant of proportionality between the difference of temperature ΔT and the voltage V between both ends of the material in an open circuit [8, 9] as follows: $V = - S \Delta T$.

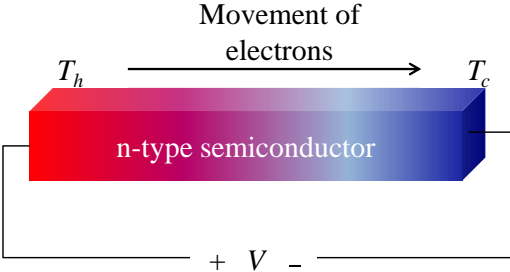


Figure 1.1: Visualization of the Seebeck effect as the movement of the dominant charge carriers (electrons in this case) in a material (n-type semiconductor in this case) under temperature gradient (T_h is the hot side and T_c is the cold side) generating an open-circuit voltage V .

Figure 1.1 displays the example of an n-type semiconductor generating an open-circuit voltage after being subjected to a difference of temperature. The higher temperature T_h at the hot side results in a higher thermal motion of the charge carriers, which leads to a thermal diffusion of the majority charge carriers (electrons, in the presented n-type semiconductor example) from the hot side towards the cold side. This thermal diffusion creates a redistribution of the charge carriers, where the majority charge carriers (electrons in our example) accumulate at the cold end, creating a difference in voltage between

both ends. When a steady-state is achieved, such difference in the charge densities between both material ends develops a voltage that balances the thermal diffusion driving force [10, 11].

Closely related to the Seebeck effect is the Peltier effect. Discovered by Jean Charles Athanase Peltier in 1834, the Peltier effect can be seen as the reverse effect of the Seebeck effect. In fact, while the latter concerns a voltage generated due to a difference in temperature, the former usually involves a temperature gradient induced as a result of a current flow through a junction between two connected materials M1 and M2. At this junction, heat will be either emitted or absorbed, depending on the direction of the current, which results in a warming up or a cooling down of the junction. Similarly to the Seebeck coefficient, a Peltier coefficient Π can be defined as follows: $Q = \Pi I$, where Q is the appearing Peltier heat per time unit and I the electrical current [8].

The Peltier effect is related to the Seebeck effect as $\Pi_{M1} - \Pi_{M2} = (S_{M1} - S_{M2})T$ [12].

Another effect related to the Seebeck and Peltier effects is the Thomson effect, observed by Lord Kelvin in 1855. In various materials, the Seebeck coefficient is not a constant value, but instead, varies with the variation of temperature across the material. In fact, as the current flows through a semiconducting material subjected to a temperature gradient, heat will be emitted or absorbed, because the Seebeck coefficient is a temperature-dependent property. At every point of the material, the appearing heat (Thomson heat) is then generated or absorbed, and can be expressed through $q_x = -\tau_T j_x \frac{\partial T}{\partial x}$, where τ_T is the Thomson coefficient, j_x is the electrical current density and $\frac{\partial T}{\partial x}$ is the temperature gradient. The Thomson coefficient is defined as $\tau_T = T \frac{\Delta S}{\Delta T}$ [13, 14].

These effects introduced above are known as the thermoelectric effects and they are the basis of the function of different thermoelectric devices [15]. The function of thermoelectric generators (TEGs) in particular is based on the Seebeck effect; however, it is important to keep in mind that the Peltier and Thomson effects also act on a TEG, simultaneously to the Seebeck effect. Further details about these TEGs and their development will be presented in the following sections.

1.2. Thermoelectric Devices

In order to be implemented into technological applications, n- and p-type semiconducting thermoelectric materials need to be assembled together into a thermoelectric device [15]. This device is composed of optimized n- and p-type TE materials arranged electrically in series and thermally in parallel, interconnected with metallic layers. Thermoelectric devices can be operated in two different modes: refrigeration and power generation. In the first mode, which utilizes the Peltier effect, a DC power supply provides an electric current which creates a Peltier heat flow along the device, leading to the cooling of

one of the device surfaces. The second mode, which is based on the Seebeck effect, results in a current flow, a voltage across the thermoelectric legs, and an electrical power output created by a difference of temperature. Both are represented in Figure 1.2.

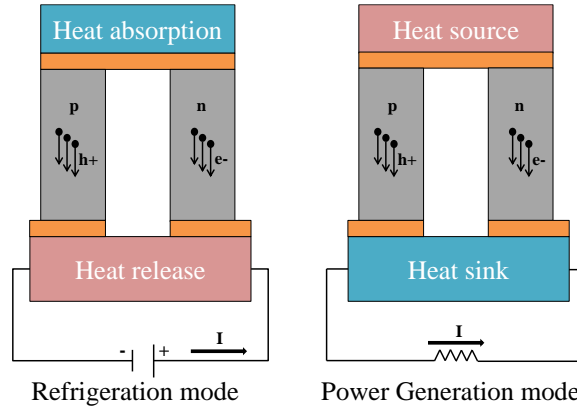


Figure 1.2: Refrigeration (left) and power generation (right) modes for thermoelectric devices.

The efficiency of a thermoelectric device depends on the efficiency of its TE legs and the quality of the contact between them [7, 16]. The performance of a TE material is characterized by its figure of merit $zT = \sigma S^2 T / \kappa$, where σ is the electrical conductivity, S the Seebeck coefficient, T the absolute temperature and κ the thermal conductivity. In order to improve the performance of a TE material, researchers have been trying to increase the power factor $PF = \sigma S^2$, while trying to lower the thermal conductivity κ . To achieve the former and improve the electrical properties, band structure engineering has been implemented to obtain an optimum S and σ . As for the thermal conductivity κ , it is the sum of the lattice thermal conductivity κ_L , the bipolar thermal conductivity κ_{bi} and the electronic thermal conductivity $\kappa_e = L\sigma T$, where L is the Lorenz number. In order to minimize κ , methods like alloying or nanostructuring have been employed, which would lower the lattice thermal conductivity κ_L . However, when a TE material is optimized by increasing its electrical conductivity σ , the electronic thermal conductivity κ_e , hence the total thermal conductivity κ , also increases. This duality represents one of the biggest challenges in thermoelectricity. To counteract this, new methods relying on studying point defects and their formation energies to simultaneously optimize the electrical and thermal properties are being researched.

As for TE devices, their performance can be determined through their efficiency η which is the ratio of power output ($P = Q_{in} - Q_{out}$) to the heat input $\eta = P/Q_{in}$ [17-19]. Considering that η_n and η_p are respectively the efficiencies of the n and p type elements, $\eta = (\eta_n Q_n + \eta_p Q_p) / (Q_n + Q_p)$ [20]. The more n-p couples a device has, the larger the power output. Assuming temperature-independent material properties, the device's maximum efficiency is given by

$$\eta_{\max} = \frac{\Delta T}{T_h} \frac{\sqrt{1+ZT}-1}{\sqrt{1+ZT}+\frac{T_c}{T_h}} \quad \text{Equation 1.1}$$

From Equation 1.1, it is clear that the conversion efficiency of a device is related to the Carnot factor $\frac{\Delta T}{T_h}$ –which is the ratio of the difference of temperature across the TE legs (ΔT) by the hot side temperature T_h – and is dependent on the device figure of merit ZT [21, 22], which is defined as

$$ZT = \frac{S_{\text{dev}}^2 T}{RK} = \frac{S_{\text{dev}}^2 T}{(R_{\text{leg}}+R_c)(K_{\text{leg}}+K_b)} \quad \text{Equation 1.2 .}$$

ZT is the sum value for all n- and p-type legs. In Equation 1.2, S_{dev} is the Seebeck coefficient of the device which is the summation of the Seebeck coefficients of the n-type (S_n) and p-type legs (S_p) as $S_{\text{dev}} = N(|S_n| + |S_p|)$ with N being the number of n-p leg pairs, R is the total electrical resistance and K the total thermal conductance. R_{leg} , R_c , K_{leg} and K_b are respectively the total electrical resistance of the TE legs, the electrical contact resistances, the thermal conductance of the TE legs (which also includes the thermal contact resistances) and the thermal conductance of the parasitic heat paths that bypass the legs (thermal losses due to convection and radiation). The electrical contact resistances hinder the flow of the current in the device, while the thermal contact resistances change the real temperature that is actually felt by the TE material. In fact, due to the thermal resistances of the various layers that need to be added to the TE material (metallization layer, solder layer, external ceramic layer, etc.), the temperature that reach the TE material from the hot side of the device is lower than the initial externally input temperature. Therefore, in order to have an optimized and efficient TE device, not only do the TE materials need to possess optimum electrical and thermal properties, but also the contacts between these legs and the metallic layers (as well as the thermal bypass K_b) need to be optimized.

In this work, we will only focus on electrical contact resistance measurements and optimization, as they are a more imminent task in the early stages of finding contacting solutions for TEGs, compared to thermal contact resistances. Figure 1.3 shows examples of the influence of the electrical contact resistance on the device properties. Figure 1.3 a, taken from a work by Ebling *et al.* [23], demonstrates the influence of the electrical contact resistance on different modules' ZT with different Bi_2Te_3 leg lengths. Figure 1.3 b, taken from Goupil *et al.* [24], displays the decrease the efficiency of a Zn_4Sb_3 -based TE device as the electrical contact resistance increases (shows by the arrow on the figure). Note here that Figure 1.3 a presents values of the electrical contact resistance R_c which is not the usual quantity used for comparison. Instead, the specific electrical contact resistance $r_c = R_c \times A$, (A is the area) is usually utilized to qualify good or bad contacts, as it is independent of the surface area.

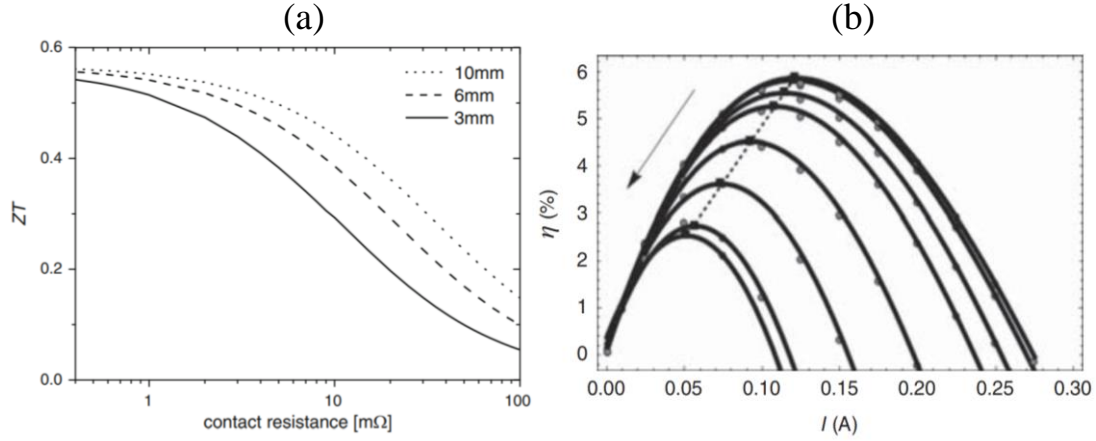


Figure 1.3: a) Sample curves of simulation results of the impact of the total electrical contact resistance R_c on a) ZT of modules using different Bi_2Te_3 leg lengths (taken from [23]). b) Efficiency of a Zn_4Sb_3 -based TE device as R_c is varied between 0 and $1000 \mu\Omega \text{ cm}^2$. The direction of the increase of R_c is displayed by the arrow. The points represent the calculated values and the solid lines represent polynomial fits. (taken from [24]).

As can be seen from Figure 1.3, an increase in R_c ultimately results in a decrease in ZT (as defined by Equation 1.2) and thus in the maximum efficiency of the device. Therefore, minimizing the electrical contact resistance is crucial in developing highly performing TE devices. One of the ways to increase the output power of a device is to lower the length of the TE legs. However, usually, a minimum leg length is imposed by the contact resistance between the actual leg and the metallization layer.

Some of the highly optimized thermoelectric materials presented in literature are PbTe [25-28], half Heusler compounds [29-31], Skutterudites [32-34], SnSe [35] and $\text{Mg}_2(\text{Si}, \text{Sn}, \text{Ge})$ materials [1, 3, 36-41]. For most of these material systems (and particularly Bi_2Te_3 -based materials), efficient n- and p-type have been reported, fulfilling the first step in TE module building. The next step is to find suitable metallic electrodes to contact these single legs [42].

The next section (Chapter 1.3) introduces this thesis' TE material system of interest which is the Mg_2X system. Contacting will be discussed in further details in a following section (Chapter 1.4).

1.3. Thermoelectric Materials: Mg_2X ($\text{X} = \text{Si}, \text{Sn}$)

Among the material systems that are studied recently are the Mg_2X binaries and their solid solutions due to the several attractive properties they possess. In fact, this material system has a low density and is composed of cheap and abundant elements, and is non-toxic and environment-friendly. Thus, it is very attractive for several industry fields [43]. The most studied Mg_2X materials are Mg_2Si , Mg_2Ge and Mg_2Sn , as well as their solid solutions [39, 44, 45].

Commercially, based on a PubChem database search performed in August 2021, undoped Mg_2Si is available as powder (e.g. -20 mesh (~ 0.8 mm) particle size from Sigma-Aldrich) or in larger pieces (3~12 mm piece size from VWR International). Other Mg_2X compounds, however, aren't as easily found. In fact, Mg_2Sn isn't available for purchase, and Mg_2Ge is only provided by a limited number of distributors and can cost about 8 times as much as Mg_2Si . Similarly, up to date, no thermoelectric generators based only on the Mg_2X system are commercially available. Nevertheless, some technological applications of Mg_2X -based thermoelectric generators could be automotive and aircraft industries where light-weight materials are preferred and would increase the power density as reported in the work of Kim. *et al* where they studied an n-type Mg_2Si and a p-type higher manganese silicide (HMS) based TEG [46].

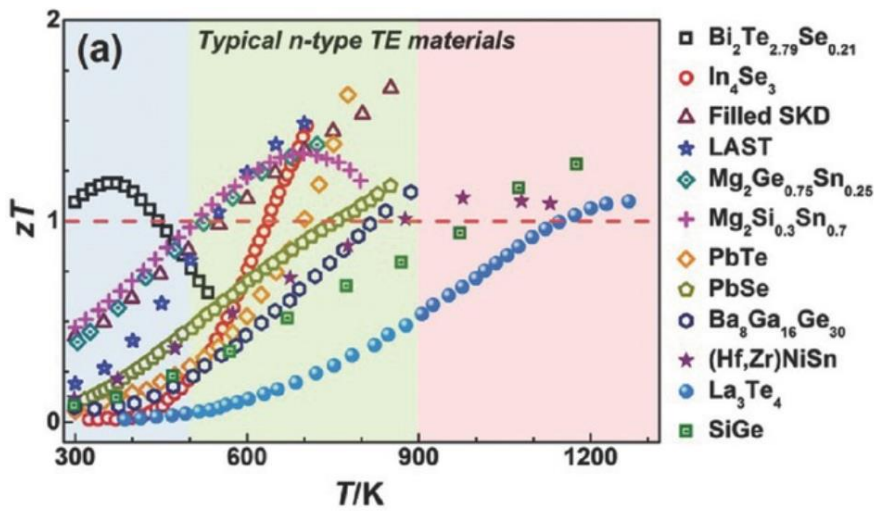


Figure 1.4: State-of-the-art comparison of ZT in different n-type materials (taken from Zhu *et al.* [47])

So far, n-type Mg_2X materials were thoroughly synthesized and studied, with improved reports of their thermoelectric properties [48-50]. Figure 1.4 also shows the high ZT of n-type $\text{Mg}_2\text{Si}_{0.3}\text{Sn}_{0.7}$ and $\text{Mg}_2\text{Ge}_{0.75}\text{Sn}_{0.25}$ in the mid-range temperatures. As efficient p-type Mg_2X was harder to achieve, higher manganese silicides (HMS) were first used as the p-type counterpart to the n-type Mg_2X materials [51, 52]. However, differences in the coefficient of thermal expansions (CTE) of both material systems lead to inevitable thermal stresses that would cause device failure [53]. In fact, the CTE of n-type $\text{Mg}_2(\text{Si},\text{Sn})$ materials usually ranges between 16 and $18 \times 10^{-6} \text{ K}^{-1}$, while the p-type HMS system has a CTE ranging between 9 to $13 \times 10^{-6} \text{ K}^{-1}$ [54-56]. The difference in the elements composing the TE material system would also present an issue while trying to develop contacting solutions for the TE devices, as different elements react differently with the electrode materials. In fact, having the same materials on both sides of the thermoelectric pair guarantees a similar behavior of the legs under mechanical and thermal stresses, which facilitates the study of the systems, as well as the achievement of thermomechanical

durability. For these reasons, p-type Mg_2X was also well studied, and optimized properties have been recently reported [57-60].

One challenge in optimizing TE materials and obtaining high zT rests on the challenge in finding efficient dopants that would provide an optimum amount of charge carriers to the semiconductor, enhancing its conduction. In fact, as introduced before, zT depends on the electrical conductivity σ and the Seebeck coefficient S , which are both functions of the charge carrier concentration. In semiconductors, both electrons and holes contribute to the Seebeck voltage and current generation, however, to a different extent depending on the material type. In fact, the majority charge carriers, which are electrons in n-type and holes in p-type, have a more significant contribution to the TE properties. For simplicity, we can usually disregard the contribution of the minority charge carriers. Nevertheless, it is important to keep in mind that in some cases such as small band gap materials ($E_g \sim \kappa_B T$) at high temperatures, the contribution of the minority charge carriers will be more significant, as both the electrons and the holes would contribute to the charge transport. In this case, the Seebeck coefficient (as well as the Hall effect [61, 62]) would be greatly affected.

In the case where the contribution of the minority charge carriers is disregarded, the concentration of the majority charge carriers determines the electrical conductivity as shown by the equation $\sigma = n e \mu$, where n is the charge carrier density, and μ is their mobility. Similarly, the Seebeck coefficient can be expressed as $S = \frac{8\pi^2 k_B^2}{3eh^2} m_D^* T \left(\frac{\pi}{3n}\right)^{\frac{2}{3}}$, assuming a highly doped semiconductor, where m_D^* is the effective mass of the carriers [63]. Figure 1.5 portrays this relation between zT and the charge carrier concentration, showing a special window of carrier concentration for which high zT values can be reached, and beyond which zT decreases. This window typically ranges from 10^{19} and 10^{21} per cm^3 .

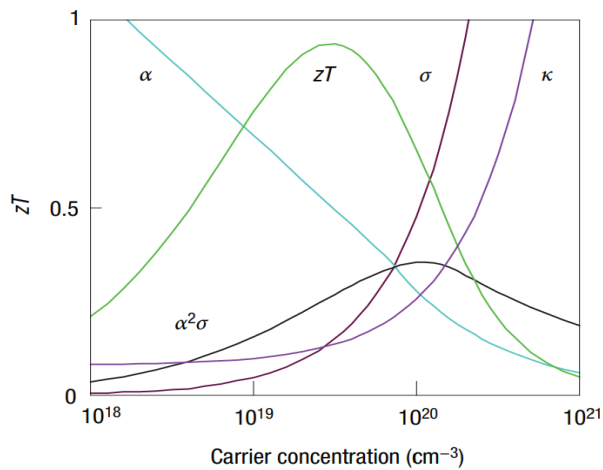


Figure 1.5: Dependence of the dimensionless figure of merit zT on the charge carrier concentration (taken from [63]).

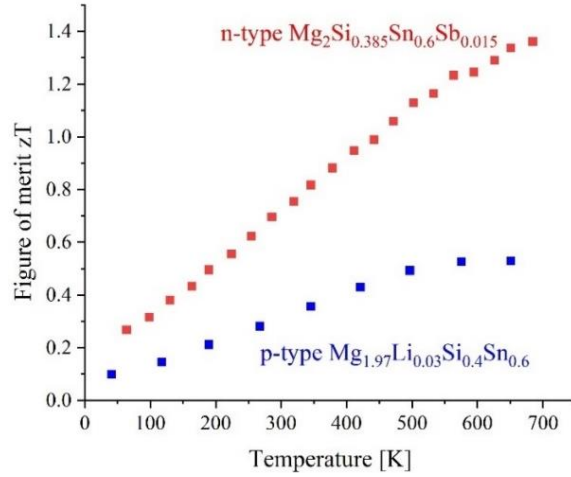


Figure 1.6: Optimized zT of p- (Li doped) and n- (Sb doped) type $Mg_2Si_{0.4}Sn_{0.6}$ composition. Data was taken from [28] and [29] respectively.

In the scope of this thesis, the solid solutions of Mg_2Si and Mg_2Sn are the main focus, because they show better TE properties than the binaries [58, 59, 64]. Recent literature reported both optimized n- and p-type counterparts with high zT reaching ~ 1.4 and 0.55 at 700 K respectively, for the solid solution $Mg_2Si_{1-x}Sn_x$ with $x = 0.6$, as shown in Figure 1.6 above [1, 3]. For these compositions, the corresponding Seebeck coefficient at 700 K is $S \sim -220 \mu V/K$ for n-type and $S \sim 200 \mu V/K$ for p-type. Sb was used as an efficient dopant for the n-type conduction, while Li was used for the p-type conduction. A previous work of Chen *et al.* using Sb as a dopant for $Mg_2Si_{0.4}Sn_{0.6}$ reported compared Seebeck values, where $S = -220 \mu V/K$ was reached at 700 K for 1% Sb doping [65]. In a different work, Bi was also used as an n-type dopant for $Mg_2Si_{1-x}Sn_x$ and showed very attractive properties with S ranging between $-110 \mu V/K$ at room temperature and $-190 \mu V/K$ at 700 K for 3.5% Bi concentration [2]. This Bi concentration corresponded to a $zT \sim 1.3$ at 700 K [2]. As for p-type, Li doping in $Mg_{2(1-x)}Li_xSi_{0.3}Sn_{0.7}$ ($x = 0.00-0.07$), S between 150 and $160 \mu V/K$ at 700 K was reported in a work by Zhang *et al.* for $x = 0.03-0.07$, corresponding to zT values between 0.4 and 0.5 [66].

In this work, Bi-doped n-type and Li-doped p-type $Mg_2Si_{1-x}Sn_x$ will be evaluated with a few metallic electrode materials as a necessary first step in TE module building (Chapters 3 and 4). Nevertheless, the binary compounds Mg_2Si and Mg_2Sn will also be considered when studying the interplay of the material's defects with the electrode-induced defects in the material (Chapter 5), as they are easier to understand compared to defects in solid solution.

1.4. Contacting and Electrode Selection

In actual technological applications of thermoelectricity, the optimized n- and p-type legs are typically connected electrically in series through a conducting multi-layer composed of a metallization layer (also called metallic electrode), a solder layer, a conducting strip commonly called bridge, and a ceramic plate as shown in Figure 1.7.

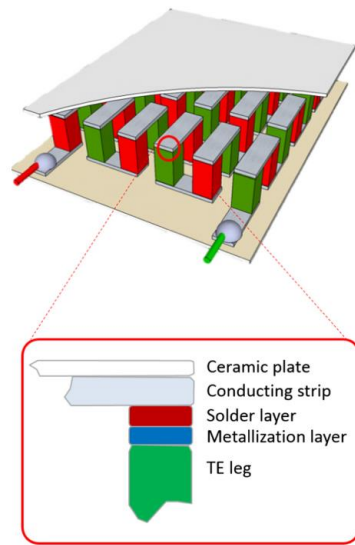


Figure 1.7: Configuration of a functional TE module containing a set of TE legs joined by a conducting multi-layer (Taken from [18]).

The purpose of this multi-layer is to connect the TE legs to each other, so they can be used in a TEG device and current can go through. However, with each added layer, added electrical and thermal resistances come into play, especially between the metallic layer and the TE material. In fact, poor contacts result in a large loss of the ZT and power output of the TE device [67]. Therefore, it is crucial to develop good and reliable contacts to guarantee the durability and the efficiency of the final device.

In this work, we focus only on the contact point between the TE leg and the metallization layer. This layer will be referred to as electrode in the rest of the manuscript. Up to date, there are no clear guidelines as to what qualifies a perfect contact. However, a preliminary list of requirements for electrode selection could be dressed and would include:

- A metallic conducting electrode with high electrical and thermal conductivity
- A good mechanical adhesion between the electrode and the TE leg
- A matching coefficient of thermal expansion (CTE) between the electrode and the TE material of choice to guarantee a similar thermo-mechanical behavior under temperature gradient and thermal cycling

- A controlled reaction and diffusion between both materials, which would guarantee chemical stability
- A low specific electrical contact resistance r_c at the interface, with an acceptable threshold $< 10 \mu\Omega \text{ cm}^2$ ([42]) between the interface contact resistance and the total device resistance, as displayed by Figure 1.8.

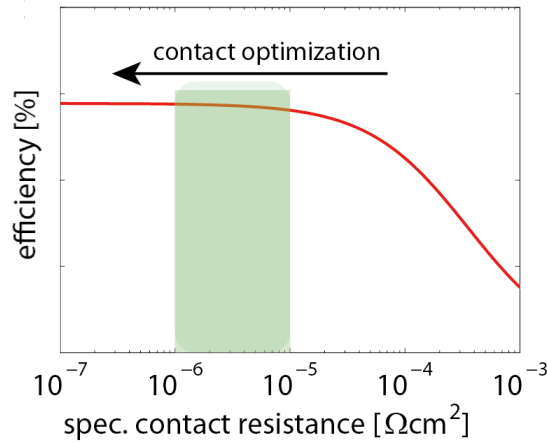


Figure 1.8: Schematic of the efficiency of a TE device as a function of the specific contact resistance.

Contacting on the binary Mg_2X material system was tested with a few electrode materials, and preliminary results were reported in the literature [5, 68-70]. Among these electrodes, Ni was tested several times with n- Mg_2Si , and showed to be more stable up to 400 °C compared to other electrodes [71]. It also resulted in a low specific electrical contact resistance $r_c < 10 \mu\Omega \text{ cm}^2$, even after 168 h of annealing [68]. In the same work, the resulting reaction layer between the electrode and the TE material did not change after thermal treatment, which confirms the stability of the contacts.

Cu electrodes were also evaluated with undoped Mg_2Si [72]. The results showed a good mechanical adhesion between the electrode and the TE materials, and no cracks were observed inside the sample. However, the obtained r_c was relatively high ($\sim 15 \text{ m}\Omega \text{ cm}^2$). The authors related such observation to the fact that the used TE material was undoped, and claimed that, when used with a doped material, lower r_c values would be achieved.

However, as no optimized p-type Mg_2X was reported yet, and as the solid solutions of $\text{Mg}_2(\text{Si},\text{Sn})$ show improved TE properties compared to the binaries, it is more attractive then to develop contacting solutions for the ternary compositions. Prior to this thesis, Ag and Ni were tested on both n- and p- type $\text{Mg}_2\text{Si}_{1-x}\text{Sn}_x$ with $x = 0.6 - 0.7$ [4]. Ag showed a low contact resistance with p-type, but not with n-type. As for Ni, r_c was low for both material types; however, a lot of cracks were observed in the TE material, potentially due to the mismatch in the CTE.

Another interesting feature that was reported in [4] is the change of the Seebeck value of n-type $\text{Mg}_2\text{Si}_{0.3}\text{Sn}_{0.7}$ during contacting with Ag, while no such behavior was observed with the p-type counterpart. As the main difference between the n- and p-type materials is the dopant, this might suggest a connection between the dominant charge carrier type –therefore defects– and the contacting behavior. Chapter 1.6 introduces point defects and their importance in semi-conductors. The main defects in the Mg_2X ($\text{X} = \text{Si}, \text{Sn}$) system are also discussed.

1.5. Electrical contact resistance

The concept of electrical contact resistance was mentioned above as being an important parameter to consider when selecting contacting electrodes (Chapter 1.4) and building TEGs (Chapter 1.2). The electrical contact resistance R_c , as the name implies, is the resistance that the electrical current faces when crossing a contact surface between two different conducting or semi-conducting materials. When two materials M1 and M2 are in contact under a given pressure, both material surfaces are in touch, and, assuming no surface film (such as contamination or oxide layers), there is direct contact between the materials. A current passing from M1 to M2 will encounter a resistance at the junction between M1 and M2 that will hinder its flow. The measure of this contact resistance of the current flow depends on several factors: (i) the class of materials and their conductivity: R_c between two metallic materials will be lower than R_c between a metal and a semi-conductor; (ii) the geometry of the contact surface and its condition (cleanliness, roughness, if there is added lubricant, if there is an interface layer...), and (iii) the applied mechanical pressure holding the contact together.

This work mainly focuses on contacts between a metal and a highly doped semiconductor, so we talk about “*ohmic contacts*” [73-77], as opposed to non-ohmic/rectifying Schottky contacts [78-80]. Ohmic contacts are contacts where the interface potential barrier resulting from the difference in the Fermi levels between the metal and the semiconductor doesn’t manifest itself and/or is narrow and therefore can be easily surpassed by the charge carriers. They are also contacts where the I - V curve has a linear behavior, and where the current can run in both directions across the interface surface [75, 76]. A good ohmic contact would have a negligible contact resistance that maintains the linear I - V behavior and would only generate a voltage drop that is small compared to the voltage drop along the semiconducting material [81].

Figure 1.9 shows an energy band diagram of a contact between a metal and an n-type semiconductor before contacting (a) and after contacting (b). The work function of the metal Φ_M and the work function of the semiconductor Φ_S are respectively defined as the difference in energy between the Fermi level of the metal and the vacuum level, and the Fermi level of the semiconductor with the vacuum level. X is the electron affinity of the semiconductor, and is defined as the difference in energy between the

conduction band edge and the vacuum level. In order to reach equilibrium conditions when both materials are brought into contact, the Fermi levels of the metal and the semiconductor equalize, which results in a bending at the interface in the band gap edges (conduction band with energy E_C and valence band with energy E_V) as shown in Figure 1.9 (b). This bending creates the potential barrier that would need to be surpassed by the charge carriers during their transfer between the materials, and the potential drop across the interface is a function of the difference in the Fermi levels of both materials.

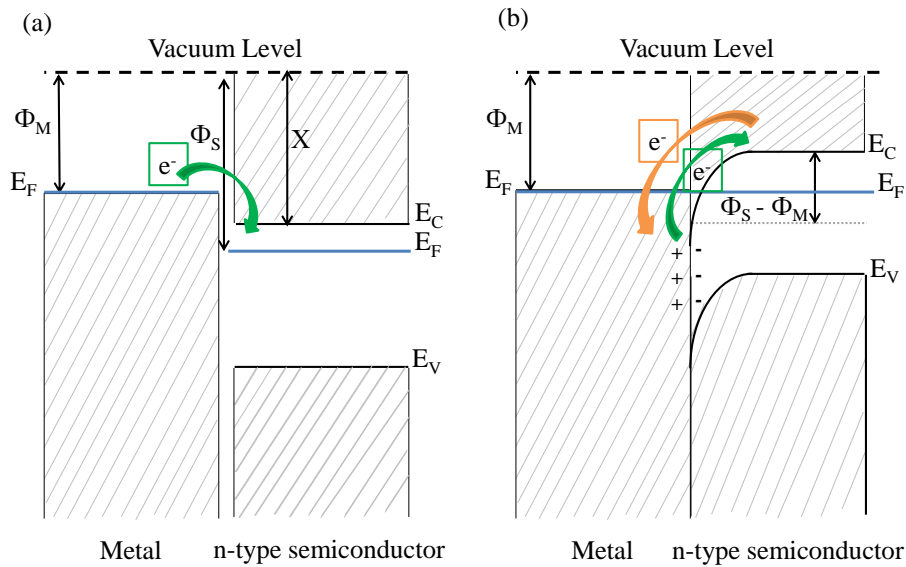


Figure 1.9: Schematic diagram of the energy bands at the interface between a metal and a heavily-doped n-type semiconductor (a) before contacting and (b) after contacting. As soon as a contact is established, the electrons flow from the metal to the semiconductor because $\Phi_M < \Phi_S$ (electron movement shown by the green arrow in (a)). This movement results in an accumulation of positive charge at the edge of the metal and negative charge at the edge of the semiconductor. As the Fermi levels equalize, the transfer of charge from the metal to the semiconductor continues without having an added potential barrier to cross. The symbols utilized in this figure are explained in the text above. Eventually, when an external voltage is applied to the shown junction, electrons will be able to easily flow between both materials in both directions (electron movement shown by the green and orange arrows in (b)). As this is a characteristic of ohmic materials, such contacts are called ohmic contacts [77, 82].

In the case of an ohmic contact between a metal and an n-type semiconductor as shown in Figure 1.9, $\Phi_M < \Phi_S$. Therefore, electrons will easily flow from the metal to the semiconductor without any energy barrier to cross (electron movement shown by the green arrows in Figure 1.9 b). Such charge transfer results in an accumulation of positive charge at the metal surface near the junction, and a negative charge at the semiconductor surface. The energy levels (band edges of the semiconductor) will also be changed by $\Phi_S - \Phi_M = E_F(\text{semiconductor}) - E_F(\text{metal})$. When the Fermi levels are equalized and the energy bands of both the metal and the semiconductor overlap, the eventual transfer of electrons from the semiconductor to the metal (under the effect of an external applied voltage) would also occur easily, as there is also no charge barrier for the electrons to overcome. Therefore, in such contacts, electrons can

easily flow between both materials in both directions, and the junction acts as a metal or an ohmic material, hence the name *ohmic contact*. In the case of p-type semiconductor, the work function of the metal is higher ($\Phi_M > \Phi_S$) and the Fermi level is closer to the valence band. Nevertheless, the same principles as explained above still apply to the junction, considering holes as the major charge carriers instead of electrons.

Our particular research interest is centered on the ohmic contacts between metallic electrodes and the $\text{Mg}_2\text{Si}_{1-x}\text{Sn}_x$ TE material. The geometry of the surfaces in contact is fixed, as will be explained in the method section (2). However, as the contacting experiments are done under high temperature, diffusion and reaction between both materials is expected, possibly resulting in an added reaction layer. This reaction layer can potentially contain new phases that are less conductive, which inevitably adds resistance and hinders the current flow. Moreover, as the surfaces of both materials are rough, the contact regions will be limited to localized points instead of a continuous flat area. These regions of interrupted contacts also hinder the current and add resistance.

In case of a perfect contact between two surfaces of materials M1 and M2, the current lines can homogeneously cross the contacting surface. In case of a non-perfect contact, which is more realistic, the current lines have restricted isolated crossing areas, which results in a locally higher current density, as displayed in Figure 1.10.

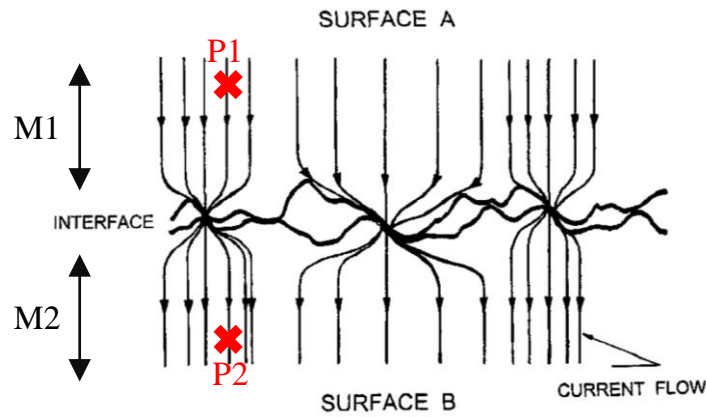


Figure 1.10: Schematic diagram of the current flow lines across an interface with restricted crossing points. (taken from [83]). The labels M1, M2, P1 and P2, indicating respectively Material 1, Material 2, Point 1 and Point 2, were added in this work for the sake of the in-text discussion.

The electrical contact resistance can be explained qualitatively based on Ohm's law. If we assume that V is the voltage drop between two points P1 on M1 and P2 on M2 (Figure 1.10) along the same current line, and I the electric current that flows from M1 to M2 through the contact surface, the total contact resistance is given by $R_c = V/I$. This total resistance includes three different resistance contributions $R_c = R_A + R_i + R_B$:

- 1- The resistance R_A originating from the streamline effect due to the current line constrictions in surface A on M1
- 2- The resistance R_i originating from the passage across the interface between surfaces A and B
- 3- The resistance R_B originating from the streamline effect due to the current line constrictions in surface B on M2

In this section, this subdivision of R_c is only introduced for the sake of theoretical knowledge. The value of the total electrical contact resistance R_c is what matters for technological purposes. Related to this total electrical contact resistance is the specific contact resistance, defined as r_c which is more meaningful to use because it is independent of the surface area that can change from case to case. r_c will be used in the rest of this work.

1.6. Point defects

Crystallographic point defects are disturbances to a perfect arrangement of atoms in the lattice structure of a material; they can be missing atoms, atoms in irregular positions or foreign atoms. These defects have strong and different effects on the material's behavior, depending on their concentration and charge state.

There are four types of point defects:

- self-interstitial atoms: atoms from the crystal positioned into an interstitial site ordinarily not occupied.
- vacancies: atoms missing from their normal lattice site.
- substitutional atoms: atoms replacing different atoms on their lattice positions. When an atom from the main lattice sits on a different crystal lattice site, the defect is called antisite.
- impurity interstitial atoms: external atoms, different from the material's original atoms, filling interstitial sites.

Defects play a particularly important role in semiconducting materials because their type and concentration can majorly change the material's electronic properties. Other material properties like diffusion and mechanical strength are also strongly dependent on defects. In fact, as H. J. Queisser stated, "*imperfections in a nearly perfect crystal*" are the guiding principles for semiconductor science and technologies [84].

Semiconductors have native defects, also named intrinsic defects. They can be self-interstitials, anti-sites and vacancies; they control basic processes like self-diffusion, and they can change the band

structure. For example, Ögüt *et al.* showed that the increase of Zr_{Sn} antisite defect content leads to a decrease of the band gap of the ZrNiSn based half-Heusler alloys [85].

Doping a semiconductor with atoms other than the main lattice atoms generates extrinsic defects that are often more stable than the intrinsic defects of the material, causing a change in the electrical conductivity. In fact, incorporating extrinsic point defects in specific concentrations into a lattice results in a change in the electronic properties of the material, e.g. by tuning the carrier concentration and/or by adding scattering centers by alloying. Extrinsic point defects can be substitutional, thus occupying positions of one of the atoms from the main lattice, or can be interstitial. Such point defect control methods were already tested in several TE materials like Bi_2Te_3 [86], $CoSb_3$ [87] and $Mg_2(Si,Sn)$ [88].

Jund *et al.* [89] studied the relative defect stabilities of Mg_2Si and Mg_2Ge using first principles calculations, based on a comparison of their intrinsic defects. Their results showed that defect stabilities in these material systems depend on the growth conditions. Under Mg-rich conditions, the Mg vacancies (V_{Mg}) and the interstitial Mg (I_{Mg}) defects are the most stable, while under Mg-poor conditions, the X on Mg substitution defect (X_{Mg}) becomes very stable (the most stable in Mg_2Ge). Under stoichiometric conditions, I_{Mg} becomes less stable, while V_{Mg} becomes more stable. One important parameter to keep in mind here is that Jund *et al.* only considered neutral defects in their work; they did not take into consideration the different charge states that defects can have. Nevertheless, their findings highlight the relation between the formation energies of defects (their stability) and their concentration. Growth conditions are hence important because they determine the concentrations of the defects, and therefore their effect on the conduction type and carrier concentration of semiconductors.

Quantitatively, the relation between the defect's formation energy and the defect's concentration can be seen from the following equation $\Delta_{def}E_{multi}(\mu_e) = \frac{\Delta_f E_{defect}(\mu_e) - \Delta_f E_{multi}}{x_{defect}}$ reported in a recent work from A. Berche and P. Jund [90], as an example among others. In this equation, $\Delta_{def}E_{multi}$ is the defects' formation energy taking into consideration their charge, $\Delta_f E_{defect}$ is the formation energy of the phase containing the charged defect, μ_e the electron chemical potential, $\Delta_f E_{multi}$ is the formation energy of a multi-phased region that corresponds to the exact composition of the defective cell, and x_{defect} is the defects' concentration in the cell.

In the case of the Mg_2X system, which is our system of interest in this work, thorough investigations were already processed to establish the native point defects of the material. Kato *et al.* studied the Mg_2Si system using density functional theory (DFT) calculations, and tried to identify the origin of the persistent n-type conduction of this material. Their results showed that the I_{Mg} charged defects are the most energetically stable defects under different electron chemical potential conditions (Mg-rich or Si-rich), and these defects act as electron donors of charge $q = 2+$, which explains the constant n-type conduction and the experimental difficulty to synthesize good p-type Mg_2Si [91].

Liu *et al.* [41] also used first-principle calculations to determine the defects formed in Mg_2X ($X=Si, Ge, Sn$) and discussed their effect on the thermoelectric performance of the system. Results showed that Mg vacancies V_{Mg} and Mg interstitials I_{Mg} are the dominant defects in Mg_2X , as they have relatively low formation energies in the whole Mg chemical potential range. Figure 1.11, taken from [41], shows calculation results for the intrinsic defect formation energies and their dependence on the chemical potential in Mg_2Si, Mg_2Ge and Mg_2Sn . In this figure, the band gaps are shown as the Fermi energy range, and the valence band maxima (VBM) is pinned at $E_F = 0$ eV. From the figure, it can be clearly seen that, in fact, V_{Mg} is the defect with the lowest formation energy in all material cases at higher values of Fermi energy, i.e. near the conduction band minima, when the material has a more n-type behavior. Also, as mentioned before, the figure shows that I_{Mg} are also very stable. They are the defect with the second lowest formation energy for all materials under Mg-rich conditions near the conduction band. Under X-rich conditions ($X= Si, Ge, Sn$), the substitutional defects of the X atoms on the Mg (X_{Mg}) sites are stable as well.

Liu *et al.* established through their work that Mg_2Si is always an n-type material, while Mg_2Sn and Mg_2Ge show both n- and p-type conduction type depending on the Mg chemical potential. In fact, the interplay between I_{Mg} and V_{Mg} is what determines the conduction type, as the former is a donor defect of charge 2+ while the latter is an acceptor defect of charge 2-. In the case of Mg_2Ge , under Mg rich conditions, the concentration of I_{Mg} is higher than that of V_{Mg} , thus the material has an n-type conduction. However, under stoichiometric and Ge rich conditions, the material is p-type, as V_{Mg} becomes more stable. Similarly, Mg_2Sn also exhibits a transition in the conduction type from p- to n- as the Mg chemical potential, and therefore, the concentration of I_{Mg} increases.

Compared to these Mg-related defects, X atoms related defects have higher formation energies; therefore, they are less probable to occur during crystal growth and have less influence on the general charge carrier concentration. In fact, X atoms have much larger atomic radii ($Si = 2.71 \text{ \AA}$, $Ge = 2.72 \text{ \AA}$, $Sn = 2.94 \text{ \AA}$) compared to the atomic radius of Mg (0.66 \AA), which means that the strain energy and local disorders caused by the X atom defects are much larger compared to those created by Mg atom defects. These findings join what was reported above by Jund *et al.* concerning the importance of growth conditions, as they set the chemical potential environment, and their effect on the defect densities which determines the material's charge carrier concentration.

As doping is known to be an efficient strategy to improve the electronic properties of semiconductors, it is also a vital strategy to produce efficient n- and p-type thermoelectric materials for power generation. For example, Tani *et al.* [35] used first-principles calculations in a systematic study of several elements namely B, Al, Ga, In, N, P, As, Sb, Cu Ag and Au, which were used as extrinsic dopants to observe their effect on Mg_2Si . Results showed that only Ga induced p-type conduction, while As, P, Sb, Bi, Al and N all resulted in n-type conduction. The other elements (In, Ag, Cu and Au) had different conduction types, depending on Mg and Si chemical potentials. Another example can be the work of Jiang *et al.* [88] where

they tried to enhance the TE properties of $\text{Mg}_2(\text{Si},\text{Sn})$ solid solutions through inclusion of Sb impurities on Si/Sn sites, and studied the interplay between these extrinsic defects with the main defects I_{Mg} and V_{Mg} . In their work, they demonstrated that the Sb ratio influenced the concentration of Mg vacancies, and that excess Mg facilitates the formation of I_{Mg} defects, which effectively influenced the carrier concentration. A theoretical $zT \sim 1.1$ was also obtained for Sb content $x > 0.1$ in the system $\text{Mg}_2\text{Si}_{0.4}\text{Sn}_{0.6-x}\text{Sb}_x$.

In this work, Bi was chosen as the effective n-type dopant [69, 92, 93], while Li was used as the effective p-type dopant [3] for the $\text{Mg}_2\text{Si}_{1-x}\text{Sn}_x$ solid solutions. The n-type conduction is a result of the Bi atom substituting Si/Sn atoms ($\text{Bi}_{\text{Si/Sn}}$) and the samples were synthesized under Mg-rich chemical potential conditions. The p-type conduction results from the Li on Mg substitution defect (Li_{Mg}), but, as the interstitial Li_i defects can also easily form, a fraction of the added Li will be *lost* as interstitials instead of the intended Mg substitution, hence the system would be under an Mg-poor synthesis environment.

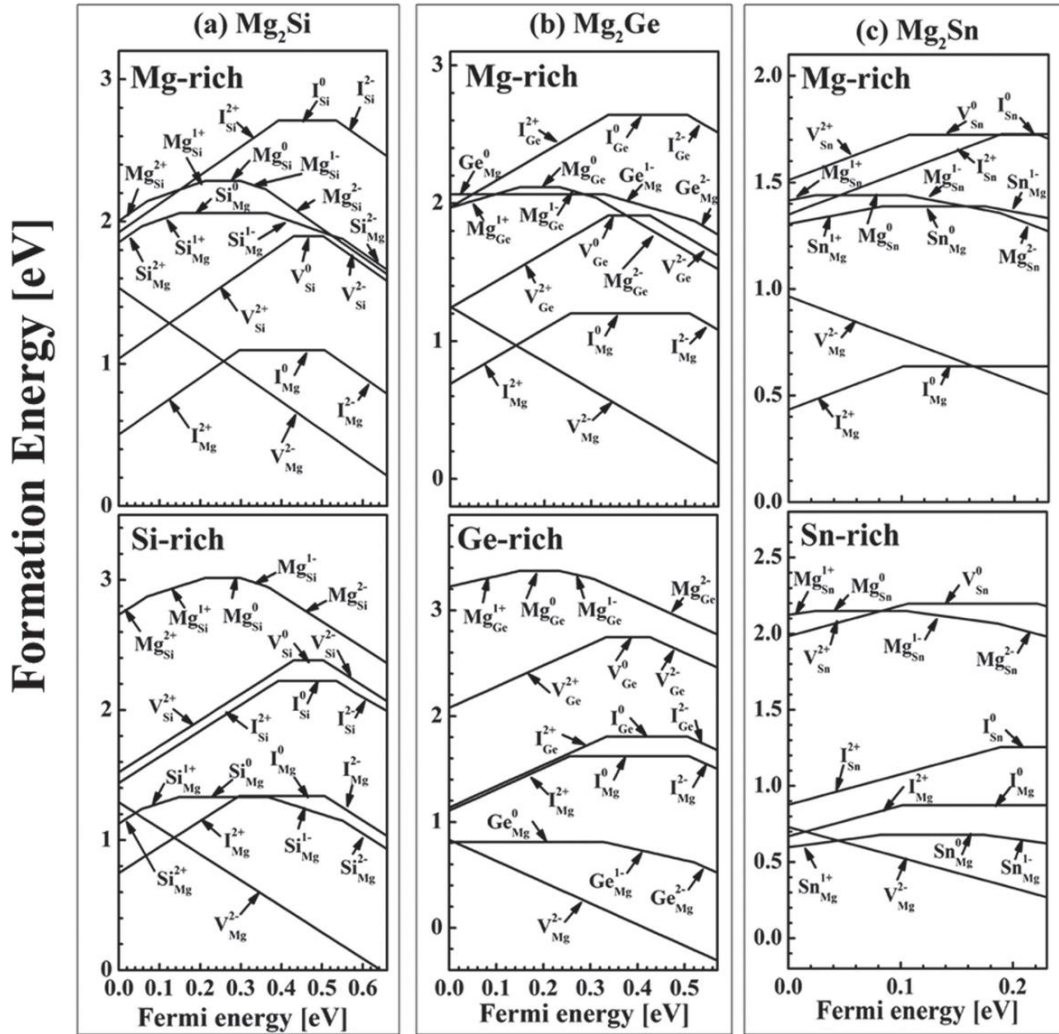


Figure 1.11: Calculated formation energies for intrinsic point defects in Mg_2X ($X = \text{Si}, \text{Ge}, \text{Sn}$) as functions of the Fermi energy. For each material type, the calculations are done under Mg-rich chemical potential conditions, as well as X-rich chemical potential conditions. The figure is taken from [41].

1.7. Research Summary

1.7.1. Research Question

In order to develop functional TEGs, research must not stop at optimizing the TE legs, but should take a step further and look into finding suitable electrodes for contacting. In finding contacting solutions, several established requirements should be fulfilled. However, these requirements are neither exhaustive nor exclusive, and electrodes matching the set criteria could easily still not work for the TE material of choice. A few electrodes were tested for $\text{Mg}_2\text{Si}_{1-x}\text{Sn}_x$ and preliminary results were reported, but these electrodes were not suitable enough according to the mentioned requirements. Some electrodes also displayed an unexpected behavior which was not well understood and explained.

So far, Ag was reported as being the best contacting electrode, but only for p-type $\text{Mg}_2\text{Si}_{1-x}\text{Sn}_x$. The same result was not obtained for n-type $\text{Mg}_2\text{Si}_{1-x}\text{Sn}_x$, which solves, then, only half of the problem. Moreover, no report on the thermal stability of the contact with Ag was provided, which is a necessary requirement for the implementation of the electrode into the actual device. In fact, the contacting procedure will result in potential diffusion between the electrode material and the TE material, as well as added thermomechanical stresses due to the differences in the coefficients of thermal expansion. The effect of these two mentioned parameters (among others) will be enhanced by thermal cycling to which a TEG would be subjected, and, if not controlled, would result in the failure of the generator.

In general, the problem of contacting is not very well studied and understood. So far, electrodes were selected only based on the *pre-testing* requirements that they are stable metals with matching coefficients of thermal expansions to that of the TE material. Another *post-testing* criterion is also used to judge the suitability of an electrode, namely the specific electrical contact resistance r_c , and previous studies indicated that $r_c < 10 \mu\Omega \text{ cm}^2$ was an acceptable threshold. From this short list of criteria, it is clear that the main problem with contacting is the absence of thorough guidelines to help narrow down the selection pool and make the search procedure for suitable contacts more efficient and effective. On a smaller and more specific scale, no successful electrode was found for $\text{Mg}_2\text{Si}_{1-x}\text{Sn}_x$ materials. Both these topics will be tackled in this work while testing several possible electrodes.

1.7.2. Thesis Overview

In this thesis, the aim is to develop contacting solutions for $\text{Mg}_2\text{Si}_{1-x}\text{Sn}_x$ by testing a few selected electrodes and trying to build guidelines for electrode choice to help further research. Using a pre-established synthesis and contacting procedure, we start by evaluating Cu and $\text{Ni}_{45}\text{Cu}_{55}$ electrodes with n- and p-type $\text{Mg}_2\text{Si}_{1-x}\text{Sn}_x$ as both the electrodes and the TE materials have similar CTE coefficients

(Chapter 3). We discuss the microstructure of the obtained reaction layers and measure the electrical contact resistance for each electrode.

Annealing experiments were also done on the Cu-contacted samples to investigate the thermal stability of the reaction layers and the diffusion of the electrode inside the TE materials. Moreover, as Cu is known to be a fast diffuser, an investigation of the effect of the sintering current on the contacting procedure was done. The aim was to figure out if the Cu diffusion would be affected by the current, and to verify if it is only temperature-induced diffusion or if it is also happening due to electromigration. Results of this work are introduced in Chapter 4.

As for the Ni₄₅Cu₅₅ electrode, contacting experiments were also processed because both Ni and Cu gave low electrical contact resistance values, and because the alloy has a closer CTE to the TE material than Ni. Diffusion from the electrode was observed, and the CTE match was still not good enough, as several cracks were seen inside the TE material and along the contacting interface. Similar to the Cu case, studies of the effect of the sintering current were done on Ni₄₅Cu₅₅-contacted samples, and preliminary results are provided in Chapter 6.1.1. This particular topic is also further discussed in the Appendix.

The Ag electrode was already tested with Mg₂Si_{1-x}Sn_x materials in a previous work [4], and yielded to unexpected results that were not fully explained. In fact, a change in the Seebeck value after contacting was observed in n-type Mg₂Si_{1-x}Sn_x samples, while no change was recorded for the p-type samples, but no clear explanation was provided. It was however stated that the differences between the results obtained for n- and for p-type samples could be related to the major charge carriers inside the TE materials. To follow this lead and understand the reported data, an investigation of the intrinsic and extrinsic point charged defects is provided for Mg₂Si and Mg₂Sn contacted with Ag. The defect formation energies were calculated using a hybrid-DFT method, and an analysis of the experimental results with the calculation data is provided and explains the observed behaviors (Chapter 5).

Such dependence of the behavior of the contacted TE material on the major charge carrier wasn't only observed with Ag. In fact, it was also observed with Cu and Ni₄₅Cu₅₅. Therefore, the method used to correlate experimental data to hybrid-DFT calculation data was extended to Cu and Ni materials. Calculations of defect formation energies between these electrodes and the binaries are provided in Chapter 6.2. A summary of the comparisons between the different experiment joining cases and the corresponding hybrid-DFT calculations is also provided, in order to evaluate the reliability of the method. An extension of this method to a new electrode material Ti is provided in the Appendix, where results of contacting with n- and p-type Mg₂Si_{0.3}Sn_{0.7} as well as calculations of the defect formation energies are provided. Ti was selected because it can be also used as a diffusion barrier for the Mg₂(Si,Sn) system.

Finally, collecting the obtained contacting results from this work and previous research, we try to compile a list of selection criteria to choose a “good” and suitable electrode for technological applications on Mg₂(Si,Sn) materials.

Chapter 2

2. Methods

In this section, the experimental procedures and methods used to synthesize and characterize the samples are introduced. A melting route and high energy ball milling were used to synthesize the initial powder, and optimized condensed pellets were sintered by current-assisted sintering pressing. Contacting of the pellets with metallic foils was also done using the same sintering facility. Experimental characterization involved SEM/EDX investigations, as well as a Potential & Seebeck Microprobe (PSM) mapping facility. First-principle calculations based on Density Functional Theory (DFT) performed by Byungki Ryu, Sungjin Park and Sudong Park from the Korea Electrotechnology Research Institute (KERI) within the frame of a collaborative work were employed for analysis and were compared with experimental data. All of the mentioned methods, including the hybrid-DFT calculations, are explained in the following sections.

2.1. Powder synthesis and hot pressing

2.1.1. Induction melting

In this work, n- and p-type powder samples of the $Mg_2Si_{1-x}Sn_x$ solid solutions were synthesized through induction melting. This synthesis route consists of melting the desired amounts of the starting elements together in a graphite crucible, following a procedure described by Farahi *et al.* [2]. The procedure is done in a direct-current sintering press chamber (Dr. Fritsch GmbH, DSP 510 SE) under Ar gas atmosphere, and is divided in three melting cycles. Each cycle is divided into three steps of temperature increase. For the most used composition in this work, which is $Mg_2Si_{0.3}Sn_{0.7}$, the final temperature of the first melting cycle is 800 °C, that of the second melting cycle is 850 °C, and the final melting temperature of the last cycle is 900 °C. During each cycle, the first temperature increase is stopped at 300 °C, and the second temperature increase reaches 600 °C for n-type and 575 °C for p-type. The reason behind the different temperatures is the Mg content that is initially lower in the p-type compositions compared to the n-type composition. Therefore, the melting of p-type is maintained at a slightly lower temperature to avoid further Mg loss.

This procedure is shown in Figure 2.1, but for simplicity and to avoid repetition, only the third temperature-increase cycle reaching 900 °C is shown. Each ramping up was done in 10 mins, and then held for 20 mins, apart from the first temperature step (300 °C) that was only held for 10 mins. The used precursors were Mg turnings (Merck), Si (<6 mm, ChemPur), Sn (<71 μm, Merck) along with the

dopants which are Bi granules (99.999%, Goodfellow, ~7 mm) for n-type, and Li granules (> 99.5%, Labochemie) for p-type.

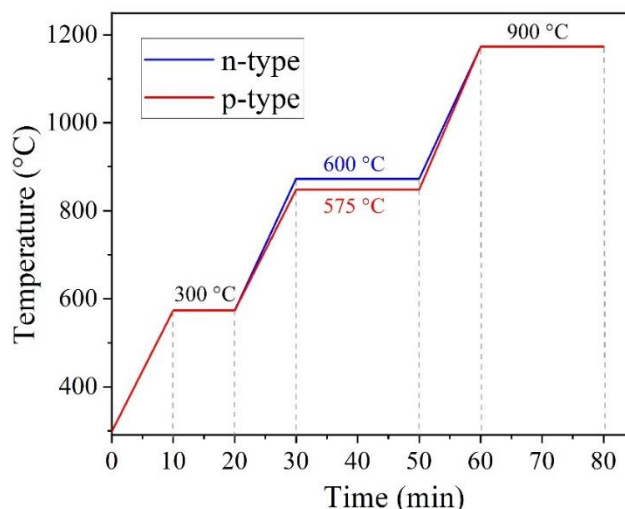


Figure 2.1: Diagram representing the third and last melting cycle of the induction melting route for n- (in blue) and p- (in red) type powder samples, reaching the final temperature of 900 °C.

The n-type samples were doped with 3.5 at% Bi and the p-type samples with 3 at% Li, leading to the nominal compositions $\text{Mg}_{2.06}\text{Si}_{0.3}\text{Sn}_{0.665}\text{Bi}_{0.035}$ and $\text{Mg}_{1.97}\text{Li}_{0.03}\text{Si}_{0.3}\text{Sn}_{0.7}$ respectively. The n-type samples were synthesized with 3 at% excess Mg to compensate for the Mg losses that occur during the higher temperature step of the material preparation, as well as the longer sintering time for n-type compared to p-type [1, 2, 36]. The ingot obtained from this melting procedure is ball-milled for one hour with stainless-steel balls and vials in a high energy ball mill (SPEX 8000D Shaker Mill) to obtain a fine homogeneous powder, ready for sintering.

The graphite crucible is held stable inside the DSP's air-tight chamber through a plunger providing a force of ~ 4200 N, to keep the crucible close and the reaction contained, as shown in Figure 2.2. A direct electric current runs through the graphite crucible and heats it up, and the transfer of heat from the crucible to the elements inside it occurs through conduction and radiation/convection. The temperature at the inner wall of the crucible is kept in check through a type K-type thermocouple inserted in the wall of the crucible, as shown in the zoomed-in upper right part of Figure 2.2. As the temperature increases, elemental Mg and Sn liquify and start to react together to form Mg_2Sn containing some Si, which will later incorporate more Si to form the final composition.

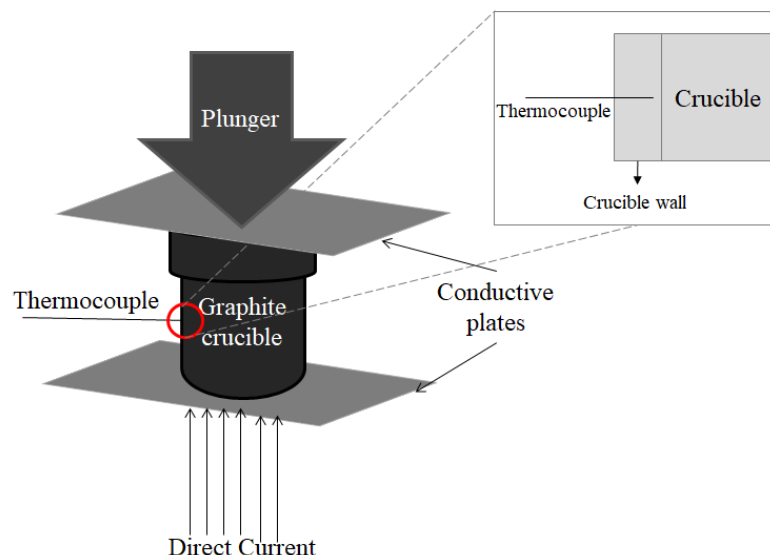


Figure 2.2: Schematic representation of the graphite crucible fixed inside the Direct Sintering Press (DSP) chamber. The zoomed-in section shows the thermocouple that just remains inside the wall of the crucible, very close to the inner edge, but without actually going inside the crucible.

2.1.2. High energy ball milling (HEBM)

High energy ball milling (HEBM) is a method commonly used to synthesize powder materials [94, 95]. In this process, mechanical energy is applied on a fast-rotated stainless-steel jar containing stainless-steel balls and the material of interest, and this energy will move the balls rapidly inside the jar. The movement of the balls and their high energy collisions transfer kinetic energy to the material and results into cold-welding and fracturing. After a set time and rotation speed, this process, also known as mechanical alloying, significantly changes the structural and chemical properties of the material and produces fine powders.

In other works, HEBM was used for low temperature material synthesis, where precursors are added together in stoichiometric composition in the milling jar with the milling balls, according to a desired ball-to-powder ratio, then the whole system was subjected to the external mechanical energy of the shaker [1, 36, 37]. During this procedure, the particles are repeatedly subjected to collisions with the balls, which causes fracturing to the material, breaks chemical bonds and provides kinetic energy for new bonds to form.

However, in this work, the reaction of Mg, Si and Sn into $Mg_2Si_{1-x}Sn_x$ was (mainly) achieved during the induction melting (Chapter 2.1.1). HEBM was only used to break the melted ingot and produce fine powder [4, 96, 97], allowing for a better compaction and homogenization in the sintering step. The ingot was broken manually into smaller parts with a chisel, then milled inside the stainless-steel vial under the effect of the milling balls (1 ball per 10 g of material). The used apparatus was a SPEX 8000D shaker

mill. Fine homogeneous powder with an average particle size ranging between 7 and 10 μm was obtained, ready for pellet sintering. The pressing method used is explained in the following section.

2.1.3. Sample compaction

Current-assisted sintering and hot pressing are among the most commonly used processes for powder compaction. In this work, current-assisted sintering using a direct sinter press (DSP) is the main followed route; however, experiments where the current was blocked from running through the samples were also done for the sake of particular studies as explained in Chapters 2.2, 4 and 6.1.1. As current-assisted sintering shares common features with hot pressing, particularly in the case of blocked current, this section will start with a short introduction to hot-pressing first, followed by a description of the current-assisted method as being the main compaction route.

Hot-pressing is a process that involves a simultaneous temperature load and uniaxial pressure to produce high density condensed samples. During hot pressing, a mechanical load along the vertical axis from an external hydraulic system is applied, along with heating from the furnace. The pressure plunger transfers a force to the punches that are pressing powder inside a die. These punches and die are usually made of graphite, due to its attractive thermal and mechanical properties. The system is also often kept in a non-oxidizing atmosphere (vacuum or inert gas). Along with the vertical pressure, a radial pressure is caused by the inner walls of the die. In fact, as the powder material and the die material have different coefficient of thermal expansions (CTE) (respectively $\sim 17 \times 10^{-6} \text{ K}^{-1}$ in the case of $\text{Mg}_2\text{Si}_{1-x}\text{Sn}_x$ and $< 10 \times 10^{-6} \text{ K}^{-1}$), their expansion rates under thermal stresses are different, resulting in expansion forces originating from the powder towards the graphite die. Reciprocally, a counter force from the inner walls of the die will be applied on the powder. The differential stress between both pressures (vertical and radial) applied on the powder creates a shear stress proportional to the applied stresses and that enhances particle bonding [98]. This shear stress, combined with the right temperatures (material specific) which are usually not as high as other compaction processes such as hot isostatic pressing (HIP) [99], can produce samples with maximum density and a limited grain growth [100, 101].

In certain hot-pressing processes, heat can be provided by an assisted applied electric field, and we talk then about current-assisted sintering. Such process allows the improvement of the heating rate and the pressing efficiency. An electric current runs through the die and sample system, similar to the setting shown in Figure 2.2 (replacing, in this case, the graphite crucible on the figure by a graphite die), generating a convection/radiation resistive heating that will elevate the temperature of the powder sample until reaching a temperature high enough to initiate a plastic deformation regime. In this regime, the powder particles plastically yield to the applied pressure and temperature, and the contact area between the particles is increased [100]. The initial densification phase starts with powder compacting and shaping as the powder particles rearrange and grain boundaries form under the effect of the uniaxial

pressure. As temperature increases and densification continues, high temperature deformation and creep by grain boundary diffusion occurs, allowing pore closure [98]. Finally, the system is often allowed to cool down to room temperature passively, and the uniaxial pressure is sometimes also released during this step.

In this work, the powder as obtained after high energy ball milling is sintered into pellets, mainly using a current-assisted direct sinter press (DSP), achieving densification and reaction completion. The powder is stabilized inside the die through a graphite foil (15 μm thick) wrapped around the inside of the die, graphite foil disks to avoid powder loss, and pistons pressing on both ends. The lot is then fixated with graphite legs. Most sample pellets were made with 1.2 g of powder and hot pressed in a 15.15 mm diameter graphite die at specific temperatures and times, resulting in a ~ 1.5 mm thick pellet. One particular study (Chapter 5) where a thicker sample was required, involved ~ 5 g of powder that was sintered into a ~ 7 mm thick pellet.

n-type samples were pressed at $T = 700$ °C for $t = 1200$ s, while p-type samples were pressed at $T = 700$ °C for $t = 600$ s. These selected pressing conditions were reported by [3] and [1] to obtain optimized TE properties for both material types.

All sintering experiments were done in the same direct sinter press used for the induction melting (Chapter 2.1.1) step, under a pressure of 66 MPa, and the heating rate was 1 K/s. All experiments were conducted under vacuum condition ($\sim 10^{-5}$ bar). The sintering method (including powder synthesis) is shown in Figure 2.3.

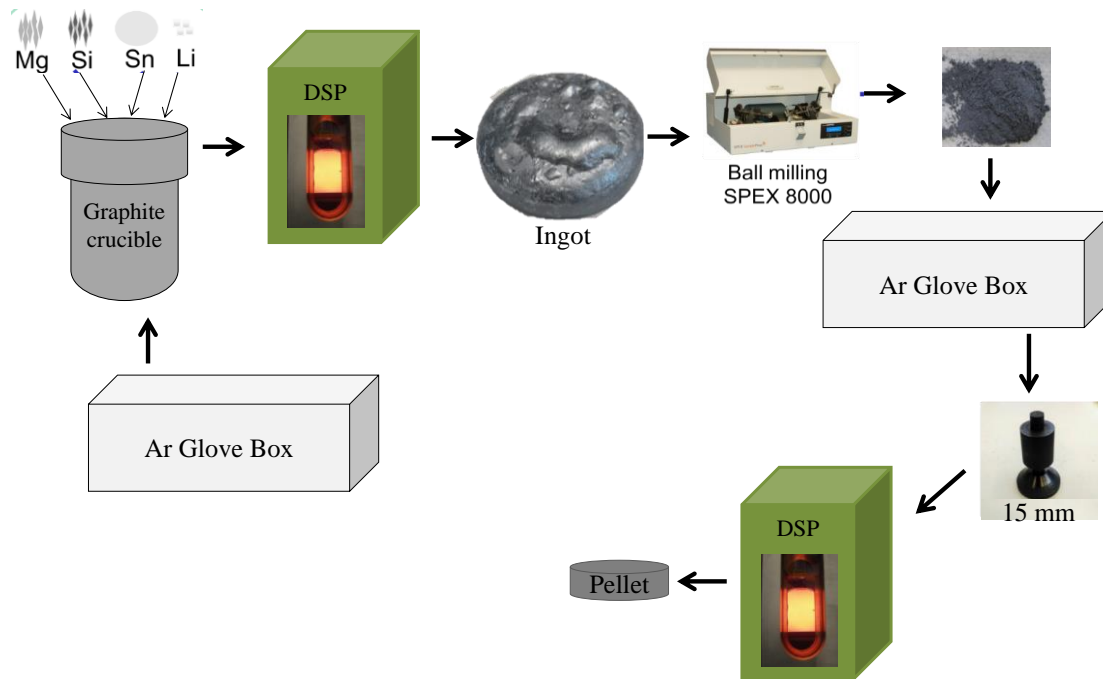


Figure 2.3: Synthesis method for p-type $\text{Mg}_2\text{Si}_{1-x}\text{Sn}_x$ (The same method is used for n-type with Bi as dopant). The method is divided into three steps until the final pellet is obtained: a melting of the precursors following a route explained above (Chapter 2.1.1), high energy ball milling of the ingot obtained from melting (Chapter 2.1.2), and pressing in the direct sinter press (Chapter 2.1.3). The synthesis parameters depend on the desired composition.

2.2. Joining by sintering

The obtained n- and p-type pellets were wet ground using SiC paper down to a 2500-micron size and ethanol to remove the sticking graphite foil and obtain pellets with parallel surfaces. The parallelism of the surfaces was obtained by grinding utilizing an aid tool that allows a homogeneously distributed pressing force on the whole surface of the sample, then was checked using a digital caliper by measuring at different parts of the sample, allowing an error $\sim 1\%$. The grinded pellets were then contacted with different metallic electrode foils in the DSP, at different temperatures depending on the electrode material. All joining temperatures are presented in Table 2-1. These temperatures were selected as being around half of the melting temperature of the electrode, all the while making sure not to reach 700°C , which would affect the optimized TE properties of our pellets. In all cases, the heating rates were 1 K/s , the pressure and the holding time were maintained at 28 MPa and 10 min . Due to the limited spatial resolution the Potential & Seebeck Microprobe (PSM) facility (Chapter 2.4.2), the total thickness of the electrode was set to a minimum of $150\ \mu\text{m}$. In case of thin foils, several disks of the same material were stacked up to provide the necessary electrode thickness.

Table 2-1: Joining temperatures used with the different studied metallic electrodes. Several temperature points were tested and are presented in the table. The final used temperature is marked in bold and underlined.

Selected Electrode	Provider	Joining Temperature (°C)
Ag	VWR International GmbH	<u>450</u> , 475, 600
Cu	Goodfellow 99,99%	500, <u>600</u>
Ni ₄₅ Cu ₅₅	Goodfellow Ni ₄₅ Cu ₅₅ Fe _{0,0025} Mn _{0,0075}	<u>550</u>
Ni	Thomas Geyer GmbH	600, 650, <u>700</u> , 750

For the joining step between the TE material pellet and the selected metallic electrodes, two different methods were tested to understand the potential effect of the electrical current of the DSP on the contacting results (interdiffusion of elements, reaction layer, electrical contact resistances...). The first method was done simply by stacking graphite foil, metallic electrode foil and the TE material pellet inside a graphite die, then subjecting the system to the current of the sinter press. This method was called “*direct resistive heating*” where the heating of the system would mainly occur through a Joule heating of the sample, as the current runs directly through the TE material and the metallic electrode. A small fraction of the current distribution would also pass the graphite die and pistons, but this portion is usually negligible.

The second method was achieved by adding an extra layer of resistive boron nitride (BN) solution, which is an electrically insulating ceramic material with a large bandgap $E_g = 4$ eV [102], coated on the inside of the graphite pistons to hinder the electric current from running through the sample directly. Instead, the current would mainly go through the graphite die, and the heating of the sample would occur through radial heating from Joule heating of the die. This method is called “*indirect resistive heating*”, as the current does not pass the samples directly.

Both methods are schematically portrayed in Figure 2.4. In these methods, the electrode material softens when the target temperature is reached, and adheres to the rough surface (surface scratch depth ~ 2 μm) of the TE pellet. Diffusion and reaction also occur between the electrodes and the pellet with different rates depending on the electrode material.

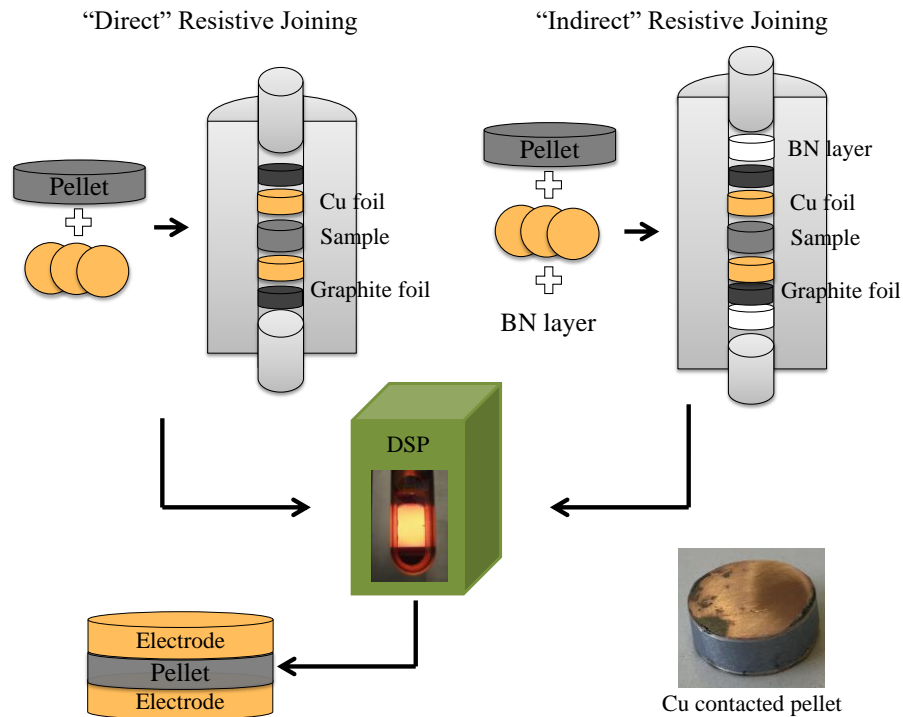


Figure 2.4: Different joining methods of pressed pellets with Cu foil as an example. The first joining method referred to as *direct resistive heating* method, is a procedure during which the current from the direct sinter press (DSP) runs freely through the sample. The second joining method, called *indirect resistive heating*, is a procedure where layers of a boron nitride solution are added on top and bottom of the sample arrangement. By doing so, the current from the DSP is hindered from passing vertically through the sample and, instead, has to go through the graphite die around.

2.3. Sample preparation (cutting, grinding, embedding, polishing)

After joining, the samples undergo a series of preparation steps for microstructure analysis and electrical contact resistance measurement. Each 15 mm \varnothing pellet is first cut into four elongated pieces of 3 ~ 4 mm width each. The used apparatus is an automatic dicing disco saw (DISCO, DAD 3231) with an approach speed of 0.3 mm s⁻¹ and disk speed of 30.000 rpm. Typically, two pieces would be used for a direct analysis, while the two remaining pieces would be kept for annealing studies if needed. For the purpose of SEM/EDX analysis, a piece of the sample is embedded with its cross-section side up in conductive resin (graphite and mineral filled phenolic thermoset, BUEHLER, Konductomet) using an embedding apparatus (Struers, CitoPress-20). The embedding is done in two steps under a sensitive mode of the machine to avoid added stresses that would cause cracking in the TE material. In the first step, the temperature is increased to 180 °C for 2 min under a pressure of 50 bar, and in the second step, the reached temperature (180 °C) is held for 5 mins while the pressure is increased to 200 bar. Cooling is done passively.

Each embedded sample is wet grinded with a grinding machine (ATM Metallography, SAPHIR 250 M2) using ethanol and four different SiC grinding papers of roughness 800, 1200, 2500 and 4000-micron size to obtain a mirror-like surface. For a cleaner surface, and in order to be able to see grain boundaries when needed, the samples are also polished using an automatic grinding and polishing machine (ATM Metallography, SAPHIR 550) with alcohol-based diamond solutions (Schmitz Diamond suspensions). Different polishing disks are used, along with different polishing solutions with particle sizes 3 μm , 1 μm , 0.25 μm and 0.05 μm . Each polishing step is done under a pressure of 15 N for 5 min. Between each polishing step, the samples are gently rinsed with ethanol. A final cleaning step is done in the same polishing instrument using a cloth disk under constant input of ethanol for 10 mins, and under a pressing force of 10 N. Finally, the samples are put in a supersonic bath (in ethanol) for 10 mins to guarantee a surface as free from the diamond solution as possible.

For electrical contact resistance measurements, a different non-embedded sample piece is grinded on the cross section and on the edges to form a rectangular shape. The cross section is grinded with SiC paper until 2500 roughness, then the prepared sample is put in the Potential & Seebeck Microprobe (PSM) facility for Seebeck and electrical contact resistance mapping.

Both the SEM/EDX and the PSM facilities are introduced in the next section (Chapter 2.4.1 and Chapter 2.4.2, respectively).

2.4. Sample characterization

2.4.1. Scanning electron microscopy (SEM)

The embedded samples are observed in a scanning electron microscopy (SEM) facility (Zeiss Ultra 55) to investigate the microstructure of the samples, and particularly the contacting interface/reaction layer. SEM is a technique that generates detailed high-resolution images using a focused monochromatic electron beam across the surface of the studied sample, and detecting backscattered or secondary electron signals [103]. The samples are studied under vacuum using high energy electrons (15 keV).

To quantitatively study the local chemical composition and phase approximation (present elements, distribution and concentration), energy dispersive X-ray spectroscopy (EDX) is employed. In this spectroscopy method, the electron beam hits a localized portion of the sample, and the resulting emitted X-rays would serve to identify the chemical composition. The microstructure and contrast between different compositions are observed under a back-scattered detection mode (BSE), producing contrasted images that indicate differences in the atomic numbers of the present elements. Brighter areas indicate heavier elements, while darker areas indicate lighter elements. In this study, a combination of

composition and elemental mappings, line scans and compositional point analysis is utilized to study the reaction layers resulting from the contacting between the TE material and the metallic electrode.

Despite being a state-of-the-art facility, the SEM/EDX still holds shortcomings that cannot be avoided such as the difficulty in detecting light-weight elements. This is relevant in our case as we use Li as dopant for the p-type samples, and it is not possible to properly quantify such elements with SEM/EDX. What is needed in this case would be Wavelength dispersive X-ray spectroscopy (WDS) [104]. The latter allows a better energy resolution and prevents peaks overlap that is commonly encountered in EDX. Nevertheless, WDS would cause greater damage to the samples because of the high beam currents, and it is also costly.

Other limitations of the utilized SEM/EDX apparatus are ~ the 1 nm beam spatial resolution for SEM imaging with low working distance, and the 1 μm EDX spatial resolution for mappings under a voltage of 15 kV. Lastly, the used Oxford software has a quantitative detection limit of ~ 2 at%, which does not allow a reliable detection of some diffused elements with low atomic percentages. The detected concentrations could also vary depending on the detection angle at which the sample is set, and this can lead to some uncertainties.

2.4.2. Potential & Seebeck Microprobe (PSM)

An in-house built Potential & Seebeck Microprobe (PSM) facility is utilized to map the Seebeck profile of the contacted samples, as well as the voltage drops along their cross section [105, 106]. The latter is used to calculate the electrical contact resistances at the interface between the TE material and the metallic electrode. In this work, all PSM measurements are done at room temperature.

The PSM machine probes simultaneously the local Seebeck values at different positions, as well as the difference in potential between one end of the sample and the point of measurement. This mapping provides line scans of the Seebeck coefficient and the voltage along the cross section of the sample. During the measurement, the sample is clamped between two Cu blocks, to mechanically fix the sample during the measurements, and to allow an undisturbed passage of the electrical current for the voltage pick up. The voltage drop along the sample is measured using a lock-in amplifier (LIA-BV-150-L, FEMTO Messtechnik GmbH) in a three-point scheme, as the voltage is tapped between the measuring tip, the low potential holder electrode and the high potential holder electrode.

To measure the sample's Seebeck coefficient S_s , a heated microprobe connected to a type T (Cu-CuNi) thermocouple is placed on the surface of the sample, heating a small volume around it, and consequently inducing a temperature gradient that generates a thermovoltage in the vicinity of the contact point. Considering T_0 as the temperature picked up by the thermocouple at the heat sink - sample contact point

and T_1 as the local temperature at the point of contact, two voltages U_1 and U_2 can be measured, as shown in Figure 2.5 a. As the tip can move in three dimensions, a complete mapping of the desired sample surface can be achieved.

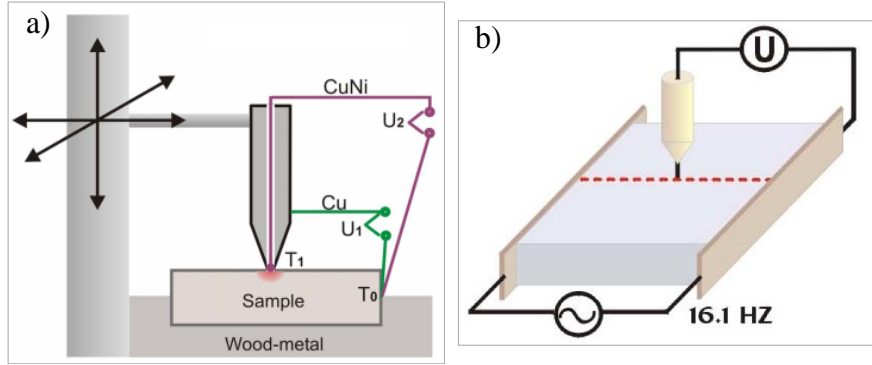


Figure 2.5: Schematic of the a) Seebeck coefficient microprobe measurement, b) the potential drop measurement in the PSM facility (taken from [105]).

Using the following equations where S_{Cu} and S_{CuNi} are respectively the known Seebeck coefficients of Cu and CuNi [105],

$$U_1 = (S_s - S_{Cu}) \times (T_1 - T_0) \quad \text{Equation 2.1}$$

$$U_2 = (S_s - S_{CuNi}) \times (T_1 - T_0) \quad \text{Equation 2.2}$$

we can obtain S_s as

$$S_s = \frac{U_1}{U_2 - U_1} \times (S_{Cu} - S_{CuNi}) + S_{Cu} \quad \text{Equation 2.3}$$

As the Seebeck coefficient of relevant TE semiconductors tends to show a non-linear behavior with temperature, a temperature difference ($\Delta T = T_1 - T_0$) below 10 K is desired, in order to guarantee the linearity of the function as introduced in Equation 2.3 [107]. During our measurements, ΔT is kept around 5 K. The expected total error of the absolute Seebeck value as recorded by the PSM is expected to range between 10 to 15%, depending on the measured sample's thermal properties as reported in [107]. This value holds for semiconductors with absolute Seebeck values between 50 and 250 $\mu\text{V/K}$, which is where our samples fall. For low S semiconductors, as well as for metals, the error values can rise up to 40%.

The potential drop across the sample is also measured using the same microprobe, however with a different technique. An electrical AC current is provided to the sample, and as the microprobe scans at different positions, a reading of the local electric potential is picked up, as shown in Figure 2.5 b. This measurement not only gives a scanning of the voltage drop along the semiconductor (TE material), but

also a scanning of the voltage drops across the contacting interface between the TE material and the metallic electrode. Knowing the applied electric current and the resulting (measured) electric potential drop, an estimation of the electrical contact resistance R_c can be calculated using the basic Ohm's law

$$R_c = \frac{\Delta V}{I} = \frac{V_{\text{elec}} - V_{\text{TE}}}{I} \quad \text{Equation 2.4}$$

where ΔV is the difference in voltage between the contacting electrode V_{elec} and the TE material V_{TE} at the interface, and I is the applied AC current.

Though this equation was used in various literatures before [72, 108-110], it is only valid in the case of a homogeneous current density running through the sample. However, in realistic cases, the homogeneity of the current distribution cannot be guaranteed. In fact, there is a high probability of internal and external disturbances that will hinder the current flow, such as improper clamping of the sample between the Cu holder blocks, non-perfect contacts between the electrode and the TE material, local impurities inside the TE material and along the contacting interfaces, etc. Under such conditions, the real current density running through the sample and the current density calculated from the current value read by the PSM are not the same, as the latter inevitably assumes a homogeneous current density.

To check this, an approximation of the actual current density j that passes the sample using the intrinsic properties of the TE material is used to compare with the PSM current density (output current value by the sample cross section in contact with the holder). Note that the output current value given in the final PSM output file is a constant value (for all line scans during a measurement). This value is measured by evaluating the voltage drop over a 1Ω precision shunt resistor (PBV, ISA-Plan® Isabellenhütte) which is connected in series with the sample holder. It is, thus, mainly dependent on the input voltage and the resistor's resistance. As for the TE material in play, as long as the measured sample has a low internal resistance (and a low electrical contact resistance for contacted samples), the contribution of the material's resistance to the total resistance of the circuit is considered minor, and therefore can be overlooked.

Using the properties of the measured TE material, the specific electrical contact resistance independent of the geometry, defined as $r_c = R_c \times A$, where A is the area crossed by the current lines, is utilized and it is calculated as described below:

$$r_c = \frac{(V_{\text{elec}} - V_{\text{TE}}) R_{\text{TE}} * A}{\Delta V_{\text{TE}}} \quad \text{Equation 2.5}$$

with

$$R_{\text{TE}} = \frac{l_{\text{TE}}}{A \sigma_{\text{TE}}} \quad \text{Equation 2.6}$$

where ΔV_{TE} and R_{TE} are the voltage drop and the resistance across the TE material, and l_{TE} and σ_{TE} are the length and electrical conductivity, respectively. A representative line scan of the simultaneously

measured S and U is provided in Figure 2.6 as an example, using an annealed n-type $\text{Mg}_2\text{Si}_{0.3}\text{Sn}_{0.7}$ joined with Cu. ΔV_{TE} can be read from the potential line scans as being the voltage drop due to the resistivity of the TE material and l_{TE} is the length of the TE material portion of the measured sample. σ_{TE} is measured on the TE material (after grinding off the electrode layer) utilizing an in-house built High Temperature Seebeck- σ (HTS- σ) setup based on the four-probe technique. As the PSM measurements are done at room temperature, the room temperature σ_{TE} value is taken.

In Figure 2.6, the interface positions where the voltage drop $V_{\text{elec}} - V_{\text{TE}}$ is measured are determined by the large change in the Seebeck profile line. In fact, as the contact here involves a metal and a TE material, S of the metal would be $\sim -10 \mu\text{V/K}$, while S of the semiconductor would be much lower ($\sim -230 \mu\text{V/K}$ in the example presented in the figure). The point where S changes from the metal value to the semiconductor value is determined to be the interface region. The voltage values of interest are then read right before and after the interface (or Seebeck drop) region.

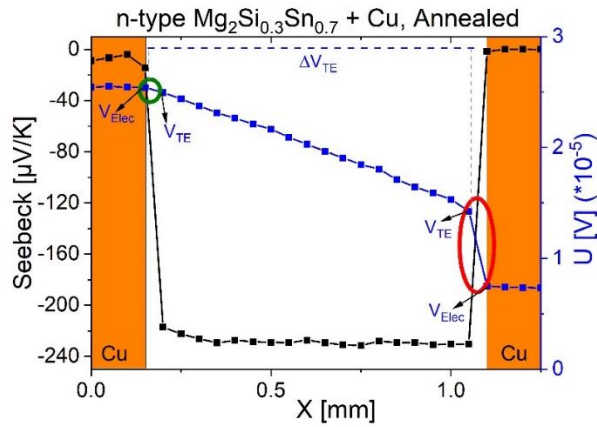


Figure 2.6: Representative line scan of the Seebeck profile (in black) and the potential profile (in blue) for an annealed n-type $\text{Mg}_2\text{Si}_{0.3}\text{Sn}_{0.7}$ sample contacted with Cu foil. The orange rectangles delimit the thickness of the Cu electrodes, and the green and red circles indicate the region where $V_{\text{elec}} - V_{\text{TE}}$ is read in order to calculate the electrical contact resistance. In this example, the left hand-side marked by the green circle shows a very smooth transition from the electrode region to the TE material region. Therefore, the specific electrical resistance r_c is expected to be low. However, on the right-hand side marked with the red circle, the passage from the TE material to the electrode exhibits a large drop in the potential line. Here, r_c is expected to be high. ΔV_{TE} would be the difference between the voltage value at the left-hand side (at $x = 0.15 \text{ mm}$) and the voltage value at the right-hand side of the TE sample (at $x = 1.05 \text{ mm}$).

The difference between both contact resistance calculation methods (Equation 2.4 and Equation 2.5) resides mainly in the value of the electrical current/current density. In the first approach, the value of I provided by the PSM is simply read on the Cu holder blocks as being the voltage provided by the external lock-in amplifier (SR830, SRS) divided by a reference circuit internal resistance (shunt resistor). In this case, specificities of the measured sample (interfaces, impurities, bad contacts...) and their influence on the current density are not taken into consideration. Therefore, the sample is considered homogeneous and a homogeneous current density is assumed. The second approach, however, provides a closer current

density to the actual one, considering the actual internal resistance of the sample. In fact, in this case, the density is obtained through an approximation of the actual sample's resistivity and the actual voltage drop along its cross section, which would factor in more local irregularities in the area crossed by the current lines, causing an inhomogeneous density.

Calculating specific electrical contact resistances r_c using both different current values introduced above provides a verification method for the homogeneity of the sample/contacts. If both r_c values are similar, the sample/contacts are likely to be homogeneous and free of impurities, cracks, pores, etc. that would hinder the current flow and allow a homogeneous current distribution across the sample. If the joining experiment resulted in newly formed phases, the newly formed interfaces between them would then be conductive.

If both r_c values are different, the value obtained using the second approach (using the current approximated from the sample properties) is more reliable and would be better to use. In this case, the current density would look more like the schematic presented in Figure 1.10, where the areas crossed by the current lines are more restricted than what is assumed in the case of homogeneous samples (the current density would be calculated along the whole contact area between the sample holder and the sample). Moreover, in such a situation, the homogeneity of the sample including the TE material and the newly formed interfaces, the contacts between the metallic electrode and the TE material, and potentially the clamping of the sample between the holder blocks need to be checked and improved.

As explained in Chapter 1.4 (Figure 1.8), a threshold of $10 \mu\Omega \text{ cm}^2$ is defined to qualify a low and acceptable specific electrical contact resistance r_c .

2.5. Annealing for thermal stability evaluation

To study the thermal stability of some contacted samples, annealing experiments were processed after joining. The samples were coated with a thick boron nitride (BN) and ethanol solution to minimize Mg losses through evaporation (Figure 2.6 a), and then sealed at room temperature in quartz ampoules under Argon atmosphere with a pressure of 560 Torr. Mg flakes (~ 0.5 g) were also added inside the quartz ampoule before sealing to help minimize Mg evaporation and losses during the annealing procedure, and to maintain a constant Mg partial pressure. The quartz ampoules were then kept in an annealing furnace for 7 days, at a temperature of 450 °C. The heating rate was 1 K/s, and the cooling process was through radiative free cooling.

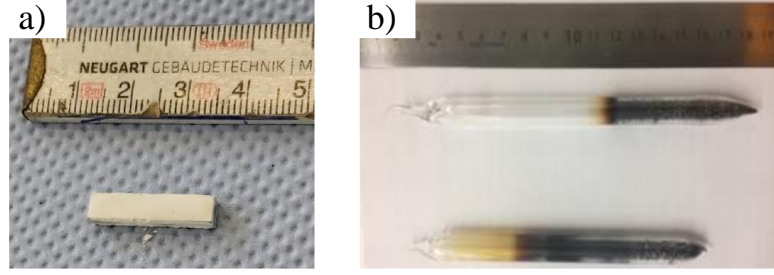


Figure 2.7: Pictures of a) coated cut sample before annealing, b) ampoules after annealing. The darker areas of the ampoules indicate evaporated Mg that deposited on the inner walls.

2.6. Hybrid-Density Functional Theory

In this section, a short introduction to Density Functional Theory (DFT) calculations is provided, followed by a segment about hybrid-DFT [111]. Note that all work related to DFT and hybrid-DFT as presented and discussed in this manuscript was exhaustively done by our collaborators Byungki Ryu, Sungjin Park and Sudong Park at the Korea Electrotechnology Research Institute (KERI). However, the data analysis and comparison with experiments were done by our group at DLR under close collaboration with the group in KERI.

2.6.1. Background on Density Functional Theory

The DFT method is a set of calculations that are used to obtain the quantum mechanical wave function of a system and to determine its allowed energy states, providing all needed information about the structural, magnetic and electronic properties of defects, molecules and materials in general [112-114]. It is basically a method to solve the Schrödinger equation $\hat{H}\Psi = E\Psi$, where \hat{H} is the Hamiltonian operator, Ψ is the wave function and E is the energy level. For an N -body system, it is not possible to directly solve the Schrödinger equation. The Hamiltonian operator in this case is expressed as

$$\hat{H} = \hat{T} + \hat{V} = E_{\text{kin}}(\text{ion}) + E_{\text{kin}}(\text{elec}) + v_{\text{ee}}(\vec{r}) + v_{\text{ii}}(\vec{R}) + v_{\text{ei}}(\vec{r}, \vec{R}) \quad \text{Equation 2.7}$$

Where \hat{T} is the total kinetic energy operator, \hat{V} the total potential energy operator, $E_{\text{kin}}(\text{ion})$ and $E_{\text{kin}}(\text{elec})$ are the kinetic energies of the ions and the electrons respectively, $v_{\text{ee}}(\vec{r})$, $v_{\text{ii}}(\vec{R})$ and $v_{\text{ei}}(\vec{r}, \vec{R})$ are respectively the interaction energies between the electrons, the ions and the electrons and ions. \vec{r} and \vec{R} are the 3D coordinates of the electrons and the ions, respectively.

The heart of DFT is the Hohenberg-Kohn (HK) theorem which states that the ground-state electron density $\rho(r)$ at each point r determines the external potential $v(r)$ (due to the nuclei) [115, 116]. A

normalization of $\rho(r)$ will then determine the total number of electrons N , with $\int \rho(r) dr = N$. Within this theorem, the minimum (ground-state) energy of a system can be expressed as

$$E = \min_{\rho} \left\{ \int v_{\text{ions}}(\vec{r}) \rho(\vec{r}) d^3\vec{r} + F[\rho(\vec{r})] \right\} \quad \text{Equation 2.8}$$

However, within this theorem, the functional $F[\rho(\vec{r})]$, which includes the kinetic energies of the system and the interaction energy terms, is unknown. To facilitate the issue, the Born-Oppenheimer approximation states that the ions of a system, being heavy and slow particles compared to the electrons, can be considered fixed in space i.e. ($E_{\text{kin}}(\text{ion}) = 0$) [117-119]. Within this approximation, the functional $F[\rho(\vec{r})]$ as introduced in Equation 2.8 is simplified, and we define then the Born-Oppenheimer Hamiltonian as follow

$$\hat{H}_{\text{BO}} = E_{\text{kin}}(\text{elec}) + v_{\text{ee}}(\vec{r}) + v_{\text{ei}}(\vec{r}, \vec{R}) \quad \text{Equation 2.9}$$

The Mean Field approximation follows the Born-Oppenheimer approximation in simplifying the Schrödinger equation by eliminating the $3N$ dimensionality of the wavefunction. In fact, this approximation states that the wavefunction of all the electrons can be rewritten as the product of single electron orbitals, giving $\Psi(\{\vec{r}_i\}) = \Phi_1(r_1) \times \Phi_2(r_2) \times \dots \times \Phi_N(r_N)$. We move then from a problem with many electrons to many one-electron problems, and we can assume that each electron moves independently in the external potential created by the fixed ions and the rest of the electrons. This system is called a system of non-interacting electrons.

Applying this Mean Field approximation into the Schrödinger equation leads to the Hartree equations, which are basically a set of single electron Schrödinger equations. Within the Hartree approach, the electron-electron interaction term can be expressed as $v_{\text{ee}}(\vec{r}) = \sum_i^N e^2 \int \frac{|\Phi_i(r')|^2}{|r-r'|} d^3r'$, and the Schrödinger equation becomes

$$\left[E_{\text{kin}}(\text{elec}) + v_{\text{ei}}(\vec{r}, \vec{R}) + \sum_{i \neq j}^N e^2 \int \frac{|\Phi_i(r')|^2}{|r-r'|} d^3r' \right] \Phi_j(r') = E \Phi_j(r') \quad \text{Equation 2.10}$$

where $\left[E_{\text{kin}}(\text{elec}) + v_{\text{ei}}(\vec{r}, \vec{R}) + \sum_{i \neq j}^N e^2 \int \frac{|\Phi_i(r')|^2}{|r-r'|} d^3r' \right]$ is the effective Hamiltonian \hat{H} .

The Hartree theory assumes that the electrons are distinguishable (electron 1 is for orbital Φ_1 , electron 2 is for orbital $\Phi_2 \dots$), which is not the case. Another shortcoming of the Hartree approach is that it doesn't consider the fact that wavefunctions describing fermions are anti-symmetric, meaning that the output should change sign when particle coordinates are interchanged [120, 121]. Therefore, the Hartree approach fails when electrons interchange positions in the orbitals. To solve this issue, the Hartree-Fock equations add to the Hartree approach an exchange interaction term that caters to the anti-symmetric nature of the wavefunction [122, 123]. In this approach, the expectation value of the effective Hamiltonian is then expressed as

$$\langle \hat{H} \rangle = E_{\text{kin}}(\text{elec}) + v_{\text{ei}}(\vec{r}, \vec{R}) + v_{\text{ee}}(\vec{r}) - \sum_{i < j}^N \int d^3r d^3r' e^2 \frac{\phi_i^*(r) \phi_j^*(r') \phi_i(r') \phi_j(r)}{|r-r'|},$$

where $\sum_{i < j}^N \int d^3r d^3r' e^2 \frac{\phi_i^*(r) \phi_j^*(r') \phi_i(r') \phi_j(r)}{|r-r'|}$ is the exchange interaction term that represents the orbitals i and j evaluated over the electrons at the positions r and r' .

The Hartree-Fock equations still miss the correlation energy term which is introduced by the Kohn-Sham equations [124].

The Kohn-Sham approach is based on the idea of single electron orbitals and a system of non-interacting electrons which has the same ground-state electron density as the real physical system [125]. The Kohn-Sham (KS) equations can be then written as:

$$E(\rho(r)) = \underbrace{\text{Non-interacting kinetic energy} + \text{Hartree term (electron-electron interaction)} + \text{External potential (ion-electron interaction)}}_{\text{Hartree equation}} + \underbrace{\text{Exchange - Correlation energy term}}_{V_{\text{xc}}}$$

Kohn-Sham Equation = Hartree equation + V_{xc}

Following this formulation, the Kohn-Sham equations can be solved if all unknown terms are moved to the exchange and correlation term V_{xc} . The exact solution to the remaining portion (Hartree equation) is known as described above. In order to approximate a solution for the exchange-correlation term V_{xc} , exchange and correlation functionals are needed, and these functionals can be either plane wave or localized basis sets are needed. Two of the commonly used functionals are *Local density approximation* (LDA) and *Generalized gradient approximation* (GGA).

Local density approximation (LDA) is an approximation method based on an integration over space of a function that only depends on the local density $\rho(\vec{r})$ at the point r [126, 127]. In this approximation, the exchange term corresponds to an exact equation for a homogeneous non-interacting electron gas and can be written as $E_{\text{x}}^{\text{LDA}}[\rho(r)] = -\frac{3q^2}{4} \left(\frac{3}{\pi}\right)^{1/3} \int d^3\rho \rho^{4/3}$ [112, 128]. This approximation, though, only works for homogeneous electron gases with no gradients or variations in the density. As for the correlation term, LDA does not provide an analytical solution. However, numerical solutions to this term can be obtained through Monte Carlo simulations applied also on homogeneous electron gases [129, 130].

Generalized gradient approximation (GGA) is a functional that depends on both the local density and the density gradient [131-133]. Within this approximation, the exchange term can be written as $E_{\text{x}}^{\text{GGA}}[\rho(r)] = \int d^3\rho e_{\text{xc}}^{\text{GGA}}(\rho(r), \nabla\rho(r))$ [112], where $e_{\text{xc}}^{\text{GGA}}(\rho(r), \nabla\rho(r))$ is a GGA exchange functional that depends both on the electron density $\rho(r)$ and its gradient $\nabla\rho(r)$. Such functionals work better than LDA, particularly in situations where the electron gas has strong density variations, like

defect calculations [134, 135]. There are various parametrizations in GGA, and the most popular one is called PBE (Perdew, Burke, Ernzerhof) [131, 136, 137].

Even though DFT provides an accessible solution to several calculations in different scientific fields, it still has many limitations. In particular, DFT calculations fail in properly describing strongly correlated systems, such as estimating the fundamental energy band gaps in semiconductors and insulators, which is crucial in semiconductor development and dopability [138]. In fact, the gaps estimated by DFT and the Kohn-Sham equations in semiconductors are usually smaller than the actual gap by about 50% [139]. For these reasons among others, hybrid-DFT was developed as a new approach to compensate the limitations of conventional DFT in such systems.

2.6.2 Hybrid Density Functional Theory

In this work, hybrid-DFT calculations were performed by B. Ryu and S. Park to study charged point defects of the materials of interest. First principle electronic structure calculations were performed to compare the stability of the materials' charged point defects and investigate their potential interplay to predict their effect on the material's total charge carrier concentration [111, 140].

In these calculations, the Heyd-Scuseria-Ernzerhof functional (HSE06) used for the electron exchange correlation energy function, is a hybrid between exact Hartree-Fock and GGA-PBE. These calculations are adopted to overcome the DFT band gap errors, and the formation energies of these defects were calculated using the following equation

$$E_{\text{form}}(D^q, \mathbf{Mg}_2\mathbf{X}) = E_{\text{tot}}[D^q] - E_0 - \sum_j (\mu_j \Delta n_j) + q(E_F + E_{\text{CBM}}) \quad \text{Equation 2.11}$$

where D is the defect and q its charge, $E_{\text{tot}}[D^q]$ and E_0 are the total energies with and without defect in the supercell, μ_j is the atomic chemical potential of species j in the supercell, Δn_j is the number change of atomic species j in the defective supercell with respect to the pristine supercell without defects, E_F is the electron Fermi level, and E_{CBM} is the energy of the conduction band minimum (CBM) [140-143]. In this equation, the Fermi level is referenced to E_{CBM} , meaning that at the conduction band minimum, $E_F = 0$ eV.

Following this equation, a defect is formed by changing the number of atoms of species j in the sample, which results in a change in energy due to the addition or the removal of the atom. This change is quantified by μ_j of each species. Similarly, an addition or a removal of an electron to form a certain defect results in a change of energy according to the Fermi energy, which is the electrochemical potential. As for the difference between $E_{\text{tot}}[D^q]$ and E_0 , it is obtained by constructing the supercells of the pristine cell and calculating the difference in energies of these supercells with and without the defect of interest [144].

To model the system, a (2×2×2) cubic supercell was utilized, using the lattice parameters 6.35 Å for Mg₂Si and 6.75 Å for Mg₂Sn. The supercell contains 64 Mg and 32 Si/Sn atoms, then the dopants are either added, removed or replaced to generate the defective supercells for interstitial, vacancy and substitutional defects. The calculations were done using the Vienna Ab Initio Simulation package, and the hybrid exchange-correlation function used was HSE06 with an exact-exchange parameter of 25% and a screening parameter of 0.208 Å⁻¹. The projector-augmented wave pseudopotentials were used for the atomic potentials, and the planewave energy basis set was used with the energy cutoff of 296 eV.

Both n- (Bi-doped) and p-type (Li-doped) counterparts of the Mg₂(Si,Sn) system are studied in this work with hybrid-DFT. As these materials were contacted with various electrodes (Chapter 2.2), the potentially occurring interactions between the TE material and the electrode materials are investigated from a charged point defect perspective.

Paper Catalogue

Chapter 3: Paper 1

Chapter 4: Paper 2

Chapter 5: Paper 3

Chapter 3: Paper 1

3. Developing Contacting Solutions for $\text{Mg}_2\text{Si}_{1-x}\text{Sn}_x$ -based Thermoelectric Generators: Cu and $\text{Ni}_{45}\text{Cu}_{55}$ as Potential Contacting Electrodes

As established in the chapters before, it is necessary to find contacting solutions in order to develop thermoelectric generators (TEGs) ready for application. In the case of $\text{Mg}_2(\text{Si},\text{Sn})$ -based TEGs, only a couple of electrodes were tested and reported, namely Ni (with doped Mg_2Si [5], and with $\text{Mg}_2\text{Si}_{1-x}\text{Sn}_x$ [4]), Cu (with undoped Mg_2Si [72]), and Ag (with $\text{Mg}_2\text{Si}_{1-x}\text{Sn}_x$ [4]). Here, we tested Cu, as well as the alloy $\text{Ni}_{45}\text{Cu}_{55}$, as electrodes for the solid solution $\text{Mg}_2\text{Si}_{1-x}\text{Sn}_x$ with $x = 0.7$. In both cases, the contacting experiments were done with n- and p-type compositions, where Bi and Li were used as dopants, respectively. The synthesis of the TE materials was done following an upscaling procedure established by Farahi *et al.* [2], and the contacting experiments were done using recommended conditions reported in [4]. Through this work, we found that the Cu electrode resulted in good adhesion, no cracking and low electrical contact resistance values r_c ($< 10 \mu\Omega \text{ cm}^2$) with both TE material types, and these values remained relatively low even after annealing for 7 days at $T = 450 \text{ }^\circ\text{C}$. One major issue, however, with this electrode is the strong diffusion of Cu into the $\text{Mg}_2(\text{Si},\text{Sn})$ matrix, that resulted in very thick reaction layers. Such diffusion also continued during the annealing procedure, which resulted in the change of a big portion of the optimized TE material into the newly formed phases after diffusion and reaction. As for $\text{Ni}_{45}\text{Cu}_{55}$, good adhesion was also observed, but more cracks were seen in the TE material, which could be due to the difference in the coefficient of thermal expansions of the joined materials. Higher r_c values were also obtained (between 15 and $30 \mu\Omega \text{ cm}^2$). Diffusion-wise, the contacting with $\text{Ni}_{45}\text{Cu}_{55}$ resulted in uneven interfaces on both sides of the material, which was correlated with a potential combination of electromigration of the Ni and Cu cations and the new Ni-Si formed phases that act as a diffusion barrier to Cu. As the contacted samples showed cracks already, no annealing experiments were done with this electrode.

In this manuscript, the **submitted revised version of the paper, following the journal's template**, is provided. This work was published on 17 October 2019 in *ACS Applied Materials & Interfaces* journal, Volume 11, Issue 43, from page 40769 to page 40780.

The DOI of the article is <https://doi.org/10.1021/acsami.9b12474>.

Developing Contacting Solutions for Mg₂Si_{1-x}Sn_x-based Thermoelectric Generators: Cu and Ni₄₅Cu₅₅ as Potential Contacting Electrodes

S. Ayachi^{1}, G. Castillo Hernandez^{1,2}, N.H. Pham¹, N. Farahi¹, E. Müller^{1,2}, and J. de Boor¹*

¹*German Aerospace Center, Institute of Materials Research, Dep. Of Thermoelectric Materials & Systems, Cologne, North Rhein-Westphalia, 51147, Germany,*

²*JLU Giessen, Institute of Inorganic and Analytical Chemistry, Giessen, Hessen, 35390, Germany*

Email addresses: Sahar.ayachi@dlr.de, Gustavo.Castillo-Hernandez@dlr.de, nganph38@gmail.com, nader.farahi@gmail.com, Eckhard.Mueller@dlr.de, Johannes.deBoor@dlr.de.*

Abstract

Magnesium silicides can be used for thermoelectric energy conversion, as high values of figure of merit zT were obtained for n-type (1.4 at 500 °C) and p-type (0.55 at 350 °C) materials. This, however, needs to be complemented by low resistive and stable contacting to ensure long-term thermogenerator operation and minimize losses. In this study, we selected Cu and Ni₄₅Cu₅₅ as contacting electrodes for their high electrical conductivity, similar coefficient of thermal expansion (CTE) and good adhesion to Mg₂(Si,Sn). Both electrodes were joined to Mg₂Si_{0.3}Sn_{0.7} pellets by hot pressing in a current-assisted press. Microstructural changes near the interface were analyzed using SEM/EDX analysis, and the specific electrical contact resistance r_c was estimated using a travelling potential probe combined with local Seebeck scanning. Good contacting was observed with both electrode materials. Results show low r_c with Cu, suitable for application, for both n-type and p-type silicides ($< 10 \mu\Omega\text{-cm}^2$), with the occurrence of wide, highly conductive diffusion regions. Ni₄₅Cu₅₅ joining also showed relatively low r_c values ($\sim 30 \mu\Omega\text{-cm}^2$) for n- and p-type, but had a less inhomogeneous reaction layer. We also performed annealing experiments with Cu-joined samples at 450 °C for one week to investigate the evolution of the contact regions under working temperatures. r_c values increased (up to $\sim 100 \mu\Omega\text{-cm}^2$) for annealed n-type samples, but remained low ($< 10 \mu\Omega\text{-cm}^2$) for p-type. Therefore, Cu is a good contacting solution for p-type Mg₂(Si,Sn), and a potential one for n-type if the diffusion causing contact property degradation can be prevented.

Keywords

Thermoelectrics; contacting; interface; electrical contact resistance; annealing.

I. Introduction

Thermoelectric (TE) materials can convert heat into electricity, providing an effective option for sustainable energy conversion in any system generating waste heat ¹. The performance of such TE materials is governed by the dimensionless figure of merit zT , defined as:

$$zT = \frac{\sigma S^2}{\kappa_{\text{tot}}} T \quad \text{Eq. (1)}$$

where σ is the electrical conductivity, S is the Seebeck coefficient, $\kappa_{\text{tot}} = \kappa_{\text{lat}} + \kappa_{\text{el}}$ is the total thermal conductivity, which is the summation of the lattice thermal conductivity κ_{lat} and the electronic thermal conductivity κ_{el} , and T is the absolute temperature. Improved TE materials with optimized Seebeck coefficient and electrical and thermal conductivities are necessary for the development of high-performance thermoelectric generators (TEG), as the efficiency of the TEGs depends on zT ²⁻³.

The efficiency of a TEG is governed by the efficiency of the n- and p-type legs, as well as the losses generated through different mechanisms, including thermal radiation, non-optimized current, material inhomogeneity of the legs, and electrical and thermal resistances between the TE material and the other interfaces such as metallic bridges. Resistances, being the major sources of loss, are being constantly investigated. Device efficiency is directly related to the device figure of merit which is defined as ⁴⁻⁵:

$$ZT = \frac{S_{\text{dev}}^2 T}{RK} = \frac{S_{\text{dev}}^2 T}{(R_{\text{leg}} + R_c)(K_{\text{leg}} + K_b)} \quad \text{Eq. (2)}$$

where S_{dev} is the Seebeck coefficient of the device, R the total electrical resistance and K the total thermal conductance. R_{leg} and R_c are the electrical resistances of the TE legs and the contacts, K_{leg} is the thermal conductance of the TE legs and K_b the thermal conductance of the parasitic heat paths that bypass the legs. To stay within the focus of this paper, K_b will not be taken into consideration. More locations where contact resistances can appear come into play with more mature TEG prototypes, like the resistance between the contacting layers and the metallic bridges, but these can usually be neglected as they are metal-metal interfaces.

From Eq. (2), it is clear that, for a high device efficiency, the electrical contact resistance (R_c) between the legs and the joining electrodes must be low. An acceptable ratio between contact resistance and the total resistance of the device is $< 10\%$ ⁶. The joining should also be stable, and there should be no cracks or delamination between the electrode and the TE legs. This can be avoided by choosing a joining electrode with a coefficient of thermal expansion (CTE) similar to that of the TE material.

The CTE matching assures a similar behaviour of both materials under the effect of temperature and minimises the occurrence of cracks ⁷ which can grow further under mechanical load or thermal cycling

stress, leading to an eventual failure and breakage of the TE leg. Such cracks can also increase the internal resistance of the material, which wouldn't be beneficiary for the device performance.

Interdiffusion or local reactions often occur between the contacting electrode and the TE material, forming reaction layers. It is crucial to study these new layers in order to know their effect on the contact resistance, their inertness with respect to the composition and function of the TE material as well as their stability and development under thermal cycling or long-term annealing.

Among the efficient TE materials are magnesium silicide-based materials, which are cheap, non-toxic, abundant and environment friendly. They are also lightweight and possess good thermal and mechanical stability. These properties make them very attractive to industries such as aerospace and automotive⁸. The binary Mg_2Si has been thoroughly studied⁹⁻¹⁰, and contact development has shown promising results. Ni worked well as a contacting electrode with Mg_2Si showing good adhesion, low specific contact resistance ($< 10 \mu\Omega\text{cm}^2$) and temperature stability^{9, 11-14}.

Cu has also been tested as a joining electrode for undoped Mg_2Si in ref. no¹⁵. The samples showed good adhesion of the interlayer and no cracks within the sample, but the obtained r_c was moderately high ($\sim 15 \text{m}\Omega\text{cm}^2$) before and after thermal stability testing. It has also been stated, that, as the specific contact resistance depends on the carrier concentration, doping is expected to decrease r_c .

Solid solutions of Mg_2Si and Mg_2Sn show improved thermoelectric properties compared to the binary Mg_2Si ¹⁶. In fact, n-type and p-type $\text{Mg}_2\text{Si}_{1-x}\text{Sn}_x$, with $0.6 < x < 0.7$, show $zT_{\text{max}} \sim 1.4$ and ~ 0.55 , respectively, at mid-range temperatures ($350 \sim 450 \text{ }^\circ\text{C}$)¹⁷⁻²². These solid solutions become, then, more attractive for technological applications and device development. Traditionally, higher manganese silicides (HMS) have been used as the p-type counterpart to n-type $\text{Mg}_2(\text{Si},\text{Sn})$ materials due to their abundance, relatively good stability and high zT ²³⁻²⁴. A few research papers also reported trials for module building using n-type Mg_2Si with p-type HMS materials²⁵⁻²⁷. However, due to the recently improved TE properties of p-type $\text{Mg}_2\text{Si}_{1-x}\text{Sn}_x$ materials¹⁷, they are an excellent alternative to HMS. In fact, using them as counterparts to n-type $\text{Mg}_2\text{Si}_{1-x}\text{Sn}_x$ reduces chemical complexity in further investigations and potentially simplifies contacting electrode selection and study.

So far, concerning contacting solutions, Ni and Ag have been tested as contacting electrodes for $\text{Mg}_2(\text{Si},\text{Sn})$ compounds. Ni joining results in small electrical contact resistance, but cracks were observed due to the high CTE mismatch between Ni and the TE materials (Ni: $13 \cdot 10^{-6} \text{ K}^{-1}$, $\text{Mg}_2\text{Si}_{0.4}\text{Sn}_{0.6}$: $18 \cdot 10^{-6} \text{ K}^{-1}$). As for Ag, low contact resistance was obtained only with p-type, while it was about one or two orders of magnitude higher for n-type²⁸.

In this work, n- and p-type $\text{Mg}_2\text{Si}_{1-x}\text{Sn}_x$ with $x = 0.7$ have been synthesized and joint with two different metallic electrodes, namely Cu and $\text{Ni}_{45}\text{Cu}_{55}$. The $\text{Mg}_2\text{Si}_{0.3}\text{Sn}_{0.7}$ composition has been chosen in particular because it shows the best TE properties for n-type. As p-type also has its best TE properties

for compositions with $0.6 < x < 0.7$ ²⁹, $x = 0.7$ has been selected for a better comparability of the results. It is also favourable to use similar n- and p-type materials as this simplifies contact development³⁰. The selection of Cu and Ni₄₅Cu₅₅ was based on their CTE which matches with the selected TE material: Cu: $17 \cdot 10^{-6} \text{ K}^{-1}$ ³¹, Ni₄₅Cu₅₅: $14.9 \cdot 10^{-6} \text{ K}^{-1}$ ³², Mg₂Si_{0.3}Sn_{0.7}: $17.5 \cdot 10^{-6} \text{ K}^{-1}$ ²⁸.

The joining with both electrodes resulted in interfaces that were investigated with SEM/EDX, and the resistance of the contacts was determined from local mappings of the electrical potential and the Seebeck coefficient.

Results show good joining for both Cu and Ni₄₅Cu₅₅. As expected, Cu diffuses into the TE material, creating an inhomogeneous reaction layer and diffusion zones of different size. Nevertheless, the specific contact resistance is very low for both n- and p-types ($< 10 \mu\Omega\text{cm}^2$). Similarly, for Ni₄₅Cu₅₅, both Ni and Cu diffuse into the Mg₂Si_{0.3}Sn_{0.7} matrix, with inhomogeneous interface and thick localized diffusion zones, but r_c is higher than that obtained from Cu contacting. This could be explained by the different resulting interfaces, as well as the differences in CTE matching between the electrodes and the TE material. From this perspective, Cu would be preferred as a potential contacting solution for technological optimization.

Annealing was also done for Cu joined samples. The obtained results show a proceeding diffusion of the electrode material into the TE material, and a low r_c for p-type materials. N-type materials, however, show a slightly different behaviour causing r_c results to be higher than for p-type.

II. Materials and methods

N- and p-type powder materials were synthesized with starting compositions of Mg_{2.06}Si_{0.3}Sn_{0.665}Bi_{0.035} and Mg_{1.97}Li_{0.03}Si_{0.3}Sn_{0.7}, respectively³³. N-type samples were initially synthesized with 3% excess Mg to compensate for the Mg evaporation that occurs during the sintering time, which is double the sintering time needed for p-type samples. Both types were pressed in a 15 mm diameter graphite die at 700 °C for 1200 s for n- and 600 s for p-type, utilizing a direct sinter press DSP 510 SE from Dr. Fritsch GmbH, Fellbach, Germany, under vacuum, with a pressure of 66 MPa and a 1 K/s heating rate. These pressing conditions have been selected as to obtain optimal TE properties for both compositions³⁴⁻³⁵. All studied samples had a high relative density ($\geq 97\%$). Further details on measurements of Seebeck coefficient and electrical conductivity can be found in the literature³⁴⁻³⁶.

Each sample was joined with three stacked disk shape foil layers on each side; each foil having a thickness of $\sim 50 \mu\text{m}$. Such thickness of the electrodes was selected to simplify the contact resistance scanning measurements which have a limited lateral resolution. Cu (99,9%; Goodfellow) and Ni₄₅Cu₅₅

(Ni₄₅Cu₅₅Fe_{0.0025}Mn_{0.0075}; Goodfellow) foils were joined to the pressed pellets for 600 s at 600 °C and 550 °C respectively. These temperatures were chosen to be around half of the melting temperatures of the used materials ($T_{\text{melt}}(\text{Cu}) \approx 1085 \text{ °C}$, $T_{\text{liquidus}}(\text{Ni}_{45}\text{Cu}_{55}) \approx 1300 \text{ °C}$). As Ni₄₅Cu₅₅ has a higher melting point, a higher joining temperature was expected. However, joining it 600°C led to melting and breakage of the sample; which is why a lower temperature was chosen. A more elaborate selection would have been based on thermodynamic data for Cu and Ni-Cu, but such data is not fully described in the ternary systems Cu-Mg-Sn and Cu-Mg-Si and to the best of our knowledge, no quaternary description is available. Therefore, the processing temperatures were determined from experimental results.

As joining temperatures are preferred to be as low as possible, 500 °C was also tried for both electrodes, but it was not sufficient for a good adhesion to the thermoelectric material. Delamination between individual foils of the joining electrodes was also observed at 500 °C. During all joining steps, no insulation layer to prevent current flow through the samples was applied.

The final samples were imaged along their cross section after being cut, grinded and polished. Microstructure and properties of the joining interfaces were investigated under SEM using Zeiss Ultra 55 equipped with an energy dispersive X-ray (EDX) detector with a 15 kV acceleration voltage. The spatial resolution corresponding to this voltage ($E_0 = 15 \text{ keV}$) and to the density of the material used ($\rho = 3.11 \text{ g cm}^{-3}$) is $R = \frac{0.064 (E_0^{1.68} - E_c^{1.68})}{\rho} \approx 2 \text{ }\mu\text{m}$, where $E_c = 3.44 \text{ keV}$ is the critical excitation energy³⁷. Measured compositions were compared with expected phases from literature equilibrium diagrams for the ternary systems Cu-Mg-Si³⁸ and Cu-Mg-Sn³⁹, as well as the binary Ni-Si⁴⁰.

The contact resistance was calculated from the potential and Seebeck results obtained by an in-house built Potential & Seebeck Scanning Microprobe (PSM)^{13, 41}.

Annealing was also processed for Cu-joined samples to study the stability of the contact under set conditions of time and temperature. Each sample has been coated with a thick boron nitride layer to minimize Mg losses due to evaporation at high temperatures, sealed in quartz ampules filled with Argon, and then annealed for one week at 450 °C.

III. Results:

1. Microstructure:

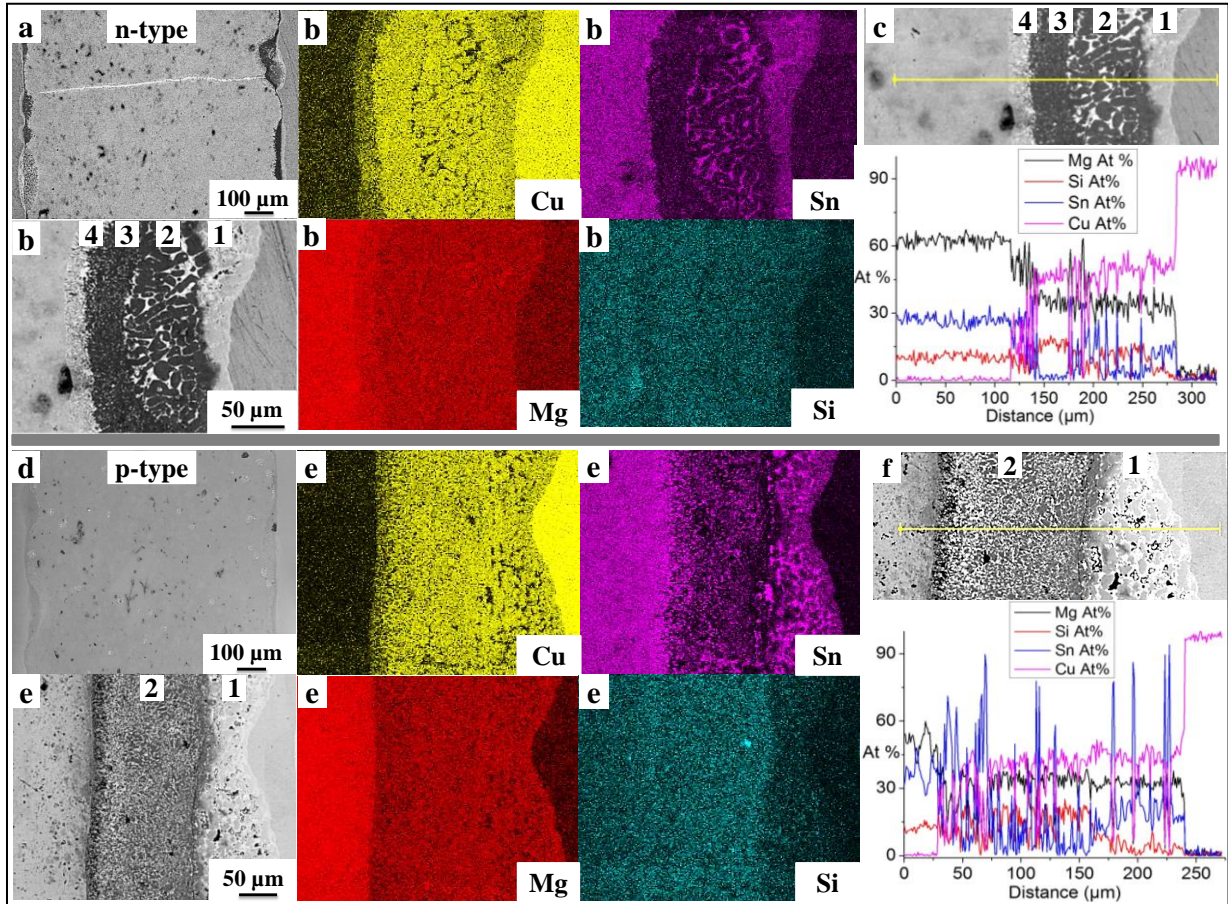


Figure 1: SEM - EDX results of Cu-joined n- (a–c) and p-type (d–f) $Mg_2Si_{0.3}Sn_{0.7}$: (a,d) overview of joined samples, (b,e) element mappings at an interface (c,f) line scans over interface layers.

Figure 1 shows SEM - EDX results of both n- and p-type $Mg_2Si_{0.3}Sn_{0.7}$ samples joined with Cu. **Figures 1 (a)** and **(d)** show only selected sections of the samples; however, the visible size is $> 3 \text{ mm}^2$ and thus representative. The adhesion is good for both material types and neither delamination nor cracks between the electrodes and the TE material were observed (**Figure 1 (a)** and **(d)**). In fact, high magnification analysis proved that the darker “lines” along the interface between thermoelectric material and electrode are not cracks but thinner parts of the reaction layer. No cracks were also observed in the TE material itself, apart from one penetrating crack that can be seen on **Figure 1 (a)** as a horizontal channel running through the sample, which is believed to be rich in Mg_2Sn .

Both samples contain darker and brighter spots scattered over the TE $Mg_2Si_{0.3}Sn_{0.7}$ matrix. These are, respectively, Si-rich $Mg_2(Si,Sn)$ phases and Sn segregates. The Si-rich phases are presumably residuals

from the synthesis process, which has been confirmed through comparative SEM investigations before and after contacting³⁴; while the Sn-rich phases appear in the second sintering step. In fact, these Sn-rich phases were most probably formed during the joining with Cu, under occurring current-induced temperature gradients that differently affect local inhomogeneities (local compositions, difference in grain size, micro-cracks...) in the sample, inducing Mg losses, and leaving the matrix locally rich in Sn.

Table 1: EDX composition analysis results of interface layers 1–3 from **Figure 1 (c)** of the n - $Mg_2Si_{0.3}Sn_{0.7}$ joined with Cu.

	Layer 1	Layer 2		Layer 3
		Dark segregates	Bright Region	
Cu (at.%)	~ 50	~ 50		~ 50
Mg (at.%)	~ 35	~ 35		~ 35
Sn (at.%)	~ 15	< 5		< 5
Si (at.%)	< 5	~ 15		~ 17
Likely phase	γ ($Cu_{1.55}MgSn_{0.45}$)	τ_1 ($Cu_{1.5}MgSi_{0.5}$)	Mg_2Sn	τ_1 ($Cu_{1.5}MgSi_{0.5}$)

The reaction layers forming from contacting both n-type and p-type $Mg_2Si_{0.3}Sn_{0.7}$ are thick and visible even at low magnification. They are uneven in thickness ($25 \sim 30 \mu m$) and inhomogeneous in microstructure, with locally thicker zones of diffusion of $150 \sim 200 \mu m$. Besides inhomogeneous current distributions during the pressing, the location of these thicker diffusion zones might be related to inhomogeneities of the thermoelectric material (local fluctuations in composition, varying grain sizes ...) which serve as a seed for a faster reaction between electrode and thermoelectric material. EDX investigation of some of these diffusion zones is shown in **Figure 1 (b)**, **(c)**, **(e)** and **(f)** and their descriptions are presented in **Table 1** and **Table 2**, respectively. Note that these selected diffusion zones in **(b)** and **(e)** are taken from parts of the samples that are not shown in **(a)** and **(d)**. EDX detected percentages that are lower than 5% were not taken into consideration due to detection limitation and potential errors and artefacts. References n^o 38 and 39 were respectively used as references for interpretation and phase identification in the Cu-Mg-Si and Cu-Mg-Sn ternary phase diagrams.

For n-type (**Figure 1 (c)**), the diffusion zone shows dendritic growth from the Cu side inside the TE material. It contains different regions that can be categorized in four separate layers, each with a different composition. The outermost layer, numbered 1, has a thickness $\sim 25 \mu m$. Combining composition results from EDX investigations and interpretations based on the used phase diagram³⁹, this layer seems to be mainly composed of one phase, the γ phase from the Cu-Mg-Sn phase diagram, which is $Cu_{2+x-y}Mg_{1-x}Sn_y$ with $x = 0$ and $y = 0.45$, giving the $Cu_{51.7}Mg_{33.3}Sn_{15}$ composition. This phase is similar in structure to the Cu_2Mg binary but with Sn atoms sitting on some Cu sites. As Cu diffuses into the TE material matrix which is rich in Sn, nucleation and growth occur, leading to the formation of the γ phase in the first layer of the interface.

The following layer, numbered 2, is the thickest ($\sim 75 \mu\text{m}$). The scatter in greyscale colours indicates that it is composed of more than one phase. In fact, from the EDX element mapping, the black spots are Cu segregates (dendrites) that have grown within a brighter matrix, which is Sn rich. From the line scan, one can see that where the Sn content peaks, that of Cu and Si drops. Mg content on the other hand doesn't vary a lot throughout the whole layer. This can be interpreted as the ternary τ_1 ($\text{Cu}_{1.5}\text{MgSi}_{0.5}$) phase for the darker segregates, and the Mg_2Sn matrix for the brighter area. Nucleation and growth of the τ_1 phase happen towards the TE material side of the γ phase, as Cu continues to diffuse inside the TE material.

The third layer has a thickness of $\sim 30 \mu\text{m}$ and it seems to be similar in composition to the first layer as it is mainly composed of three elements but with Sn being replaced by Si. The stoichiometry (see **Table 1**) fits with the ternary τ_1 phase ($\text{Cu}_{1.5}\text{MgSi}_{0.5}$) of the Cu-Mg-Si system.

The fourth layer, adjacent to the TE material, is the thinnest one ($\sim 20 \mu\text{m}$) and most complicated in composition. All four elements exist with non-negligible atomic percentage ($\geq 10 \text{ at. } \%$), which make phase recognition difficult. Nevertheless, a closer investigation of the line scan across this layer as well as the correlation with the SEM data shows the existence of at least two phases, potentially $\text{Mg}_2\text{Si}_{0.3}\text{Sn}_{0.7}$ and the τ_1 phase ($\text{Cu}_{1.5}\text{MgSi}_{0.5}$). This is similar with the phases composing layer 2 (τ_1 and Mg_2Sn), but as we are closer to the TE material side, the concentration in Si is higher.

Cu-joined p-type investigations of a localized diffusion zone are presented in **Figure 1 (e)** and **(f)**. This diffusion zone has a thickness of $\sim 200 \mu\text{m}$ and, similar to the n-type case, it is composed of four layers. Two of these layers are very thin ($< 10 \mu\text{m}$) and will therefore be disregarded in the following analysis.

Table 2: EDX composition analysis results of interfaces of p-type $\text{Mg}_2\text{Si}_{0.3}\text{Sn}_{0.7}$ joined with Cu

	Layer 1	Layer 2
Cu (at.%)	~ 45	~ 45
Mg (at.%)	~ 35	~ 35
Sn (at.%)	$\sim 15 \sim 20$	< 5
Si (at.%)	< 5	$\sim 15 \sim 20$
Possible phases	$\gamma + \text{Sn} / \text{Mg}_2\text{Sn}$	$\tau_1 + \text{Sn} / \text{Mg}_2\text{Sn}$

From the element mapping and the line scan, Cu and Mg are roughly constant throughout the layer scheme, except for the Sn-rich spots. On the other hand, Si and mostly Sn fluctuate a lot. The outermost layer numbered 1 is mainly composed of Cu, Mg and Sn, and the difference in greyscale colours indicates the coexistence of more than one phase. The atomic compositions match with the ternary γ phase observed in layer 1 of **Figure 1 (b)**. The higher Sn concentrations, though, can be related to elemental Sn or a mixture of Mg_2Sn and elemental Sn that accumulates as the brighter islands visible in the SEM figures. This is in line with the observation of high Sn content (peaks) in the corresponding line scan.

Layer number 2 has at least two phases: the darker part that is mostly Cu, Mg and Si, and the brighter spots are, here again, Sn-rich segregates. In this region, the atomic compositions correspond to the τ_1 phase that was also observed in the n-type case. Sn line scan in **Figure 1 (f)** oscillates a lot between values ≤ 5 at. % and ≥ 80 at. %, which correlates very well with the scattered appearance of the bright Sn-rich microstructures.

Figure 2 is a composition mapping that shows a section of a diffusion zone from the reaction layer of p-type with Cu under very high magnification. The dendritic growth of Cu-containing phases as it precipitates out of the matrix is clearly visible as the grey elongated shapes seen in the figure below. These dendrites contain about 50 at. % Cu, 30 at. % Mg and 20 at. % Si, but no Sn. Such stoichiometry corresponds to the τ_1 phase from the Cu-Mg-Si ternary system, already mentioned above. Sn is mainly filling the white areas around the dendrites, with measured atomic percentages varying between 50% and 80%. This proves that the Cu-Mg-Si phases are more stable than the Cu-Mg-Sn phases, which explains the favourable crystallization of the τ_1 phase and the left out elemental Sn. As Mg seems to be also present in these white areas with concentrations between 30 and 50%, whereas Si and Cu are not, the matrix surrounding the dendrites could be a mix of elemental Sn and some Mg_2Sn . **Figure 2** also shows some local black spots, which seem to contain $\sim 90\%$ of Sn according to the composition mapping. As Sn is the heaviest element in the matrix and is so expected to be the brightest, these black spots are then presumably pores and the readings of the mapping at these black spots are artefacts. Further work and better spatial resolution are required to confirm whether it is Sn or Mg_2Sn (or both).

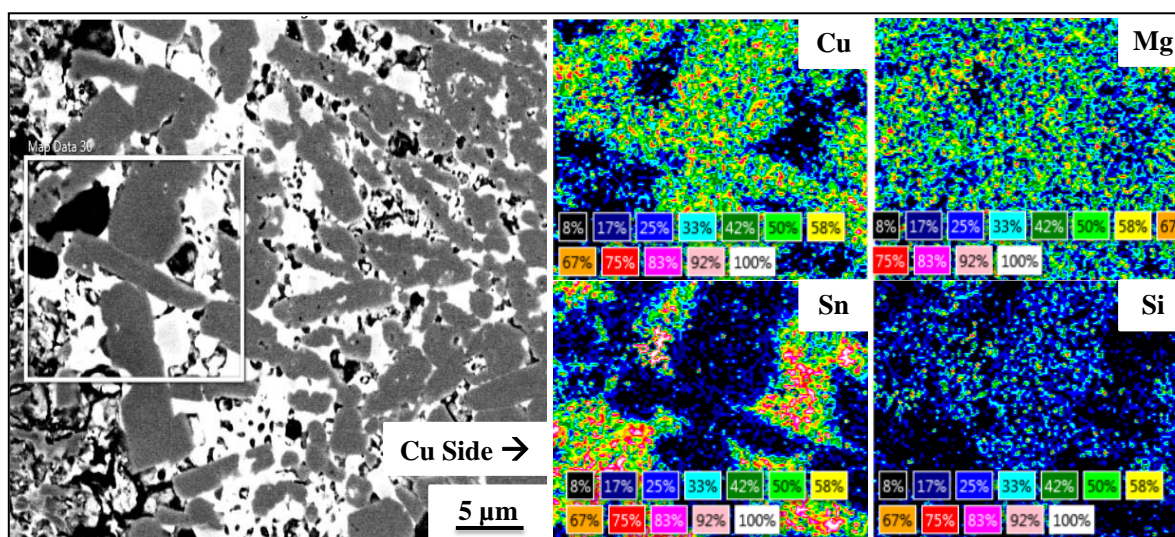


Figure 2: Composition mapping on the reaction layer of Cu-joined p-type $Mg_2Si_{0.3}Sn_{0.7}$ (Cu on right hand side)

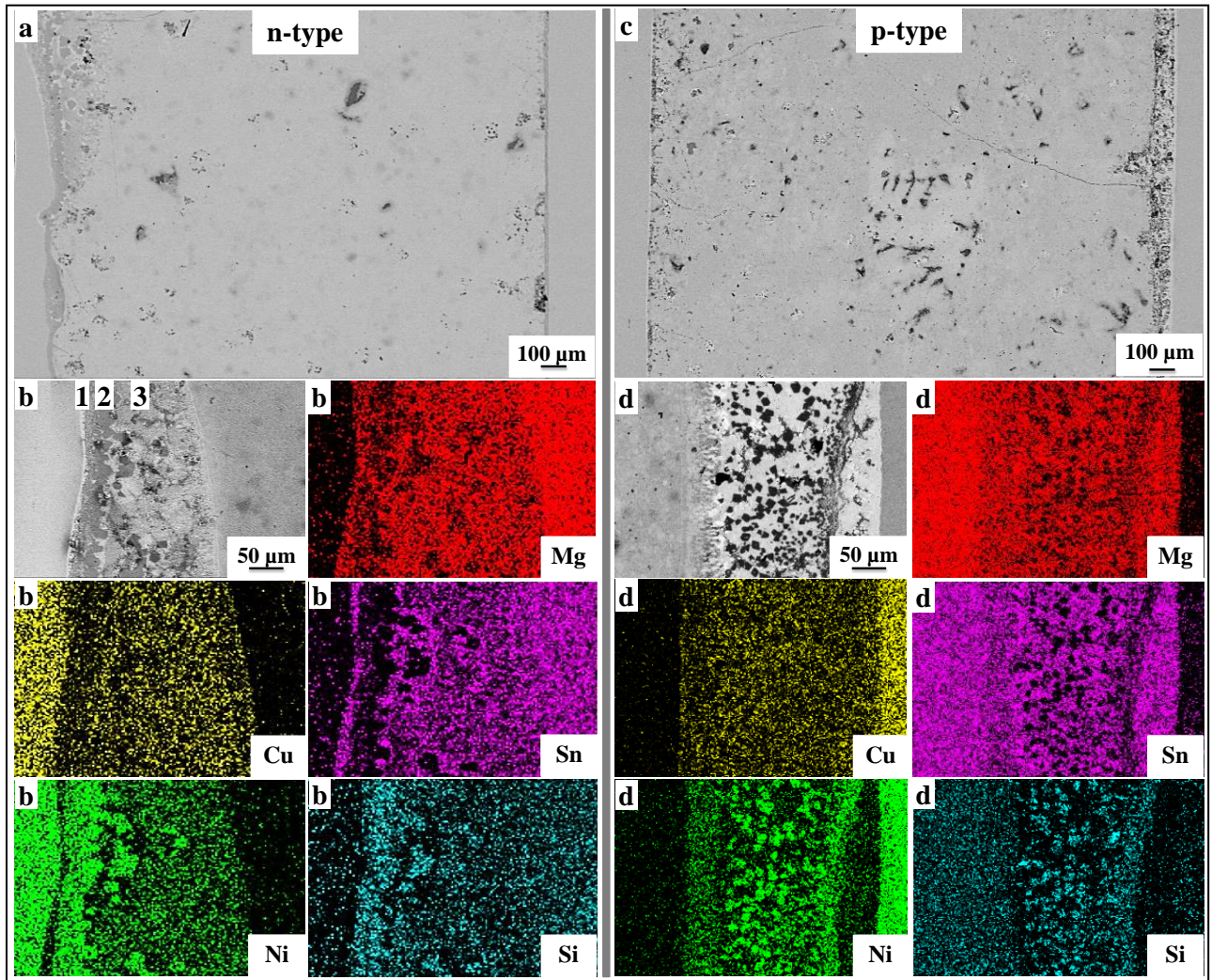


Figure 3: SEM - EDX results of a $Ni_{45}Cu_{55}$ -joined n- and p-type $Mg_2Si_{0.3}Sn_{0.7}$: (a) overview of joined n-type, (b) overview of joined p-type, (c) element mapping on interface of n-type, (d) element mapping on interface of p-type

Figure 3 shows SEM/EDX investigations of the joining of $Ni_{45}Cu_{55}$ with n- and p-type $Mg_2Si_{0.3}Sn_{0.7}$ doped with Bi and Li, respectively. Similar to the case of Cu joining, no delamination was observed. The dark Si-rich phases due to the synthesis process are visibly scattered across the samples, but no Sn-rich segregates were observed. As the appearance of such phases in the Cu joined cases has been correlated with temperature gradients and local overheating inside the sintering chamber, their absence in this $Ni_{45}Cu_{55}$ joining case could be due to the lower joining temperature ($550^{\circ}C$ for $Ni_{45}Cu_{55}$, $600^{\circ}C$ for Cu) and therefore lower local overheating. **Figure 3 (c)** also shows some cracks inside the p-type TE material, starting from the reaction layers towards the inside of the material.

An interesting feature occurring with $Ni_{45}Cu_{55}$ and which has not been seen with Cu is the difference between the reaction layers on each side of the samples. As **Figure 3 (a)** and **(c)** show, the interface is much thicker on one side of each sample than on the other. The thin layers have a thickness of 15 ~ 20

μm , while the thick ones have a thickness of $150 \sim 190 \mu\text{m}$, are inhomogeneous and contain different regions.

Figure 3 (b) presents an EDX element mapping of the interface of the joint n-type. Both thin and thick layer have a similar composition and microstructure, so only an analysis of the thick side is presented here. The first region labeled 1 on the figure, a very thin layer closest to $\text{Ni}_{45}\text{Cu}_{55}$ side is mainly Cu, Mg and Sn, but no Ni or Si. The layer doesn't look single phased, so it could potentially contain the binary Mg_2Sn with some elemental Cu, or it could also be a mix of Mg_2Sn and a Cu-Mg-Sn ternary phase. As the γ ($\text{Cu}_{1.55}\text{MgSn}_{0.45}$) phase occurred often in the case of Cu contacting, it could be the existing ternary phase here, and this first layer would then contain Mg_2Sn and γ .

The following layer, layer 2, is a larger Ni- and Si- rich layer, and the third and last layer, which is the thickest and closest to TE material, contains all five elements, with square-shaped precipitates of Ni and Si. A similar description can be made for the interface of the joint p-type, as can be seen from **Figure 3 (d)**. Here also, we can see a first layer that doesn't contain any Ni or Si, and could possibly be $\text{Mg}_2\text{Sn} + (\text{Sn,Cu})$. The Ni-Si accumulations also exist in an Mg-Cu-Sn matrix, and occur even more often than in the case of n-type.

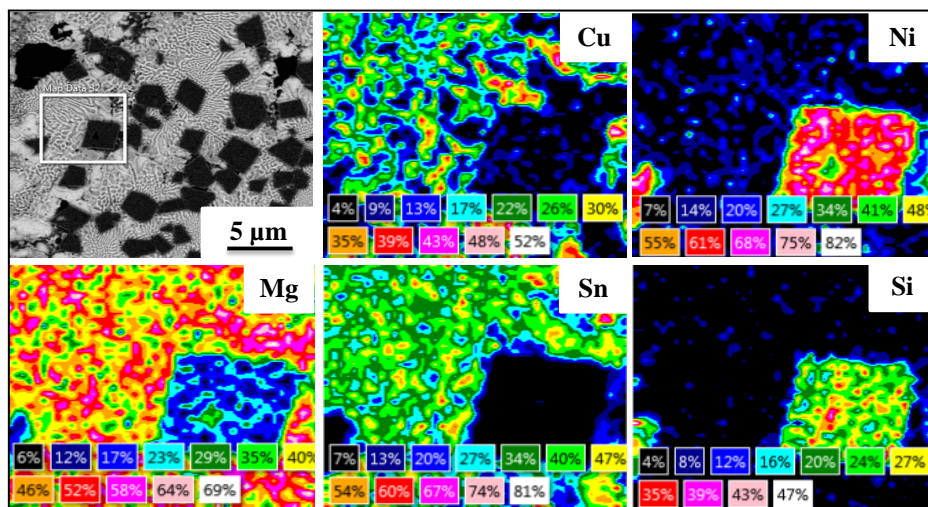


Figure 4: Composition mapping on interface of $\text{Ni}_{45}\text{Cu}_{55}$ -joined p-type $\text{Mg}_2\text{Si}_{0.3}\text{Sn}_{0.7}$

To confirm the microstructure of these Ni-Si accumulations, composition mapping in the middle of the interface of the joined p-type sample is presented in **Figure 4**. The obtained data show that these square shapes have an atomic composition of $50 \sim 75 \text{ at. \% Ni}$ and $20 \sim 35 \text{ at. \% Si}$. Such Ni-Si phase formation has been observed in the literature¹⁴ before, in $\text{Mg}_2\text{Si}/\text{Ni}$ contacts where a single reaction layer of $\text{Ni}_{31}\text{Si}_{12}$ ($\text{Ni} \sim 73 \text{ at. \%}$ and $\text{Si} \sim 27 \text{ at. \%}$) was identified. The Ni-Si precipitates shown in **Figure 4** are surrounded by a eutectic-like morphology with an average composition of $\sim 50 \text{ at. \% Mg}$,

~ 35 at. % Sn and ~ 20 at. % Cu which falls in a non-fully determined region of the Cu-Mg-Sn equilibrium diagram. As the micrographs show at least two different phases, it could be τ_1 -CuMgSn with the binary Mg_2Sn .

2. Electrical Contact Resistance:

The resulting contact resistance is calculated using the electrical potential data obtained from the PSM measurements, as well as the properties of the employed TE material. In case of a homogeneous current density $j = I/A$ passing through the sample and the contact, the bulk contact resistance R_c can be obtained using this equation:

$$R_c = \frac{V_{elec} - V_{TE}}{I} \quad (\text{Eq.3})$$

where V_{elec} and V_{TE} are the local voltages measured on the electrode and the TE material, respectively, on both sides of the interface. Previous literature^{15, 42-45} also uses the same equation.

However, the homogeneity of the electrical field can be distorted by irregularities in the material and non-homogeneous interfaces⁴⁵. Given the complex and sub-structured interfaces observed in the samples, a homogeneous current density distribution can therefore not be assumed a priori. If one assumes that the current density j is approximately constant in the direction of the line scan (which is a less strict assumption) j can be estimated using the properties of the TE material, where the specific contact resistance $r_c = R_c * A$ is

$$r_c = \frac{V_{elec} - V_{TE}}{j} \quad (\text{Eq.4})$$

with

$$j = \frac{\Delta V_{TE}}{R_{TE} * A} \quad (\text{Eq.5})$$

$$R_{TE} = \frac{l_{TE}}{A \sigma_{TE}} \quad (\text{Eq.6})$$

where ΔV_{TE} and R_{TE} are the voltage and the resistance across the material, l_{TE} and σ_{TE} are its length and electrical conductivity, respectively. The average cross section A for all measured samples is around 3.5 mm^2 .

Thus, r_c can be estimated from

$$r_c = \frac{(V_{elec} - V_{TE}) l_{TE}}{\Delta V_{TE} * \sigma_{TE}} \quad (\text{Eq.7})$$

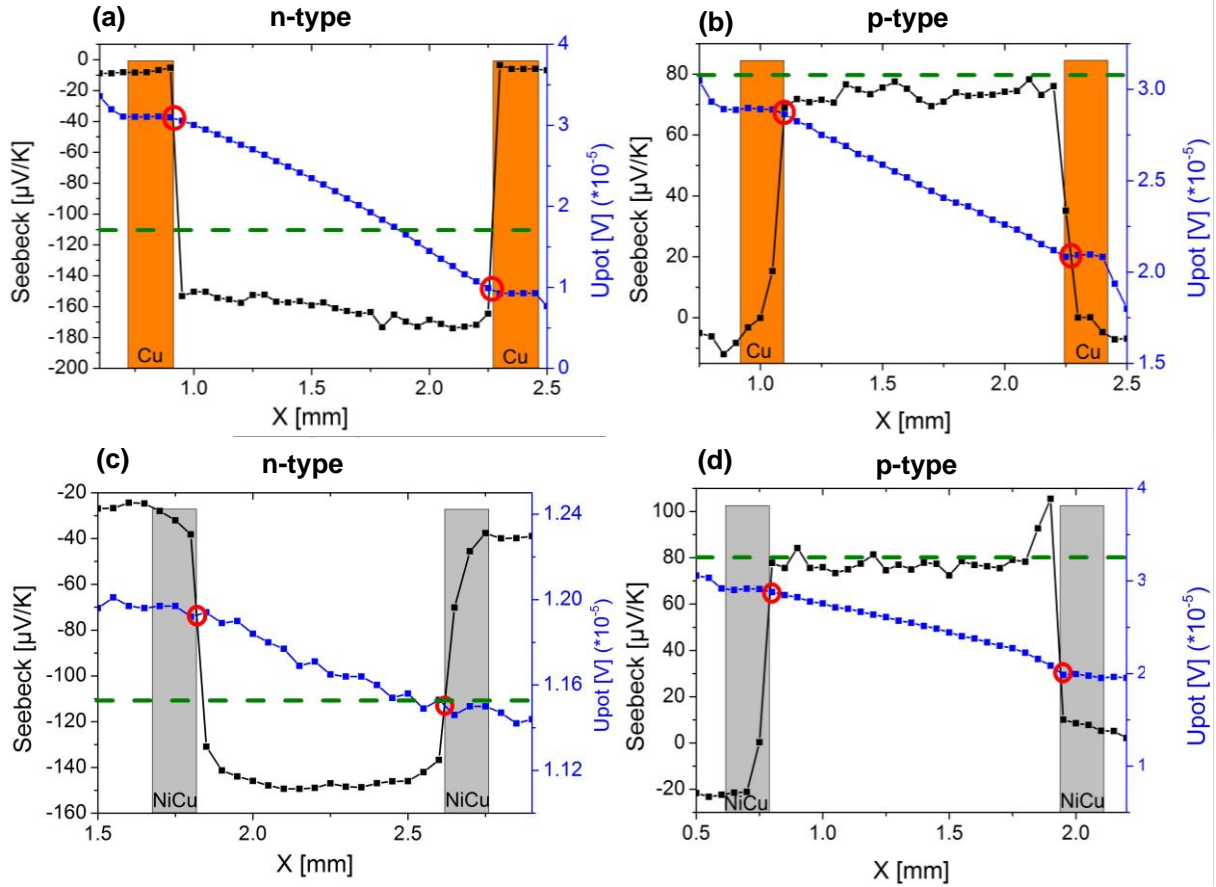


Figure 5: PSM graphs of (a): n-type $\text{Mg}_2\text{Si}_{0.3}\text{Sn}_{0.7}$ joined with Cu, (b): p-type with Cu, (c): n-type with $\text{Ni}_{45}\text{Cu}_{55}$ and (d): p-type with $\text{Ni}_{45}\text{Cu}_{55}$. The dashed green lines indicate the value of the sample's Seebeck coefficient before joining.

Figure 5 shows typical results of line scans of the Seebeck coefficient and the electrical potential obtained from PSM measurements. The drop in the Seebeck graph is used to determine the position of the interface. From that position, the values of the voltages V_{elec} and V_{TE} are read from the U graph at the positions just before and after the interface. Several line scans are used to obtain an average result for r_c .

All four graphs shown above display a smooth decrease in U towards the low potential side within the sample. The absence of sudden potential drops at the interface positions (marked with red circles) indicates that the contact resistance is low.

Quantitative results for r_c using the material properties (Eq.7) and r_c assuming constant current density (Eq.3) are presented in **Table 3**.

Table 3: Specific contact resistance values of n- and p-type $Mg_2Si_{0.3}Sn_{0.7}$ joined with Cu and $Ni_{45}Cu_{55}$. The relative measurement uncertainty is the standard deviation of all line scans for each sample

Sample	r_c (Eq. 7) / ($\mu\Omega cm^2$)	r_c (Eq. 3) / ($\mu\Omega cm^2$)
n + Cu	6 ± 4	9 ± 6
p + Cu	8 ± 5	3 ± 2
n + $Ni_{45}Cu_{55}$	24 ± 17	4 ± 3
p + $Ni_{45}Cu_{55}$ (thin interface side)	11 ± 6	15 ± 8
p + $Ni_{45}Cu_{55}$ (thick interface side)	53 ± 26	73 ± 36

As shown in the table, r_c (Eq. 7) values are indeed relatively low, especially for the case of Cu joining.

Note that the change in potential across the sample is very low and that the signal is noisy for n-type contacted with $Ni_{45}Cu_{55}$ (**Figure 5 (c)**), which indicates a low current density in the measurement region.

For $Ni_{45}Cu_{55}$ with p-type samples, r_c was around 6 times higher than Cu joined with p-type. The values for the thick and thin layer sides were respectively $\sim 11 \mu\Omega cm^2$ and $53 \mu\Omega cm^2$ (Eq. 7) yielding an average r_c value of $\sim 30 \mu\Omega cm^2$. Such difference can be correlated with the corresponding S graph in **Figure 5** where a higher peak is visible on the right-hand side of the graph, indicating a local change of the material properties at the position of the thick interlayer.

Comparing results from r_c (Eq. 7) and r_c (Eq. 3), all obtained values are similar, except for n-type joint with $Ni_{45}Cu_{55}$. For this sample, further SEM/EDX investigations have shown the existence of “diffusion channels” of $\sim 100 \mu m$ width running between interfaces on both sides. These channels are mainly composed of metallic phases that create a short circuit in the samples, which explains the observed small change in potential and increases measurement uncertainties due to line to line differences. In general, if the material properties are known, Eq. 7 is more reliable than Eq. 3 as its applicability requires fewer conditions.

Besides the low contact resistances, a change in the TE properties has been observed in n-type samples joint with both Cu and $Ni_{45}Cu_{55}$. In fact, **Figure 5 (a)** and **(c)** show that the S values of the samples after joining are $-150 \sim -160 \mu V/K$, while the initial value before contacting was $\sim -110 \mu V/K$ (marked with green dashed line). Such change in S is not observed with p-type samples where the S value remains constant after joining ($\sim 80 \mu V/K$). For this reason, σ_{TE} has been measured again for n-type contacted samples and implemented in Eq. 7 to obtain correct r_c values⁴⁶.

Table 4 below summarizes the changes in S values and provides estimations for the corresponding carrier concentrations. As $Mg_2(Si,Sn)$ is a well-studied material system and it had been shown that single parabolic band model can be used to describe the electrical transport for both n-type^{22, 47-48} and p-type^{17, 19, 29}, we used a well-established SPB model that was developed in our group to estimate carrier concentration values²⁹. For these calculations, we assume $m_D^* = 2.5$ ⁴⁹ for n-type samples and $m_D^* =$

1.5 for p-type samples ²⁹ and use $S = \frac{k_b}{e} \left(\frac{2F_1}{F_0} - \eta \right)$ and $n = 4\pi \left(\frac{2m_D^* k_b T}{\hbar^2} \right)^{1.5} F_{\frac{1}{2}}(\eta)$ to estimate the carrier concentration n from the measured Seebeck coefficient.

The table also presents the ratios of electrical contact resistances to the resistance of the thermoelectric material with assumed dimensions of length $l = 5 \text{ mm}$ and area $A = 1 \text{ cm}^2$. As the actual samples used were not designed for module building, they had different thicknesses.

Table 4: Seebeck coefficients S , estimated carrier concentrations n and ratios of contact resistance to material resistance for contacted samples.

Type	Contact	S ($\mu\text{V}/\text{K}$)	n (cm^{-3})	σ (S/cm)	r_c ($\mu\Omega\text{cm}^2$)	R_{TE} ($\times 10^{-4}\Omega$)	$2r_c/(A \times R_{TE})$
n	None	-110	2.9×10^{20}	1851	--	2.7	--
	Cu	-160	1.38×10^{20}	710	6 ± 4	7.04	1.70 %
	Ni ₄₅ Cu ₅₅	-160	1.38×10^{20}	710	24 ± 17	7.04	6.82 %
p	None	80	2.35×10^{20}	683	--	4.39	--
	Cu				8 ± 5		3.64 %
	Ni ₄₅ Cu ₅₅ (thin side)				11 ± 6		5.01 %
	Ni ₄₅ Cu ₅₅ (thick side)				53 ± 26		24.14 %

It can be seen that the estimated reduction in carrier concentration is significant and in line with the observed reduction in electrical conductivity. The ratio of contact to material resistances is in the lower percentage range for Cu and n-type contacted with Ni₄₅Cu₅₅, and somewhat higher for p-type contacted with Ni₄₅Cu₅₅.

3. Annealing:

As Cu contacted samples show better r_c results, they have been annealed at 450 °C for one week to study their thermal stability under thermal treatment. This temperature has been selected because it is around the actual working temperature of the final Mg₂Si_{1-x}Sn_x-based thermoelectric device.

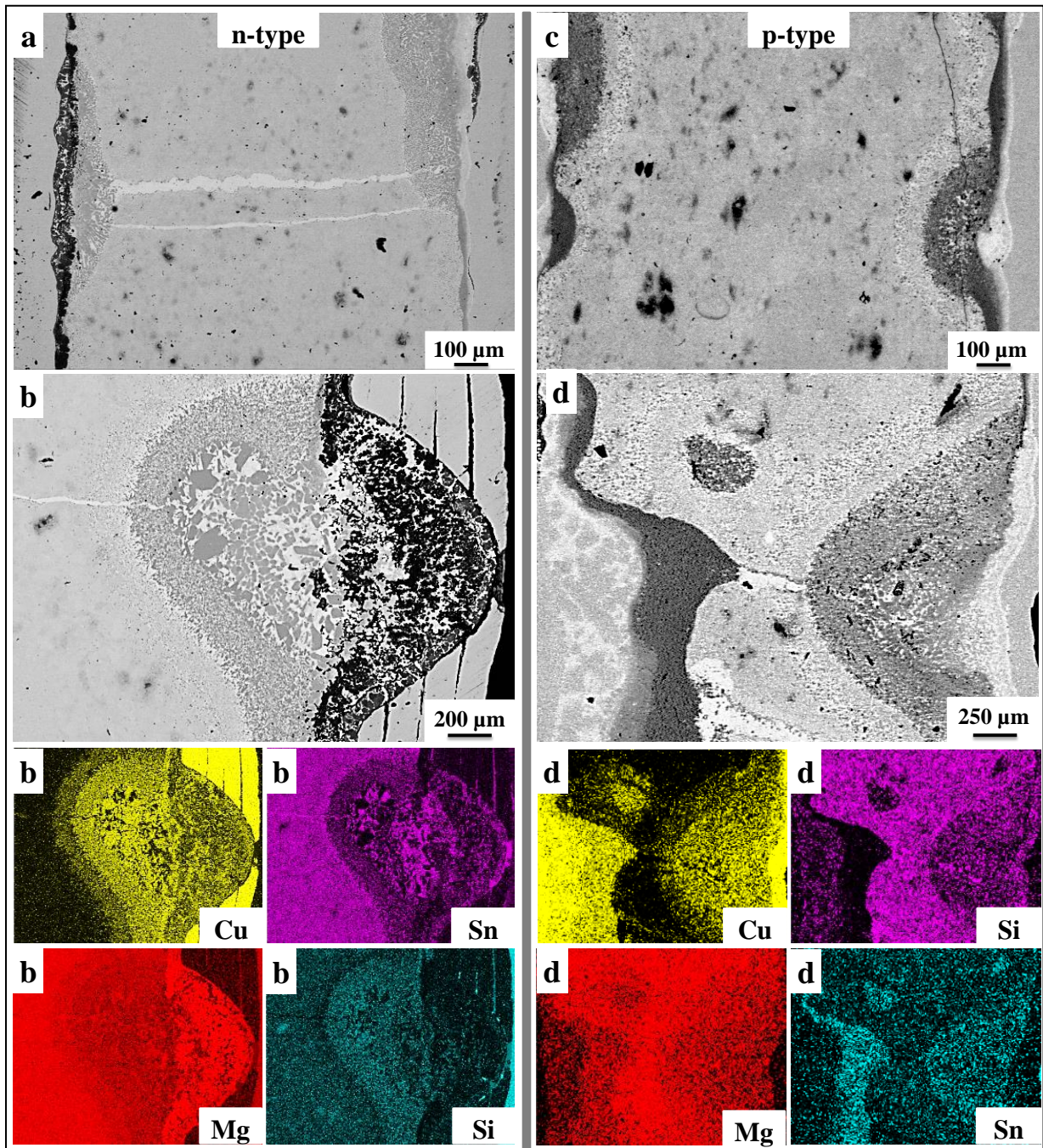


Figure 6: SEM pictures of annealed Cu joined $Mg_2Si_{0.3}Sn_{0.7}$: (a): overview of joint n-type, (b): EDX element mapping of localized n-type joined interface, (c): overview of joined p-type, (d): EDX element mapping of localized p-type joined interface

Figure 6 shows the SEM results of annealed Cu-joint n- and p-type samples. At low magnification, the annealed n-type $Mg_2Si_{0.3}Sn_{0.7}$ looks similar to the non-annealed sample, but, as expected, the interface and the local diffusion zones have expanded respectively to $\sim 250 \mu m$ and $\sim 600 \mu m$. Two bright lines joining the diffusion zones from the interfaces on both sides are visible in **Figure 6 (a)**. As it was taken in backscattering mode, the brightest regions are Sn-rich, Sn being the heaviest element. One more

interesting feature was also observed and is shown in **Figure 6 (b)** which is the diffusion of the TE material inside the Cu layers, causing a delamination of the foils.

EDX element mappings show that the microstructure and composition of the diffusion layers on the joint n-type interface remain almost the same after annealing: Cu dendrites agglomerate in a Sn-rich environment. The part that diffuses inside Cu is mostly Mg. Sn areas locally exist but Si is completely absent. Literature on inter-diffusion of Cu and Mg under temperatures $\sim 450^\circ\text{C}$ ⁵⁰ shows that the binary compositions Mg_2Cu and MgCu_2 occur. As the formation energy of Mg_2Cu is lower than that of MgCu_2 , the former binary compound would form before the latter. This could explain the higher concentration of Mg diffused in Cu.

The annealed Cu-joined p-type sample on **Figure 6 (c)** shows also stronger diffusion, similar to n-type, with diffusion zones $\sim 200\ \mu\text{m}$ thickness. One crack can also be seen inside the sample parallel to the interface.

Figure 6 (d) shows very thick localized diffusion zones $\sim 450\ \mu\text{m}$ each, where Cu has penetrated far inside the material from both sides. From the difference in greyscale, the diffusion zones seem to have different compositions, but as general overview, they both seem to be mainly composed of Mg-Cu-Si phases in Sn-rich $\text{Mg}_2(\text{Si},\text{Sn})$ matrix.

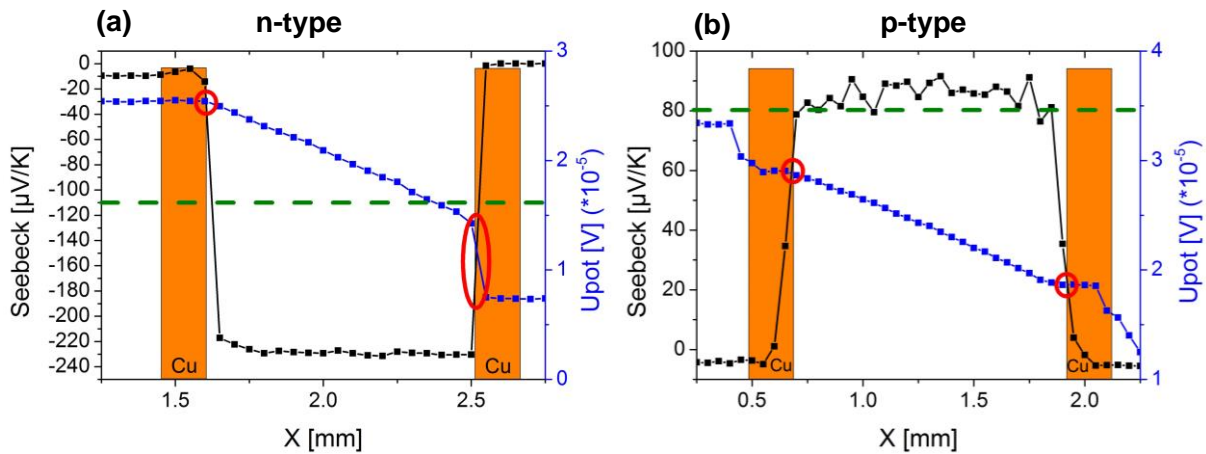


Figure 7: PSM graphs of annealed (a): n- and (b): p-type Cu joined $\text{Mg}_2\text{Si}_{0.3}\text{Sn}_{0.7}$. The dashed green lines indicate the value of the sample's Seebeck coefficients before joining.

Figure 7 shows the Seebeck and potential graphs of the annealed samples. P-type samples still show no drop at the interfaces, indicating a low r_c . However, the potential line for n-type shows a large drop at the right-hand side interface, even though the left-hand side shows none. This indicates that changes have occurred at the interfaces under annealing, which caused the potential to drop. Another possibility could be that the scanned region had cracks or localized delamination between Cu and the TE material.

The averaged results using Eq. 3 and Eq. 7 are displayed in **Table 5**. As expected from the PSM graphs in **Figure 7**, r_c is low for p-type. For n-type, the final averaged r_c has been disentangled for interfaces on both sides.

Table 5: Specific contact resistance values of annealed n- and p-type $Mg_2Si_{0.3}Sn_{0.7}$ joined with Cu (450°C, 1 week)

Sample	$r_c(Eq. 7) / (\mu\Omega cm^2)$	$r_c(Eq. 3) / (\mu\Omega cm^2)$
Annealed n + Cu (left side)	11 ± 6	13 ± 7
Annealed n + Cu (right side)	155 ± 30	181 ± 30
Annealed p + Cu	7 ± 5	6 ± 4

Similar to the non-annealed case, S of n-type changed to $\sim -230 \mu V/K$. Here again, new measurements for σ_{TE} have been obtained and implemented in Eq. 7. Here also, we provide estimations for the carrier concentrations (using $m_D^* = 2.5$ ⁴⁹ for n-type and $m_D^* = 1.5$ for p-type²⁹) as well as ratios of electrical contact resistances to total resistances in **Table 6**.

Table 6: Seebeck coefficients S , estimated carrier concentrations n and ratios of contact resistance to material resistance for contacted samples.

Sample	S ($\mu V/K$)	n (cm^{-3})	σ (S/cm)	r_c ($\mu\Omega cm^2$)	R_{TE} ($\times 10^{-4} \Omega$)	$2r_c / (A \times R_{TE})$
n + Cu (left side)	-230	5.5×10^{19}	450	11 ± 6	11.1	1.98 %
n + Cu (right side)				155 ± 30		27.92 %
p + Cu	80	2.35×10^{20}	683	7 ± 5	4.39	3.19 %

It can be seen that the resistance ratio remains small also after annealing, with the exception of the right side of the n + Cu sample.

IV. Discussion

Results for n- and p-type $Mg_2Si_{0.3}Sn_{0.7}$ contacted with Cu and $Ni_{45}Cu_{55}$ electrodes are presented. Both electrodes showed mechanically stable joining to both material types, with no delamination. SEM/EDX investigations show Cu diffusion into n- and p-types, resulting in thick inhomogeneous reaction layers and diffusion zones of complex structures. These diffusion layers contain dendrites of Cu growing into a Sn-rich matrix, which occurred due to heterogeneous nucleation. In fact, heterogeneous nucleation, which is common in solid solutions, occurs at phase boundaries or around impurities, initiating the growth process of the dendrites⁵¹. In our case, the dendritic growth presumably initiates as Cu diffuses

along the grain boundaries⁵²⁻⁵³ and grows due to the temperature gradient caused by the local heating under direct joining current, which disturbs the equilibrium conditions.

The composition and microstructure of the diffusion zones are different. In both n- and p-type cases, the ternary phases γ ($\text{Cu}_{51.7}\text{Mg}_{33.3}\text{Sn}_{15}$) and τ_1 ($\text{Cu}_{1.5}\text{MgSi}_{0.5}$) exist, but with different layering order and different thicknesses. The size and distribution of the dendrites are also different. While some thickness variation of the interface layer is often observed, comparison with literature^{15, 28} indicates that the combination of Cu and Sn is responsible for the strong variations observed in our Sn-rich samples, as Cu and Sn tend to form various phases a wide range of temperatures and concentrations⁵⁴.

Similar diffusion behaviour was observed in joining with $\text{Ni}_{45}\text{Cu}_{55}$, except for the difference in interface thicknesses on both sides of each sample. This could be explained by the direct current running through the materials inside the sintering die. In fact, the (technical) current runs through the samples from bottom to top, which would favor the electromigration of Ni and Cu cations in that particular direction. Therefore, the thicker interfaces would be on the bottom side of the joint samples, while the thinner ones would be on top. As such behavior was not observed with Cu-joining, Ni is expected to play an important part in this electromigration process. It is carried by the current from the electrode to the sample, but it acts as a diffusion barrier to Cu when the diffusion happens in the opposite direction of the current flow⁵⁵. In fact, Ni, but also metallic silicide materials (Ni-Si in this case) are known to be good barriers to Cu diffusion^{53, 56-57}. The difference in joining temperatures with Cu and $\text{Ni}_{45}\text{Cu}_{55}$ (600 °C and 550 °C respectively) is another possible explanation that cannot be excluded²⁸.

For both electrodes, inhomogeneous diffusion occurred, leading to different reactions with the TE material, and the formation of new phases with new properties. Even though some diffusion is preferred as it helps the adhesion of the electrode to the TE material, too much diffusion would cause a loss of the initial functional material with the desired TE properties. The new resulting phases would also bring new CTE values into play, which increases the risk of higher CTE mismatches and hence results in further cracks under thermal cycling.

Local potential and Seebeck mapping were used to determine the specific electrical contact resistance. r_c was low ($< 10 \mu\Omega\cdot\text{cm}^2$) for Cu joint with both n- and p-types, indicating that the interfaces are mainly composed of conductive phases that do not hinder the current flow. As Cu has a CTE that matches the CTE of $\text{Mg}_2(\text{Si},\text{Sn})$ solid solutions better than that of the binary Mg_2Si , such good contacting was expected. This also proves the prediction of Cai et al.¹⁵ that doped $\text{Mg}_2(\text{Si},\text{Sn})$ would work better than undoped Mg_2Si , which had a quite high contact resistance ($r_c = 13.7 \text{ m}\Omega\text{cm}^2$) when joined with Cu. However, despite the differences in CTE, no cracks were observed in both the solid solution and the binary cases, indicating that the CTE mismatch is not the only relevant criterion of choice for contacting electrodes. In fact, it seems as if the order is also important, with the preferred case of the electrode having the higher CTE.

The r_c values of Cu joint $\text{Mg}_2\text{Si}_{0.3}\text{Sn}_{0.7}$ are also lower than those obtained from Ni and Ag joining²⁸. Even though Ag joint with p-type $\text{Mg}_2\text{Si}_{1-x}\text{Sn}_x$ at 450 °C had a low contact resistance ($< 10 \mu\Omega\text{cm}^2$), results with n-type were higher. Such behaviour was correlated with the fact that, as Ag is a p-type dopant, unexpected p-type doping occurred close to the Ag/n-type interface, resulting in a carrier density depletion area which led to the higher contact resistance.

On the other hand, values for samples joined with $\text{Ni}_{45}\text{Cu}_{55}$ were higher for p-type and with higher uncertainty for n-type, due to the different interfaces in the reaction layers and the metallic channels connecting the interfaces, respectively. Previous studies on Ni joining reported that Ni was a good contacting solution for Mg_2Si , with low r_c ($< 10 \mu\Omega\text{cm}^2$)¹³⁻¹⁴, but it was not a good option for the solid solution, as cracks have developed due to the CTE mismatch and local r_c values were somewhat higher ($\sim 35 \mu\Omega\text{cm}^2$)²⁸. From that perspective, $\text{Ni}_{45}\text{Cu}_{55}$ was expected to have better contacting results than Ni. However, as the CTE of $\text{Ni}_{45}\text{Cu}_{55}$ still does not perfectly match that of $\text{Mg}_2\text{Si}_{0.3}\text{Sn}_{0.7}$, some cracks still occurred.

After contacting, a change in S values from $-110\mu\text{V}/\text{K}$ to $-160\mu\text{V}/\text{K}$, and therefore a change in carrier concentration, was observed for the case of n-type samples joined with both Cu and $\text{Ni}_{45}\text{Cu}_{55}$, while they remained unchanged ($\sim 85 \mu\text{V}/\text{K}$) for p-type. No clear explanation to this behaviour has been obtained so far. However, one hypothesis is the difference in Si and Sn ratio (30:70 for p, 30:66.5 for n), though very small, between both material types as Bi substitutes Sn in n-type. Another possible cause could be the difference in Mg content, as n-type materials are made with 3% excess Mg, but also Li substitutes Mg in p-type materials. The dopants themselves could also add to this observed difference in behaviour. As similar results were observed in $\text{Mg}_2(\text{Si},\text{Sn})$ joined with Ag²⁸, it is clear that we have a carrier type dependence of the behaviour of the $\text{Mg}_2\text{Si}_{1-x}\text{Sn}_x$ material system which needs to be studied further.

Annealing experiments were carried out at 450°C during one week for Cu joining to study the thermal stability and the development of r_c . As expected, the diffusion of Cu was intensified, which affected the contact resistance and is expected to change the material properties on the long run. r_c values remained relatively low ($< 10 \mu\Omega\text{cm}^2$) for p-type after annealing, while n-type samples show a different behaviour. In fact, the averaged contact resistance was quite high because of the sudden potential drop on one side of the sample (**Figure 7 (a)**). This can be correlated with both the changes in interfaces at diffusion zones and the delamination that was observed due to the inter-diffusion of Mg and Cu. In fact, in case of foil delamination, extra resistance terms at each interface would be added (foil to foil, or foil to TE material), and due to the limited spatial resolution of the PSM, these added resistances are picked up as part of the total contact resistance, leading to high r_c values.

The Seebeck value has also changed for n-type after annealing, reaching a value of $-230 \mu\text{V}/\text{K}$, which did not happen with p-type. We then observe a clear dependence of the change in material properties, and thus contact resistances, on the dominant carrier type, similarly to what was observed for Ag²⁸ with

Mg₂(Si,Sn). A dependence of interface properties on dominant carrier type has also been reported for the Bi₂-Te₃ system where n-type Bi₂Te_{2.7}Se_{0.3} and p-type Bi_{0.4}Sb_{1.6}Te₃ showed different behaviours at the interfaces when joined with Ni⁵⁸. Whether this is due to (local) changes in the composition or is related to defects in the material requires further investigations. However, as such change in TE properties did not happen after annealing non-contacted Mg₂Si_{0.3}Sn_{0.7} at 450°C for one month³³, it can be safely assumed that the observable changes here are due to contacting and continuous inhomogeneous diffusion, and not only annealing.

V. Conclusion

In this work, contacting of n- and p- type Mg₂Si_{0.3}Sn_{0.7} with Cu and Ni₄₅Cu₅₅ electrodes was investigated. Both electrodes have shown stable contacting and adhesion with no delamination. Strong diffusion of both metals was observable inside the TE material, resulting in complex interfaces and thick diffusion zones. The specific electrical contact resistance r_c was low for Cu ($< 10 \mu\Omega\text{cm}^2$) but higher for Ni₄₅Cu₅₅ ($< 50 \mu\Omega\text{cm}^2$), which could be a result of the cracks that occurred due to a higher CTE mismatch.

The stability of the Cu contacting has been tested by annealing the joined samples for one week under a temperature of 450°C. The obtained results show a stronger diffusion of Cu, and even a diffusion of the TE material into the electrode, which caused local delamination. Moreover, the specific contact resistance r_c remained relatively low, except for one case where the delamination occurred. However, the diffusion changed the microstructure and the thermoelectric properties of the n-type material, which does not guarantee optimized properties anymore, possibly reducing zT and TE efficiency. Therefore, the diffusion needs to be controlled in order for Cu to be a potential technological contacting solution. Sputtering of a thin diffusion barrier layer is a possible option to remediate this issue.

Finally, the results of this work show that CTE match is not the only criterion for electrode material selection. Though necessary, it appears like there is a favourable order in the CTE comparability (CTE_{electrode} \geq CTE_{TE material} better than CTE_{electrode} \leq CTE_{TE material}). It is also important to consider the phases in the reaction layer as well as potential interactions between electrode and TE material. As we have shown here, these can depend on the dominant carrier type of the TE material.

Conflicts of interest

The authors declare no competing financial interest.

Acknowledgements

The authors would like to gratefully acknowledge the endorsement for the DLR executive Board Members for Space Research and Technology, as well as the financial support from the Young Research Group Leader Program. G.C.H would like to thank the financial support of the Mexican Science and Technology Ministry (CONACyT), and N.F and N.H.P would like to thank the DAAD fellowship programs No. 248 and 57265854, respectively. Lastly, we would also like to acknowledge Pawel Ziolkowski and Przemyslaw Blaschkewitz for their help and assistance with the thermoelectric measurements.

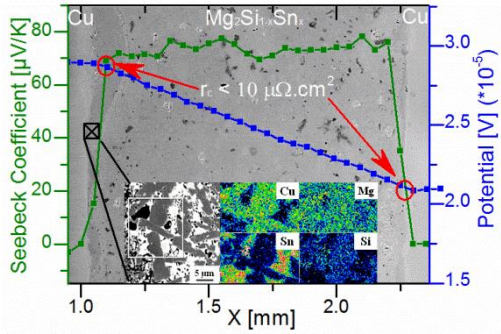
References for Chapter 3/Paper 1:

- (1) Bell, L. E. Cooling, heating, generating power, and recovering waste heat with thermoelectric systems. *Science* **2008**, *321* (5895), 1457-1461.
- (2) Tritt, T. M. Thermoelectric phenomena, materials, and applications. *Annual Review of Materials Research* **2011**, *41*, 433-448.
- (3) DiSalvo, F. J. Thermoelectric cooling and power generation. *Science* **1999**, *285* (5428), 703-706.
- (4) Aswal, D. K.; Basu, R.; Singh, A. Key issues in development of thermoelectric power generators: High figure-of-merit materials and their highly conducting interfaces with metallic interconnects. *Energy Conversion and Management* **2016**, *114*, 50-67.
- (5) Priya, S.; Inman, D. J. *Energy Harvesting Technologies*, Springer: **2009**; Vol. 21.
- (6) Rowe, D. M. Conversion efficiency and figure-of-merit. *Handbook of Thermoelectrics*; CRC press: **1995**; 31-37.
- (7) Liu, W.; Jie, Q.; Kim, H. S.; Ren, Z. Current progress and future challenges in thermoelectric power generation: From materials to devices. *Acta Materialia* **2015**, *87*, 357-376.
- (8) Luo, A. A. In *Recent Magnesium Alloy Development for Automotive Powertrain Applications*, Materials Science Forum, Trans Tech Publ: **2003**; 57-66.
- (9) Santos, R.; Yamini, S. A.; Dou, S. X. Recent progress in magnesium-based thermoelectric materials. *Journal of Materials Chemistry A* **2018**, *6* (8), 3328-3341.
- (10) Zaitsev, V. K.; Isachenko, G. N.; Burkov, A. T. Efficient thermoelectric materials based on solid solutions of Mg₂X compounds (X= Si, Ge, Sn). In *Thermoelectrics for Power Generation-A Look at Trends in the Technology*; InTech: **2016**.
- (11) Ferrario, A.; Battiston, S.; Boldrini, S.; Sakamoto, T.; Miorin, E.; Famengo, A.; Miozzo, A.; Fiameni, S.; Iida, T.; Fabrizio, M. Mechanical and electrical characterization of low-resistivity contact materials for Mg₂Si. *Materials Today: Proceedings* **2015**, *2* (2), 573-582.
- (12) Sakamoto, T.; Taguchi, Y.; Kutsuwa, T.; Ichimi, K.; Kasatani, S.; Inada, M. Investigation of barrier-layer materials for Mg₂Si/Ni interfaces. *Journal of Electronic Materials* **2016**, *45* (3), 1321-1327.
- (13) de Boor, J.; Gloanec, C.; Kolb, H.; Sottong, R.; Ziolkowski, P.; Müller, E. Fabrication and characterization of nickel contacts for magnesium silicide based thermoelectric generators. *Journal of Alloys and Compounds* **2015**, *632*, 348-353.
- (14) de Boor, J.; Droste, D.; Schneider, C.; Janek, J.; Mueller, E. Thermal stability of magnesium silicide/nickel contacts. *Journal of Electronic Materials* **2016**, *45* (10), 5313-5320.

- (15) Cai, L.; Li, P.; Wang, P.; Luo, Q.; Zhai, P.; Zhang, Q. Duration of thermal stability and mechanical properties of Mg₂Si/Cu thermoelectric joints. *Journal of Electronic Materials* **2018**, *47* (5), 2591-2599.
- (16) Ngan, P. H.; Christensen, D. V.; Snyder, G. J.; Hung, L. T.; Linderoth, S.; Nong, N. V.; Pryds, N. Towards high efficiency segmented thermoelectric unicouples. *Physica Status Solidi (a)* **2014**, *211* (1), 9-17.
- (17) de Boor, J.; Dasgupta, T.; Saparamadu, U.; Müller, E.; Ren, Z. Recent progress in p-type thermoelectric magnesium silicide based solid solutions. *Materials Today Energy* **2017**, *4*, 105-121.
- (18) Bashir, M. B. A.; Said, S. M.; Sabri, M. F. M.; Shnawah, D. A.; Elsheikh, M. H. Recent advances on Mg₂Si_{1-x}Sn_x materials for thermoelectric generation. *Renewable and Sustainable Energy Reviews* **2014**, *37*, 569-584.
- (19) de Boor, J.; Saparamadu, U.; Mao, J.; Dahal, K.; Müller, E.; Ren, Z. Thermoelectric performance of Li doped, p-type Mg₂(Ge, Sn) and comparison with Mg₂(Si, Sn). *Acta Materialia* **2016**, *120*, 273-280.
- (20) Zaitsev, V.; Fedorov, M.; Gurieva, E.; Eremin, I.; Konstantinov, P.; Samunin, A. Y.; Vedernikov, M. Highly effective Mg₂Si_{1-x}Sn_x thermoelectrics. *Physical Review B* **2006**, *74* (4), 045207.
- (21) Fedorov, M. I.; Zaitsev, V. K.; Isachenko, G. N. In *High effective thermoelectrics based on the Mg₂Si-Mg₂Sn solid solution*, Solid State Phenomena, Trans Tech Publ: **2011**; 286-292.
- (22) Liu, W.; Tan, X.; Yin, K.; Liu, H.; Tang, X.; Shi, J.; Zhang, Q.; Uher, C. Convergence of conduction bands as a means of enhancing thermoelectric performance of n-type Mg₂Si_{1-x}Sn_x solid solutions. *Physical Review Letters* **2012**, *108* (16), 166601.
- (23) Liu, W. D.; Chen, Z. G.; Zou, J. Eco-friendly higher manganese silicide thermoelectric materials: Progress and future challenges. *Advanced Energy Materials* **2018**, *8* (19), 1800056.
- (24) Girard, S. N.; Chen, X.; Meng, F.; Pokhrel, A.; Zhou, J.; Shi, L.; Jin, S. Thermoelectric properties of undoped high purity higher manganese silicides grown by chemical vapor transport. *Chemistry of Materials* **2014**, *26* (17), 5097-5104.
- (25) Skomedal, G.; Holmgren, L.; Middleton, H.; Eremin, I.; Isachenko, G.; Jaegle, M.; Tarantik, K.; Vlachos, N.; Manoli, M.; Kyratsi, T. Design, assembly and characterization of silicide-based thermoelectric modules. *Energy Conversion and Management* **2016**, *110*, 13-21.
- (26) Kim, H. S.; Kikuchi, K.; Itoh, T.; Iida, T.; Taya, M. Design of segmented thermoelectric generator based on cost-effective and light-weight thermoelectric alloys. *Materials Science and Engineering: B* **2014**, *185*, 45-52.
- (27) Nakamura, T.; Hatakeyama, K.; Minowa, M.; Mito, Y.; Arai, K.; Iida, T.; Nishio, K. Power-generation performance of a π -structured thermoelectric module containing Mg₂Si and MnSi_{1.73}. *Journal of Electronic Materials* **2015**, *44* (10), 3592-3597.
- (28) Pham, N. H.; Farahi, N.; Kamila, H.; Sankhla, A.; Ayachi, S.; Müller, E.; and; Boor, J. d. Contact development for p- and n-type Mg₂Si_{1-x}Sn_x thermoelectric generator using Ni and Ag. *Materials Today Energy* **2018**.
- (29) Kamila, H.; Sahu, P.; Sankhla, A.; Yasserli, M.; Pham, H.-N.; Dasgupta, T.; Mueller, E.; de Boor, J. Analyzing transport properties of p-type Mg₂Si-Mg₂Sn solid solutions: Optimization of thermoelectric performance and insight into the electronic band structure. *Journal of Materials Chemistry A* **2019**, *7* (3), 1045-1054.
- (30) Rogl, G.; Zhang, L.; Rogl, P.; Grytsiv, A.; Falmbigl, M.; Rajs, D.; Kriegisch, M.; Müller, H.; Bauer, E.; Koppensteiner, J. Thermal expansion of skutterudites. *Journal of Applied Physics* **2010**, *107* (4), 043507.
- (31) *Handbook of Chemistry and Physics*, 55th Ed.; CRC Press: USA, **1974**.
- (32) Davis, J. R. *Copper and Copper Alloys*, ASM international: **2001**.
- (33) Farahi, N.; Stiewe, C.; Truong, D. N.; de Boor, J.; Müller, E. High efficiency Mg₂(Si, Sn)-based thermoelectric materials: scale-up synthesis, functional homogeneity, and thermal stability. *RSC Advances* **2019**, *9* (40), 23021-23028.
- (34) Sankhla, A.; Patil, A.; Kamila, H.; Yasserli, M.; Farahi, N.; Mueller, E.; de Boor, J. Mechanical alloying of optimized Mg₂(Si, Sn) solid solutions: Understanding phase evolution and tuning synthesis parameters for thermoelectric applications. *ACS Applied Energy Materials* **2018**, *1* (2), 531-542.
- (35) Kamila, H.; Yasserli, M.; Pham, N.; Farahi, N.; Müller, E.; de Boor, J. Synthesis of p-type Mg₂Si_{1-x}Sn_x with $x = 0-1$ and optimization of the synthesis parameters. *Materials Today: Proceedings* **2019**, *8*, 546-555.

- (36) de Boor, J.; Stiewe, C.; Ziolkowski, P.; Dasgupta, T.; Karpinski, G.; Lenz, E.; Edler, F.; Mueller, E. High-temperature measurement of Seebeck coefficient and electrical conductivity. *Journal of Electronic Materials* **2013**, *42* (7), 1711-1718.
- (37) Yasserli, M.; Farahi, N.; Kelm, K.; Mueller, E.; de Boor, J. Rapid determination of local composition in quasi-binary, inhomogeneous material systems from backscattered electron image contrast. *Materialia* **2018**, *2*, 98-103.
- (38) N. Bocharov, E. Lysova, L. Rokhlin, Cu-Mg-Si (Copper-Magnesium-Silicon), Light Metal Systems. Part 4, Springer Materials **2006**.
- (39) L. Rokhlin, E. Lysova, Cu-Mg-Sn (Copper-Magnesium-Tin), Light Metal Systems. Part 4, Springer Materials **2006**.
- (40) Nash, P.; Nash, A. The Ni-Si (Nickel-Silicon) system. *Bulletin of Alloy Phase Diagrams* **1987**, *8* (1), 6-14.
- (41) Platzek, D.; Karpinski, G.; Stiewe, C.; Ziolkowski, P.; Drasar, C.; Muller, E. Potential-Seebeck-microprobe (PSM): Measuring the spatial resolution of the Seebeck coefficient and the electric potential, Thermoelectrics, 2005. ICT 2005. *24th International Conference on, IEEE: 2005*; 13-16.
- (42) Chen, K.; Fan, A.; Tan, C.; Reif, R. Contact resistance measurement of bonded copper interconnects for three-dimensional integration technology. *IEEE Electron Device Letters* **2004**, *25* (1), 10-12.
- (43) Schroder, D. K. *Semiconductor Material and Device Characterization*, John Wiley & Sons: **2006**.
- (44) Nakamura, S.; Mori, Y.; Takarabe, K. i. Analysis of the Microstructure of Mg₂Si Thermoelectric Devices. *Journal of Electronic Materials* **2014**, *43* (6), 2174-2178.
- (45) Thimont, Y.; Lognoné, Q.; Goupil, C.; Gascoin, F.; Guilmeau, E. Design of apparatus for Ni/Mg₂Si and Ni/MnSi_{1.75} contact resistance determination for thermoelectric legs. *Journal of Electronic Materials* **2014**, *43* (6), 2023-2028.
- (46) Snyder, G. J.; Toberer, E. S. Complex thermoelectric materials. In *Materials For Sustainable Energy: A Collection of Peer-Reviewed Research and Review Articles from Nature Publishing Group*; World Scientific: **2011**; 101-110.
- (47) Liu, W.; Chi, H.; Sun, H.; Zhang, Q.; Yin, K.; Tang, X.; Zhang, Q.; Uher, C. Advanced thermoelectrics governed by a single parabolic band: Mg₂Si_{0.3}Sn_{0.7}, A canonical example. *Physical Chemistry Chemical Physics* **2014**, *16* (15), 6893-6897.
- (48) de Boor, J.; Gupta, S.; Kolb, H.; Dasgupta, T.; Mueller, E. Thermoelectric transport and microstructure of optimized Mg₂Si_{0.8}Sn_{0.2}. *Journal of Materials Chemistry C* **2015**, *3* (40), 10467-10475.
- (49) Farahi, N.; Prabhudev, S.; Botton, G. A.; Salvador, J. R.; Kleinke, H. Nano- and microstructure engineering: an effective method for creating high efficiency magnesium silicide based thermoelectrics. *ACS Applied Materials & Interfaces* **2016**, *8* (50), 34431-34437.
- (50) Dai, J.; Jiang, B.; Zhang, J.; Yang, Q.; Jiang, Z.; Dong, H.; Pan, F. Diffusion kinetics in Mg-Cu binary system. *Journal of Phase Equilibria and Diffusion* **2015**, *36* (6), 613-619.
- (51) Liu, X. Heterogeneous nucleation or homogeneous nucleation? *The Journal of Chemical Physics* **2000**, *112* (22), 9949-9955.
- (52) Wang, S.-Q. Barriers against copper diffusion into silicon and drift through silicon dioxide. *MRS bulletin* **1994**, *19* (8), 30-40.
- (53) Liu, B.; Yang, L.; Li, X.; Wang, K.; Guo, Z.; Chen, J.; Li, M.; Zhao, D.; Zhao, Q.; Zhang, X. Ultrathin amorphous Ni-Ti film as diffusion barrier for Cu interconnection. *Applied Surface Science* **2011**, *257* (7), 2920-2922.
- (54) Fürtauer, S.; Li, D.; Cupid, D.; Flandorfer, H. The Cu-Sn phase diagram, Part I: New experimental results. *Intermetallics* **2013**, *34*, 142-147.
- (55) Kale, A.; Beese, E.; Saenz, T.; Warren, E.; Nemeth, W.; Young, D.; Marshall, A.; Florent, K.; Kurinec, S. K.; Agarwal, S. In Study of nickel silicide as a copper diffusion barrier in monocrystalline silicon solar cells, *Photovoltaic Specialist Conference (PVSC)*, **2017 IEEE 44th**; 1-4.
- (56) Min, S. K.; Kim, D. H.; Lee, S. H. Nickel silicide for Ni/Cu contact mono-silicon solar cells. *Electronic Materials Letters* **2013**, *9* (4), 433-435.
- (57) Yang, L.; Wang, S. J.; Huo, J. C.; Li, X. H.; Guo, J. X.; Dai, X. H.; Ma, L. X.; Zhang, X. Y.; Liu, B. T. Investigation of Ta/Ni-Al integrated film used as a diffusion barrier layer between Cu and Si. *Surface Review and Letters* **2014**, *21* (06), 1450079.
- (58) Liu, W.; Wang, H.; Wang, L.; Wang, X.; Joshi, G.; Chen, G.; Ren, Z. Understanding of the contact of nanostructured thermoelectric n-type Bi₂Te_{2.7}Se_{0.3} legs for power generation applications. *Journal of Materials Chemistry A* **2013**, *1* (42), 13093-13100.

Graphic Abstract:



Chapter 4: Paper 2

4. Contacting Cu Electrodes to $\text{Mg}_2\text{Si}_{0.3}\text{Sn}_{0.7}$: Direct vs Indirect Resistive Heating

The work of this chapter was based on the results of Chapter 3, where the contacting of Cu resulted in a thick and uneven reaction layer with both TE materials, but also a change in the Seebeck value S was recorded in the n-type material from $-110 \mu\text{V/K}$ to $-160 \mu\text{V/K}$. Moreover, a further change of S to $-220 \mu\text{V/K}$ was recorded after annealing. No such change was observed in the p-type materials neither after joining nor after annealing. Both of these observations (diffusion layer and change of S) were obtained for samples joined under *direct resistive heating (DRH)* conditions, where the samples were simply stacked inside a graphite die and then joined under a sintering current that was free to run through the TE material and the electrode. In order to investigate if the sintering current contributes to the obtained results, comparative experiments where the current was blocked from running through the sample were conducted. To this purpose, a boron nitride (BN) layer was coated on the inner sides of the graphite punches, and the method was called as *indirect resistive heating (IRH)*. In this method, the sintering current would mainly be running the graphite die around, and the heating of the sample would occur through Joule heating of the die. The *IRH* samples were also annealed under the same conditions as the *DRH* samples as reported in Chapter 3.

This study showed that obtained results of n- and p-type with Cu under both *DRH* and *IRH* were similar after contacting and annealing. The newly formed interfaces were still thick and inhomogeneous under *IRH* conditions for both material types, and diffusion continued during annealing. In all the cases, the electrical contact resistance was also low ($< 10 \mu\Omega \text{ cm}^2$), and the change in S for the n-type materials was also recorded, reaching comparable values for both current conditions (within the error bars) after joining and after annealing. Therefore, we could conclude here that, in the case of Cu joined with $\text{Mg}_2\text{Si}_{1-x}\text{Sn}_x$, the contacting results are not strongly influenced by the sintering current, and that the diffusion of Cu inside the $\text{Mg}_2(\text{Si},\text{Sn})$ system is mainly temperature-induced (electromigration is not so prominent).

An in-depth discussion about both contacting methods is introduced in Chapter 6.1.1. Results using $\text{Ni}_{45}\text{Cu}_{55}$ as an electrode are introduced, along with a more detailed discussion about the indirect heating process. Section A.1 in the Appendix also continues the topic, with a more technical comparison of both joining methods.

In this manuscript, **the submitted revised version of the paper, following the journal's template**, is provided. This work was published on 16 December 2019, in the 53th Volume, 13th Issue of *Semiconductors* journal, from page 1825 to page 1830.

The DOI of the article is <https://doi.org/10.1134/S1063782619130025>

Contacting Cu electrodes to $\text{Mg}_2\text{Si}_{0.3}\text{Sn}_{0.7}$: direct vs indirect resistive heating

S. Ayachi¹, G. Castillo Hernandez^{1,2}, E. Müller^{1,2}, and J. de Boor¹

¹German Aerospace Center, Institute of Materials Research, Germany,

²JLU Giessen, Institute of Inorganic and Analytical Chemistry, Giessen, Germany

Corresponding author: Sahar Ayachi, email address: Sahar.ayachi@dlr.de

Abstract

$\text{Mg}_2(\text{Si},\text{Sn})$ -based thermoelectric materials have been gaining interest in the past years due to their attractive properties. In this work, we present the outcome of using two different approaches to contact n- and p- type $\text{Mg}_2\text{Si}_{0.3}\text{Sn}_{0.7}$ legs with Cu electrodes to study the influence of current on the joining procedures. The first approach is a direct current heating procedure where the current runs directly through the sample, while the second approach uses the current as an indirect source of resistive heating. Results show that Cu diffuses into n- and p-type materials, creating relatively thick and complex reaction layers, both under direct and indirect resistive heating, and these layers have, respectively, an average thickness of 200 μm and 100 μm . Electrical contact resistance r_c values are also similar for both types, under both joining conditions ($< 10 \mu\Omega \cdot \text{cm}^2$). The directly and indirectly contacted samples were then annealed, and the results for all samples were similar. The reaction layers developed similarly in all cases and the contact resistances remained low ($< 10 \mu\Omega \cdot \text{cm}^2$).

Introduction

The field of thermoelectricity, which allows the conversion of waste heat into electricity, has been growing in the past decades. In fact, thermoelectricity provides an independent, renewable and environmental-friendly energy alternative that can be applied in various fields of industry (aerospace, automobile...). A large selection of thermoelectric (TE) materials is being studied and implemented into functional thermoelectric generators (TEG) such as Bi_2Te_3 or PbTe . The performance of these materials is determined by the value of their dimensionless figure of merit $zT = \sigma S^2 T / \kappa_{tot}$, where σ is the electrical conductivity, S is the Seebeck coefficient, T is the absolute temperature and $\kappa_{tot} = \kappa_{elec} + \kappa_{lat}$ is the total thermal conductivity with κ_{elec} being its electronic component and κ_{lat} lattice component [1, 2].

To obtain a stable and efficient TEG, the optimized n- and p- type TE materials have to be contacted and assembled using metallic electrodes and bridges to form a TEG device. The interfaces resulting from these joining steps induce thermal and electrical contact resistances that vary in magnitude depending on the chosen materials. Therefore, the selection of these electrodes and joining procedures is a critical step, which has to ensure that the contact resistances are as low as possible [3, 4].

Other criteria to take into consideration while contacting metallic electrodes to TE materials are the difference in their coefficients of thermal expansion (CTE), and the joining methods. Both require experimental testing, but the latter is not as straightforward as the former, and might therefore need deeper investigations.

In this paper, we discuss the joining step of $\text{Mg}_2\text{Si}_{0.3}\text{Sn}_{0.7}$ TE materials with Cu foils as metallic electrodes under two different conditions, and we report the results for the reaction layer microstructures and the electrical contact resistances.

Magnesium silicide-based materials have been selected because they possess a set of properties that make them attractive to the field of thermoelectricity. In fact, they are non-toxic, abundant and cheap. They are also lightweight and have good thermal and mechanical stability. We study $\text{Mg}_2\text{Si}_{1-x}\text{Sn}_x$ solid solutions because these show improved TE properties compared to binary Mg_2Si [5, 6]. The specific composition of $\text{Mg}_2\text{Si}_{0.3}\text{Sn}_{0.7}$ has been selected because the material shows high zT_{max} values for both n- and p- type samples (~ 1.4 and ~ 0.55 , respectively) at mid-range temperatures ($350 \sim 450$ °C) [7-9].

Cu has been chosen as the contacting electrode because it has a coefficient of thermal expansion (CTE) close to that of the studied TE material (Cu: $17 \cdot 10^{-6} \text{ K}^{-1}$ [10] and $\text{Mg}_2\text{Si}_{0.3}\text{Sn}_{0.7}$: $17.5 \cdot 10^{-6} \text{ K}^{-1}$ [11]). Cu has also been tested with the binary Mg_2Si in [12], showing good preliminary results. Cai *et al.*[12], reported that the Cu contacted samples had good adhesion and that no cracks have been observed. However, they reported a high value of electrical contact resistance r_c ($\sim 15 \text{ m}\Omega \cdot \text{cm}^2$) which was stated to decrease after doping.

The two joining conditions we used here differ in the way the samples (TE material + Cu) were heated during the sintering step. In the first case, the current from the sintering press was running through the samples and heating them up to the desired temperature. We called this procedure “*direct resistive heating*”. However, in the second case, an extra layer of an electrically insulating compound was added on top and bottom of the samples to block the direct passing of current through them. Here the heating was done indirectly through radial conduction from the sides to the inside of the samples, and we called this procedure “*indirect resistive heating*”.

All samples were then annealed under the same conditions to study their thermal stability. In all cases, the reaction layers resulting from the contacting were studied with SEM/EDX, and the electrical contact resistances were resolved using electrical potential and Seebeck coefficient local mappings.

Experimental Setup

Powder batches of n-type $\text{Mg}_{2.06}\text{Si}_{0.3}\text{Sn}_{0.665}\text{Bi}_{0.035}$ and p-type $\text{Mg}_{1.97}\text{Li}_{0.03}\text{Si}_{0.3}\text{Sn}_{0.7}$ have been produced and pellets were sintered in a direct sinter press facility (DSP 510 SE from Dr. Fritsch GmbH, Fellbach, Germany)[13]. These pellets were pressed in a 15 mm die under vacuum at 700 °C, for 1200 s for n- and 600 s for p-type, with a pressure of 66 MPa and a heating rate of 1 K/s. All pressed pellets had a high relative density ($\geq 97\%$), and were contacted with three disk shaped Cu foils on each side; each with thickness of 50 μm . The number of foils was chosen to account for the lateral resolution of the electrical contact resistance scanning measurements.

In the *direct resistive joining* procedure, n- and p-type pellets along with the Cu foils were stacked in the graphite die, then put into direct contact with the graphite pistons on top and bottom, which allows the sintering current to run directly through the electrodes and the sample.

However, in the *indirect resistive joining* procedure, the inner ends of the graphite pistons were covered with a thick layer of boron nitride (BN), and then used to press the Cu foil and pellet. The electric current, thus, flows along the walls of the graphite die and the joining reaction occurs by radial heat transfer.

To prepare for the annealing tests, cut pieces of the contacted samples were coated with a thick boron nitride layer to minimize Mg loss by evaporation. Then, they were sealed in quartz ampules under Argon gas and annealed in annealing furnaces for 7 days at 450 °C.

In the results section, eight samples will be presented. To simplify sample reference, sample names have been attributed as suggested in the table below:

Sample name	Experimental conditions
S_n_d	n- type, direct joining
S_p_d	p- type, direct joining
S_n_d_a	n- type, direct joining, annealed
S_p_d_a	p- type direct joining annealed
S_n_i	n- type indirect joining
S_p_i	p- type indirect joining
S_n_i_a	n- type indirect joining, annealed
S_p_i_a	p- type indirect joining, annealed

The results of all the above-mentioned samples were investigated under SEM/EDX (Zeiss Ultra 55 with a 15 kV acceleration voltage) to study the microstructures of the resulting reaction layers, and using a Potential & Seebeck Scanning Microprobe (PSM) [14, 15] to determine the electric contact resistances.

Results and discussion

- Microstructure

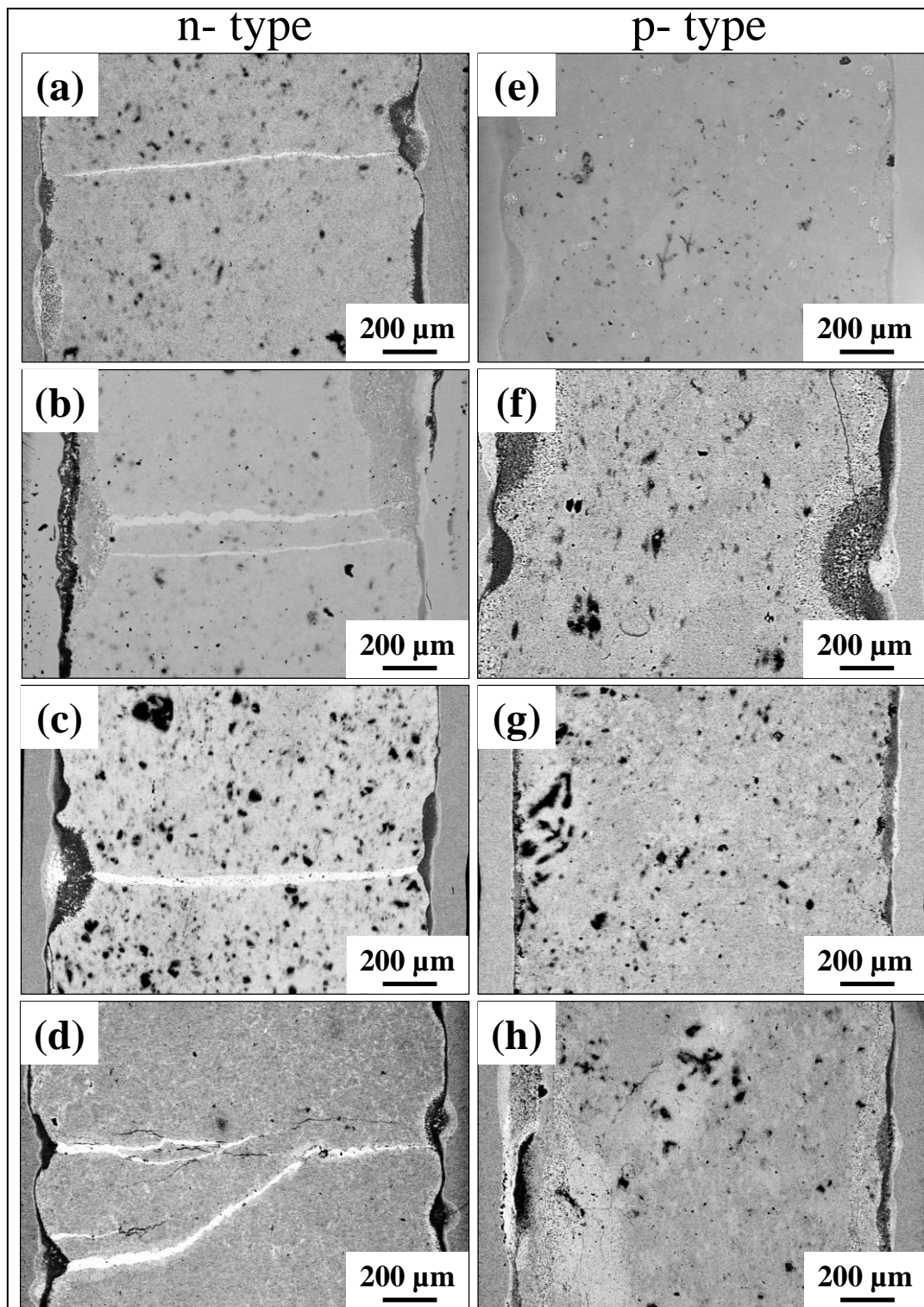


Figure 1: Cu contacted n- and p-type $Mg_2Si_{0.3}Sn_{0.7}$ samples: (a) & (e): under direct heating, (b) & (f) under direct heating and annealed, (c) & (g): under indirect heating, (d) & (h): under indirect heating and annealed.

Figure 1 shows the SEM/EDX results of all samples. The left column and right column contain n- and p-type samples, respectively. Starting with the directly joined samples S_n_d (**Figure 1 (a)**) and S_p_d (**Figure 1 (e)**), it is clear that both cases display thick and complex reaction layers, each containing various diffusion zones (100 ~ 200 μm thick each). These reaction layers are not single-phased; instead they are composed of several layers of different microstructures and compositions. Some of the phases contained in these layers are γ ($\text{Cu}_{1.55}\text{MgSn}_{0.45}$), τ_1 ($\text{Cu}_{1.5}\text{MgSi}_{0.5}$) which forms as Cu-rich dendrites, and Mg_2Sn . More details about the microstructure and the kinetics of the reaction layer formation are discussed in another work.

Along the TE material surface, localized darker and brighter areas can be seen. The darker areas are Si-rich $\text{Mg}_2\text{Si}_{0.3}\text{Sn}_{0.7}$ matrix, while the brighter regions are Sn-rich. In the p-type samples, Sn-rich areas are more scattered along the sample surface and appear as small agglomerations of ~ 20 μm diameter, while in n-type samples, they are seen as thin channels (Mg_2Sn -channel) running across the sample, from one Cu contacted end to the other. Such channel could be the result of Sn interdiffusion from one reaction layer to the other and Mg_2Sn formation as the channel progresses inside the TE material. So far, no exact explanation has been obtained to correctly explain why Sn in particular seems to crystallize out of the $\text{Mg}_2\text{Si}_{0.3}\text{Sn}_{0.7}$ matrix after Cu contacting.

After annealing (**Figure 1 (b) and (f)**), more Cu diffusion was observed, creating thicker diffusion zones and more Si-rich regions. It is clear here that when directly joined with $\text{Mg}_2\text{Si}_{0.3}\text{Sn}_{0.7}$, Cu diffuses easily and rapidly, and this diffusion progresses even further after just 7 days at 450 °C. As TEG often undergo continuous thermal cycling, contacting the TE materials with metallic electrodes that diffuse uncontrollably does not guarantee a constant efficiency and will cause material and generator damage.

The decision to test Cu contacting under *indirect resistive heating* conditions was to investigate any potential effect of the current on the joining and the Cu diffusion. However, as the SEM pictures on **Figure 1 (c) and (g)** show, indirect heating results look very similar to direct heating, for both n- and p-type samples. In fact, the inhomogeneous reaction layers with thicker diffusion zones are clearly visible, as well as the scattered Si-rich darker areas along the sample surfaces. Mg_2Sn -channels are also observed in this case, which proves that these channels are not a result of electromigration, but instead, of another diffusion mechanism. One probable explanation here could be that during contacting, micro cracks develop near the interface, and as Sn is the element with the lowest melting point, it liquefies faster and runs through them, reacting with Mg from the TE material as it diffuses. Such process causes the cracks to progress even further inside the sample, opening even more diffusion path for Sn inside the TE material.

Another interesting feature that is also observed in all SEM figures above is the demixing of the $\text{Mg}_2\text{Si}_{0.3}\text{Sn}_{0.7}$ initial matrix into what seems to two sub-matrices, one which is rich in Si and one which

is rich in Sn. This behaviour also clearly just happens after contacting under the effect of time and temperature. The electric current doesn't seem to play a big role.

After annealing, the indirectly heated samples (*Figure 1 (d) and (h)*) didn't show any big difference from the directly heated ones. Despite the fact that the reaction layers and the diffusion zones seem to be not as thick (respectively $\sim 50 \mu\text{m}$ and $\sim 100 \mu\text{m}$) as they were in the case of direct heating (respectively $\sim 100 \mu\text{m}$ and $\sim 200 \mu\text{m}$), the Mg_2Sn -channels and the demixing of the initial matrix of the TE material were still observed.

As an initial conclusion, it is clear that whether $\text{Mg}_2\text{Si}_{0.3}\text{Sn}_{0.7}$ and Cu are contacted under direct or indirect heating, the resulting interfaces are similar. The diffusion of Cu inside the TE material, as well as matrix de-mixing and other observed behaviors are independent of current and mainly driven by temperature and time. The next step here would be to investigate how these complex reaction layers affect the electrical contact resistance.

- Electrical Contact Resistance

The electrical contact resistance resulting from the contacting of Cu with $\text{Mg}_2\text{Si}_{0.3}\text{Sn}_{0.7}$ is calculated through PSM measurements [14, 15]. If we have a homogeneous current density $j = I/A$ passing through the electrodes and the sample, the bulk electrical contact resistance R_c is calculated as follow:

$$R_c = \frac{V_{\text{el}} - V_{\text{TE}}}{I}$$

(Eq.3)

where V_{el} and V_{TE} are the local voltages measured on the electrode and the TE material, respectively [12, 16, 17].

However, in our case, the occurrence of a homogeneous current density is very unlikely, due to the complex interfaces and the irregularities (demixing) observed inside the TE material. Therefore, we have to assume an inhomogeneous current flow, and the value of the current density j used here can be approximated using the TE properties of the material. In this case, instead of the bulk resistance R_c defined above, we define the specific electrical contact resistance $r_c = R_c * A$, A being the area, as follows:

$$r_c = \frac{V_{\text{elec}} - V_{\text{TE}}}{j}$$

with

$$j = \frac{\Delta V_{TE}}{R_{TE} * A} \quad (\text{Eq.4})$$

$$R_{TE} = \frac{l_{TE}}{A \sigma_{TE}} \quad (\text{Eq.5})$$

where ΔV_{TE} and R_{TE} are the voltage and the resistance across the material, l_{TE} and σ_{TE} are its length and electrical conductivity, respectively. Hence, the final specific electrical contact resistance is defined as

$$r_c = \frac{(V_{elec} - V_{TE}) l_{TE}}{\Delta V_{TE} * \sigma_{TE}} \quad (\text{Eq.6})$$

Furthermore, due to the demixing observed in the samples, the electrical conductivity was re-measured after contacting and after annealing, and the new values were put in (Eq. 6) to obtain correct r_c values.

Results of PSM scanning measurements as well as calculations of the electrical contact resistances are presented below.

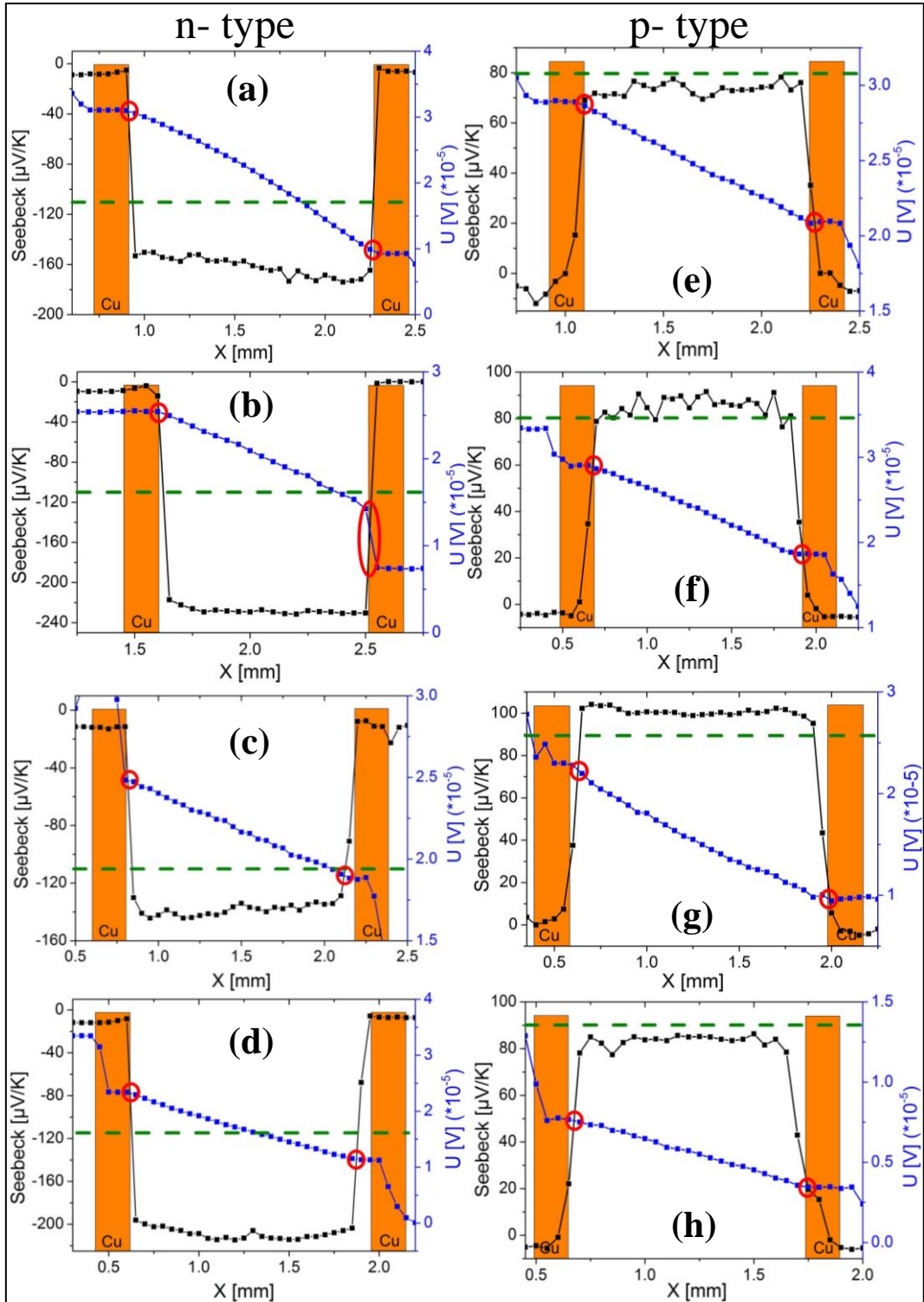


Figure 2: PSM plots of Cu contacted n- and p-type $Mg_2Si_{0.3}Sn_{0.7}$ samples: (a) & (e): under direct heating, (b) & (f) under direct heating and annealed, (c) & (g): under indirect heating, (d) & (h): under heating current and annealed.

Figure 2 shows typical line scans of Seebeck and electrical potential that are used to determine the location of the interface and calculate the contact resistances. The interface locations are marked by the

red circles on the graphs, and it is evident that at these positions, the U plots do not show big drops. Instead, they display a smooth transition between the metallic electrodes and the TE material, which means that there is no major resistance added from the newly grown reaction layers. One exception to this general behavior is the n-type annealed directly heated sample (**Figure 2 (b)**): The U graph shows a large drop at the right-hand side interface. Further SEM/EDX investigations have shown that for that sample in particular, Mg has diffused inside the Cu layer causing the foils to delaminate, which explains the sudden increase in resistance.

The obtained r_c values for n- and p- type samples are presented in the **Tables 1** and **2** below. Equations 3 and 6 have been used to compare different potential r_c values to have a better idea of the homogeneity of the current flow across the samples.

Table 2: Electrical contact resistance r_c values for n-type $Mg_2Si_{0.3}Sn_{0.7}$ samples contacted with Cu under direct and indirect heating, non-annealed and annealed conditions.

Sample	r_c (Eq. 6) / $\mu\Omega \cdot \text{cm}^2$	r_c (Eq. 3) / $\mu\Omega \cdot \text{cm}^2$
S_n_d	6 ± 4	9 ± 6
S_n_d_a (left side)	11 ± 6	13 ± 7
S_n_d_a (right side)	155 ± 30	181 ± 30
S_n_i	7 ± 4	10 ± 7
S_n_i_a	4 ± 1	11 ± 1

Table 3: Electrical contact resistance r_c values for p-type $Mg_2Si_{0.3}Sn_{0.7}$ samples contacted with Cu under direct and indirect heating, non-annealed and annealed conditions.

Sample	r_c (Eq. 6) / $\mu\Omega \cdot \text{cm}^2$	r_c (Eq. 3) / $\mu\Omega \cdot \text{cm}^2$
S_p_d	8 ± 5	3 ± 2
S_p_d_a	7 ± 5	6 ± 4
S_p_i	7 ± 5	11 ± 7
S_p_i_a	9 ± 5	9 ± 5

As expected from the PSM graphs in Figure 2, the electrical contact resistances are very low for all samples, at all joining conditions, before and after annealing. The values of r_c obtained with Eq. 6 and Eq. 3 are also very comparable considering the measurement uncertainty, which indicates that the PSM current runs homogeneously through all the samples. The complex interfaces as well as the demixing of the initial TE material matrix did not hinder the current flow.

One interesting behavior, however, can be seen for the Seebeck graphs in Figure 2, which is the change in S values of n-type samples a first time after contacting ($\sim -150 \mu\text{V/K}$), and a second time after annealing ($\sim -230 \mu\text{V/K}$). This is visible in the considerable difference between the initial S values ($\sim -110 \mu\text{V/K}$) for n-type $\text{Mg}_2\text{Si}_{0.3}\text{Sn}_{0.7}$ marked with the green dashed lines on the graphs and the actual S values after contacting or annealing. Such behavior occurs independently of the heating method (direct or indirect), and is not observed for p-type samples. The change in S values indicates a change in the TE properties of the material, and the limitation of the occurrence to just one sample type suggests a dependence of the material behavior on the dominant carrier type.

So, despite the fact that r_c was low for $\text{Mg}_2\text{Si}_{0.3}\text{Sn}_{0.7}$ contacted with Cu, the change in TE properties suggests that the diffusion strongly affects the n-type TE material, which requires a certain control (e.g. diffusion barrier) in order for Cu to be a technological solution.

Finally, the way of applying the electric current during the joining step might have an influence on the final results; however, it seems to be weaker than the effect of temperature and pressure, and thus cannot be clearly observed.

Conclusion

Two different contacting approaches were used in this work to understand the effect of the electric current on the contacting results and properties. When n- and p-type $\text{Mg}_2\text{Si}_{0.3}\text{Sn}_{0.7}$ were contacted with Cu electrodes, similar results were obtained, independently on the joining procedure. In all cases, the contacts had good adhesion, Cu diffused into the TE material, creating a thick and inhomogeneous reaction layer with localized thicker diffusion zones, and we obtained low r_c values. Additionally, the irregularities observed in the TE materials after joining occurred for both contacting approaches, which tells that electric current is not the only parameter to influence microstructure results. During annealing, Cu diffusion continued in all samples, though with different ratios, while values of r_c remained low ($\leq 10 \mu\Omega \cdot \text{cm}^2$). Thus, it is clear that the results of Cu contacting are not sensitive to the current path, and that blocking the current is not sufficient to control the metal's diffusion.

Acknowledgment

The authors would like to gratefully acknowledge Dr Alex Burkow and the ISCTA conference organizers for the invitation. We would also like to acknowledge the endorsement for the DLR executive Board Members for Space Research and Technology, as well as the financial support from the Young Research Group Leader Program. And last but not least, we would like to thank Pawel Ziolkowski and Przemyslaw Blaschkewitz for their help and assistance with the thermoelectric measurements.

References for Chapter 4/Paper 2

- [1] T.M. Tritt, Annual review of materials research 41 (2011) 433-448.
- [2] F.J. DiSalvo, Science 285 (1999) 703-706.
- [3] D.K. Aswal, R. Basu, A. Singh, Energy conversion and management 114 (2016) 50-67.
- [4] S. Priya, D.J. Inman, Energy harvesting technologies, Springer, (2009).
- [5] P.H. Ngan, D.V. Christensen, G.J. Snyder, L.T. Hung, S. Linderoth, N.V. Nong, N. Pryds, Physica status solidi (a) 211 (2014) 9-17.
- [6] M.I. Fedorov, V.K. Zaitsev, G.N. Isachenko, Solid State Phenomena, Trans Tech Publ, 170 (2011) 286-292.
- [7] J. de Boor, T. Dasgupta, U. Saparamadu, E. Müller, Z. Ren, Materials Today Energy 4 (2017) 105-121.
- [8] J. de Boor, U. Saparamadu, J. Mao, K. Dahal, E. Müller, Z. Ren, Acta Materialia 120 (2016) 273-280.
- [9] H. Kamila, P. Sahu, A. Sankhla, T. Dasgupta, E. Mueller, J.d. Boor, (Submitted) (2018).
- [10] Handbook of Chemistry and Physics, CRC Press, USA, (1974).
- [11] N.H. Pham, N. Farahi, H. Kamila, A. Sankhla, S. Ayachi, E. Müller, and, J.d. Boor, Materials Today Energy (2018).
- [12] L. Cai, P. Li, P. Wang, Q. Luo, P. Zhai, Q. Zhang, Journal of Electronic Materials 47 (2018) 2591-2599.
- [13] N. Farahi, C. Stiewe, D.Y.N. Truong, J.d. Boor, E. Müller, (Submitted) (2018).
- [14] J. de Boor, C. Gloanec, H. Kolb, R. Sottong, P. Ziolkowski, E. Müller, Journal of Alloys and Compounds 632 (2015) 348-353.
- [15] D. Platzek, G. Karpinski, C. Stiewe, P. Ziolkowski, C. Drasar, E. Muller, ICT 2005, (2005),13-16.
- [16] K. Chen, A. Fan, C. Tan, R. Reif, IEEE Electron Device Letters 25 (2004) 10-12.
- [17] S. Nakamura, Y. Mori, K.i. Takarabe, Journal of Electronic Materials 43 (2014) 2174-2178.

Chapter 5: Paper 3

5. On the Relevance of Point Defects for the Selection of Contacting Electrodes: Ag as an Example for Mg₂(Si,Sn)-based Thermoelectric Generators

As the change of S that was observed in the n-type samples joined with Cu could not be explained by the sintering current, another perspective was followed. What initiated this study, also, was the work of Pham *et al.* where a change in S was recorded after joining n-type Mg₂Si_{1-x}Sn_x with Ag, while no change was seen for the p-type samples [4]. Both our findings and those of the mentioned literature show that this dependence on the dominant carrier type is not dependent on one electrode in particular. It is, instead, a general trend that needs to be studied and understood, as its implications affect the optimized TE properties of the material in use. We decided, then, to look into the intrinsic and extrinsic defects of the studied materials, as the main difference between the used n- and p-type samples resides in the dopant and the chemical potential of the electrons. For this purpose, *ab initio* hybrid-DFT calculation of the formation energies of charged point defects in Bi-doped and Li-doped Mg₂(Si,Sn) were processed [111]. These calculations were done by our collaborators Byungki Ryu, Sungjin Park and Sudong Park at the Korea Electrotechnology Research Institute (KERI). We chose to continue this study with the Ag electrode instead of the Cu electrode (both in the experiments and the calculations) because Ag contacting resulted in a very thin reaction layer (< 30 μm). Therefore, we could avoid the issues and uncertainties that would arise due to thick reaction layers and new phases in the case of Cu, which would also simplify the calculations as the thin reaction layer could be dismissed. The binaries Mg₂Si and Mg₂Sn were utilized in this study instead of the solid solution composition for simplicity, but also to verify two points: (i) if, experimentally, both ends of the solid solution would show a similar behavior, which would indicate a comparable behavior for all the compositions in between, and (ii) if using the calculations on both binaries would provide good predictions that match the experimental results, which would allow the interpolation of the calculation results for the solid solutions.

Results showed that, as expected, a change in S was observed for the Ag-joined Mg₂Si and Mg₂Sn, and that the defect formation energy calculations provided plausible explanations to the observed TE property change. In fact, the Ag substitutional defect on the Mg site (Ag_{Mg}) is a stable defect with a low formation energy, and as it is an electron acceptor defect, it would act as a trap to the free conduction electrons provided by the Bi on Si/Sn defect. This trapping mechanism would cause a compensation in the charge carriers that would be experimentally picked up as an increase in S (in absolute value).

Through this work, we could establish that hybrid-DFT provides good predictions that could explain unexpected experimental observations, and that the method should be implemented more often in the screening process of potential contacting electrodes.

In this manuscript, **the submitted revised version of the paper, following the journal's template**, is provided. This work was available online on 31 October 2020 and published in January 2021 on Materials Today Physics, volume16, starting from page 100309.

The DOI of the article is <https://doi.org/10.1016/j.mtphys.2020.100309>

On the Relevance of Point Defects for the Selection of Contacting Electrodes: Ag as an Example for Mg₂(Si,Sn)-based Thermoelectric Generators

Sahar Ayachi^{*a}, *Radhika Deshpande*^a, *Prasanna Ponnusamy*^a, *Dr. Sungjin Park*^b, *Dr. Jaywan Chung*^b, *Dr. SuDong Park*^b, *Dr. Byungki Ryu*^b, *Prof. Eckhard Müller*^{a,c}, *Dr. Johannes de Boor*^{*a}

a: German Aerospace Center, Institute of Materials Research, Department of Thermoelectric Materials and Systems, Cologne, North Rhein-Westphalia, 51147, Germany

b: Energy Conversion Research Center, Electrical Materials Research Division, Korea Electrotechnology Research Institute (KERI), Changwon 51543, Korea

c: JLU Giessen, Institute of Inorganic and Analytical Chemistry, Giessen, Hessen, 35390, Germany

*Corresponding Authors: Sahar Ayachi: Sahar.ayachi@dlr.de, Johannes deBoor: Johannes.deBoor@dlr.de

Keywords: thermoelectrics, contacting, electrodes, defects, diffusion

Abstract:

In developing thermoelectric generators, optimizing interfaces between thermoelectric materials and contacting electrodes is a crucial step. Among the tested electrodes for Mg₂(Si,Sn)-based generators, Ag shows good adhesion, controllable interfaces and low electrical contact resistances. However, it induces unexpected changes in the Seebeck coefficient of n-type samples, while no change is observed in p-type.

In order to understand said behavior, contacting results for Bi-doped Mg₂Si, Mg₂Sn and Mg₂Si_{1-x}Sn_x with Ag are compared with predictions based on defect formation energies obtained within hybrid-density functional theory (DFT). A qualitative description of the Ag diffusion mechanism in Mg₂X is also introduced.

Calculation results show that Ag-induced defects have sufficiently low formation energies to influence charge carrier concentrations, particularly Ag substitution on the Mg site (Ag_{Mg}). Ag_{Mg} acts as an acceptor and causes a counter-doping effect by compensating the electrons provided by Bi. However, in Li-doped p-type, as Li-defects have the lowest formation energies, a negligible charge carrier concentration change is predicted, which fits with experimental observations. Concerning solid solutions, interpolation from the binaries predicts a similar behavior, which also meets experimental findings. Therefore, this work not only establishes the calculation method and explains the observed effect, but also proves the importance of defects in selecting contacting electrodes.

1. Introduction

Thermoelectric (TE) materials are used in several industrial fields such as aerospace, automotive, and industry; and research to develop more environmental-friendly TE generators is continuously expanding [1-4]. In order to have a highly efficient TE device, contacting the TE legs is as important as optimizing the TE material [5, 6]. In fact, this step adds contact resistances and potential chemical interactions between the contact materials and the TE material, and both can be detrimental to the TE device if not controlled. The electrical contact resistances R_c , as well as the thermal contact resistances, have to be kept as low as possible, and the electrodes should be chemically and physically stable metals or conductive intermetallics that (mechanically) adhere well to the TE material [7, 8]. There should also preferably be very limited diffusion between the metal and the semiconductor that would result in reactions forming new phases. All the mentioned conditions should remain stable in the long term under working temperature and thermal stress [9]. That is also why the electrode and the TE material should have similar coefficients of thermal expansion (CTE), which would guarantee a stable behavior free of failure under temperature cycling.

Several studies on developing contacting solutions were conducted, studying different material systems for thermoelectric applications. In fact, finding suitable contacts is a material specific problem, as the outcome will depend on the TE material, the metallic electrode and the potential interactions between them (CTE, adhesion, diffusion, reaction ...). Among others, Ni [10, 11] and Fe [12] were studied with

PbTe showing good bonding results thin interface layers and low electrical contact resistances, Ti [13] and Fe-Ni [14] were successfully tested for skutterudites materials, and Mo [15] and Ag [16] were used with half-Heusler systems.

One of the also frequently studied TE materials are $Mg_2Si_{1-x}Sn_x$ solid solutions as they consist of abundant elements, are environmentally friendly, and have improved thermoelectric properties compared to their binaries [17-21]. Contacting of $Mg_2Si_{1-x}Sn_x$ materials was tested using Ag [22] Ni [22-24] and Cu [7, 25, 26] electrodes, and electrical contact resistances and microstructure of the reaction layers were reported.

In this work and for the first time, contacting $Mg_2Si_{1-x}Sn_x$ based-TEGs is studied from a point defect perspective. We discuss here experimental results of contacting for the binaries Mg_2Si and Mg_2Sn as well as the $Mg_2Si_{1-x}Sn_x$ solid solutions with Ag as a suitable example for the importance of point defects in the thermoelectric material in the selection of joining electrodes.

The issue was first observed while contacting n- and p- type $Mg_2Si_{1-x}Sn_x$ (with $x = 0.4$ and $x = 0.3$, respectively) with Ag, where the results showed different behaviors of the TE materials after joining [22]. In fact, not only the electrical contact resistances were very different ($r_c \sim 400 \pm 38 \mu\Omega \text{ cm}^2$ for n-type vs. $\sim 9 \pm 1 \mu\Omega \text{ cm}^2$ for p-type, both joined at 450 °C), but also a change in the Seebeck values of the n-type samples was measured after joining (from $\sim -110 \mu\text{V K}^{-1}$ to $\sim -200 \mu\text{V K}^{-1}$ at room temperature), while they remained unchanged for p-type samples ($\sim 100 \mu\text{V K}^{-1}$).

A similar behavior was also observed after contacting n- and p-type $Mg_2Si_{0.3}Sn_{0.7}$ with Cu [25]. Seebeck values of n-type samples also changed during contacting (from $\sim -110 \mu\text{V K}^{-1}$ to $\sim -160 \mu\text{V K}^{-1}$) and annealing (to $\sim -230 \mu\text{V K}^{-1}$), while no change was observed for p-type samples. In this study, only Ag will be considered because it showed a less complex reaction layer and much less diffusion than what was observed with Cu as reported in [22] and in [25].

However, $Mg_2Si_{1-x}Sn_x$ solid solutions are known to suffer from demixing under certain conditions [27-29] and indeed demixing into Si-rich and Sn-rich phases was observed for both Cu and Ag contacted samples, potentially also influencing the Seebeck coefficient. In order to reduce the chemical complexity

and identify the origin of the observed alteration of the Seebeck coefficient, we contacted n-type Mg_2Si and Mg_2Sn with Ag at different temperatures. To further understand the observed Seebeck behavior, an investigation of the intrinsic and extrinsic point defects of the studied binaries is required. This does not come as a surprise, as point defects are known to play a crucial role in determining semiconductors' conduction types [30-33]. In fact, for materials like Bi_2Te_3 , references [34, 35] reported that, under anion-rich conditions, the antisite defect Te on Bi (Te_{Bi}) account for the n-type conduction, while, under cation-rich conditions, the negatively charged antisite defects such as Bi on Te sites (Bi_{Te}) account for the p-type conduction. As for the case of Bi_2Se_3 , the n-type conduction was related to the Se on Bi antisite defect (Se_{Bi}) under anion-rich conditions, while it was related to the Se vacancies (V_{Se}) under cation-rich growth conditions.

Defect studies and computation of their formation energies can be easier done for binaries than for solid solutions, and an interpolation to the intermediate ternary compositions can be achieved from the results of the binaries. This explains why almost all respective research focuses on the binary Mg_2X ($\text{X} = \text{Si}, \text{Sn}, \text{Ge}$) rather than to their solid solutions.

In the case of Mg_2X materials, Kato *et al.* [36] used density-functional theory (DFT) calculations to evaluate point defect formation energies in Mg_2Si and to understand the origin of the previously reported intrinsic n-type conduction of this material [37, 38] Their results showed that the n-type conduction comes from the positively charged ($q = 2+$) Mg ions at interstitial sites (I_{Mg}), which are the most energetically stable point defects under both Mg-rich and Mg-poor (Si-rich) conditions.

Jund *et al.* [39] studied the relative stabilities of Mg_2Si and Mg_2Ge using first principles calculations with different functionals. They showed that the stability of the point defects strongly depends on the growth conditions. In case of Mg_2Si , under stoichiometric and Mg rich conditions, Mg interstitials (I_{Mg}) is the most stable defect, while under Mg poor conditions, Si_{Mg} is more stable. This contradicts what was reported by Kato [36], but Kato *et al.* considered charged defects and dependence of the formation energies on chemical potentials, while Jund *et al.* considered neutral defects.

Another work by Liu *et al.* [40] stated that Mg vacancies V_{Mg} and Mg interstitials I_{Mg} are the dominant defects in Mg_2Si and Mg_2Sn , independently of the chemical environment (Mg-rich or Si/Sn-rich). The concentration of these defects is what determines the conduction type in each material. V_{Mg} is an acceptor ($q = 2^-$) more favorable under Mg-depleted conditions, and I_{Mg} is a donor more favorable under Mg-rich conditions. Si/Sn related defects are less likely to occur in the binaries, partly because their ionic radii (2.72 Å/2.94 Å) are larger than that of Mg (0.66 Å), so the local disorder and strain due to these defects are much larger than the strain caused by Mg related defects.

Meanwhile, there have been few studies on intrinsic defects in Mg_2Sn mitigated by the band gap underestimation in conventional DFT calculations, i.e. using the local density approximation or generalized gradient approximation. While Liu *et al.* [40] reported a quantitative analysis of the possible intrinsic defects in Mg_2Si , Mg_2Ge , and Mg_2Sn , their quantitative analysis of the defect densities suffers from a severe band gap underestimation: most of the major carriers are compensated by the minority carriers due to the small band gap calculated by DFT. This underestimation of the band gap persists with other works using conventional DFT, including the works of Kato *et al.* [36] and Jund *et al.* [39] mentioned above. In agreement with this, our conventional DFT calculations also showed that the band gap is obtained negative for Mg_2Sn . Such band gap underestimations affect the electronic chemical potential, which in turn affects defect stabilities. To overcome this issue, advanced computational methods such as hybrid-DFT [41] and quasi-particle calculations [42] were found to be important. Our recent hybrid functional study on intrinsic defects in Mg_2Si and Mg_2Sn finally quantitatively describes the intrinsic defect properties of these material systems [43].

Besides intrinsic defects, extrinsic defects (e.g. due to doping) are used to tune the carrier concentration of TE materials as the most common way to improve zT [44-47]. As these “added” defects can be more stable than the intrinsic defects of the material and influence the charge carrier concentrations in the chemical potential region of interest, both defect types need to be taken into consideration in order to have a full picture and predict the materials’ behavior [48].

The aim of this paper is to understand the unexpected behavior of Ag contacted n-type $\text{Mg}_2\text{Si}_{1-x}\text{Sn}_x$ using first principle calculations of point defect formation energies. In order to model the experimental

situation (doped Mg_2X in contact with Ag), we investigate the simultaneous presence of intrinsic and extrinsic defects in n- and p-type Mg_2Si and Mg_2Sn employing hybrid DFT calculations [41].

An understanding for the solid solutions can then be extrapolated. The considered dopants for n- and p-type conduction are respectively Bi and Li, and both Mg-rich (for n-type) and Mg-poor (for p-type) conditions are discussed.

Our findings show that the extrinsic defects generated after joining Ag with $\text{Mg}_2\text{Si}_{1-x}\text{Sn}_x$, namely Ag_{Mg} , are behind the experimentally observed Seebeck changes in n-type materials. Ag_{Mg} acts as an electron trap for the conduction electrons provided by Bi (Bi_{Si} for Mg_2Si and Bi_{Sn} for Mg_2Sn), leading to a decrease in the majority charge carrier density. In case of p-type materials, Ag related defects have higher formation energies than Li defects, which makes the influence of Ag_{Mg} or I_{Ag} not as visible as in n-type materials.

This example highlights that, in thermoelectricity, defect calculations are not just important for TE material development and dopant selection, but they also need to be taken into consideration when selecting contacting electrodes.

2. Material and methods

2.1. Sample Preparation and Characterization

Mg_2Si and Mg_2Sn were prepared from ball milled powder as reported in [18] with the respective nominal stoichiometries $\text{Mg}_{2.06}\text{Si}_{0.97}\text{Bi}_{0.03}$ and $\text{Mg}_{2.15}\text{Sn}_{0.97}\text{Bi}_{0.03}$. The powders from each material were pressed into three 15 mm diameter pellets for 10 min, at 800 °C for Mg_2Si and at 600 °C for Mg_2Sn [49] in a direct sinter press and then joined with Ag foil. The contacting experiments were also done through current assisted joining in the same direct sinter press. Each pellet was joined at a different temperature: 450, 500 and 550 °C for Mg_2Si , and 400, 450 and 500 °C for Mg_2Sn . The heating rate was 1 K s⁻¹ and the holding time was 10 min for each sample. These temperatures were selected because 450 °C showed to be a good joining temperature for $\text{Mg}_2\text{Si}_{1-x}\text{Sn}_x$ [22].

The solid solution $\text{Mg}_2\text{Si}_{1-x}\text{Sn}_x$ samples were prepared with the following stoichiometry: $\text{Mg}_{2.06}\text{Si}_{0.3}\text{Sn}_{0.665}\text{Bi}_{0.035}$ for n-type and $\text{Mg}_{1.98}\text{Li}_{0.02}\text{Si}_{0.4}\text{Sn}_{0.6}$ for p-type according to the procedures reported in [22], [25] and [50]. Three extra samples were prepared for this particular study following the procedure described in [22] to further investigate the observed trends: the first of these samples was prepared using 5 g of n-type $\text{Mg}_2\text{Si}_{0.3}\text{Sn}_{0.7}$ powder instead of the usual 1.2 g, which was then pressed in a 15 mm diameter pellet (700 °C, 20 min) and contacted with Ag foil at 450 °C for 10 min. The second and the third samples were made out of pre-pressed n- and p-type pellets that were joined together with Ag foils in between, also at 450 °C for 10 min. These samples were joined in two different experiments, one where the n-type pellet was at the bottom and the p-type pellet was on top of the Ag foil (referred to as $n//\text{Ag}/p$) and one where the stacking order was reversed ($p//\text{Ag}/n$).

Property characterization of the samples was done with SEM/EDX for microstructure investigations along the cross sections, and with an in-house built Potential & Seebeck Scanning Microprobe (PSM) [23, 51] for Seebeck measurements. Estimations of carrier concentration n and reduced chemical potential η were obtained from experimental results of the Seebeck coefficient combined with the effective mass (m_D^*) values from a single parabolic band (SPB) model based on the following equations [19, 52-54]

$$S = \frac{k_B}{e} \left(\frac{2F_1(\eta)}{F_0(\eta)} - \eta \right) \quad (1)$$

$$n = 4\pi \left(\frac{2m_D^* k_B T}{h^2} \right)^{1.5} F_{\frac{1}{2}}(\eta) \quad (2)$$

where k_B is Boltzmann's constant and $F_i(\eta)$ is the Fermi integral of order i .

2.2. Hybrid-DFT Calculations for Defect Formation Energies

First-principles calculations were performed to investigate the electrical properties of intrinsic and extrinsic defects in Mg_2Si and Mg_2Sn within the hybrid-DFT calculations [55] using the Vienna Ab Initio Simulation Package [56, 57]. The hybrid exchange-correlation energy function of HSE06 was employed with the exact-exchange mixing parameter of 25% and the screening parameter of 0.208 \AA^{-1} .

The planewave energy basis set was used with the energy cutoff of 296 eV. The projector-augmented wave pseudopotentials were used for atomic potentials.

To model the defective system, a $(2 \times 2 \times 2)$ cubic supercell was used with the lattice parameters of 6.35 Å and 6.75 Å for Mg_2Si and Mg_2Sn , respectively. In the supercell, there are 64 Mg and 32 Si/Sn atoms, and the dopant atom is added, removed, or replaced in the host supercell to generate defective supercells for vacancy, substitutional, and interstitial defects. The Γ -centered $(2 \times 2 \times 2)$ k -point mesh was sampled for charge density integration over the Brillouin zone. The atomic positions were fully relaxed until the magnitude of the remaining forces was smaller than $0.005 \text{ eV \AA}^{-1}$.

The charged defect formation energy of a defect D in the charge state q (D^q) in the Mg_2X was obtained using the following equation

$$E_{\text{form}}(D^q, \text{Mg}_2\text{X}) = E_{\text{tot}}[D^q] - E_0 - \sum_j (\mu_j \Delta n_j) + q(E_F + E_{\text{CBM}})$$

where $E_{\text{tot}}[D^q]$ and E_0 are the total energies with and without defect in the supercell, j is the atomic species in the supercell, Δn_j is the number change of atomic species j in the defective supercell with respect to the pristine supercell without defects, E_F is the electron Fermi level, and E_{CBM} is the energy of the conduction band minimum (CBM) [43, 58, 59]. Note that for the defects, the total energies were calculated using HSE06. However due to the huge computational cost, the spin-orbit interaction is not included.

3. Results

3.1. Mg₂Si/Sn with Ag

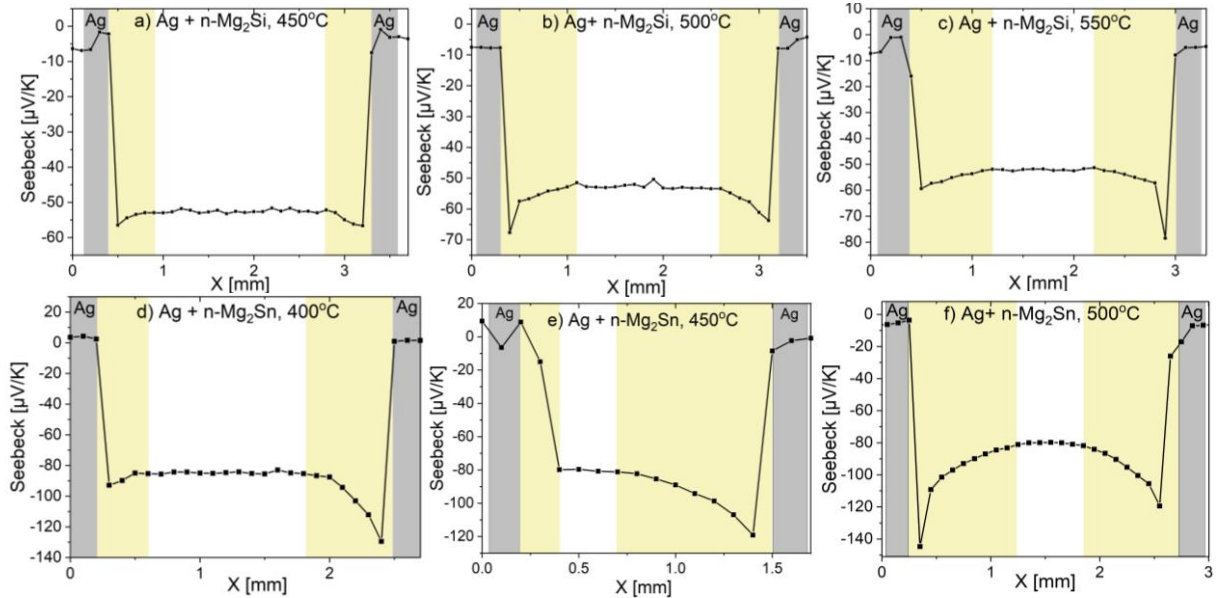


Figure 1: Representative Seebeck profiles for Mg₂Si and Mg₂Sn contacted with Ag at different temperatures.

The grey rectangles indicate the Ag foil and the yellow rectangles delimit the length where the Seebeck coefficient is altered.

Seebeck scan lines by the PSM at room temperature of n-Mg₂Si and n-Mg₂Sn joined with Ag at 3 different temperatures, (450°C, 500°C, 550°C) and (400°C, 450°C, 500°C) respectively, are presented in **Figure 1**. All the samples displayed an interesting Seebeck profile where the S values peak near the interfaces and then return back to the bulk value beyond a certain depth. The portions of the samples where S changed are marked with yellow rectangles on **Figure 1**. As no significant local variation was observed in the samples before the joining step, it must be linked to the interaction with the electrode. The observed changes in the Seebeck coefficient are believed to be caused by the diffusion of Ag into the TE material. For each binary, the diffusion of Ag, observed by the zone width of the altered Seebeck coefficient, differs with temperatures as can be seen in **Figure 1**. The presented line scans of the Seebeck coefficient are representative of the general behavior for each sample.

The average change in Seebeck coefficient in the Mg₂Si samples is comparable for all joining temperatures. The Seebeck value of the bulk of the TE material is maintained around -55 μV K⁻¹ for all samples, and the average values close to the interface are -57 ± 1 μV K⁻¹, -63 ± 10 μV K⁻¹ and -58 ± 2 μV K⁻¹ respectively for 450 °C, 500 °C and 550 °C. The high standard deviation observed for the sample joined at 500 °C comes from the line to line scatter, potentially due to local inhomogeneities in the sample. Moreover, while the maximum drop of the Seebeck coefficient recorded for 450 and 550 °C were respectively -65 μV K⁻¹ and -81 μV K⁻¹, it locally reached -115 μV K⁻¹ for 500 °C.

The Mg₂Sn samples showed a similar Seebeck gradient behavior, but unlike for the Mg₂Si samples, we consistently observed differences between the two contacting interfaces. As can be seen from **Figure 1**, Mg₂Sn joined at 400 and 450 °C exhibit steep drops on the one side, but almost no drop on the other. Whether this is due to the electromigration of Ag during the current-assisted joining or due to different reaction layers on both sides cannot be clearly stated. Interestingly, in the case of the sample joined at 500 °C, both sides have similar average Seebeck behavior. Even though the graph shown in **Figure 1 f**) displays an uneven (local) situation, line to line variation averages both sides to similar values. Averages of the Seebeck values near the interfaces and their corresponding estimated carrier concentrations for both Mg₂Si and Mg₂Sn are provided in **Table S 1** in the Supplementary Material.

Another difference which can be observed in the samples depending on the joining temperature is the increase of the width of the layer where S is different from bulk values (interior of the TE material). In the case of Mg₂Si samples, while this layer has a length of only 0.3 mm for $T_{join} = 450$ °C, it increases to 0.6 mm for $T_{join} = 500$ °C and 0.8 mm for $T_{join} = 550$ °C.

To have a better description of Ag diffusion inside Mg₂X systems as well as gain an understanding of the dependence of this diffusion on temperature, a simple exponential decay function (Equation 1) was used to fit the experimental results and quantify the observed changes:

$$S(x) = S_{bulk} + A \exp\left(\frac{-x}{\tau}\right) \quad (3)$$

where S_{bulk} is the Seebeck of the TE material, A is the amplitude and τ the effective diffusion length.

As each Seebeck line scan contains two graded sections opposite in decay direction, each line scan was divided into two fits: the first fit was the right-hand side gradient to which Equation 1 was applied as is, while the second fit was the left-hand side gradient which was first mirrored then fitted to the same equation. The fitting results are presented in **Table 1** and divided as described into left and right sides. A verification of this model based on the fitting with Equation 3 is provided in section I of the Supplementary Material. A good agreement between the modelling and the experimental data can be deduced from Figure S1 of the Supplementary Material.

Table 1: Fitting results of the diffusion length τ and the amplitude A from Seebeck line scans of Mg_2Si and Mg_2Sn . S_{inter} is the result of Equation 3 at the interface and n_{inter} the corresponding carrier concentration obtained using Equations 1 and 2 and the constants reported in [19] and [18]. Bulk values before contacting are $S = 55 \mu V K^{-1}$, $n = 2.5 \times 10^{20} cm^{-3}$ for Mg_2Si and $S = 80 \mu V K^{-1}$, $n = 3 \times 10^{20} cm^{-3}$ for Mg_2Sn

	T_{join} – side	τ [mm]	A [$\mu V K^{-1}$]	S_{inter} [$\mu V K^{-1}$]	n_{inter} ($10^{20} \times cm^{-3}$)
Mg_2Si	450 – Left side	0.13	3.4	58	2.4
	450 – Right side	0.09	6.2	61	2.2
	500 – Left side	0.19	10	65	2.0
	500 – Right side	0.15	22.5	78	1.5
	550 – Left side	0.28	8.1	63	2.1
	550 – Right side	0.38	9.9	65	2
Mg_2Sn	400 – Left side	0.11	12	92	2.8
	400 – Right side	0.15	32	112	2.1
	450 – Left side	–	–	–	–
	450 – Right side	0.24	45.5	125	1.6
	500 – Left side	0.22	42.2	122	1.7
	500 – Right side	0.17	46.4	127	1.5

Table 1 shows that the diffusion of Ag in Mg_2Si at each temperature has comparable diffusion lengths τ and amplitudes A on both contacted sides. The table also shows an overall increase of τ and A with temperature.

As for Mg_2Sn samples, the difference in amplitude originates from the difference in interface Seebeck coefficient values between both sides of each sample, particularly those joined at 400 and 450 °C. The left side of the 450 °C sample was omitted because there was no S gradient. τ values do not show a clear temperature dependence like in Mg_2Si , as a deeper diffusion is seen at 450 °C, though just on one side.

The obtained values of τ and A were implemented in Equation 1, and values of $S(x)$ and corresponding carrier concentrations n at the interface were also reported in **Table 1**. The latter were estimated using Equations 1 and 2, assuming $m_D^* = 1.1 m_0$ [60] and $m_D^* = 2 m_0$ [61].

Using the obtained values of τ , diffusion coefficients and activation energies were calculated. Using $\tau = \sqrt{Dt}$ where τ is the diffusion length (mm), D is the diffusion coefficient ($\text{m}^2 \text{s}^{-1}$) and t is the diffusion time (s), we can estimate the diffusion coefficient $D(T)$ for each joining temperature using averaged values of τ from both sides as given in **Table 1** and $t = 600$ s as the holding contacting time. The temperature-independent proportionality constant D_0 ($\text{m}^2 \text{s}^{-1}$) and the activation energy E_A (J mol^{-1}) are obtained from fitting the Arrhenius equation $D(T) = D_0 \exp(-\frac{E_A}{RT_{\text{join}}})$ [62]. In this equation, the molar gas constant R is fixed at $8.314 \text{ J mol}^{-1} \text{ K}^{-1}$ and T is the absolute temperature (K).

Here, we only present results for Mg_2Si , as they display a systematic behavior with temperature, unlike Mg_2Sn . The obtained values of E_A and D_0 were respectively $111 \text{ kJ mol}^{-1} = 1.15 \text{ eV}$ and $1.8 \times 10^{-3} \text{ m}^2 \text{ s}^{-1}$. They were both extracted from the slope and the intercept of the fitting line to the Arrhenius plot presented in **Figure 2**.

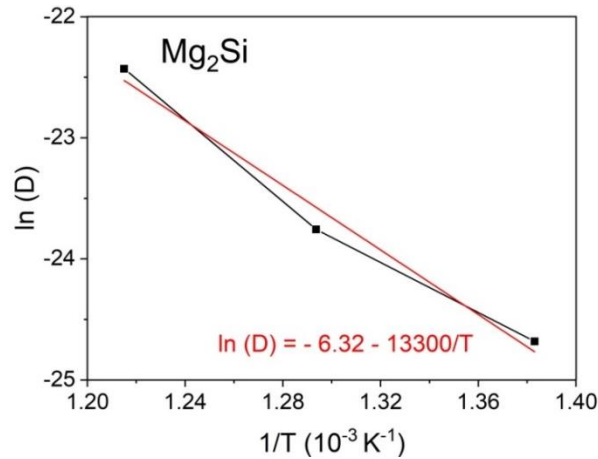


Figure 2: Arrhenius plot of the diffusion constant of Ag in Mg_2Si

3.2. Mg₂Si_{1-x}Sn_x with Ag

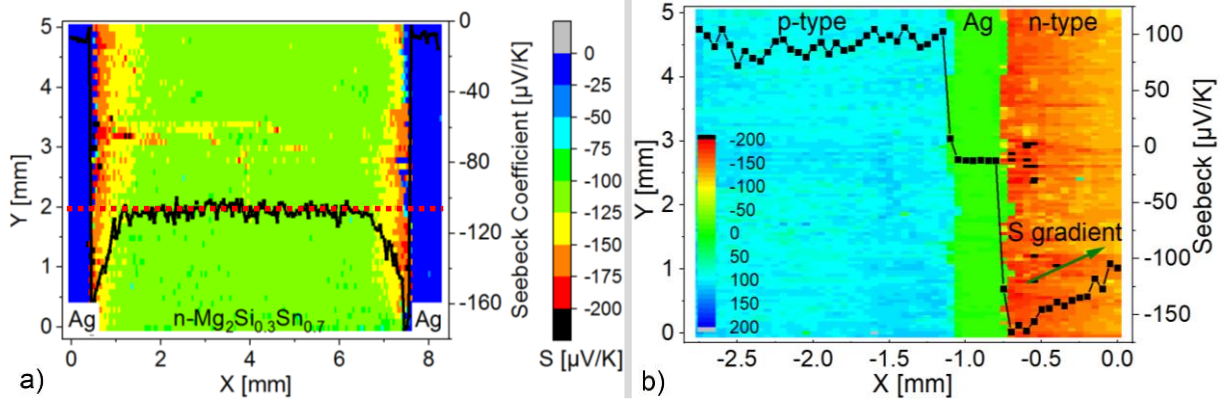


Figure 3: Exemplary Seebeck profile scans and 2D surface plots of a) thick n-type Mg₂Si_{0.3}Sn_{0.7} joined with Ag at 450 °C, and b) simultaneously joined p-type (bottom), Ag (middle) and n-type (top) materials displaying a Seebeck gradient only for the n-type. The selected Seebeck profile line scans correspond to the scan positions $y = 0.6$ mm and $y = 5$ mm for a) and b) respectively.

After confirming the change of Seebeck behavior during contacting on the Mg₂Si and Mg₂Sn binaries, further experiments on the solid solution were conducted. Unlike the previously reported case with thin samples where S changed along the whole sample thickness [22], the thick n-type Mg₂Si_{0.3}Sn_{0.7} sample presented in this work showed a seemingly different behavior after joining. In fact, as shown in **Figure 3** (a), S value changes occurred near the interfaces only, reaching $S_{max} \sim -170 \mu\text{V K}^{-1}$, which is qualitatively similar to what was observed for the binaries. This change of Seebeck corresponds to a change in carrier concentration from $n = 2.9 \times 10^{20} \text{ cm}^{-3}$ to $n = 1.18 \times 10^{20} \text{ cm}^{-3}$ assuming $m_D^* = 2.5 m_0$ [17]. It is clear through the line scan as well as the 2D plot in **Figure 3** (a) that there is a gradient of the Seebeck near the electrodes, but that S values go back to the bulk value ($\sim -110 \mu\text{V K}^{-1}$, marked with the red dashed line) after a depth of ~ 0.75 mm on each side. Taking this depth into account, the results of the thick sample are not inconsistent with those of the previously reported thin samples, because the thin samples have a thickness of ~ 1.5 mm, which is completely covered by the actual depth of the gradient zones on both sides.

The same fitting procedure (Equation 1) used for the binaries was also applied here, and an average value for the diffusion length $\tau(T_{join})$ from both joining interfaces was obtained. The obtained values are

$\tau(T_{join}) = 0.38$ mm and $D(T_{join}) = 2.4 \times 10^{-10}$ m² s⁻¹. These numbers are closer to those obtained for Mg₂Sn at 450 °C / 723 K (9.6×10^{-11} m² s⁻¹) than those for Mg₂Si (1.9×10^{-11} m² s⁻¹), which is not surprising as the used ternary is rich in Mg₂Sn (~ 70%).

The simultaneously joined n- and p- type stacked samples were produced by joining pre-pressed n- and p- pellets with Ag foil in between. No Ag foil was added on the external sides of the pellets. The purpose of this experiment was to investigate a simultaneous diffusion/electromigration of Ag, and to rule out preparation and technical uncertainties. Seebeck scans of the *p//Ag//n* sample were collected and are presented in **Figure 3** (b), while results for the *n//Ag//p* sample are provided in the Supplementary Material (**Figure S 2**).

As shown in the 2D plots in **Figure 3** (b), a Seebeck gradient is only visible in the n-type side of the stacked sample, while no such gradient was observed in p-type. Similar results were observed in the second stacked sample (*n//Ag//p*) where, the change in *S* was again only recorded in the n-type pellet (stacked at the bottom of the sample arrangement). This shows that the Ag diffusion has a stronger and more visible effect in n-type, and that it is mainly not driven by current (electromigration). Instead, it is driven by temperature, and the extent of the diffusion and its effects seem to depend on the dominant carrier type.

4. Discussion

The observed behavior might in principle and qualitatively be explained by Ag-induced point defects in the thermoelectric material. The formation energy of charged defects is a function of the Fermi level and will thus differ between n and p-type counterparts of the “same” composition, potentially leading to different abundance of defects in the n and p-type materials. The lattice diffusion process is governed by the diffusion barrier of the relevant defect, which is the sum of its formation energy and its migration barrier [63], and is therefore also dependent on the Fermi level of the electrons. For example, as negatively charged defects have lower formation energies in n-type than in p-type, they will be more abundant, and more mobile in n-type than in p-type. Based on our experimental results, we thus

speculate that negatively charged acceptor-like defects will be generated during contacting the TE legs, affecting the charge carrier concentration and the Seebeck coefficient. To substantiate this hypothesis, calculations of the formation energies of these defects are performed for the binaries Mg_2Si and Mg_2Sn . This also establishes a base for interpolation to interpret the result for the ternary combinations.

Figure 4 shows the calculated formation energy curves of the relevant intrinsic and extrinsic defects in n- and p-type Mg_2Si and Mg_2Sn doped with Bi and Li, respectively, and contacted with Ag. Defects related to Bi and Li were considered as dopants for Mg_2Si and Mg_2Sn , while Ag point defects were considered to understand the possible influence of the electrode on the thermoelectric materials. In both material cases, the conduction band minimum (CBM) is fixed at $E = 0$ eV. So, using the calculated values of the band gaps from hybrid-DFT, we obtained the positions of the valence band maxima (VBM) for Mg_2Si and Mg_2Sn as 0.570 eV and 0.145 eV. These values are comparable to the experimental band gaps which are 0.77 and 0.35 eV, respectively [64]. Note that within conventional DFT calculations using local-density approximation and GGA, the band gaps are severely underestimated to be ~ 0.2 eV and ~ -0.19 eV for Mg_2Si and Mg_2Sn , respectively [41], and the defect stability could be improperly described.

As n-type samples are made with 3 at% excess Mg, we might suppose that they are under Mg-rich chemical potential conditions. However, Mg losses are expected to occur during the initial pellet pressing step and then the joining step. Even though these losses are not straightforward to quantify, we also consider Mg-poor conditions for n-type Mg_2Si and Mg_2Sn . In **Figure 4**, only the relevant defects with formation energies lower than 1 eV are presented. Full figures with complete formation energies under all conditions are provided in the Supplementary Material, with **Figure S 3** and **Figure S 4** representing all the defects in Mg_2Si and Mg_2Sn , respectively.

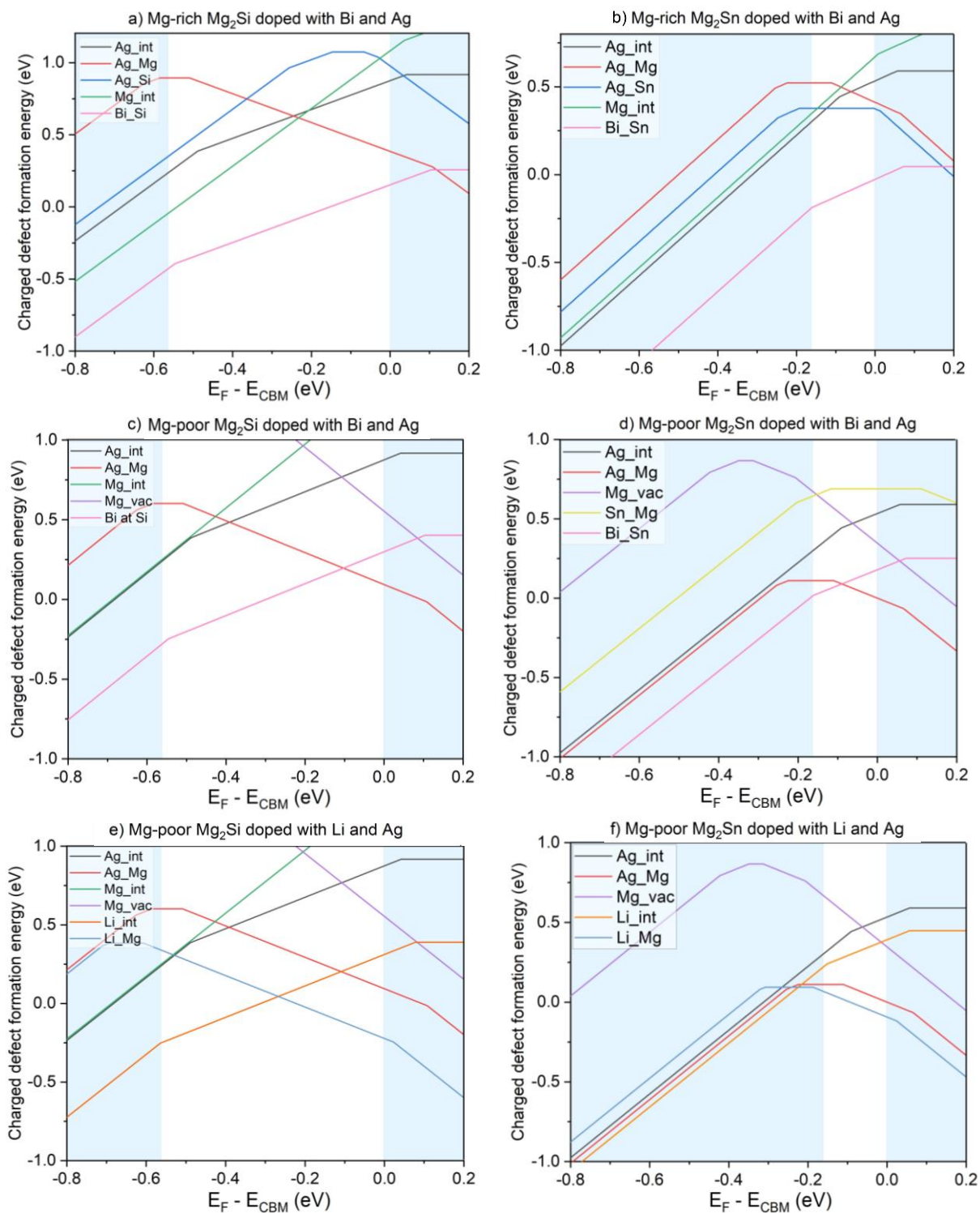


Figure 4: Formation energy curves for a) Bi- and Ag-related defects in Mg-rich Mg₂Si, b) Bi- and Ag-related defects in Mg-rich Mg₂Sn, c) Bi- and Ag-related defects in Mg-poor Mg₂Si, d) Bi- and Ag-related defects in Mg-poor Mg₂Sn, e) Li- and Ag-related defects in Mg-poor Mg₂Si and f) Li- and Ag-related defects in Mg-poor Mg₂Sn. E_F is given with respect to the conduction band maximum, and the white regions indicate the band gaps.

In n-type Mg_2Si on **Figure 4** (a), Bi_{Si} becomes the most stable defect with the lowest formation energy. It is a shallow donor defect with the charge state of $q = 1+$ for both low and high doped Mg_2Si (up to $E_F = 0.1$ eV, which is where the Fermi level can be pinned). It is also more stable than I_{Mg} which is the main (intrinsic) defect behind the n-type conduction in non-doped Mg_2Si . Such observation can be underpinned by experimental findings showing that the tuning range of the carrier concentration with extrinsic dopants is wider than by just adjusting Mg content. Kato *et al.*[36], in fact, demonstrated that they could tune the carrier concentration by less than $1 \times 10^{20} \text{ cm}^{-3}$ with changing Mg content, while they could reach $1 \sim 2 \times 10^{20} \text{ cm}^{-3}$ through Bi or Sb doping.

Under Mg-poor conditions, as displayed on **Figure 4** (c), Bi_{Si} is also the most stable defect, however only for a smaller chemical potential range than Mg-rich conditions. In fact, the pinned Fermi level E_F is at -0.1 eV, if Ag point defects are considered. However, if we disregard the Ag defects potentially generated due to the contacting electrode, Bi_{Si} would be the most stable defect up until a chemical potential of 0.1 eV.

For the n-type samples, the chemical potential for the electrons is $E_F \sim 0$ eV. Under both (Mg) chemical potential conditions, the second defect of interest is Ag_{Mg} , a shallow acceptor defect with $q = 1-$. As shown in **Figure 4** (a) and (c), in the range of $E_F = -0.5$ to 0.1 eV, Bi_{Si} and Ag_{Mg} have opposite charges, as the former is a $1+$ donor and the latter is a $1-$ acceptor. These two most stable defects will then compensate, which causes a decrease in the charge carrier concentration in the n-type material. With increasing E_F , the defect density of $\text{Ag}_{\text{Mg}}^{1-}$ increases, and at a certain energy, $\text{Ag}_{\text{Mg}}^{1-}$ can be the major defect. Note also that the Ag_{Mg} defect formation energy becomes lower when the Mg atomic chemical potential changes from Mg-rich to Mg-poor.

Considering the defect density equation $n(D, q) = N_0 e^{-\frac{E_{\text{form}}(D, q)}{k_B T}}$, where N_0 is the total density of possible sites that can form a defect D at charge state q [65], $n(D, q)$ of a defect decreases quickly with increasing formation energy $E_{\text{form}}(D, q)$. Therefore, the compensation effect of $\text{Bi}_{\text{Si}}^{1+}$ by $\text{Ag}_{\text{Mg}}^{1-}$ is more visible when the formation energies of both defects are either close or when $E_{\text{form}}(\text{Ag}_{\text{Mg}}) < E_{\text{form}}(\text{Bi}_{\text{Si}})$. Our experimental samples are heavily doped, with $E_F \sim 1 k_B T \sim 0.026$ eV. Around this

chemical potential, E_{form} of Ag_{Mg} and Bi_{Si} are comparable, so the charge compensation effect would be detectable, which matches the experimental data. For lower Fermi level samples, the difference in formation energy between the two defects increases, corresponding to a smaller expected compensation.

Using the method of climbed nudged elastic band (cNEB) calculations [59, 66, 67], we reveal that Ag defects in Mg_2Si can easily diffuse to form Ag_{Mg} defects via the interstitial diffusion of the I_{Ag} interstitial defect with a migration energy barrier of 0.652 eV. When the Fermi level is 0 (i.e. $E_F = E_{CBM}$), as the formation energies of I_{Ag}^{1+} are 0.88 and 0.53 eV in Mg-rich Mg_2Si and Mg_2Sn respectively, the diffusion barrier will be in the range of 1.2 – 1.5 eV. When the diffused I_{Ag} is split into Ag_{Mg} (electron trap) and I_{Mg}^{2+} (donor), and the separated I_{Mg}^{2+} defect diffuses far away (e.g. to grain boundary or electrode), the remaining Ag_{Mg} defect will finally act as the electron trap and is the source of charge compensation. In the previous study, we showed that Mg diffuses easily in Mg_2Si via the interstitial position [43].

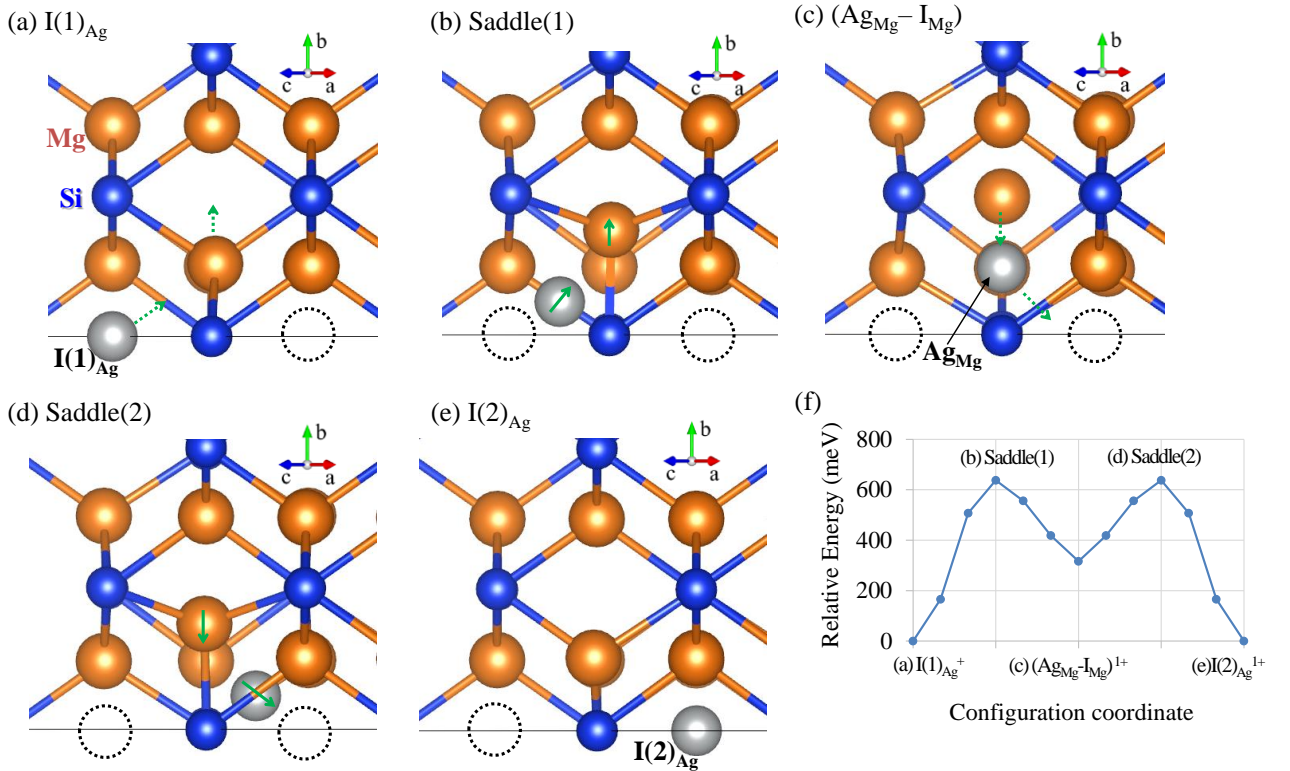


Figure 5: Suggested diffusion mechanism of Ag in Mg_2Si . The individual steps are presented in (a)-(e). The calculated relative energies of configuration coordinates during Ag diffusion are given in (f).

Figure 5 (a), (b), (c), (d) and (e) shows the atomic configurations during the Ag diffusion. For the interstitial diffusion of I_{Mg} , we consider the initial configuration of the I_{Ag}^{1+} defect in Mg_2Si (**Figure 5** (a)) and the intermediate configuration of the defect complex of $(Ag_{Mg}-I_{Mg})^{1+}$ (**Figure 5** (c)). The defect I_{Ag} can be transformed into an Ag_{Mg} and an I_{Mg} defect. In this step-1, the I_{Ag} defect moves toward an Mg site to form Ag_{Mg} . At the same time, the pushed Mg atom moves to one of the adjacent interstitial sites to form I_{Mg} . These diffusion steps are described by the saddle 1 presented in **Figure 5** (b). **Figure 5** (f) shows the relative energy between the configurations during the diffusion path. Note that the energy for the intermediate state of $(Ag_{Mg}-I_{Mg})^{1+}$ is higher by 0.359 eV than that for the initial configuration state of I_{Ag}^{1+} , and the migration energy barrier of the “saddle 1” step is found to be 0.652 eV. After this step-1 (**Figure 5** (a), (b) and (c)), the $(Ag_{Mg}-I_{Mg})^{1+}$ defect cluster can be transformed again into a single I_{Ag}^{1+} defect at an adjacent interstitial position. The Mg at the interstitial site can push the Ag atom at the Mg site (“saddle 2”, **Figure 5** (d)), and then the pushed Ag_{Mg} moves to one of the adjacent interstitial sites (**Figure 5**(e)). Thus, Ag_{Mg} and I_{Mg} can be combined into a single I_{Ag} interstitial defect: we call this step-2. This step is the exothermic reaction with the energy difference of 359 meV with a migration energy barrier of 293 meV. Note that the exothermic reaction step-2 is the reverse process of step-1. Depending on the diffusion path, the I_{Ag} can be located at the original interstitial site or at a next lattice interstitial site via combination of step-1 and step-2. Thus, with multiple repetitions of step-1 and step-2, the Ag defect can easily diffuse throughout the Mg_2Si in the form of I_{Ag}^{1+} . During the diffusion of I_{Ag}^{1+} , the decomposed defect of I_{Mg}^{2+} can separately diffuse back into the electrode region. Then the remaining Ag_{Mg}^{1-} defects can cause the charge compensation of electron carriers which were donated by Bi donors.

From the charged defect formation energies, we found that when E_F is at the CBM, the defect formation energy of I_{Ag} is ranging between 0.88 and 0.53 eV in Mg_2Si and Mg_2Sn . Therefore, the diffusion barrier, the sum of the defect formation energy and the migration energy barrier, is calculated to be 1.2-1.5 eV, which is comparable to the activation energy of 1.15 eV reported in section 2.1.

From the defect density equation given above, an increase in T leads to an increase of defect density. Consequently, Ag related defects are expected to be higher in number as T increases, and so is the compensation effect. The number of Bi-related defects on the other hand, most likely doesn't increase

with temperature, as there is no source for new Bi incorporation and the defect configuration is frozen after material synthesis. However, a quantitative comparison between the experimental results and the predictions by DFT are difficult as, first, the carrier concentrations are also affected by the (unknown) Mg content/Mg chemical potential in the samples and second, we are clearly not in an equilibrium situation.

In n-type Mg_2Sn , as presented in **Figure 4** (b), Bi_{Sn} is the most energetically stable defect. Similar to Bi_{Si} , it is a single shallow donor. The defects with the next lowest formation energies are Ag_{Sn} and Ag_{Mg} . However, in the chemical potential range of $E_F = -0.2 \sim 0$ eV (E_{CBM}), Ag_{Sn} is a neutral defect ($q = 0$) and therefore doesn't affect charge carrier concentration. Ag_{Mg} is a single acceptor, which basically compensates the carriers provided by Bi_{Sn} , just like it did for Mg_2Si .

These observations complete the experimental results discussed in the previous section, where a change in the Seebeck values of both binaries was observed near the contacting interfaces. We also conclude that a similar behavior can be expected for Mg_2Si and Mg_2Sn n-type solid solutions. In all cases, Ag_{Mg} defects are expected to trap conduction electrons provided by $\text{Bi}_{\text{Si/Sn}}$, leading to a depletion of carrier concentration. Such results are detected experimentally as an increase of the Seebeck values (in absolute value), which fits with the experimental results of **Figure 3** and explains the findings of previous reports [22] and [25].

Figure 4 (e) and (f) show the defect formation energies for Mg_2Si and Mg_2Sn doped with Li and Ag under Mg-poor conditions, as p-type samples are synthesized with Li substituting Mg. It is worth noticing on **Figure 4** (e) that the Fermi level in Mg_2Si is pinned deep inside the band gap, which explains the experimental challenges in making good p-type Mg_2Si [19, 65]. For Mg_2Sn , Li doping can induce p-type conduction under Mg-poor conditions due to the narrow band gap, while Li hardly gives p-type characteristics under Mg-rich conditions (see Supplementary Material).

In contrast to Ag defects in n-type $\text{Mg}_2\text{Si/Sn}$, the Ag related defects in p-type $\text{Mg}_2\text{Si/Sn}$ doped with Li have much higher formation energies than major Li defects. This means that the addition of Ag doesn't influence the p-type conduction determined by Li defects.

As for p-type $\text{Mg}_2\text{Si}_{1-x}\text{Sn}_x$ studied here and in [22], a behavior similar to Mg_2Sn is expected, as the samples are Mg_2Sn rich (70 and 60%). Li-related defects are expected to be the most stable, and Ag-related defects to have high enough formation energies so that no doping effect would be experimentally detectable in a Seebeck mapping, as is experimentally observed. Similarly, the hybrid-DFT calculation results confirm that, for $\text{Mg}_2\text{Si}_{1-x}\text{Sn}_x$, Li is a better p-type dopant than Ag.

In such analysis, it is important to keep in mind potential interactions between the electrode and the TE material, as well as the resulting interfaces between them. In our case, the actual diffusion process of Ag is presumably more complex than considered here. As shown in [22], Ag and $\text{Mg}_2(\text{Si},\text{Sn})$ are practically not in direct contact but are separated by an Ag containing intermetallic layer. This, as well as potential other diffusion paths inside the thermoelectric material, will influence the diffusion of Ag, and a microscopic model is required to analyze this in depth. Nevertheless, the Seebeck coefficient profile predicted based on our simple diffusion model shows good agreement with the actual experimental $S(x)$, as shown in **Figure S 1** of the Supplementary Material. Thus, due to the good qualitative and quantitative agreement between experiment and calculation in our work, we believe our effective model provides valuable insight.

Technologically, it is also important to keep in mind that Ag diffusing into the n-type $\text{Mg}_2\text{Si}_{1-x}\text{Sn}_x$ causes a loss of major charge carriers; hence the functional material does not possess its optimum thermoelectric properties anymore, which leads to the degradation of the TE device. To illustrate this, a comparison between the properties of $\text{Mg}_2\text{Si}_{1-x}\text{Sn}_x$ before and after joining is presented.

To calculate zT and the efficiency of the pristine sample (before contacting), electrical resistivity and thermal conductivity, ρ and κ , data was taken from previous measurements [18]. For contacted samples, properties as observed at the interface were assumed for the whole sample, taking the interface properties as hypothetical equilibrium state after Ag saturation. As local experimental measurements of the conductivities were unfeasible and using a simple SPB model to approximate carrier concentration from S then approximating ρ and κ does not hold at high temperatures (contribution of minority charge carriers becomes substantial), the needed thermoelectric properties were taken from literature which provides a full TE study of a sample with similar S as observed at the interface of **Figure 3** [68]. Therefore, the

following calculations are rough estimations due to certain differences between the literature and our current work (synthesis method, dopant...). However, these effects are expected to be minor and the general trend in zT and efficiency is believed to be similar. More details about the calculation and approximation procedures are provided in section III in the Supplementary Material.

The initial TE material is synthesized and doped to have optimum carrier concentration which guarantees maximum zT . Any loss of majority charge carriers caused by Ag diffusion, for example, results in a decrease in zT as schematically shown in **Figure 6**.

Simulation results also show that, for an $\text{Mg}_2\text{Si}_{1-x}\text{Sn}_x$ leg of 5 mm length with a hot side temperature of 700 K and a cold side temperature of 300 K, the loss of carriers corresponds to a decrease of maximum efficiency from 10.5% to 7.2% and of maximum power output from 0.028 to $0.013 \times 10^6 \text{ W m}^{-2}$. Further decrease in these values is expected to occur as Ag continues diffusing inside the TE material and might alter its TE properties further beyond what we assumed to be the equilibrium state. This also establishes the importance of defect consideration in contacting electrode selection and module building.

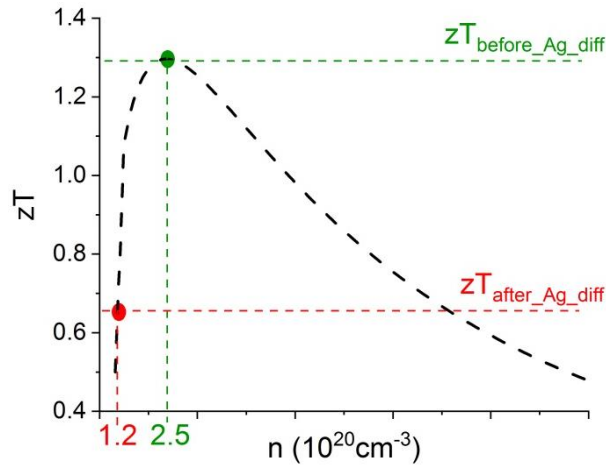


Figure 6: Schematic dependence of zT on carrier concentration for n-type $\text{Mg}_2\text{Si}_{1-x}\text{Sn}_x$ before and after Ag diffusion at $T = 700\text{K}$.

5. Conclusion

In this work, we re-assess the selection of Ag as a contacting solution for $\text{Mg}_2\text{Si}_{1-x}\text{Sn}_x$ -based thermoelectric generators by describing the Ag diffusion mechanism and correlating unexpected experimental results with hybrid-DFT defect calculations. The observed change in Seebeck values of n-type binaries Mg_2Si , Mg_2Sn and their solid solutions is explained by Ag_{Mg} defects which have low enough formation energy to counteract Bi-related defects and cause a diminution in charge carrier concentration. This qualitative agreement between experiments and calculations establishes the credibility of both methods, as well as the importance of a potential doping effect of the contacting electrode. Thus, we clearly show that, Ag is not a suitable electrode for n-type Mg_2X without further technological steps (e.g. diffusion barriers).

Furthermore, we show that the intrinsic and extrinsic defects of the considered TE material and the joining material are important criteria to consider while screening for contacting electrodes.

CRedit authorship contribution statement

Sahar Ayachi: Methodology, Validation, Formal analysis, Investigation, Writing – original draft, Visualization.

Radhika Deshpande: Validation, Investigation.

Prasanna Ponnusamy: Software, Validation.

Sungjin Park: Software, Validation, Formal analysis, Investigation (theoretical).

Jaywan Chung: Software.

Sudong Park: Software, Validation, Writing - review & editing, Supervision, Funding acquisition.

Byungki Ryu: Conceptualization, Methodology, Software, Validation, Formal analysis, Investigation (theoretical), Writing – original draft, Project administration, Funding acquisition.

Eckhard Müller: Writing – review & editing, Supervision.

Johannes de Boor: Conceptualization, Methodology, Writing – review & editing, Supervision, Project administration.

Declaration of competing interest

The authors declare that they have no known competing financial interests or personal relationships that could have appeared to influence the work reported in this paper.

Acknowledgements

The authors would like to gratefully acknowledge the endorsement for the DLR executive Board Members for Space Research and Technology, as well as the financial support from the Young Research Group Leader Program. We would also like to thank Pawel Ziolkowski and Przemyslaw Blaschkewitz for their help and assistance with the thermoelectric measurements.

This work was also supported by the Korea Institute of Energy Technology Evaluation and Planning (KETEP) funded by the Ministry of Trade, Industry & Energy (MOTIE), Republic of Korea: Grant No. 20188550000290. The authors from the Korea Electrotechnology Research Institute (KERI) were also supported by the Korea Electrotechnology Research Institute (KERI) Primary Research Program through the National Research Council of Science and Technology (NST) funded by the Ministry of Science and ICT (MSIT) of the Republic of Korea: Grant No. 20A01025.

J. de Boor also acknowledges support by the Deutsche Forschungsgemeinschaft (DFG, German Research Foundation) - project number 396709363.

Received: ((will be filled in by the editorial staff))
Revised: ((will be filled in by the editorial staff))
Published online: ((will be filled in by the editorial staff))

Data Availability Statement:

The raw/processed data required to reproduce these findings cannot be shared at this time due to legal or ethical reasons.

References for Chapter 5/Paper 3:

- [1] L.E. Bell, Cooling, heating, generating power, and recovering waste heat with thermoelectric systems, *Science* 321(5895) (2008) 1457-1461. <https://doi.org/10.1126/science.1158899>.
- [2] T.M. Tritt, Thermoelectric phenomena, materials, and applications, *Annual review of materials research* 41 (2011) 433-448. <https://doi.org/10.1146/annurev-matsci-062910-100453>.
- [3] F.J. DiSalvo, Thermoelectric cooling and power generation, *Science* 285(5428) (1999) 703-706. <https://doi.org/10.1126/science.285.5428.703>.
- [4] R. Santos, S.A. Yamini, S.X. Dou, Recent progress in magnesium-based thermoelectric materials, *J. Mater. Chem. A* 6 (2018) 3328-3341. <https://doi.org/10.1039/C7TA10415D>.
- [5] G. Min, D. Rowe, Optimisation of thermoelectric module geometry for 'waste heat' electric power generation, *J. Power Sources*. 38 (1992) 253-259. [https://doi.org/10.1016/0378-7753\(92\)80114-Q](https://doi.org/10.1016/0378-7753(92)80114-Q).
- [6] I. Atassi, E. Bauer, J. Nicolics, B. Dangl, L. Spendlhofer, D. Knosp, F. Faistauer, Current thermoelectric materials and an evaluation of thermoelectric materials contacting approaches, 2012 35th International Spring Seminar on Electronics Technology, IEEE (2012) 70-75.
- [7] L. Cai, P. Li, P. Wang, Q. Luo, P. Zhai, Q. Zhang, Duration of thermal stability and mechanical properties of Mg₂Si/Cu thermoelectric joints, *J. Electron. Mater.* 47 (2018) 2591-2599. <https://doi.org/10.1109/ISSE.2012.6273111>.
- [8] G. Min, D. Rowe, O. Assis, S. Williams, Determining the electrical and thermal contact resistance of a thermoelectric module, *Proc. ICT* (1992) 210-212.
- [9] S. Ganeshan, S. Shang, Y. Wang, Z.-K. Liu, Temperature dependent elastic coefficients of Mg₂X (X= Si, Ge, Sn, Pb) compounds from first-principles calculations, *J. Alloys. Comp.* 498 (2010) 191-198. <https://doi.org/10.1016/j.jallcom.2010.03.153>.
- [10] X.R. Ferreres, A. Gazder, A. Manettas, S. Aminorroaya Yamini, Solid-state bonding of bulk PbTe to nickel electrode for thermoelectric modules, *ACS Appl. Energy Mater.* 1 (2018) 348-354. <https://doi.org/10.1021/acsaem.7b00010>.
- [11] X.R. Ferreres, S.A. Yamini, M. Nancarrow, C. Zhang, One-step bonding of Ni electrode to n-type PbTe—A step towards fabrication of thermoelectric generators, *Mater. & Design*. 107 (2016) 90-97. <https://doi.org/10.1016/j.matdes.2016.06.038>.
- [12] A. Singh, S. Bhattacharya, C. Thinaharan, D. Aswal, S. Gupta, J. V. Yakhmi, K. Bhanumurthy, Development of low resistance electrical contacts for thermoelectric devices based on n-type PbTe and p-type TAGS-85 ((AgSbTe₂)_{0.15}(GeTe)_{0.85}), *J. Phys. D: Appl. Phys.* 42 (2009) 015502. <https://doi.org/10.1088/0022-3727/42/1/015502>.
- [13] D. Zhao, H. Geng, L. Chen, Microstructure contact studies for skutterudite thermoelectric devices, *Int. J. Appl. Ceram. Technol.* 9 (2012) 733-741. <https://doi.org/10.1111/j.1744-7402.2011.02703.x>
- [14] S.H. Park, Y. Jin, J. Cha, K. Hong, Y. Kim, H. Yoon, C-Y. Yoo, I. Chung, High-power-density skutterudite-based thermoelectric modules with ultralow contact resistivity using Fe–Ni metallization layers, *ACS Appl. Energy Mater.* 1 (2018) 1603-1611. <https://doi.org/10.1021/acsaem.8b00064>.
- [15] J. Shen, Z. Wang, J. Chu, S. Bai, X. Zhao, L. Chen, T. Zhu, Low contact resistivity and interfacial behavior of p-type NbFeSb/Mo thermoelectric junction, *ACS Appl. Mater. Interfaces* 11 (2019) 14182-14190. <https://doi.org/10.1021/acsaem.9b02124>.
- [16] P.H. Ngan, N. Van Nong, B. Balke, L. Han, E.M.J. Hedegaard, S. Linderoth, N. Pryds, On the challenges of reducing contact resistances in thermoelectric generators based on half-Heusler alloys, *J. Electron. Mater.* 45 (2015) 594-601. <https://doi.org/10.1007/s11664-015-4156-z>.
- [17] N. Farahi, S. Prabhudev, G.A. Botton, J.R. Salvador, H. Kleinke, Nano-and microstructure engineering: an effective method for creating high efficiency magnesium silicide based thermoelectrics, *ACS Appl. Mater. Interfaces* 8 (2016) 34431-34437. <https://doi.org/10.1021/acsaem.6b12297>.
- [18] A. Sankhla, A. Patil, H. Kamila, M. Yasserli, N. Farahi, E. Mueller, J. de Boor, Mechanical alloying of optimized Mg₂(Si, Sn) solid solutions: understanding phase evolution and tuning synthesis parameters for thermoelectric applications, *ACS Appl. Energy Mater.* 1 (2018) 531-542. <https://doi.org/10.1021/acsaem.7b00128>.
- [19] H. Kamila, P. Sahu, A. Sankhla, M. Yasserli, H.-N. Pham, T. Dasgupta, E. Mueller, J. de Boor, Analyzing transport properties of p-type Mg₂Si–Mg₂Sn solid solutions: optimization of thermoelectric performance and insight into the electronic band structure, *J. Mater. Chem. A* 7 (2019) 1045-1054.

<https://doi.org/10.1039/C8TA08920E>.

- [20] V. Zaitsev, M. Fedorov, E. Gurieva, I. Eremin, P. Konstantinov, A.Y. Samunin, M. Vedernikov, Highly effective $Mg_2Si_{1-x}Sn_x$ thermoelectrics, *Phys. Rev. B* 74 (2006) 045207. <https://doi.org/10.1103/PhysRevB.74.045207>.
- [21] M.I. Fedorov, V.K. Zaitsev, G.N. Isachenko, High effective thermoelectrics based on the Mg_2Si - Mg_2Sn solid solution, *Solid State Phenom.: Trans Tech Publ.* 170 (2011) 286-292. <https://doi.org/10.4028/www.scientific.net/SSP.170.286>.
- [22] N.H. Pham, N. Farahi, H. Kamila, A. Sankhla, S. Ayachi, E. Müller, J. de Boor, Ni and Ag electrodes for magnesium silicide based thermoelectric generators, *Mater. Today Energy* 11 (2019) 97-105. <https://doi.org/10.1016/j.mtener.2018.10.016>.
- [23] J. de Boor, C. Gloanec, H. Kolb, R. Sottong, P. Ziolkowski, E. Müller, Fabrication and characterization of nickel contacts for magnesium silicide based thermoelectric generators, *J. Alloys Compd.* 632 (2015) 348-353. <https://doi.org/10.1016/j.jallcom.2015.01.149>.
- [24] J. de Boor, D. Droste, C. Schneider, J. Janek, E. Mueller, Thermal stability of magnesium silicide/nickel contacts, *J. Electron. Mater.* 45 (2016) 5313-5320. <https://doi.org/10.1007/s11664-016-4716-x>.
- [25] S. Ayachi, G. Castillo Hernandez, N.H. Pham, N. Farahi, E. Müller, J. de Boor, Interfaces, Developing contacting solutions for $Mg_2Si_{1-x}Sn_x$ -based thermoelectric generators: Cu and $Ni_{45}Cu_{55}$ as potential contacting electrodes, *ACS Appl. Mater. Interfaces*, 11 (2019) 40769. <https://doi.org/10.1021/acsami.9b12474>.
- [26] S. Ayachi, G.C. Hernandez, E. Müller, J. de Boor, Contacting Cu electrodes to $Mg_2Si_{0.3}Sn_{0.7}$: Direct vs. indirect resistive heating, *Semiconductors* 53 (2019) 1825-1830. <https://doi.org/10.1134/S1063782619130025>.
- [27] M. Yasserli, A. Sankhla, H. Kamila, R. Orenstein, D.N. Truong, N. Farahi, J. de Boor, E. Mueller, Solid solution formation in $Mg_2(Si, Sn)$ and shape of the miscibility gap, *Acta Mater.* 185 (2020) 80-88. <https://doi.org/10.1016/j.actamat.2019.11.054>.
- [28] R. Viennois, C. Colinet, P. Jund, J.-C. Tédénac, Phase stability of ternary antiferrotype compounds in the quasi-binary systems Mg_2X - Mg_2Y (X, Y= Si, Ge, Sn) via ab-initio calculations, *Intermetallics* 31 (2012) 145-151. <https://doi.org/10.1016/j.intermet.2012.06.016>.
- [29] A. Kozlov, J. Gröbner, R. Schmid-Fetzer, Phase formation in Mg-Sn-Si and Mg-Sn-Si-Ca alloys, *J. Alloy Compd.* 509 (2011) 3326-3337. <https://doi.org/10.1016/j.jallcom.2010.12.052>.
- [30] H.J. Queisser, E. E. Haller, Defects in semiconductors: some fatal, some vital, *Science* 281 (1998) 945-950. <https://doi.org/10.1126/science.281.5379.945>.
- [31] L. Liu, Z. Mei, A. Tang, A. Azarov, A. Kuznetsov, Q.-K. Xue, X. Du, Oxygen vacancies: The origin of n-type conductivity in ZnO, *Phys. Rev. B* 93 (2016) 235305. <https://doi.org/10.1103/PhysRevB.93.235305>.
- [32] S. Chen, J.-H. Yang, X.-G. Gong, A. Walsh, S.-H. Wei, Intrinsic point defects and complexes in the quaternary kesterite semiconductor Cu_2ZnSnS_4 , *Phys. Rev. B* 81 (2010) 245204. <https://doi.org/10.1103/PhysRevB.81.245204>.
- [33] Z. Sun, Y. Pan, J. Zhou, B. Sa, R. Ahuja, Origin of p-type conductivity in layered $nGeTe_mSb_2Te_3$ chalcogenide semiconductors, *Phys. Rev. B* 83 (2011) 113201. <https://doi.org/10.1103/PhysRevB.83.113201>.
- [34] D. West, Y. Sun, H. Wang, J. Bang, S. Zhang, Native defects in second-generation topological insulators: effect of spin-orbit interaction Bi_2Se_3 , *Phys. Rev. B* 86 (2012) 121201. <https://doi.org/10.1103/PhysRevB.86.121201>.
- [35] J. Horák, Z. Sary, P. Lošťák, J. Pancíř, Anti-site defects in n- Bi_2Se_3 crystals, *J. Phys. Chem. Solids* 51 (1990) 1353-1360. [https://doi.org/10.1016/0022-3697\(90\)90017-A](https://doi.org/10.1016/0022-3697(90)90017-A).
- [36] A. Kato, T. Yagi, N. Fukusako, First-principles studies of intrinsic point defects in magnesium silicide, *J. Phys.: Condens. Matter* 21 (2009) 205801. <https://doi.org/10.1088/0953-8984/21/20/205801>.
- [37] R.G. Morris, R. Redin, G.C. Danielson, Semiconducting properties of Mg_2Si single crystals, *Phys. Rev.* 109 (1958) 1909. <https://doi.org/10.1103/PhysRev.109.1909>.
- [38] M. Yoshinaga, T. Iida, M. Noda, T. Endo, T. Takanashi, Bulk crystal growth of Mg_2Si by the vertical Bridgman method, *Thin Solid Films* 461 (2004) 86-89. <https://doi.org/10.1016/j.tsf.2004.02.072>.
- [39] P. Jund, R. Viennois, C. Colinet, G. Hug, M. Fèvre, J.-C. Tedenac, Lattice stability and formation

- energies of intrinsic defects in Mg₂Si and Mg₂Ge via first principles simulations, *J. Phys.: Condens. Matter* 25 (2012) 035403. <https://doi.org/10.1088/0953-8984/25/3/035403>.
- [40] X. Liu, L. Xi, W. Qiu, J. Yang, T. Zhu, X. Zhao, W. Zhang, Significant roles of intrinsic point defects in Mg₂X (X= Si, Ge, Sn) thermoelectric materials, *Ad. Electron Mater.* 2 (2016) 1500284. <https://doi.org/10.1002/aelm.201500284>.
- [41] B. Ryu, S. Park, E.-A. Choi, J. de Boor, P. Ziolkowski, J. Chung, S.D. Park, Hybrid-functional and quasi-particle calculations of band structures of Mg₂Si, Mg₂Ge, and Mg₂Sn, *J. Korean Phys. Soc.* 75 (2019) 144-152. <https://doi.org/10.3938/jkps.75.144>.
- [42] F. Aryasetiawan, O. Gunnarsson, The GW method, *Rep. Prog. Phys.* 61 (1998) 237.
- [43] B. Ryu, E. Choi, S. Park, J. Chung, J. de Boor, P. Ziolkowski, E. Müller, S. Park, Native point defects and low p-doping efficiency in Mg₂(Si,Sn) solid solutions: A hybrid-density functional study, *J. Alloys Compd.* 853, 157145 (2021). <https://doi.org/10.1016/j.jallcom.2020.157145>.
- [44] S.-M. Choi, T.H. An, W.-S. Seo, C. Park, I.-H. Kim, S.-U. Kim, Doping effects on thermoelectric properties in the Mg₂Sn system, *J. Electron. Mater.* 41 (2012) 1071-1076. <https://doi.org/10.1007/s11664-012-1985-x>.
- [45] Z. Du, T. Zhu, X. Zhao, Enhanced thermoelectric properties of Mg₂Si_{0.58}Sn_{0.42} compounds by Bi doping, *Mater. Lett.* 66 (2012) 76-78. <https://doi.org/10.1016/j.matlet.2011.08.031>.
- [46] I. Aoyama, H. Kaibe, L. Rauscher, T. Kanda, M. Mukoujima, S. Sano, T. Tsuji, Doping effects on thermoelectric properties of higher manganese silicides (HMSs, MnSi_{1.74}) and characterization of thermoelectric generating module using p-type (Al, Ge and Mo)-doped HMSs and n-type Mg₂Si_{0.4}Sn_{0.6} legs, *Jpn. J. Appl. Phys.* 44 (2005) 4275. <https://doi.org/10.1143/JJAP.44.4275>.
- [47] X. Chen, A. Weathers, D. Salta, L. Zhang, J. Zhou, J.B. Goodenough, L. Shi, Effects of (Al, Ge) double doping on the thermoelectric properties of higher manganese silicides, *J. Appl. Phys.* 114 (2013) 173705. <https://doi.org/10.1063/1.4828731>.
- [48] P. Gorai, V. Stevanović, E.S. Toberer, Computationally guided discovery of thermoelectric materials, *Nat. Rev. Mater.* 2 (2017) 17053. <https://doi.org/10.1038/natrevmats.2017.53>.
- [49] H. Kamila, M. Yasseri, N. Pham, N. Farahi, E. Müller, J. de Boor, Synthesis of p-type Mg₂Si_{1-x}Sn_x with x= 0-1 and optimization of the synthesis parameters, *Mater. Today: Proc.* 8 (2019) 546-555. <https://doi.org/10.1016/j.matpr.2019.02.052>.
- [50] N. Farahi, C. Stiewe, D.N. Truong, J. de Boor, E. Müller, High efficiency Mg₂(Si, Sn)-based thermoelectric materials: scale-up synthesis, functional homogeneity, and thermal stability. *RSC Adv.* 9 (2019) 23021-23028. <https://doi.org/10.1039/C9RA04800F>.
- [51] D. Platzek, G. Karpinski, C. Stiewe, P. Ziolkowski, C. Drasar, E. Muller, Potential-Seebeck-microprobe (PSM): measuring the spatial resolution of the Seebeck coefficient and the electric potential, 24th ICT IEEE (2005) 13-16.
- [52] W. Liu, H. Chi, H. Sun, Q. Zhang, K. Yin, X. Tang, Q. Zhang, C. Uher, Advanced thermoelectrics governed by a single parabolic band: Mg₂Si_{0.3}Sn_{0.7}, a canonical example, *Phys. Chem. Chem. Phys.* 16 (2014) 6893-6897. <https://doi.org/10.1039/C4CP00641K>.
- [53] Q. Zhang, L. Cheng, W. Liu, Y. Zheng, X. Su, H. Chi, H. Liu, Y. Yan, X. Tang, C. Uher, Low effective mass and carrier concentration optimization for high performance p-type Mg₂(1-x)Li_{2x}Si_{0.3}Sn_{0.7} solid solutions, *Phys. Chem. Chem. Phys.* 16 (2014) 23576-23583. <https://doi.org/10.1039/C4CP03468F>.
- [54] A.F. May, High-temperature transport in lanthanum telluride and other modern thermoelectric materials, California Institute of Technology, (2010).
- [55] A.V. Krugau, O.A. Vydrov, A.F. Izmaylov, G.E. Scuseria, Influence of the exchange screening parameter on the performance of screened hybrid functionals, *J. Chem. Phys.* 125 (2006) 224106. <https://doi.org/10.1063/1.2404663>.
- [56] G. Kresse, J. Furthmüller, Efficient iterative schemes for ab initio total-energy calculations using a plane-wave basis set, *Phys. Rev. B* 54 (1996) 11169. <https://doi.org/10.1103/PhysRevB.54.11169>.
- [57] G. Kresse, D. Joubert, From ultrasoft pseudopotentials to the projector augmented-wave method, *Physical Review B* 59 (1999) 1758. <https://doi.org/10.1103/PhysRevB.59.1758>.
- [58] S. Zhang, J.E. Northrup, Chemical potential dependence of defect formation energies in GaAs: Application to Ga self-diffusion, *Phys. Rev. Lett.* 67 (1991) 2339. <https://doi.org/10.1103/PhysRevLett.67.2339>.
- [59] B. Ryu, M.W. Oh, J.K. Lee, J.E. Lee, S.J. Joo, B.-S. Kim, B.K. Min, H.-W. Lee, S. Park, Defects responsible for abnormal n-type conductivity in Ag-excess doped PbTe thermoelectrics, *J. Appl. Phys.*

- 118 (2015) 015705. <https://doi.org/10.1063/1.4923391>.
- [60] S.K. Bux, M.T. Yeung, E.S. Toberer, G.J. Snyder, R.B. Kaner, J.P. Fleurial, Mechanochemical synthesis and thermoelectric properties of high quality magnesium silicide, *J. Mater. Chem.* 21 (2011) 12259-12266. <https://doi.org/10.1039/C1JM10827A>.
- [61] W. Liu, H.S. Kim, S. Chen, Q. Jie, B. Lv, M. Yao, Z. Ren, C.P. Opeil, S. Wilson, C.W. Chu, n-type thermoelectric material $\text{Mg}_2\text{Sn}_{0.75}\text{Ge}_{0.25}$ for high power generation, *Proc. Natl. Acad. Sci.* 112 (2015) 3269-3274. <https://doi.org/10.1073/pnas.1424388112>.
- [62] L. Sudha, R. Sukumar, K. Uma Rao, Evaluation of activation energy (E_a) profiles of nanostructured alumina polycarbonate composite insulation materials, *Int. J. Mater. Mech. Manuf.* 2 (2014) 96-100. <https://doi.org/10.7763/IJMMM.2014.V2.108>.
- [63] M. Mantina, Y. Wang, R. Arroyave, L. Chen, Z. Liu, C. Wolverton, First-principles calculation of self-diffusion coefficients, *Phys. Rev. Lett.* 100 (2008) 215901. <https://doi.org/10.1103/PhysRevLett.100.215901>.
- [64] I.H. Kim, $\text{Mg}_2\text{B}^{\text{IV}}$: Narrow bandgap thermoelectric semiconductors, *J. Korean Phys. Soc.* 72 (2018) 1095-1109. <https://doi.org/10.3938/jkps.72.1095>.
- [65] J.H. Yang, W.J. Yin, J.S. Park, S.H. Wei, Self-regulation of charged defect compensation and formation energy pinning in semiconductors, *Scientific Reports* 5 (2015) 16977. <https://doi.org/10.1038/srep16977>.
- [66] G. Henkelman, H. Jónsson, Improved tangent estimate in the nudged elastic band method for finding minimum energy paths and saddle points, *J. Chem. Phys.* 113 (2000) 9978-9985. <https://doi.org/10.1063/1.1323224>.
- [67] G. Henkelman, B.P. Uberuaga, H. Jónsson, A climbing image nudged elastic band method for finding saddle points and minimum energy paths, *J. Chem. Phys.* 113 (2000) 9901-9904. <https://doi.org/10.1063/1.1329672>.
- [68] P. Gao, I. Berkun, R.D. Schmidt, M.F. Luzenski, X. Lu, P.B. Sarac, E.D. Case, T.P. Hogan, Transport and mechanical properties of high-ZT $\text{Mg}_{2.08}\text{Si}_{0.4-x}\text{Sn}_{0.6}\text{Sb}_x$ thermoelectric materials, *J. Electron. Mater.* 43 (2014) 1790-1803. <https://doi.org/10.1007/s11664-013-2865-8>.

Supplementary Material (Chapter 5/Paper 3)

On the Relevance of Point Defects for the Selection of Contacting Electrodes: Ag as an Example for Mg₂(Si,Sn)-based Thermoelectric Generators

Sahar Ayachi, Radhika Deshpande, Prasanna Ponnusamy, Dr. Sungjin Park, Dr. Jaywan Chung, Dr. SuDong Park, Dr. Byungki Ryu, Prof. Eckhard Müller, Dr. Johannes de Boor**

In this Supporting Information (SI), we provide further information to complete the main text.

We provide complementary information for:

- I. Seebeck profile mappings
- II. Defect formation energies
- III. Device performance calculation

I. Seebeck Profile Mappings

Table S 1 presents averages of the measured Seebeck values at the interfaces (closest points to the Ag layer) at different temperatures. As S and n are directly linked, we also calculated the corresponding average carrier concentrations at the interface. The estimate is based on a single parabolic band model and the effective masses taken for Mg_2Si and Mg_2Sn are respectively $m_D^* = 1.1 m_0$ [1] and $m_D^* = 2 m_0$ [2].

Table S 1: Measured Seebeck coefficient values $S_{\text{inter,exp}}$ at the contacting interfaces and their corresponding estimated carrier concentration n

	$T_{\text{join}} [^\circ\text{C}]$	$S_{\text{inter,exp}} [\mu\text{V K}^{-1}]$	Estimated $n [10^{20} \text{ cm}^{-3}]$
Mg_2Si	Before joining	55	2.5
	450	57 ± 1	2.4
	500	63 ± 10	2.1
	550	58 ± 2	2.4
Mg_2Sn	Before joining	80	3.6
	400 – Left side	89 ± 4	3
	400 – Right side	115 ± 8	1.9
	450 – Left side	85 ± 9	3.2
	450 – Right side	125 ± 14	1.6
	500 – Left side	125 ± 17	1.6
	500 – Right side	127 ± 11	1.6

Modelling of the Seebeck Coefficient Profile

In the main manuscript, we have used a simple exponential to fit $S(x)$ and have deduced diffusion lengths and coefficients based on that. However, even if the assumed diffusion mechanism holds, the relation between the Ag content and the measured Seebeck coefficient is non-trivial and the assumed function of $S(x)$ therefore needs to be justified.

This can be done by calculating the $S(x)$ according to the assumed diffusion mechanism with the obtained fit parameters and compare this to the actually measured $S(x)$.

As an example, the Mg_2Si sample contacted with Ag at $T = 500^\circ\text{C}$ was used, and the modelling was done as follow:

- 1- Using the error function $\frac{c(x,t)-c_0}{c_s-c_0} = 1 - \operatorname{erf}\left(\frac{x}{2\sqrt{Dt}}\right)$ [3], where $c_0 = 0$ and $c_s = 1$ are the boundary conditions, $t = 600\text{s}$ and $D = 56.5 \times 10^{-12} \text{ m}^2 \text{ s}^{-1}$ is the diffusion coefficient of Ag in Mg_2Si at $T = 500^\circ\text{C}$, a profile of Ag concentration $c(x)$ is obtained.
- 2- Assuming that each Ag atom substitutes one Mg atom and provides one hole, we calculate the corresponding carrier concentration $n(x)$ as $n(x) = n_0 - \Delta n$, where n_0 is the carrier concentration of the bulk TE material and $\Delta n = c(x,t) \times (N/V)$, where $N/V = 3.12 \times 10^{22} \text{ cm}^{-3}$ is the number of Mg atoms per unit volume.
- 3- Using an SPB model, we calculate a Seebeck profile $S(x)$ corresponding to the $n(x)$ obtained above, and this calculated profile is then compared with selected experimental Seebeck lines.

From the data obtained through modelling, we only look at $S(x)$ numbers starting from $x = 0.3 \text{ mm}$. The reason for this manual adjustment is that going to low x values doesn't make sense in our case as there is an interface layer, which is not considered here.

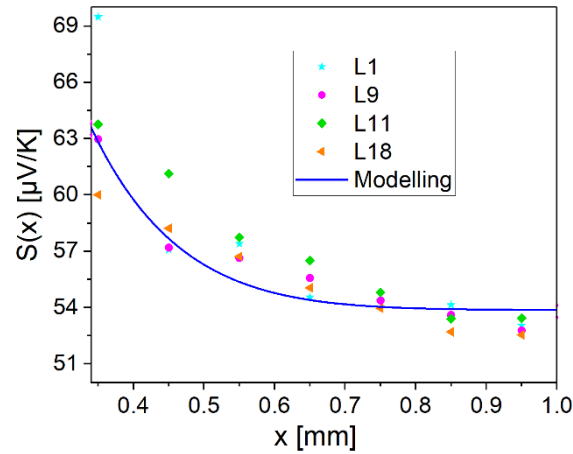


Figure S 1: Comparison of $S(x)$ calculated from the suggest diffusion model (based on a simple exponential fit from Eq 3.) with selected experimental Seebeck profile lines.

Figure S 1 shows a reasonable agreement between the data from the modelling and the experimental data. The observed difference between both can be associated to the line to line scatter during the experimental mappings as well as the limited spatial resolution of the PSM.

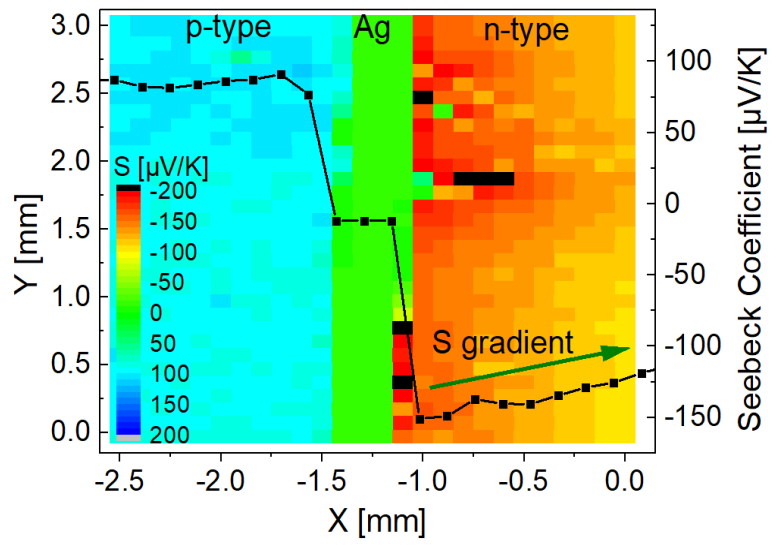


Figure S 2: 2D Seebeck plot for n//Ag//p sample stacked with n-type pellet at the bottom, Ag in the middle and p-type pellet on top. The selected Seebeck profile line scan corresponds to the scan position $y = 0$ mm.

II. Defect formation energies

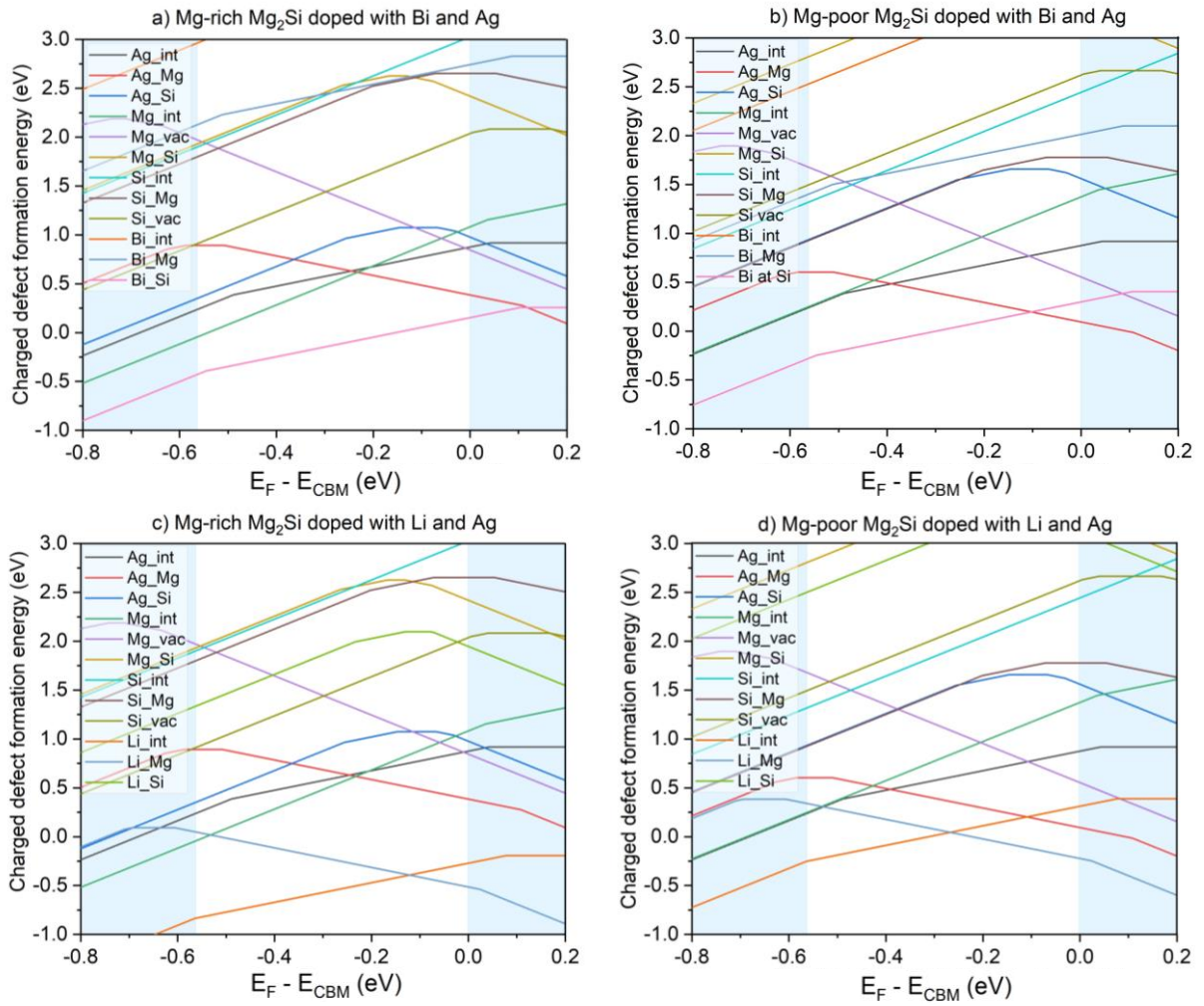


Figure S 3: All formation energy curves for Mg_2Si with a) Bi and Ag-related defects under Mg-rich conditions, b) Bi and Ag-related defects under Mg-poor conditions, c) Li and Ag-related defects under Mg-rich conditions and d) Li and Ag-related defects under Mg-poor conditions.

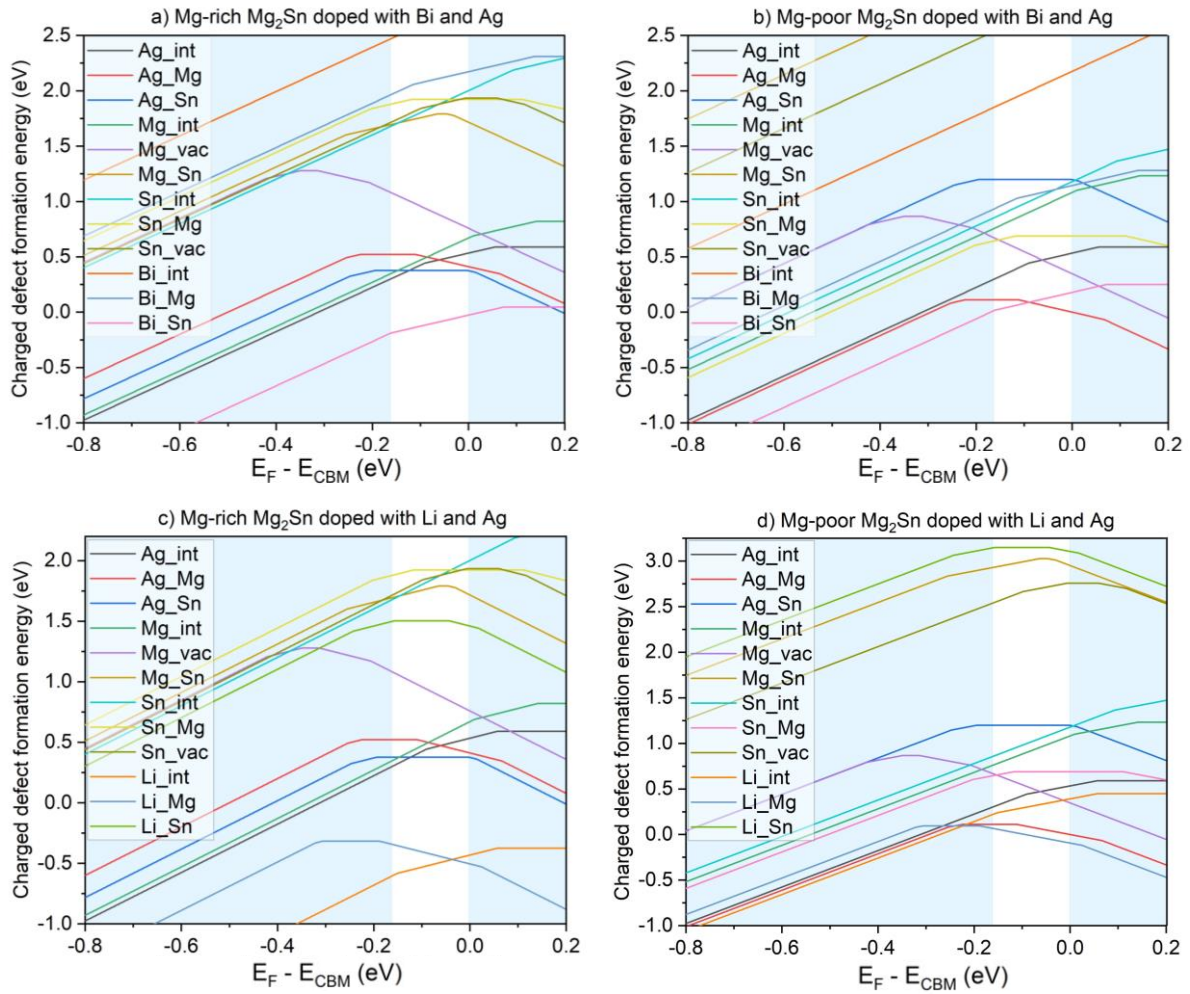


Figure S 4: All formation energy curves for Mg_2Sn with a) Bi and Ag-related defects under Mg-rich conditions, b) Bi and Ag-related defects under Mg-poor conditions, c) Li and Ag-related defects under Mg-rich conditions and d) Li and Ag-related defects under Mg-poor conditions.

III. Device performance calculation

The conversion efficiency was obtained by solving the thermoelectric heat balance equation given below, with the temperature dependent thermoelectric properties.

$$\nabla \cdot (-\kappa \nabla T) = \rho j^2 - \tau j \cdot \nabla T$$

Here κ and ρ are the thermal conductivity and electrical resistivity respectively, $j = I/A$ is the current density and τ is the Thomson coefficient $= T \frac{\partial \alpha}{\partial T}$. The power output density is obtained as the difference between the input heat flux and the output heat flux ($p = q_{in} - q_{out}$) and the device efficiency is calculated as $\eta = \frac{p}{q_{in}}$, where $q_{in} = -\kappa_h \cdot \frac{dT}{dx_h} + I \cdot \alpha_h \cdot T_h$. [4, 5]. The simulation was done for a leg length of 5 mm for a hot side temperature of 700 K and a cold side temperature of 300 K.

Electrical and thermal conductivity were taken from literature, where S was matched with S after diffusion [6].

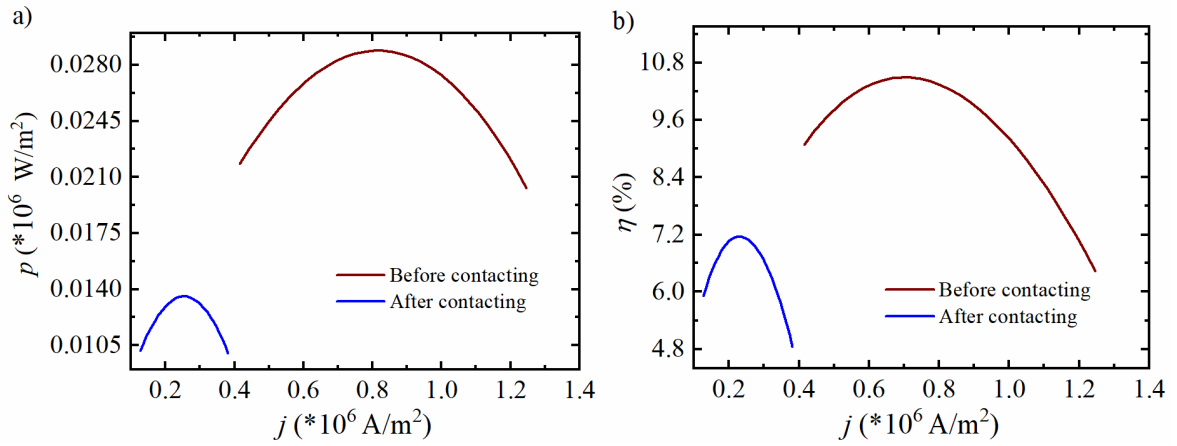


Figure S 5: (a) Power output density (p), and (b) efficiency (η) vs current density for the TE leg before and after contacting

The thermoelectric properties before and after contacting are given below.

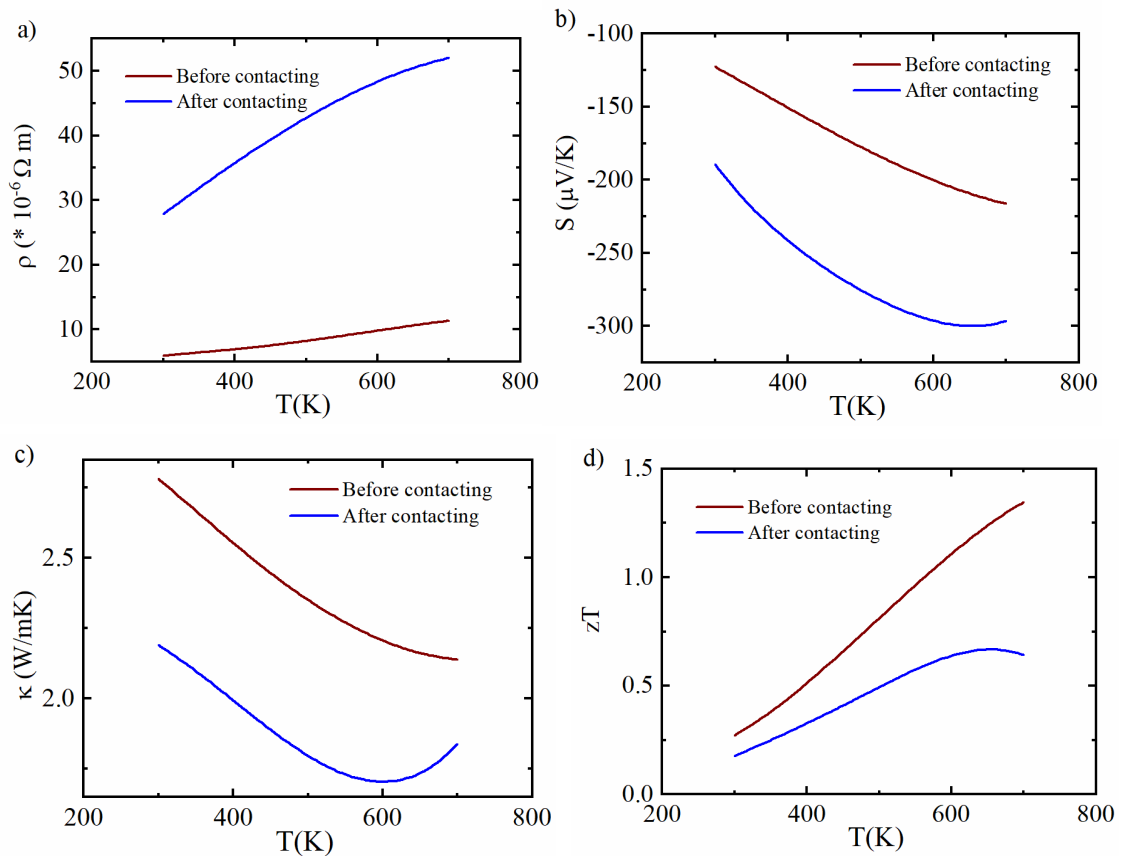


Figure S 6: Temperature dependent thermoelectric properties a) electrical resistivity b) Seebeck coefficient c) Thermal conductivity d) the corresponding zT

References for Supplementary Material of Chapter 5/Paper 3:

- [1] S.K. Bux, M.T. Yeung, E.S. Toberer, G.J. Snyder, R.B. Kaner, J.-P. Fleurial, Mechanochemical synthesis and thermoelectric properties of high quality magnesium silicide, *J. Mater. Chem.* 21 (2011) 12259-12266.
- [2] W. Liu, H.S. Kim, S. Chen, Q. Jie, B. Lv, M. Yao, Z. Ren, C.P. Opeil, S. Wilson, C.-W. Chu, n-type thermoelectric material $\text{Mg}_2\text{Sn}_{0.75}\text{Ge}_{0.25}$ for high power generation, *Proc. Natl. Acad. Scie.* 112 (2015) 3269-3274..
- [3] B.P. Van Milligen, P. Bons, B.A. Carreras, R. Sanchez, On the applicability of Fick's law to diffusion in inhomogeneous systems, *Eur. J. Phys.* 26 (2005) 913.
- [4] P. Ponnusamy, J. de Boor, E. Müller, Using the constant properties model for accurate performance estimation of thermoelectric generator elements, *Appl. Energy* 262 (2020) 114587.
- [5] A.F. Ioffe, *Semiconductor thermoelements and thermoelectric cooling*, (1957).
- [6] P. Gao, I. Berkun, R.D. Schmidt, M.F. Luzenski, X. Lu, P.B. Sarac, E.D. Case, T.P. Hogan, Transport and mechanical properties of high-ZT $\text{Mg}_{2.08}\text{Si}_{0.4-x}\text{Sn}_{0.6}\text{Sb}_x$ thermoelectric materials, *J. Electron. Mater.* 43 (2014) 1790-1803.

Chapter 6:

6. Discussion

In this section, we aim to discuss the results from Chapters 3, 4 and 5 and correlate them to have a general overview on the topic of interest. These chapters refer respectively to the published works [96], [145] and [146], and each one of them presents nominally the same content as the literature it refers to.

The main objective of our work is to put together a list of criteria to facilitate the selection process of contacting electrodes for thermoelectric generators (TEG). Our work focuses on $\text{Mg}_2\text{Si}_{1-x}\text{Sn}_x$ -based thermoelectric generators, but we believe the outcome can be generalized to further TEGs based on different material systems.

Usually, what are considered as starting requirements for a contacting electrode are, stability and the conductivity of the metal, as well as its matching coefficient of thermal expansion (CTE) to that of the thermoelectric material of interest [44, 147, 148]. Low contact resistances, both electrical and thermal, are preferred, and long-term chemical (reactions and diffusion) and physical (mechanical adhesion) stability are also necessary to avoid device failure under thermal cycling.

In other works from our group, a few electrodes, namely Ni, Ag [149] and Al [150], were tested, and this work started with testing Cu and $\text{Ni}_{45}\text{Cu}_{55}$. With these five electrodes already, it was clear that identifying suitable process parameters for the contacting procedure is quite challenging, as it depends not only on the chosen materials (TE material + contacting electrode), but also on the interactions between them (reaction, diffusion, if the electrode is treated before joining, if there are extra layers such as a diffusion barrier added...) and their joining conditions (temperature, pressure, time, with or without sintering current).

The following sub-sections discuss the examples of Cu, $\text{Ni}_{45}\text{Cu}_{55}$, Ag and Ni experimentally tested with n- and p-type $\text{Mg}_2\text{Si}_{1-x}\text{Sn}_x$ ($x = 0, 0.2, 0.7, 1$) thermoelectric materials. The first section (Chapter 6.1) discusses the effects of the preparation and joining conditions on the contacting results using the example of Cu and $\text{Ni}_{45}\text{Cu}_{55}$ electrodes. The following chapter, Chapter 6.2, joins Chapter 5 in considering the materials' point defects in the contacting. Here we look into the experimental contacting results of the mentioned electrodes (Cu and Ni) with $\text{Mg}_2\text{Si}_{1-x}\text{Sn}_x$ and compare them with predictions from calculation results of defect formation energies obtained from hybrid-DFT (introduced in Chapter 2.6). With this comparison, we try to investigate the compatibility between the results and predictions provided from both procedures (experiments and calculations, respectively), and if the output provided by the hybrid-DFT calculations can explain the experimentally observed behaviors. Through this study, I try to establish the importance of point defects for contact development, and how they can be used to

predict the effect of contacting electrodes on the electronic and thermoelectric properties of the material system. Thus, the relevance of hybrid-DFT calculations in the pre-selection of potential electrodes would be established, which adds one more criterion to the contacting list of requirements.

6.1. Effects of the preparation conditions on the contacting results

6.1.1. Effect of the synthesis method of the TE material

As explained in the Methods section (Chapter 2), the procedure used to synthesize samples in this work is mainly induction melting (IM) of the processor elements to form the target phase, followed by a short high energy ball milling (HEBM) step to crush the ingot and obtain fine powder. This method was chosen as it was proven by a previous work to be scalable and to produce high TE property powder [2]. In fact, while our HEBM synthesis route (where the precursors are mechanically alloyed in the ball-mill) can only produce 10 g of powder at once, this induction melting route can be used to synthesize 30 or even 50 g at once. Such upscaled methods are necessary in order to facilitate TE leg mass production for TEG building.

Generally, after synthesis, our IM powder made for this study looked visually homogeneous and didn't include unreacted chunks. Nevertheless, after sintering/pressing the powder into a pellet, local demixing of the $\text{Mg}_2\text{Si}_{1-x}\text{Sn}_x$ matrix was observed, and this demixing was sometimes intensified after joining the TE pellets with the contacting electrodes [4, 37, 96, 145, 151]. In order to investigate if such demixing is related to the powder synthesis method, and if contacting enhances it, high energy ball milled (HEBM) p-type $\text{Mg}_{1.97}\text{Li}_{0.03}\text{Si}_{0.3}\text{Sn}_{0.7}$ powder was synthesized by our colleague Vidushi Galwadu Arachchige.

Pellets made from this powder was then contacted with Cu electrodes under the same conditions used in Chapter 3, and the results were compared with p-type joining results from the same work where IM powder was used. The TE properties of the samples from both synthesis procedures were already studied and reported in [152] and [2]. Previous literature also reported the grain sizes for samples obtained from BM and IM. Castillo-Hernandez *et al.* reported a grain size of $7 \pm 3 \mu\text{m}$ for the IM powder of $\text{Mg}_2\text{Si}_{0.3}\text{Sn}_{0.7}$ composition [97], while Kamila *et al.* reported a grain size of $\sim 5 \mu\text{m}$ for BM powder [152]. Note that the exact compositions studied in [152] are $\text{Mg}_{2-y}\text{Li}_y\text{Si}_{0.2}\text{Sn}_{0.8}$ ($y = 0.01, 0.02$ and 0.03); nevertheless, the grain sizes of the densified samples from both synthesis methods are comparable. This implies similar properties such as grain boundary scattering, and potentially similar mechanical properties. Moreover, as the synthesis route is different (melting vs. mechanical alloying), the comparable grain sizes indicate that the sintering step plays an important role in grain size regulation [153, 154].

Figure 6.1 presents SEM images of p-type $\text{Mg}_2\text{Si}_{0.3}\text{Sn}_{0.7}$ samples, once pressed from induction melted powder (Figure 6.1 a) and once from ball milled powder (Figure 6.1 b). The results show that, generally, matrix inhomogeneity is observed in all cases, independently of the synthesis method. On these images, the darker areas (compared to the matrix) are Si-rich $\text{Mg}_2(\text{Si},\text{Sn})$ areas. Such phase separation into Si-rich and Sn-rich areas is commonly observed for the $\text{Mg}_2\text{Si}-\text{Mg}_2\text{Sn}$ system, under certain conditions, due to the presence of miscibility gaps, and has already been reported in works like [37], [97] and [155]. The comparison also shows that, for the samples in play, the induction melting route produces a more homogeneous sample, as the SEM image of the cross section shows less segregated dark regions. The reason behind this could be correlated to the fact that the powder obtained after ball milling tends to contain more unreacted Si chunks than the induction melted counterpart [1]. When pressed, if the powder contains unreacted Si, this Si would react with the excess Mg and form Mg_2Si rich agglomerates, which would be observed on the SEM images as darker areas.

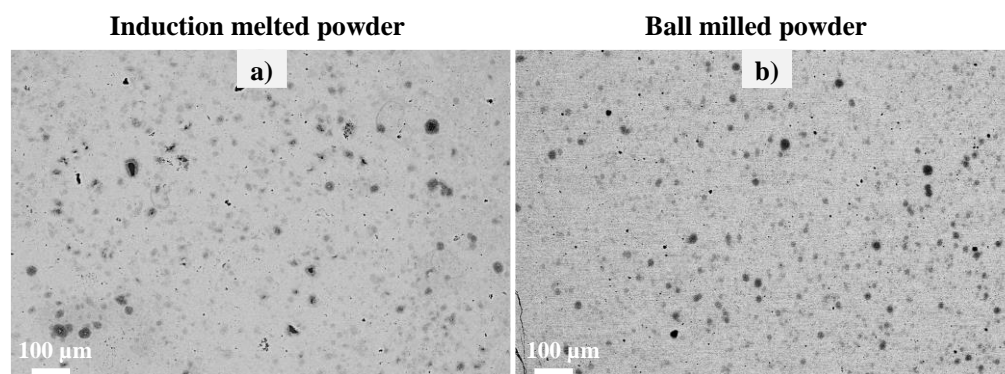


Figure 6.1: SEM images of the cross section of non-contacted p-type $\text{Mg}_{1.97}\text{Li}_{0.03}\text{Si}_{0.3}\text{Sn}_{0.7}$ obtained through a) induction melting and through b) ball milling.

To confirm that our conclusions about matrix homogeneity are not related to the contrast and brightness parameters of the SEM images, XRD analysis and a fast quantification method [156] were utilized to investigate the difference in homogeneity between the IM and BM samples, and the results are provided respectively in Figure 6.2 and Figure 6.3.

Figure 6.2 shows XRD patterns of as pressed p-type $\text{Mg}_2\text{Si}_{1-x}\text{Sn}_x$ pellets. The pellet from the ball milled powder is shown with the black pattern, while the one from the induction melted powder is shown in red. Both patterns were compared with a previously reported XRD pattern of a pure $\text{Mg}_2\text{Si}_{0.3}\text{Sn}_{0.7}$ (in blue) [97]. Even though the data reported in the literature corresponds to an undoped sample, the comparison still stands as dopants are not expected to affect XRD peak positions visibly since they are inserted in very small concentrations. In Figure 6.2, seven star-symbols are added to pinpoint extra peaks/impurities that only exist in the BM sample pattern. These are shoulder peaks, which indicate

phase separation in the studied material. As $\text{Mg}_2\text{Si}_{1-x}\text{Sn}_x$ tends to separate into Mg_2Si - and Mg_2Sn -rich phases under certain conditions [37], it is safe to conclude that these marked peaks in the BM XRD pattern indicate a less homogeneous matrix compared to the IM sample. In fact, the peaks marked with the stars on Figure 6.2 are Mg_2Sn peaks, as also marked below in the same figure in green line symbols. Some of these peaks look shifted towards slightly higher angles from the Mg_2Sn peaks, which could be related to absolute errors during the measurement due to sample positioning. Such errors would result in different shifts at different angles. Therefore, from this comparison, it can be concluded that the presented BM sample is less homogeneous than the IM sample, which also fits what was observed in the SEM images (Figure 6.1 a and b).

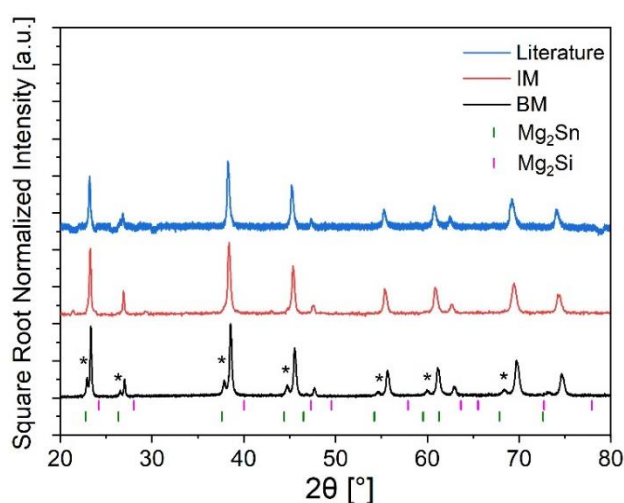


Figure 6.2: XRD spectra for the high energy ball milled (BM) and induction melted (IM) pressed p-type $\text{Mg}_{1.97}\text{Li}_{0.03}\text{Si}_{0.3}\text{Sn}_{0.7}$ powders, compared with an XRD pattern of a pure undoped $\text{Mg}_2\text{Si}_{0.3}\text{Sn}_{0.7}$ sample reported in [97]. The black star symbols pinpoint shoulder peaks in the BM sample indicating phase separation (Mg_2Sn phase).

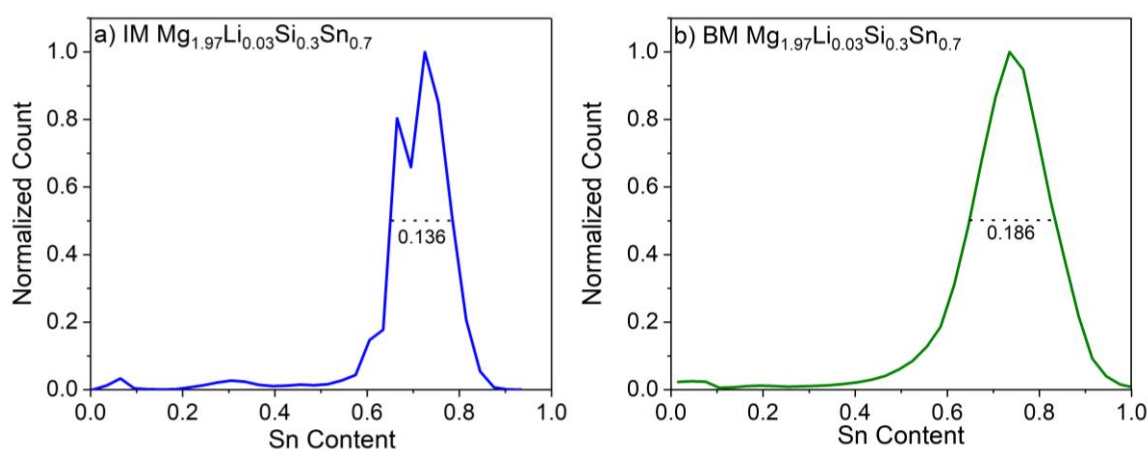


Figure 6.3: Graphs of normalized counts showing composition distribution of the a) induction melted (IM) sample and b) the ball milled (BM) sample as a function of the Sn content in $\text{Mg}_2\text{Si}_{1-x}\text{Sn}_x$ composition range. These counts are obtained from a *Gray scale analysis calibrated using EDX data* [156]. The IM sample shows a narrower range of composition distribution (FWHM = 0.136) centered around the main desired composition

$\text{Mg}_2\text{Si}_{0.3}\text{Sn}_{0.7}$, while the BM sample shows a wider distribution range (FWHM = 0.186), indicating a sample with a less homogeneous matrix and more secondary phases.

Figure 6.3 shows two graphs of normalized counts of the composition distribution of both IM (Figure 6.3 a) and BM (Figure 6.3 b) samples and represent the matrix demixing/inhomogeneity. Both histograms were made using EDX data of phase composition analysis (Sn content) done on a large area of the samples and on areas with different gray scales. This mentioned analysis method is called “*Gray scale analysis calibrated using EDX data*”, and was developed by colleagues from our group [156]. For this work, the analysis was done by our colleague Mr. G. Castillo-Hernandez. The histogram corresponding to the IM sample (Figure 6.3 a) has a composition distributed on a narrower range than the histogram of the BM sample (Figure 6.3 b), which corresponds to a more homogeneous composition. The full width at half maximum (FWHM) values for both histograms are respectively 0.136 and 0.186 for the IM and the BM sample. Moreover, the IM sample histogram is more centered around the main $\text{Mg}_2\text{Si}_{0.3}\text{Sn}_{0.7}$ composition, while the BM histogram is shifted towards a composition richer in Sn. The latter was also observed in the XRD results reported in Figure 6.2.

From the provided comparisons in this work, it can be concluded that our induction melted sample is more homogeneous and closer in composition to the target composition compared to our sample produced with HEBM. This could be explained by the fact that the induction melting procedure involves three different temperature increase steps, allowing each time more and more particles to react and form the desired composition. However, in ball milling, the particles are forced into interaction through mechanical allowing [1], but the obtained powder still needs the sintering step to complete the reaction. If some elemental Si is left unreacted during the milling step, then the powder amount used to make the pellet can be deficient in or have excess Si, leading to an inhomogeneous matrix.

As mentioned above, both IM and BM samples were contacted with Cu following the procedure reported in Chapter 3. Figure 6.4 shows SEM images of the cross-sections of Cu-contact IM and BM pellets, as well as local high magnification images of the reaction layers. It can be first observed that our BM sample (Figure 6.4 b) shows a less homogeneous microstructure, with a more demixed matrix and more frequent Mg_2Si -rich areas. In comparison, our IM sample shows a “purer” matrix (Figure 6.4 a). The reaction layers between the TE material and the contacting electrode are comparable in both cases. All interfaces have an inhomogeneous thickness, with local diffusion zones that are $\sim 150 \mu\text{m}$ thick, and the microstructure and possible phases are also similar in both cases. The Mg_2Sn -channels, as reported in 3 with the IM powder, also exist in BM powder as the bright thin horizontal line starting from the right-hand side reaction layer and running inside the TE material. Further explanation to these channels is also provided in Chapter 4.

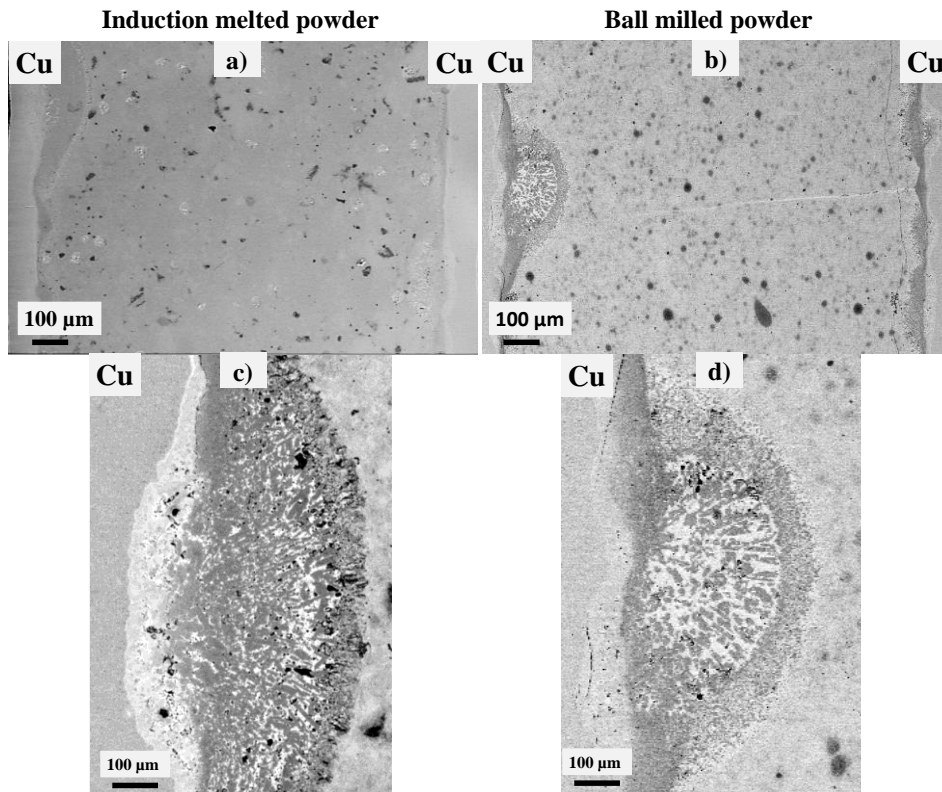


Figure 6.4: SEM images of the cross section of Cu-contacted p-type $\text{Mg}_{1.97}\text{Li}_{0.03}\text{Si}_{0.3}\text{Sn}_{0.7}$ once obtained through a) induction melting and once through b) ball milling. Images c) and d) represent local high magnifications of the interfaces of the contacted induction melted and ball milled pellets, respectively.

However, in the particular case of the IM sample, the SEM image shows different microstructures compared to the BM sample. In fact, the darker Mg_2Si -rich regions have sometimes a thin elongated shape, and new brighter accumulations are observed locally on the IM sample cross section. These bright regions were identified through EDX characterization to be Sn-rich (~ 80%). As they were not observed before joining, they are not a result of the synthesis route, but potentially of the joining experiments. What is meant by joining experiment here is not the process being related to a particular electrode (such demixing into Mg_2Si -rich and Mg_2Sn -rich areas was also observed with other electrodes as reported in Chapter 3 and [4]), but potentially the added “annealing” step during the contacting experiment, as the sample is again subjected to high temperatures (600 °C in case of Cu). To stay within the focus of this study, no further investigations were done here, as there are also other works in our group dedicated to the mixing/demixing of the $\text{Mg}_2(\text{Si},\text{Sn})$ system [1, 37, 156].

Figure 6.4 also shows local SEM images of the reaction layer resulting from the contacting of the IM and the BM powders. A careful investigation of the reaction layers of both samples, with checking each side of the contact areas (interfaces on the left and the right side of the TE pellet), confirmed that the reaction layers are similar. The composition and microstructure of the interface layers in the BM sample is also similar to that of the IM sample, which is already reported in Chapter 3. Figure 6.4 c and d show

zoomed-in regions of the reaction layers of the contacted IM and BM samples, respectively. A half spherical morphology is observed in both cases, which corresponds to the thicker local *diffusion zones* reported in Chapter 3. Such morphology could be due to a localized temperature hotspot where the temperature is higher at certain points of the sample during the joining step, which results in a locally different diffusion mechanism. Unfortunately, a verification of such hypothesis would potentially require a setup with different thermocouples to measure the temperature at different points, which is not easily achievable with our instruments. Another explanation could be the local phase separation of the TE material, as observed before in our work. In fact, different concentrations of Si and Sn in the material would lead to a different chemical environment at the interface, which results in different rates of diffusion-reaction in the contacted zone, as can also be seen from the ternary Cu-Mg-Si and Cu-Mg-Sn phase diagrams [157, 158]. This hypothesis is also supported by ternary and quaternary equilibrium phase diagrams of the Cu-Mg-Si-Sn system [159] and the nature of the used TE material (solid solution of constant Mg content and a miscibility gap [37]).

The similarities between the contacting results of the IM and the BM samples make sense and should be expected because the reaction and diffusion between the materials would mainly depend on the materials themselves, as well as the joining conditions. As the only difference between the IM and the BM samples presented in this work lies in the powder synthesis method, no major differences should be expected if the samples are sintered and then joined under the same conditions.

To conclude this section, this study shows that our IM sample is more homogeneous than our BM sample, and that changing synthesis method does not drastically impact the contacting results. Based on these findings, as well as the advantage of its scalability, the IM procedure was used as the main synthesis route for all the samples used in this work (unless indicated differently).

6.1.2. Effect of electrode treatment

Chapters 3 and 4 of this manuscript reported that contacting Cu with n-type $\text{Mg}_{2.06}\text{Si}_{0.3}\text{Sn}_{0.665}\text{Bi}_{0.035}$ and p-type $\text{Mg}_{1.97}\text{Li}_{0.03}\text{Si}_{0.3}\text{Sn}_{0.7}$ resulted in inhomogeneous reaction layers with uneven thickness that can vary from 30 to 100 μm , with locally thicker diffusion areas $\sim 200 \mu\text{m}$ thick. As an attempt to understand the reason behind such inhomogeneity, and eventually prevent it, I conducted joining experiments where the Cu foil was prepared before contacting. In fact, in the works reported in Chapters 3 and 4, thin Cu foils (50 μm thickness) were mechanically cut into 15 mm diameter disks, then cleaned in ethanol in an ultrasonic bath for 10 min, before being used for contacting. In this case, the obtained disks were wrinkled, as the foil was thin and soft, and only manually flattened, which still kept them not perfectly flat and could have perhaps resulted in locally different reaction layers. In fact, as the wrinkled foil is pressed against the pellet, the surfaces of the foil and the TE material are not perfectly parallel and

physically in contact at every point, which could result in different interactions between them: the reaction and diffusion of one system into the other would occur only at the actual points of contact. The observed continuity of the reaction layers would then result more from the continuous 3D diffusion and growth of the newly formed phases, than from a homogeneous equal diffusion of Cu into $Mg_2(Si,Sn)$ for example. Moreover, as oxide layers can form on the Cu foil surface and some impurities can remain even after the ultrasonic bath treatment, grinding or cleaning of the foils before contacting might be necessary. However, as the used foil in the first study was thin and soft, its handling was not easy, and grinding or cleaning the surface to get rid of such layer wasn't manually manageable, which could have also affected the reaction and diffusion during joining.

For the purpose of this comparative study, thicker Cu foils were used (250 μm thickness) to facilitate foil treatment/cleaning before contacting. The thick foils were also mechanically cut, but the obtained disks were less wrinkled (as shown in Figure 6.5), almost perfectly flat (apart from the edges), as the thick foil is more rigid. After that, the cut disks were manually grinded with ethanol on SiC paper of roughness 1200-micron size, then ultrasound-cleaned in ethanol before joining. The thickness of the foil, as well as its treatment, allowed a more even contact surface between the electrode and the TE material, and a minimized oxide and impurity layer in between. Such conditions are expected to allow a more homogeneous diffusion and reaction between the two materials of interest.

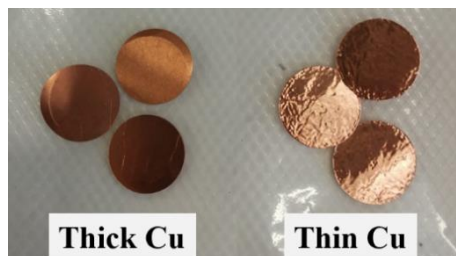


Figure 6.5: Thick (250 μm) and thin (50 μm) Cu disk foils, exhibiting the difference in surface flatness and the presence of wrinkles between them.

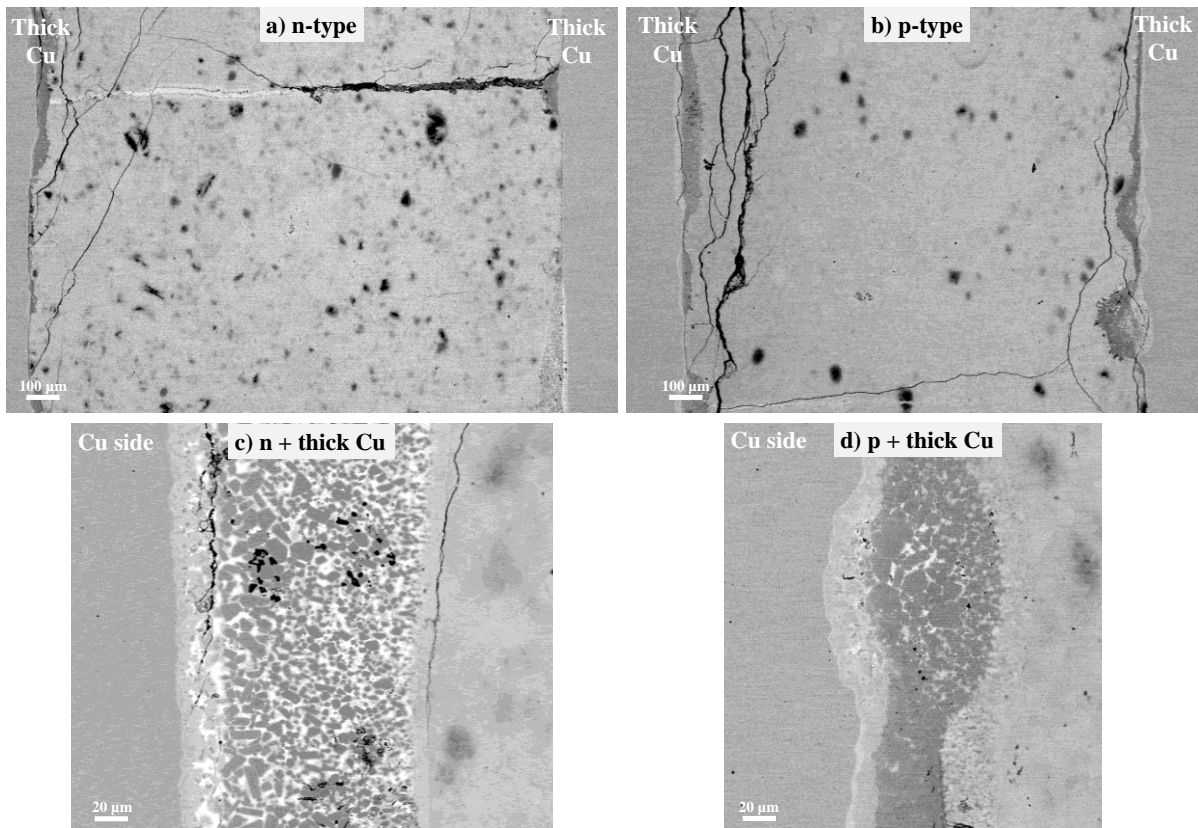


Figure 6.6: SEM images of the cross section of a) n-type $\text{Mg}_{2.06}\text{Si}_{0.3}\text{Sn}_{0.665}\text{Bi}_{0.035}$ and b) p-type $\text{Mg}_{1.97}\text{Li}_{0.03}\text{Si}_{0.3}\text{Sn}_{0.7}$ contacted with thick treated Cu foil. Figures c) and d) represent magnified images of the resulting reaction layers after reaction and diffusion between the treated Cu foil and n- and p-type samples, respectively. The reaction layers are very similar in microstructure and detected phases to the samples for which untreated foils were employed, reported in Chapter 3.

Figure 6.6 a and b show SEM image results of n- and p-type $\text{Mg}_2\text{Si}_{0.3}\text{Sn}_{0.7}$ contacted with thick Cu foil. As can be seen from the figure, both n- and p-type samples have interfaces similar to the ones obtained using thin Cu foil, reported in Chapter 3. Both material types still show the same inhomogeneous reaction layers, with thicker local diffusion zones, which indicates that the potential oxide layer and the wrinkles of the thin foil do not strongly affect the final reaction and diffusion results. SEM/EDX investigations also showed that the reaction layers had similar microstructures with both foil types, as can be seen in Figure 6.6 c and d. In both cases, the reaction layer is mainly composed of the darker segregates corresponding to the τ_1 phase ($\text{Cu}_{1.5}\text{MgSi}_{0.5}$) surrounded by the brighter matrix which is the Mg_2Sn phase, like reported in the previous work in Chapter 3. Therefore, it can be concluded that the treatment as processed here on the thick Cu foils (grinding and cleaning) does not change the contacting results, and that the inhomogeneities in the Cu diffusion and the reaction layer are caused by other reasons which could be the local inhomogeneities of the TE material, local temperature gradients due to a non-homogeneous current distribution, etc.

However, unlike the joining case with thin untreated Cu foil, the samples joined with the treated thick Cu foil contain several cracks growing in different directions across the TE material. The reason behind such behavior is not clearly understood, but, as an attempt, these cracks can be categorized in 3 different groups: (i) cracks inside the TE material, (ii) cracks inside the reaction layer and (iii) filled cracks.

The cracks inside the TE material can be seen in both n- and p-type samples, extending in different directions, parallel to the reaction layers or diagonally inside the TE pellet. Such cracks could occur due to tensile stresses (along the pressing direction) that would expand the material along a direction parallel to the XY plane, which is the plane parallel to the contact surface of the TE material and the pellet. Under these stresses, cracks would grow along the mentioned plane. However, as polycrystalline $Mg_2(Si,Sn)$ behaves as an isotropic material, there is no definite preferred direction for the tensile stresses to cause crack growth [160], which would explain the various growth directions of the cracks inside the TE pellet. In fact, even if tensile stresses cause cracks that remain planar and grow in a 2D array, material impurities (secondary phases, pores...) can divert the planar characteristic of the crack, which would then grow in 3D.

As for the cracks growing inside the reaction layers, a possible explanation would be the CTE mismatch between the Cu foil, the different newly formed phases inside the interface and the TE material. Even though Cu and $Mg_2Si_{0.3}Sn_{0.7}$ have similar CTEs, the new phases would have different CTE and a different behavior under thermomechanical stresses, which would generate cracks. In fact, after the sample system expands during heating (which is also when the new phases would be formed), and as it shrinks during the cooling process, the different regions with different CTE would shrink with different rates, some faster than others, which results in cracking. As the cracks are mostly observed in the region of the interface closest to the Cu foil, like shown in Figure 6.6 a, b and c, this layer containing the γ phase $Cu_{1.55}MgSn_{0.45}$ (as reported in Chapter 3) is then possibly the weakest point among the different layers that would yield to contraction stresses and crack.

Finally, the filled cracks, already reported in Chapters 3 and 4 as “ Mg_2Sn -channels” are actually cracks that either appeared during the early stage of the heating process or began as microcracks in the TE pellet during sintering. These microcracks would have then grown into larger cracks during the contacting step. In fact, these cracks were reported to be mainly filled with an Mg_2Sn -rich phase which is the result of Cu diffusion and reaction with the TE material. Therefore, the cracks either existed in the pellet before joining or grew during the heating step, so that it can later act as a potential channel for the liquified Mg_2Sn -rich phase to infiltrate.

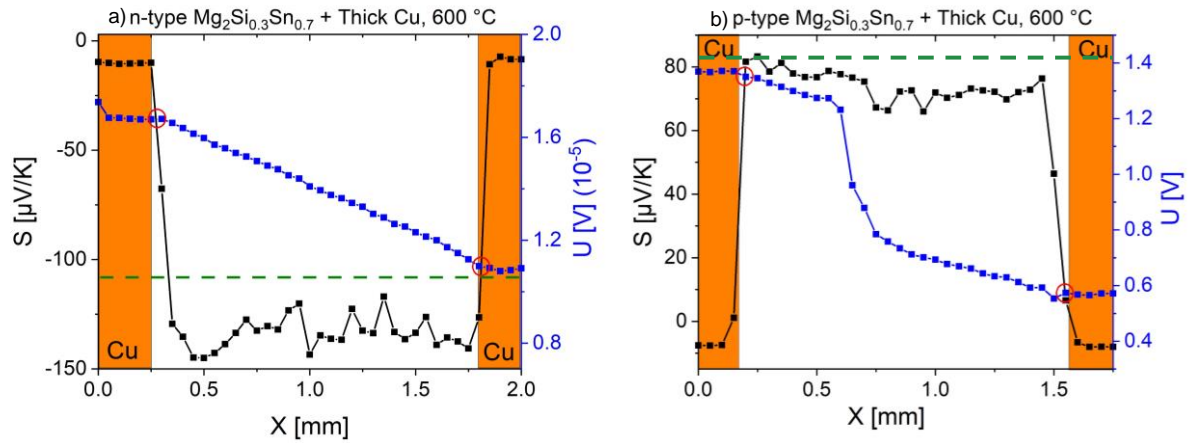


Figure 6.7: PSM line scans of a) n-type $\text{Mg}_{2.06}\text{Si}_{0.3}\text{Sn}_{0.665}\text{Bi}_{0.035}$ and b) p-type $\text{Mg}_{1.97}\text{Li}_{0.03}\text{Si}_{0.3}\text{Sn}_{0.7}$ contacted with thick pre-treated Cu foil. The Seebeck profile lines are shown with the black lines, while the potential across the samples are shown with the blue lines. The green dashed line marks the Seebeck value of the TE materials before contacting.

PSM measurements were also run on the samples contacted with thick Cu foil and results are presented in Figure 6.7. Representative Seebeck and potential line scans of the n-type and p-type sample are given in Figure 6.7. a and b, respectively. Similar to what was reported in the case of the thin Cu foil (Chapter 3), the Seebeck coefficient of the n-type sample contacted with the thick Cu foil changed from $-110 \mu\text{V/K}$ to $\sim -140 \mu\text{V/K}$. This demonstrates that Cu diffuses similarly inside the TE material whether the used foil is treated or not, and fits with the similar results of the reaction layers shown in the SEM images in Figure 6.6. Also fitting to what was reported with the thin Cu foil, no change in the Seebeck coefficient of the p-type sample was observed.

Specific electrical contact resistances r_c were calculated for both material types as explained in Chapter 2.4.2 (using the drops marked with red circles at the interfaces on the potential lines shown in Figure 6.7). As the transitions of the potential line from the Cu foils to the TE material on the left-hand side, as well as from the TE material to the Cu foil on the right-hand side, are smooth and do not display any sudden drop, low r_c are expected. Calculations of r_c do, in fact, show low values $\leq 10 \mu\Omega \text{ cm}^2$ for both material types ($5 \pm 3 \mu\Omega \cdot \text{cm}^2$ for p-type, $7 \pm 4 \mu\Omega \cdot \text{cm}^2$ for n-type). As for the observed drop in the U graph of the p-type sample around the middle of the pellet ($x = 0.6 \sim 0.7 \text{ mm}$), it is most probably caused by cracks inside the TE pellet that would increase the local resistance of the sample.

It can be concluded from this comparative study that the diffusion of Cu inside the $\text{Mg}_2\text{Si}_{1-x}\text{Sn}_x$ system is independent of the here-tested foil treatment (grinding + cleaning) before contacting. Moreover, under sintering pressure and temperature, Cu diffuses easily from the foil inside the TE material in a fast and inhomogeneous way.

The motivation behind joining with the thick foil was that the wrinkles in the thin foils would result in different pressure points on the TE pellet, leading to a different diffusion behavior of Cu and a final reaction layer with different local thicknesses. Another hypothesis was the potential oxide layer that could influence the diffusion of Cu locally, and that would be easier to remove with thicker samples, as they are easier to handle. Nevertheless, even after such foil treatment, the diffusion results were similar to the untreated foil case. The inhomogeneities in the formed reaction layers and diffusion zones could be then related to actual local impurities inside the TE material, as well as micro cracks, as both differ from pellet to pellet, more than the condition of the used foil. As the joining experiments were done under direct current, potential TE material-related impurities could hinder the current flow inside the sample, creating favorable current paths, where the current density would be locally heavier in some regions in the sample more than others. Such behavior could lead to a certain increase in the temperature locally, where the current density is higher, resulting in a potentially different diffusion behavior.

6.1.1 Effect of the sintering current on the contacting results

So far, in this chapter, all joining experiments, similar to the pellet sintering experiments, were done in a direct sinter press (DSP) as explained in Chapters 2.1.3 and 2.2. When the samples are pressed or contacted inside the DSP, a current is driven (in technical current direction) from bottom to top, starting from the lower electrode (under the graphite die containing the sample) through the sample. This current heats the sample and the die around it, and the pressing or the contacting occurs through a *resistive heating* (Joule heating) process. The contacting experiments in Chapter 3 using Cu and Ni₄₅Cu₅₅ electrodes were done following this method where the samples were heated by a Joule heating effect of the samples themselves, as schematically presented in Figure 6.8 a. In this case, the current provided by the lower electrode would pass through the lower graphite leg then the lower graphite piston and would have two potential trajectories to follow: 1) the trajectory through the graphite foil, the metallic electrode, the TE material, then all the way up to the upper piston, 2) the parallel trajectory from the lower graphite piston to the graphite die and then back to the upper graphite piston. As the sample system is maintained under a relatively high pressure (> 20 MPa) during the joining experiments, while the side contact areas between the pistons and the die are not subjected to any particular force or pressure, the first trajectory through the sample is believed to be the one comprising the larger fraction of the current. The exact current distribution actually depends on the conductivities of the involved materials and the resistances at the different interfaces between the different materials in play (see further discussion and equivalent circuits in the Appendix. However, as the electrical interface resistances usually decrease with increasing pressure, it is assumed that the first path is the main heating way to raise the temperature of the system and join the TE material and the electrode. Under these conditions we define the “*direct resistive heating*” process, which mainly occurs through a heating of the sample, yet still contains a

small contribution of the heating from the current crossing the graphite die. However, this second component is neglected for simplicity, and because it is presumably minimal compared to the main heating path through the sample.

On the other hand, as also presented in Chapter 4, the joining experiment can be done using an extra insulating layer introduced somewhere around the sample to block the passage of the electric current from the graphite surroundings to the sample. In the case where the insulating layer is added between the graphite pistons and the sample system as shown in Figure 6.8 b, the electrical current is blocked from following the direct vertical path described as the first trajectory in the case of *direct resistive heating* (paragraph above). The main remaining path for the current to follow would then be the second trajectory through the graphite die, even though the contact surfaces between the piston and the die aren't optimized. In this case, the contacting procedure occurs through an "*indirect resistive heating*" process where the sample is heated by Joule heating effect of the die around it. In all our studies presented in this work, the used insulating layer was a boron nitride (BN) layer added on the inner ends of both pistons as explained in Chapter 2.2.

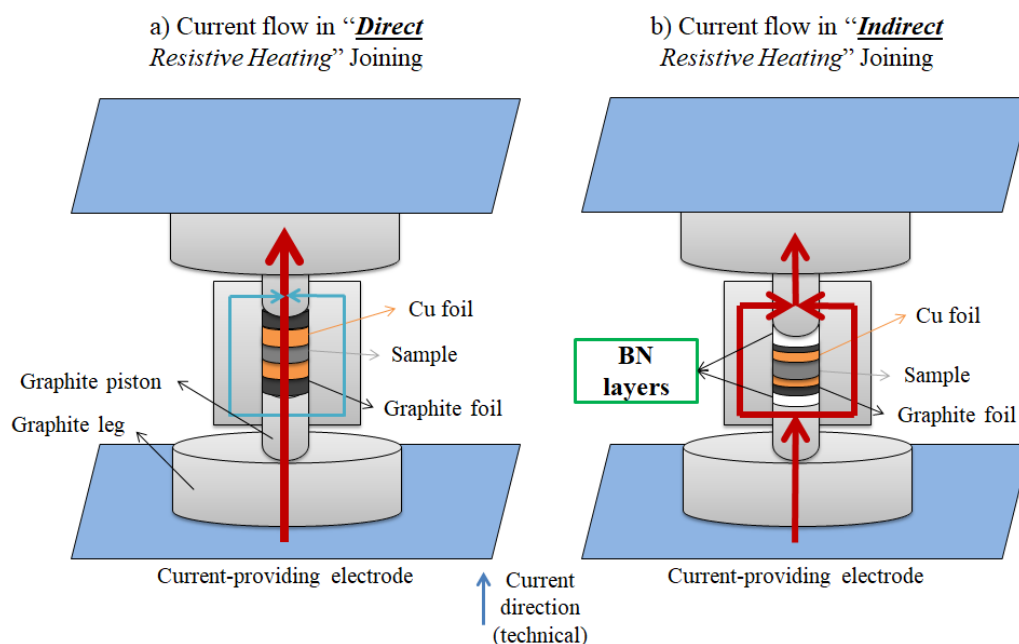


Figure 6.8: Schematic figure to show the idealized current trajectories (colored arrows) across the graphite system and the sample inside it under a) "*direct resistive heating*" and b) "*indirect resistive heating*" joining conditions. The red arrows show the main path of the current under each joining condition. In a), the blue arrows show a secondary potential current path, but with a smaller current fraction than the main path (red arrow). In b), boron nitride (BN) layers are added above and below the sample to block the current from running through it.

A practical limitation of the intended and idealized *indirect resistive heating* process outlined above could be the secondary current trajectories that would go from the surrounding graphite die back towards

the sample system (electrode + TE material). However, practically, this path includes contact surfaces between different materials (graphite-electrode, graphite-semiconductor, etc.) which in turn involve added contact resistances, making this path more resistive compared to simply flowing through the same graphite block (die). So, even though part of the current distribution would go back through the sample again, the major portion would still follow the trajectory through the graphite die. Thus, we can still assume a standing *indirect resistive heating* process with (almost) no current running through the sample.

In this section, we aim to continue the study started in Chapters 3 and 4 where we tried to investigate the potential effect of the DSP sintering current on the contacting results of n- and p-type $\text{Mg}_2\text{Si}_{0.3}\text{Sn}_{0.7}$ with Cu and $\text{Ni}_{45}\text{Cu}_{55}$ electrodes. In Chapter 3, joining results showed a strong diffusion of both electrode materials into the TE material. As these contacting experiments were done under *direct resistive heating* conditions, the resulting reaction layers and formed phases could be due to both temperature-induced diffusion and electromigration. The former would be the result of a simple difference in concentrations that leads to the diffusion of one material into the other and would be enhanced under the effect of an increase in temperature. On the other hand, the latter would occur as ions from one material are transported into the other, after part of the momentum of the moving current electrons is transferred to said ions. As the difference between *direct* and *indirect resistive heating* (as explained above) resides mainly in the electrical current passing through the sample, it is safe to assume that in the first case (*direct*), electromigration is more prone to occur, as the electrons cross the sample system. On the other hand, in the second case (*indirect*), it is also safe to assume that electromigration would not occur as much, and that the chemical diffusion of the elements would be the main process for material transport. As Chapter 4 already discussed the comparison between both joining conditions using Cu as an electrode, we provide here a preliminary comparison between *direct* (Chapter 3) and *indirect* (this section) contacting results of $\text{Ni}_{45}\text{Cu}_{55}$. The experimental conditions of the *indirect resistive heating* joining were the same as the *direct resistive heating* joining (550 °C, 10 mins), and the results are briefly introduced below. Further discussions are introduced in the Appendix of this thesis.

SEM/EDX analysis was utilized to investigate the microstructure of the contacted samples as well as the reaction layers formed between the electrodes and the TE material. Figure 6.9 shows SEM images of two n-type (a and c) and two p-type (b and d) samples contacted with $\text{Ni}_{45}\text{Cu}_{55}$ under *direct* and *indirect resistive heating* conditions, respectively.

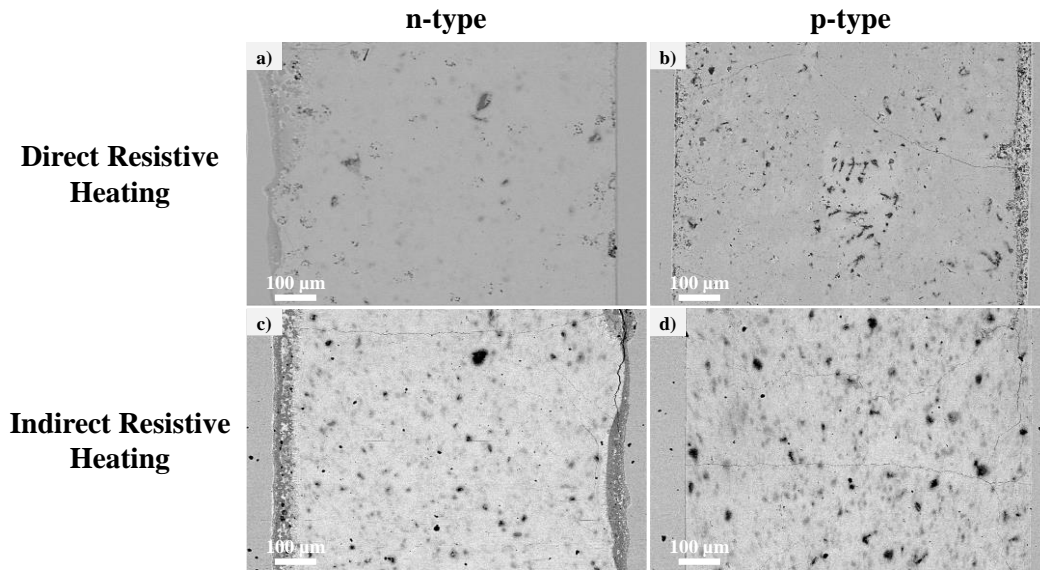


Figure 6.9: SEM images of Ni₄₅Cu₅₅-contacted n- and p-type Mg₂Si_{0.3}Sn_{0.7} a) and b) under direct resistive heating respectively, and c) and d) under indirect resistive heating, respectively.

On first glance, the microstructures of all joined TE materials is similar. The *indirectly* joined samples (shown in Figure 6.9 c and d) have an apparently more demixed TE material matrix compared to the *directly* joined samples, under the utilized SEM technical conditions of brightness and contrast. However, such strong demixing was already seen in several occasions with different electrodes [4, 150], as well as in non-contacted Mg₂Si_{1-x}Sn_x samples due to the miscibility gaps in the solid solution [37, 97]. Therefore, the demixing observed here might not be strongly correlated to the current, but could be more related to experimental variations and the initial powder selected during pellet sintering [37]. All samples also contain cracks growing in different directions, with the *indirectly* joined samples showing more cracks than their *directly* joined counterparts.

As for the reaction layers, three out of the four samples show thick interfaces (50 ~ 100 μm) that are visible already at the given magnifications. In fact, both samples joined under *direct resistive heating* (Figure 6.9 a and b) and the n-type sample joined under *indirect resistive heating* (Figure 6.9 c) have these visible reaction layers. The p-type sample joined under *indirect resistive heating* conditions (Figure 6.9 d), however, has a very thin reaction layer growing between the electrode and the TE material. An EDX investigation of the microstructure (layers, phase composition) of the reaction layers was conducted and results showed that the samples joined under *indirect* joining conditions have a similar interface composition as the samples joined under *direct* joining conditions (Chapter 3). The thin interfaces from the *IRH* samples also have a similar composition to the thin interfaces observed in the *DRH* samples from Chapter 3. Figures and an attempt to a further analysis on e.g. the asymmetry in layer thickness are provided in the Appendix.

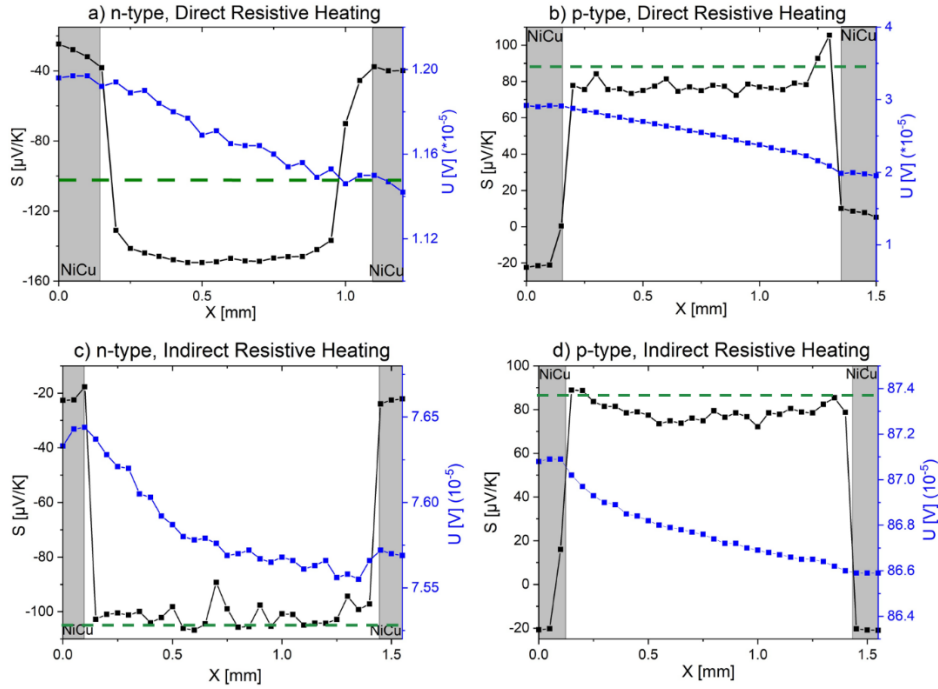


Figure 6.10: PSM line scans of n- and p-type $\text{Mg}_2\text{Si}_{0.3}\text{Sn}_{0.7}$ contacted with $\text{Ni}_{45}\text{Cu}_{55}$ under a) and b) direct, c) and d) indirect resistive heating. The black lines represent the Seebeck profiles of the samples and the blue lines represent the potential across the samples. The green dashed lined mark the Seebeck value of the TE material before contacting.

Figure 6.10 shows PSM measurements of Seebeck and potential profiles on n- and p-type $\text{Mg}_2\text{Si}_{0.3}\text{Sn}_{0.7}$ contacted with $\text{Ni}_{45}\text{Cu}_{55}$ under both *direct* and *indirect resistive heating*. The results of the direct resistive heating joining experiments are discussed in Chapter 3. Looking at the Seebeck profile lines (in black), an interesting feature can be seen in Figure 6.10 c: there is no change in the Seebeck value in the n-type sample joined under *indirect resistive heating*, unlike the case of direct resistive heating reported in Chapter 3 and shown in Figure 6.10 a. As SEM/EDX investigations showed similar microstructure results in both joining cases, this change of TE properties is presumably not related to a diffusion of the electrode elements inside the TE material. Instead it is believed to be the electromigration of charged point defects of Cu and Ni under the effect of the sintering current, and these charged defects would change the initial charge carrier concentration of the TE material. Such change in the carrier concentration would be recorded by the PSM instrument as a change in the Seebeck coefficient. Here, we could be possibly seeing the implication of electromigration and the influence of the electrical current. In fact, the effect of defect diffusion is different from the effect of diffusion of the elements, as already seen in the work of Pham *et al.*, where the authors reported a change in the TE properties on the whole thickness of the sample (~ 1.2 mm) after joining with Ag, while having a reaction layer < 10 μm thickness [4]. Further discussion about the implication of charged point defects in the contacting procedure (using Cu and Ni) and their potential interactions with the defects of n- and p-type $\text{Mg}_2(\text{Si},\text{Sn})$ systems are presented in Chapter 6.2.

As for the electrical contact resistance, a first overview of the graphs on Figure 6.10 shows smooth transitions without sudden drops at the interfaces between the electrode foils and the TE material. Therefore, the calculated specific electrical contact resistance r_c values are expected to be low. Using Equation 2.4 and Equation 2.5 of Chapter 2, the obtained r_c values for the *indirect resistive heating* samples are presented in Table 6-1. Equation 2-4 utilizes the current value as provided by the PSM output file, while Equation 2-5 utilizes the current density value as calculated using the TE properties of the studied sample. The results of the *direct resistive heating* as reported in Chapter 3 are also added in the table for an easy comparison.

Table 6-1: Specific electrical contact resistance r_c for n- and p-type joined with Ni₄₅Cu₅₅ under direct and indirect resistive heating conditions. The results were calculated using Equation 2.4 (with j_{PSM}) and Equation 2.5 (with $j_{\text{TE-props}}$), and the relative measurement uncertainty is the standard deviation of all PSM potential line scans for each samples.

Joining Conditions	r_c ($\mu\Omega$ cm ²) (Equation 2.4, j_{PSM})		r_c ($\mu\Omega$ cm ²) (Equation 2.5, $j_{\text{TE-props}}$)	
	n-type + Ni ₄₅ Cu ₅₅	p-type + Ni ₄₅ Cu ₅₅	n-type + Ni ₄₅ Cu ₅₅	p-type + Ni ₄₅ Cu ₅₅
<i>Indirect</i>	6 ± 5	13 ± 11	40 ± 25	11 ± 9
<i>Direct</i>	4 ± 3	15 ± 8 (left-hand side) * 73 ± 36 (right-hand side) *	24 ± 17	11 ± 6 (left-hand side) * 53 ± 26 (right-hand side) *

* The explanation for the separate measurements is provided in Chapter 3.

As can be seen from Table 6-1, the results for r_c calculated using both equations (horizontal comparison, light green columns) are comparable in both the cases of *direct* and *indirect* joining conditions for the case of the p-type samples. However, the values are different in the case of n-type samples (horizontal comparison, light blue columns). In fact, while the r_c calculated using Equation 2.4 for both joining conditions are $< 10 \mu\Omega$ cm², the r_c calculated using Equation 2.5 for both joining conditions are $> 20 \mu\Omega$ cm². In Chapter 3, such distinction in the values was explained by the presence of the “Mg₂Sn diffusion channels” that are $\sim 100 \mu\text{m}$ thick and that initiate from one interface to the other, running through the entire thickness of the TE material. As these channels are believed to contain mainly metallic phases, they would create a short circuit in their vicinity during the PSM measurement and disturb the current flow, which increases uncertainties in the measurements. Therefore, in this case, the r_c values obtained using Equation 2.5 are considered as more reliable.

Furthermore, comparing the r_c results for the *direct* and *indirect* joined samples obtained from the same equation (vertical comparison), the results are comparable. The r_c values for the n-type samples obtained from Equation 2.4 are similar within the error bars for both *direct* and *indirect* conditions. The results are also the same using Equation 2.5, also for n-type samples under both current conditions. Using Equation 2.4 or Equation 2.5 for the p-type samples give slightly different results as the numbers are not

divided into right-hand side and left-hand side for the *indirect* joined case; both are, in fact, similar and do not need to be separated as the reaction layers on both side are also comparable. Nevertheless, the r_c values for the *indirect* joining conditions are similar to the values obtained on the left-hand side values of the *direct* joining conditions; the right-hand side values are much higher. As stated under Table 6-1, the explanation to the separation of the r_c results into left and right is provided in Chapter 3.

From the available experimental data, and within the scope of our defined *direct* and *indirect* joining experiments, we can conclude that the sintering current plays a more prominent role in the contacting of $\text{Mg}_2\text{Si}_{0.3}\text{Sn}_{0.7}$ with $\text{Ni}_{45}\text{Cu}_{55}$ compared to contacting with Cu (Chapter 4). In both electrode cases, the current did not seem to have a strong influence on the interface layer and the microstructure. However, when looking at the TE properties of the joined samples (PSM results), while Cu displayed similar results for all sample types under both current conditions (change of S for n-type, no change of S for p-type), joining with $\text{Ni}_{45}\text{Cu}_{55}$ resulted in different TE properties of the n-type materials joined under *direct* (change of S) and *indirect* (no change of S) conditions. The p-type samples contacted with $\text{Ni}_{45}\text{Cu}_{55}$, though, had similar results under both current conditions (no S change). Such difference in the results could be either related to the electromigration of the charged point defects of the electrode materials into the TE material or related to the influence of the Mg loss (Mg vacancies that are electron acceptor defects) on the charge carrier concentration.

As for the difference in results between Cu and $\text{Ni}_{45}\text{Cu}_{55}$, Mg vacancies might be expected to have higher density for the Cu-joined samples compared to the $\text{Ni}_{45}\text{Cu}_{55}$ -joined samples, as the contacting with Cu is done at 600 °C, while that with $\text{Ni}_{45}\text{Cu}_{55}$ is done at lower temperature (550 °C). Thus, the concentrations of the main defects in the systems could be different, which would lead to different charge carrier concentrations (hence Seebeck value). Another reason could be a potential Cu-Ni interaction that would also change the stability of the material and their contribution to the carrier concentration.

More about the implication of defects in experimental joining results is introduced in the next sections of Chapter 6.2 and the Appendix.

6.1.2 Summary of Chapter 6.1

Chapter 6.1 was intended as a set of experiments to help understand the inhomogeneity in the contacting results of n- and p-type $\text{Mg}_2\text{Si}_{0.3}\text{Sn}_{0.7}$ with Cu and $\text{Ni}_{45}\text{Cu}_{55}$, concerning both the interface thickness and its layering/microstructure, as well as the demixed TE matrix. The first experiment started by comparing two samples that were produced with different synthesis methods – ball milling vs induction melting – then pressed into pellets and contacted with Cu foil under the same conditions. In the second experiment, two induction-melted samples were used and they were contacted with two different Cu foils – thin Cu

foils that were stacked as-used without any treatment vs thick Cu foils that were grinded and cleaned before joining. However, the joining conditions (temperature, time, pressure) remained the same. In the last experiment, in order to complete Chapters 3 and 4 where a study to understand the implication of the sintering current on the contacting results of Cu was provided, the same comparative method was followed and induction melted n- and p-type $\text{Mg}_2\text{Si}_{0.3}\text{Sn}_{0.7}$ with $\text{Ni}_{45}\text{Cu}_{55}$ foil were contacted under *indirect resistive heating conditions* (where a layer of resistive boron nitride was added in an attempt to block the sintering current from passing through the sample system).

The conclusions reached based on the presented experiments can be summarized as follow:

- Our tested induction melted sample was more homogeneous than our ball-milled sample, therefore induction melting was utilized as the main synthesis route for this work.
- The powder synthesis route did not influence the contacting results of our tested samples (case of p-type $\text{Mg}_2\text{Si}_{0.3}\text{Sn}_{0.7}$ with Cu).
- The electrode treatment as processed and described in Chapter 6.1.2 did not influence the contacting results of induction melted $\text{Mg}_2\text{Si}_{0.3}\text{Sn}_{0.7}$ with Cu.
- From a microstructure perspective, the sintering current did not have a visible influence on the contacting results of $\text{Mg}_2\text{Si}_{0.3}\text{Sn}_{0.7}$ with $\text{Ni}_{45}\text{Cu}_{55}$, under our described conditions of *direct* and *indirect resistive heating*.
- The major difference between the presented $\text{Ni}_{45}\text{Cu}_{55}$ -contacted $\text{Mg}_2\text{Si}_{0.3}\text{Sn}_{0.7}$ samples was observed in the case of the n-type samples, where a change in the Seebeck coefficient was observed under *direct resistive heating* conditions, while no such change was recorded in the sample joined under *indirect resistive heating* conditions. Such results were correlated with a potential diffusion of charged point defects that would occur as electromigration under the effect of the sintering current, and result in a change in the charge carrier concentration (hence the Seebeck value) of the TE material. However, when the sintering current is blocked from running through the sample, the electromigration-induced defect diffusion is not expected to occur as much.
- Our introduced *indirect resistive heating* method contains some limitations and should be improved to have more conclusive results concerning the influence of the sintering current. Nevertheless, it is plausible as presented for preliminary tests, and the obtained results could be used as a starting point for further studies.

6.2 On the relevance of electrode-induced charged point defects in the contacting of Mg₂(Si,Sn)

In this work, we discuss contacting results of previously mentioned electrodes (Cu, Ni and Ni₄₅Cu₅₅) from a novel perspective, which is the perspective of charged point defects. In particular, the focus will be on the electrode-induced charged point defects in the TE material and their interplay with the material's intrinsic and dopant defects. In fact, as can be seen from the equation $n_c - n_v = \sum_{D,q} q n(D^q)$ [140], where n_c and n_v are the electron and hole densities at the conduction bands and the valence bands respectively, and $n(D^q)$ is the density of the defect D of charge q , any change in the material's intrinsic or extrinsic defects (density or charge) results in a direct change in the charge carrier concentration. Therefore, the influence of the electrode-related defects on the carrier concentration of the material needs to be investigated as it would, in turn, influence the TE properties of the optimized material.

Such perspective was, to the best of my knowledge, never considered in contacting studies before, yet it is of high practical relevance. We utilized this perspective in our recent work reported in Chapter 5 using the example of Ag as a contacting electrode for the Mg₂(Si,Sn) system, and established the validity of involving calculations of defect formation energies in the contacting procedure. The same method will be employed throughout the following section where we aim to expand it to more electrodes.

In this work, results of the hybrid-DFT calculations [140] for the formation energies of the defects of several electrode materials in Bi-doped and Li-doped Mg₂Si and Mg₂Sn binaries are provided. These calculations were performed by our collaborators Dr. Byungki Ryu, Dr. Sungjin Park and Dr. SuDong Park at the Korea Electrotechnology Research Institute (KERI), while the interpretation and comparison with experimental data was done together with our group in DLR. In this entire section of the chapter, temperature values will be given in Kelvin (K).

As Chapters 3 and 4 provide contacting results of Mg₂Sn_{1-x}Sn_x with Cu and Ni₄₅Cu₅₅, hybrid-DFT calculation results for Cu and Ni will be discussed. Results for a third material, namely Ti, are also provided further in the Outlook section. Even though the experiments were done on the solid solution composition with 30% Si and 70% Sn, the calculations were carried out for the Mg₂Si and Mg₂Sn binaries for simplicity. It was already shown in Chapter 5 that, for prediction purposes, such comparison using the binaries holds, and that the interpolation for the ternary compositions in between can be approximated and can be expected to hold [140].

Calculation results for the electrode Ni₄₅Cu₅₅ were also studied as an attempt to investigate the validity of approximating an alloy material by its individual elements. In fact, the hybrid-DFT calculations here were not done using Ni₄₅Cu₅₅ as an alloy; instead, the results of the single elements were put together

and discussed as such. However, as this is just a preliminary study, the results are provided in the Appendix, and not in the main manuscript.

Within this study, the band gaps of the Mg₂Si and Mg₂Sn systems were calculated using hybrid-DFT and reported in Chapter 5 as 0.57 eV and 0.145 eV, respectively. The calculations of the defect formation energies were done using Equation 2.11:

$$E_{\text{form}}(D^q, \text{Mg}_2\text{X}) = E_{\text{tot}}[D^q] - E_0 - \sum_j \mu_j \Delta n_j + q(E_F + E_{\text{CBM}}).$$

As can be seen from this equation, the formation energy of a certain defect $E_{\text{form}}(D^q, \text{Mg}_2\text{X})$ depends not only on the total energies of the supercell with ($E_{\text{tot}}[D^q]$) and without (E_0) the defect, or the Fermi level E_F and the energy of the conduction band minima (E_{CBM}); it also closely depends on the chemical potential of the elements μ_j , where j is the atomic species in the supercell. This last term –among others– presents a general source of uncertainties in DFT calculations and discrepancies when comparing with experiments, as knowing the correct experimental chemical potential of a certain material is not straightforward [161].

The phase chemical potential sensitively relates to the actual element concentrations in the lattice as an element – therefore a defect – is added or removed. The knowledge of these actual concentrations is not a given. μ also depends on the new potential phases that grow as a result of reaction and diffusion between the materials of interest, as these phases will determine the chemical potential needed for the atoms to move around. Experimentally, this issue can be faced during contacting experiments where new phases would form between the TE material and the metallic electrode. Such exact information is not conspicuous, and cannot be easily determined. Therefore, correct atomic chemical potential values cannot be easily obtained.

DFT calculations are done at 0 K and assuming the defects and the environment phases to be in equilibrium. Under these conditions, a certain phase chemical potential is determined and used as reference for the calculations. Depending on the results of the formation energies, the reference phase chemical potential is modified until realistic formation energy results are obtained (in case of highly negative numbers, for example). After comparison and verification with experiments, if a match is obtained, the chemical potential used as reference for the calculations would be close to the experimental chemical potential of the studied sample. In case of a mismatch, this does not indicate that the DFT calculations are wrong; rather, they are just describing a different picture from what the experiment presents.

In general, DFT calculations, including hybrid-DFT, can only suggest approximations, which can be optimized to some extent, but will always carry certain errors and inaccuracies. Therefore, it is important to keep in mind that the calculation results discussed in this section are predictions, good but not exact,

and that the degree of correctness is case-dependent. Further explanation about the utilized hybrid-DFT method is provided in Chapter 2.6 and in the literature [111, 140].

Another important point to keep in mind is that, in this work, we calculate the formation energies of defects without considering potential interactions between them, i.e. only isolated defects are considered. When the electrostatic interaction between defects of opposite signs is considered, the real density of the counter-defect will be higher than our expectations based on the as above-calculated formation energies.

In the provided calculation results, Li is used as the p-type dopant and Bi as the n-type dopant. The formation energies are also calculated under two different chemical potential conditions: Mg-poor conditions and Mg-rich conditions. To stay close to the scope of technological applicability, only the calculation results under Mg-poor conditions are presented for the p-type samples. In fact, the p-type conduction is obtained by Li incorporation, where Li is aimed to substitute Mg (the composition would be $\text{Mg}_{2-x}\text{Li}_x$) and form the hole donor Li_{Mg} defect. However, as Li interstitials (I_{Li}) are stable defects with low formation energies, a fraction of the incorporated Li would be “lost” as I_{Li} instead of Li_{Mg} , and the final composition would be deficient in Mg.

As for the n-type samples, both Mg-poor and Mg-rich chemical potential conditions are presented and discussed, as the samples are initially synthesized with 3 at% excess Mg and the n-type conduction is obtained through Bi substituting Si/Sn (explained in Chapter 2). Therefore, unlike the p-type samples, n-type samples start with a higher concentration of Mg versus the stoichiometric composition. The samples are then under Mg-rich conditions. However, Mg is known to be volatile and to easily evaporate under high temperatures [162, 163]. As the samples are subjected to a first sintering at 973 K then a joining at 873 K, Mg losses can be expected, but cannot be measured. Therefore, the final samples could end up with an Mg concentration much lower than the stoichiometric amount, and would potentially be under Mg-poor conditions. This uncertainty in the final Mg content in the experimentally studied samples is the reason behind considering hybrid-DFT calculations results under both Mg chemical potential conditions.

Chapter 6.2.1 provides the hybrid-DFT results of Cu and how they could explain and correlate to the experimental data. Chapter 6.2.2 provides the calculations for the defects of Ni along with a comparison with previous contacting experiments from the literature [5, 68] as well as unpublished contacting results. Chapter 6.2.3 provides an overview on the presented results (Ag, Cu, Ni) and whether the data from experiments and calculations match. A discussion on the viability of involving hybrid-DFT predictions as a first screening tool in the pre-selection of contacting electrodes is also provided. Finally, Chapter 6.2.4 further discusses the potential limitations of the comparative method utilized here and in Chapter 5 and concludes the section.

6.2.1 Cu defects in Li and Bi-doped Mg₂Si and Mg₂Sn

As reported in Chapter 3 and 4, Cu was contacted with Bi-doped and Li-doped Mg₂Sn_{0.3}Sn_{0.7} at 873 K, under different current conditions (*direct resistive heating* and *indirect resistive heating*, explained and reported in Chapter 4), then annealed for 7 days at 723 K. In all situations, a change in the TE properties of the n-type Bi-doped samples was recorded, while no such behavior was observed for the p-type Li-doped samples. In fact, the Seebeck value of the n-type after contacting shifted from $-110 \mu\text{V/K}$ to $-160 \mu\text{V/K}$, then changed even more to $-220 \mu\text{V/K}$ after annealing. The Seebeck value of the p-type sample remained constant at $\sim 90 \mu\text{V/K}$ at all times, even after thermal treatment.

A similar behavior was observed in [4] where the Seebeck coefficient of only n-type samples changed after joining with Ag (no change in S of p-type), and this observation was the starting point for the study reported in Chapter 5 of this manuscript. In this particular study, the change in the TE properties after contacting was related to the diffusion of Ag charged point defects into the Mg₂(Si,Sn) system, causing a change in the system's carrier concentration, which was then detected as a change in the Seebeck profile. In fact, the Ag substitution of Mg defect (Ag_{Mg}) diffuses through interstitial sites of the matrix, and, as it is an acceptor defect of charge $1-$, it captures the free conduction electrons provided by Bi on the Si/Sn sites ($\text{Bi}_{\text{Si/Sn}}$ defect which is a donor of charge $1+$). These two defects of opposite charges have comparable formation energies in the vicinity of the conduction band minimum (CBM), which results in similar defect densities, thus causing a remarkable compensation of the charge carriers.

Hybrid-DFT calculations of the defect formation energies of Cu with Mg₂Si and Mg₂Sn

The formation energies of the charged point defects of Cu in the Li- and Bi-doped Mg₂Si and Mg₂Sn systems were calculated and results are reported in Figure 6.11. In this figure, only the relevant defects (with formation energies $E_{\text{form}} < 1 \text{ eV}$) are represented.

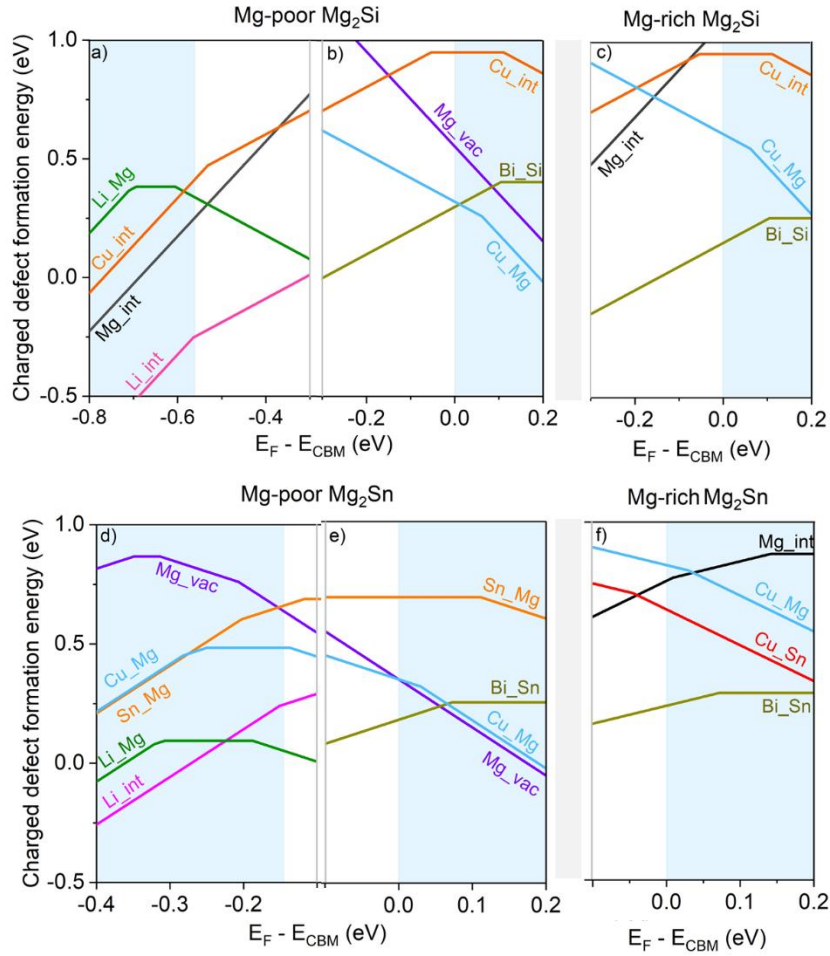


Figure 6.11: Charged defect formation energies of Cu in: a) Li-doped and b) Bi-doped Mg_2Si under Mg-poor conditions c) Bi-doped Mg_2Si under Mg-rich conditions, d) Li-doped and e) Bi-doped Mg_2Sn under Mg-poor conditions f) Bi-doped Mg_2Sn under Mg-rich conditions. For simplicity, the Li-doped Mg_2Si and Mg_2Sn are only represented in the Fermi level region around the VBM while the Bi-doped samples are represented in the Fermi level region around the CBM. The labeling X_Y of the defects (where X and Y are chemical elements) on the figure correspond to the X_Y labeling in the text. X_{int} and X_{vac} correspond respectively to I_X and V_X.

Figure 6.11 a, b and c show the defect formation energies for the Mg_2Si system for Mg-poor p-type, Mg-poor n-type and Mg-rich n-type, respectively. Even though the technological realization of sufficiently highly doped p-type Mg_2Si is limited due to the Fermi level E_F that is pinned inside the band gap, a discussion of this sample can be useful to help establish a good interpolation base for the different solid solutions of Mg_2Si and Mg_2Sn . As can be seen in Figure 6.11 a, the most stable defect in the vicinity of the valence band maximum (VBM) and further inside the band gap is the Li interstitial defect (I_{Li}). It is an electron donor defect of charge $q = 2+$ and $1+$ for electrochemical potentials below and above VBM ($E_F = -0.57$ eV) respectively. The next stable defect is the Mg interstitial (I_{Mg}), which is also an electron donor defect of charge $2+$. These two defects agree with the experimental difficulties in synthesizing efficient p-type Mg_2Si , which do not allow to reach a sufficiently high carrier density. The p-type conduction that is supposed to be provided by the Li on Mg sites (Li_{Mg}) cannot successfully be achieved to the required extent because of the relatively high formation energy of the defect (~ 0.34 eV

at VBM) compared to the formation energies of (I_{Mg}) and I_{Li} (0.25 eV and -0.25 eV, respectively, both at VBM) (see also experimental results in [36, 58]). As for Cu, the most stable related defect in p-type Mg_2Si in the vicinity of the VBM is the Cu interstitial I_{Cu} , but it also has a much higher formation energy, which indicates its low stability compared to the other defects, and correspondingly a low density. Therefore, I_{Cu} can be expected to have a very minor effect on the overall charge carrier concentration, far below the experimental detection limit by Hall measurements or PSM measurements.

As for Bi-doped Mg_2Si , the Mg poor conditions are represented in Figure 6.11 b, while the Mg rich conditions are represented in Figure 6.11 c. Under Mg-poor atmosphere (Figure 6.11 b), the most stable defects in the vicinity of CBM are Bi_{Si} and Cu_{Mg} . Bi_{Si} is the main defect behind the experimentally intended n-type conduction, with each Bi atom on an Si site providing one electron, while Cu_{Mg} is a 1- acceptor defect, with each Cu atom at the Mg site trapping one electron. The formation energies of both mentioned defects are very comparable at CBM: 0.29 eV for Bi_{Si} and 0.32 eV for Cu_{Mg} . A comparable density for both defects would also then be expected. As the former is an electron donor (1+) and the latter an acceptor (1-), charge carrier compensation is expected to occur between these two defects for n-type samples with a chemical potential around the CBM.

If we look at highly doped n-type samples ($E_F \sim 0.05$ eV), the formation energy of Cu_{Mg} is 0.27 eV while that of Bi_{Si} is 0.35 eV. In fact, for Fermi levels higher than $E_F = 0.01$ eV, Cu_{Mg} becomes more stable than Bi_{Si} . Therefore, under such chemical potential condition, Cu is expected to trap even more Bi-provided conduction electrons than it did at E_{CBM} , causing an even stronger compensation of the charge carriers. For such highly doped samples, Mg vacancies (V_{Mg}) also have low formation energies. V_{Mg} is an acceptor defect with charge 2- and $E_{form} = 0.45$ eV at $E_F = 0.05$ eV, which makes its effect on the charge carrier concentration small but not negligible. To have a better idea on the impact of each defect on the carrier concentration, we can consider the defect density equation [140]

$$n(D^q) = N_0 \exp\left(-\frac{E_{form}}{k_B T}\right),$$

with $N_0 = n_{latt} \theta_{deg}$

where N_0 is the total density of possible sites that can form a certain defect D with a charge state q , n_{latt} is the number density of available lattice sites and θ_{deg} is the number of degrees of internal freedom of a defect on a lattice site or the number of equivalent ways to form a certain defect at a particular site [164-166]. In our case, we assume that there is a unique atomic structure per defect at a certain lattice site, therefore $\theta_{deg} = 1$. From this equation we can calculate the densities for each defect and compare them to have a better idea on their interplay. As n_{latt} depends on the defect type, in the Mg_2X conventional cubic cell with 8 Mg atoms, 4 X atoms and 4 interstitial sites, and where $V = a^3$ and $a = 6.35$ Å for Mg_2Si and $a = 6.75$ Å for Mg_2Sn , we would have

	Mg ₂ Si	Mg ₂ Sn
V	$2.6 \times 10^{-22} \text{ cm}^3$	$3.1 \times 10^{-22} \text{ cm}^3$
$n_{latt}(\text{defects on Mg sites}) = 8/V$	$3.1 \times 10^{22} \text{ cm}^{-3}$	$2.6 \times 10^{22} \text{ cm}^{-3}$
$n_{latt}(\text{defects on X sites}) = 4/V$	$1.6 \times 10^{22} \text{ cm}^{-3}$	$1.3 \times 10^{22} \text{ cm}^{-3}$
$n_{latt}(\text{defects on interstitial sites}) = 4/V$	$1.6 \times 10^{22} \text{ cm}^{-3}$	$1.3 \times 10^{22} \text{ cm}^{-3}$

In this example (Bi-doped Mg₂Si, Mg-poor, $E_F = 0.05 \text{ eV}$), using $k_B = 8.62 \times 10^{-5} \text{ eV/K}$ and $T = 873 \text{ K}$ as being the joining temperature for the experimental study of Cu and Mg₂Si_{1-x}Sn_x (Chapter 3), we would have $n(D^q) = 1.53 \times 10^{20}$ for Bi_{Si}, $n(D^q) = 8.53 \times 10^{20}$ for Cu_{Mg} and $n(D^q) = 7.5 \times 10^{19}$ for V_{Mg}. Therefore, under these conditions, Cu_{Mg} and V_{Mg} are expected to cause a strong combined compensation of the conduction electrons provided by Bi_{Si}. Experimentally, we would be recording a strong change in the Seebeck coefficient of the TE material under the discussed conditions, if Cu dissolves in a before pure Bi-doped Mg₂X system.

For Bi-doped Mg₂Si under Mg rich conditions presented in Figure 6.11 c, Bi_{Si} is the most stable defect in the whole range of chemical potential $E_F = -0.2 \text{ eV}$ to $E_F = 0.1 \text{ eV}$, with formation energies ranging from -0.04 to 0.25 eV in the mentioned chemical potential window. Under these conditions too, Cu_{Mg} is also the most stable Cu-related defect; however, its formation energy is much higher than under Mg poor (0.61 eV at CBM and 0.56 eV at $E_F = 0.05 \text{ eV}$). V_{Mg} defects have a very low probability of occurrence as we are under Mg-rich conditions, and the most relevant defect in this case is I_{Cu}. However, I_{Cu} is a neutral defect in the vicinity of CBM ($q = 0$), which indicates that this defect would have an insignificant influence on the total charge carrier concentration. Thus, under Mg-rich conditions, Cu defects are not expected to influence the charge carrier concentration in a relevant manner in the here-relevant chemical potential range. Therefore, unlike under Mg-poor conditions, we wouldn't be observing significant changes in the TE properties for samples synthesized and contacted with Cu under Mg-rich conditions. The electrode-related defects would not severely affect the stability of the other material defects (intrinsic + dopant).

From the analysis of the calculated defect formation energies, it can be clearly concluded that the Cu-related defect densities, and presumably also their diffusion in n-type Mg₂Si [167], is strongly related to the Mg environment. As the most stable Cu defect is Cu_{Mg} under all conditions (n- & p-type, Mg- rich and poor), it makes sense why the Cu diffusion and the Cu-related defect density would depend on the Mg chemical conditions. When Mg loss is intensified, Cu occupying the Mg vacant sites would be more energetically probable, causing, therefore, a stronger effect through the Cu_{Mg} point defects. When the Mg content is maintained, the probability of Cu_{Mg} to occur decreases due to its higher formation energy, leading to a lower defect density and therefore a weaker effect on the material's TE properties.

The defect formation energies for p- and n-type Mg₂Sn are provided in Figure 6.11 d, e and f. Here too, the p-type conduction situation is only studied under Mg-poor conditions. From Figure 6.11 d, it can be seen that the most stable defects are Li-related. In fact, I_{Li} and Li_{Mg} are the defects with the lowest

formation energies, both below 0.25 eV at VBM. In this situation, the only stable Cu-related defect is Cu_{Mg} which is neutral in the vicinity of the VBM (for $-0.25 \text{ eV} < E_{\text{F}} < -0.14 \text{ eV}$). This indicates no influence on the charge carrier concentration determined by the combined effect of I_{Li} and Li_{Mg} . Equivalently to the Li-doped Mg_2Si discussed above, no significant experimental change is expected to occur for the TE properties of the Li-doped Mg_2Sn samples. It is, then, plausible to interpolate these findings for the whole range of Li-doped solid solution compositions $\text{Mg}_2\text{Si}_{1-x}\text{Sn}_x$ ($x = 0 \sim 1$), and to conclude that Cu contacting on Li-doped $\text{Mg}_2\text{Si}_{1-x}\text{Sn}_x$ samples is not expected to affect their TE properties, as the Cu-related defects are less stable than the intrinsic and dopant-related defects.

In Bi-doped Mg_2Sn under Mg poor conditions (Figure 6.11 e), Bi_{Sn} is the most stable defect from the band gap all the way inside the conduction band until $E_{\text{F}} = 0.05 \text{ eV}$. Similar to Bi_{Si} , Bi_{Sn} is also an electron donor defect of charge $1+$. For $E_{\text{F}} = 0 \sim 0.05 \text{ eV}$, the next most stable defects are Cu_{Mg} and V_{Mg} , both having very comparable formation energies in the considered E_{F} window. Cu_{Mg} is an electron acceptor defect with a charge $q = 1-$ for $E_{\text{F}} < 0.03 \text{ eV}$, and a charge $q = 2-$ above 0.03 eV . A comparison of the formation energies of these three defects (Bi_{Sn} , Cu_{Mg} , V_{Mg}) is provided in Table 6-2 at four different E_{F} (CBM, 0.03 eV , 0.05 eV and 0.07 eV). $E_{\text{F}} = 0.03 \text{ eV}$ is considered as being the charge transition level of Cu_{Mg} and 0.07 eV is considered as being the charge transition level for Bi_{Sn} (from $q = 1+$ to $q = 0$). The formation energies at $E_{\text{F}} = 0.05 \text{ eV}$ are also provided, as the selected comparison value for the samples in the later discussion, and will be used to approximate the defects' densities. From Table 6-2, it can be concluded that the compensation effect of Cu_{Mg} and V_{Mg} on the conduction electrons provided by Bi_{Sn} isn't expected to be as strong for chemical potentials around CBM; however, the deeper we go inside the conduction band, the lower the formation energies of Cu_{Mg} and V_{Mg} become. Therefore, as we get to higher electrochemical potential (e.g. $E_{\text{F}} = 0.05 \text{ eV}$), we would expect more compensation to occur between the relevant defects.

Table 6-2: Comparison of the formation energies of Bi_{Sn} , Cu_{Mg} and V_{Mg} defects at four different E_{F} values.

	at CBM	$E_{\text{F}} = 0.03 \text{ eV}$	$E_{\text{F}} = 0.05 \text{ eV}$	$E_{\text{F}} = 0.07 \text{ eV}$
$E_{\text{form}} (\text{Bi}_{\text{Sn}})$	0.18 eV	0.21 eV	0.23 eV	0.25 eV
$E_{\text{form}} (\text{Cu}_{\text{Mg}})$	0.35 eV	0.32 eV	0.27 eV	0.24 eV
$E_{\text{form}} (\text{V}_{\text{Mg}})$	0.35 eV	0.29 eV	0.25 eV	0.21 eV
Effect expected	Not so much compensation expected at CBM, but stronger effect of Cu_{Mg} and V_{Mg} expected as E_{F} increases (higher carrier concentration/doping)			

In order to have a clearer idea on the influence of the defects on n , we try to estimate the densities corresponding to the provided formation energies at $E_{\text{F}} = 0.05 \text{ eV}$. Similar to the analysis done for Mg_2Si , using $T = 873 \text{ K}$, the obtained values of n (D^q) for the three defects of interest would be 6.19×10^{20} , 6.65

$\times 10^{20}$ and 9.75×10^{20} respectively for Bi_{Sn} , Cu_{Mg} and V_{Mg} . As all the values are of the same order of magnitude, a visible compensation is expected to occur for highly doped Bi-doped Mg_2Sn samples under Mg-poor conditions, and should be experimentally detectable.

Under Mg-rich conditions, as shown in Figure 6.11 f, the most stable Cu related defects are Cu_{Sn} and Cu_{Mg} . They both have formation energies higher than 0.1 eV in the relevant energy range, which is too high to cause a significant effect on the Bi conduction electrons and on n .

Comparison with experimental data

As reported in Chapters 3 and 4, Cu contacting with $\text{Mg}_2\text{Si}_{0.3}\text{Sn}_{0.7}$ resulted in a change of the TE properties of the n-type samples, but no change was observed for the p-type samples. Annealing experiments also followed the same trend in results, where the p-type properties remained constant, while the n-type TE properties changed further. As these data correspond to the 30:70 (Si:Sn content) composition of the solid solution, while the hybrid-DFT calculations were provided and discussed for the binaries, an attempt to interpolate the calculations necessitates an approximation of the solid solution's electrochemical potential, to be able to approximate a window of E_{F} on the formation energy graphs. Using 0.01 eV and 0.06 eV as approximate values of the chemical potential where the Fermi level pinning is expected to be for Mg_2Si and Mg_2Sn , respectively, we can approximate the electronic chemical potential of the 30:70 solid solution composition as $0.01 \times 0.3 + 0.06 \times 0.7 = 0.045$ eV [168]. Note that this approximation can hold based on the assumption that in our case, the CBM is maintained at $E_{\text{F}} = 0$ eV, while the position of the VBM changes as a function of the Si content in $\text{Mg}_2\text{Si}_{1-x}\text{Sn}_x$. At this level, such preliminary analysis can be accepted [140].

It was already concluded above, that all the intermediate compositions for the Li-doped $\text{Mg}_2(\text{Si},\text{Sn})$ system are expected to behave the same as the end binary compositions that showed similar calculations results: no predicted influence of Cu-related defects on the charge carrier concentration. As no change in the Seebeck value of the p-type samples during contacting was experimentally recorded, we have here a good match between the calculation results and the experimental reports of both the non-annealed and annealed Li-doped samples.

However, the situation for the Bi-doped samples is trickier. In fact, a close dependence between the effect of Cu defects and the Mg chemical potential was observed from the hybrid-DFT data. Under Mg-poor conditions, Cu_{Mg} is expected to influence the charge carrier concentration of both Mg_2Si and Mg_2Sn , thus, a TE property change of the samples can be expected during Cu contacting. With the environment transitions from Mg-rich to Mg-poor, we would also expect a certain change in n as the Mg loss, along with the Cu on Mg atoms, would reduce conduction electrons. However, if we stay under Mg-rich conditions, no influence of the Cu defects is expected. As the experimental data clearly reports a strong

compensation, a match between experiments and calculation would only stand if the experimental samples are also under Mg-poor conditions. Such Mg environment is less probable (compared to the Mg-rich environment), but not completely unrealistic; and, when reached, we would have a data match. In fact, despite synthesizing the n-type samples with 3 at% excess Mg to compensate for the inevitable losses during sintering and contacting, the actual Mg quantity that is lost is not easily quantifiable, and the final real Mg environment (poor or rich) can't be known for sure. Moreover, some Mg loss does not necessarily mean deterioration of the TE properties like shown by Sankhla *et al.* in [169], therefore, having the sintered sample with optimized properties does not indicate whether it is still under Mg-rich atmosphere or not.

Though the situation of the pre-annealed n-type samples is not clear, it is possible to establish a better match between the experimental results and the hybrid-DFT calculations for the annealed sample cases. In fact, after annealing, an Mg poor environment is safe to assume, as Mg losses can be inevitable. During experimental handling, the samples were coated with an ethanol-based boron nitride solution and Mg flakes were added along with the sample inside the ampules before sealing and annealing, to minimize Mg losses, as explained in Chapter 2.5. However, these Mg losses are not completely prevented, and the detection of such loss might not be straightforward as reported by [170] where, even though a crystal stability study revealed matrix decomposition into MgO, Si and Sn, the thermopower and the electrical conductivity of the material remained unchanged after thermal cycling up to 773 K. Therefore, the stability of the TE properties does not refute matrix demixing and Mg loss.

Several studies also reported frequent Mg loss in different annealing experiments. Therefore, it is possible to assume that, after 7 days inside the annealing furnace, the samples end up under an Mg-poor environment [171-174]. If such situation is achieved, we would have a good match between the observed experimental results of the solid solution with the predicted calculation results, both showing a clear change in the charge carrier concentration. However, if the actual Mg chemical potential is maintained as Mg-rich after the annealing, then our hybrid-DFT predicted data does not match what we observe experimentally.

As a trial to disentangle the relation between the effect of the Cu defects and the Mg chemical potential (Cu substituting Mg atoms and Mg vacancy formation due to Mg loss) and to understand the interplay between both corresponding point defects (Cu_{Mg} and I_{Mg}), a comparison of our TE material after annealing with and without Cu electrodes is necessary.

A previous work reported annealing experiments on $\text{Mg}_2\text{Si}_{0.3}\text{Sn}_{0.675}\text{Bi}_{0.25}$, and results showed thermal stability of the samples, as well as an almost constant Seebeck and electrical conductivity values after annealing at 723 K for up to 30 days [2]. As the samples of the mentioned literature and the samples from our current study are synthesized using the same method and the annealing experiments were done following the same technique, it is possible to assume thermal stability of our n-type pre-contacted

samples up to 30 days. If we try to understand the reported study in [2] using defect formation energies, we can look at the CBM values on Figure 6.11 e, as the samples were made using 2.5 at% Bi content. Disregarding the Cu related defects and looking at a pre-contacted sample, the formation energy and V_{Mg} is double that of Bi_{Sn} , as reported in Table 6-2 ($E_{form}(V_{Mg}) \approx 2 \times E_{form}(Bi_{Sn})$). Both these formation energies would correspond to $n(D^q)$ values of 1.25×10^{21} and 2.58×10^{20} for Bi_{Sn} and V_{Mg} respectively. Therefore, any compensation effect caused by Mg vacancies won't drastically change the Seebeck profile, and recorded variations would remain within the error bars, which fits the experimental reports in [2].

Bringing Cu back in the picture, we already observed that after annealing, S value changes. It is, thus, possible to conclude that this observed behavior (strong n loss) in Chapter 3 is enhanced by the Cu_{Mg} defect, whose formation energy (hence density) is strongly dependent on the Mg content in the material. In fact, Cu atoms would occupy Mg vacancy sites and form Cu_{Mg} defects that would act as electron trap, and cause a decrease in the free charge carriers. That is why, under Mg poor conditions, Cu_{Mg} has a lower formation energy, and consequently a stronger compensation effect. However, under Mg-rich conditions, Cu_{Mg} is less stable and potentially has a weaker effect.

Experimentally, even if the initial n-type samples are synthesized with 3 at% excess Mg, it is not possible to guarantee that the samples are still rich in Mg after sintering at 973 K for a holding time of 20 min, as the effect of the Mg vacancy defects on the charge carrier concentration can be within the error range, as discussed above. As we start under Mg-rich conditions, the I_{Mg} defects have a higher density. The Mg losses that would occur during sintering or joining would also be losses that change the density ratio of interstitial Mg atoms and Mg vacancies, all the while keeping a high I_{Mg} defect density. In this case, we would still be in an Mg-rich environment despite the Mg loss, and the influence of Cu_{Mg} won't be as drastic.

However, if the Mg losses actually result in not only the loss of I_{Mg} , but also the formation of V_{Mg} , then we would end up in an Mg-poor environment where the Cu_{Mg} defect has a comparable formation energy as that of V_{Mg} . In this case, the combined effect of V_{Mg} and Cu_{Mg} would cause a more enhanced compensation, as both defects are stable hole donors.

To conclude, the fact that we actually experimentally record a change in the Seebeck coefficient after contacting with Cu confirms a change in the charge carrier concentration of the n-type sample. However, whether these changes are solely either due to Mg loss (an increased density of I_{Mg} defects) or due to the Cu on Mg defects remains unclear. There is a high probability that the observed effect is a combination of both defects, as Cu_{Mg} is also only stable under Mg poor chemical potential conditions. However, the results can also be due to a non-optimized control of the Mg content, which intensified losses in this work compared to the work of Farahi *et al.* [2]. The difficulty in controlling the Mg atmosphere and its

influence on the TE properties of the $\text{Mg}_2(\text{Si},\text{Sn})$ system contacted with Al was also reported in a recent work by Camut *et al.* [150].

Comparison of the Cu results with the Ag reported results

To put the discussed results into perspective, a comparison with the experimental results as well as the defect formation energy results of Ag with Mg_2Si and Mg_2Sn (Chapter 5) can be done. A previous report of Ag contacting with $\text{Mg}_2\text{Si}_{1-x}\text{Sn}_x$ can also be included in this comparison [4].

Experimentally, Pham *et al.* already reported in [4] that S of n-type $\text{Mg}_2\text{Si}_{1-x}\text{Sn}_x$ changed from $-110 \mu\text{V/K}$ to around $-220 \mu\text{V/K}$ after joining with Ag at 723 K and 873 K. This is larger in absolute value than the changed Seebeck value after joining with Cu ($-160 \mu\text{V/K}$, at 873 K), which indicates a stronger compensation from Ag, even at lower temperatures. No such change in S , and therefore in charge carrier concentration, was observed for the p-type samples joined with Ag at both tested temperatures, similar to the Cu case.

Figure 6.12 shows combined graphs for Ag and Cu defects in Bi-doped Mg_2Si and Mg_2Sn under Mg-rich and Mg-poor conditions, to facilitate the comparison between the stabilities of the Ag- and Cu-related defects. In the four graphs, it is clear that the Ag_{Mg} acceptor defect (charge $q = 1^-$) is the most stable electrode-related defect. It is comparable in formation energy to that of $\text{Bi}_{\text{Si/Sn}}$ in most cases (except Mg-rich Mg_2Sn).

In the particular case of Mg-rich Mg_2Sn , the Ag_{Sn} defect is actually the most stable Ag-defect and it acts as an electron acceptor of charge 1^- . Here, Ag_{Mg} has a higher formation energy which leads to a lower defect density; however, the combined effect of Ag_{Sn} and Ag_{Mg} is expected to cause significant changes to the charge carrier concentration. In this case also, both Ag_{Sn} and Ag_{Mg} are more stable than the most stable Cu-related defect Cu_{Sn} . In all these cases, Ag acceptor defects compensate the conduction electrons in a more enhanced manner than Cu, and independently of the Mg chemical potential. This matches the experimental data where Ag contacting resulted in a larger change in the Seebeck coefficient of $\text{Mg}_2\text{Si}_{1-x}\text{Sn}_x$ compared to Cu.

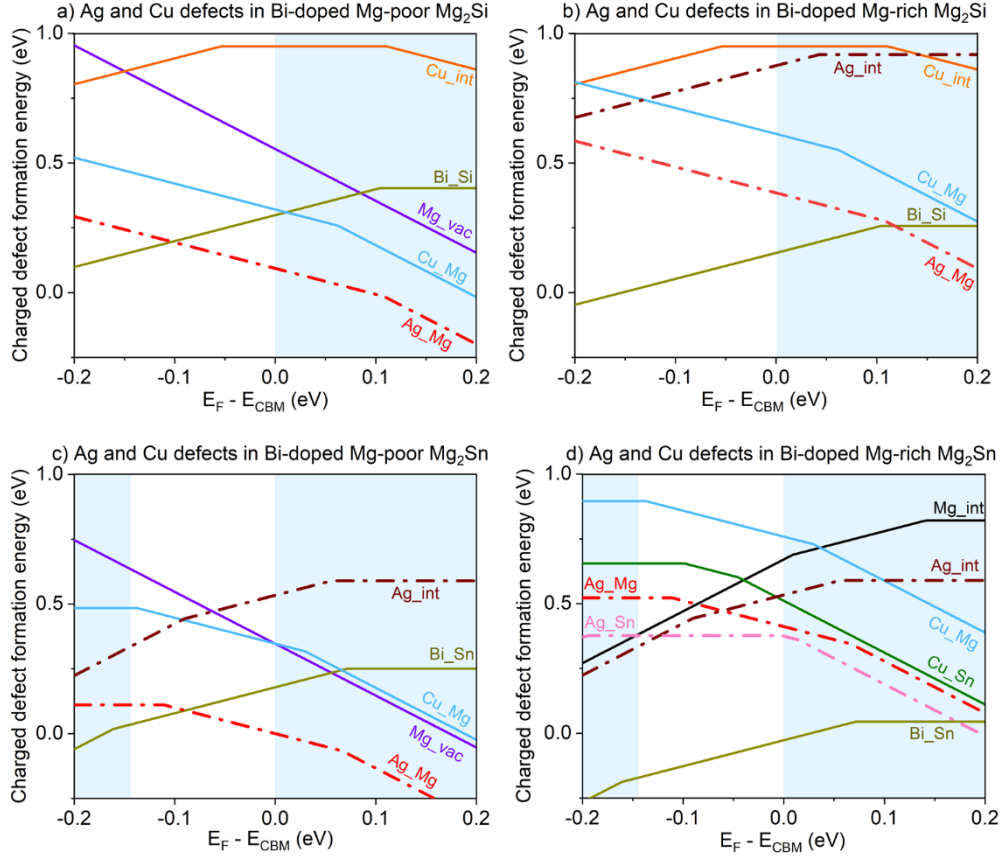


Figure 6.12: Charged defect formation energies of Ag (dashed lines) and Cu (full lines) in Bi-doped Mg_2Si a) under Mg-poor and b) Mg-rich conditions and in Bi-doped Mg_2Sn , c) under Mg-poor and d) under Mg-rich conditions. The intrinsic and dopant defects are also presented in full lines, and only the relevant defects with formation energies < 1 eV are plotted. The labeling X_Y of the defects (where X and Y are chemical elements) on the figure correspond to the X_Y labeling in the text. X_{int} and X_{vac} correspond respectively to I_X and V_X.

6.2.2 Ni defects in Li and Bi-doped Mg_2Si and Mg_2Sn

In this section, we will start by discussing the hybrid-DFT calculation results of the Ni-related defect formation energies for n- and p-type Mg_2Si and Mg_2Sn systems. As for the comparison with experimental results, previous works from de Boer *et al.* [5, 68] will be used as a reference for Mg_2Si contacting with Ni, and a previous work from Pham *et al.* [4] will be considered as a reference for the comparison with Mg_2Sn and Sn-rich compositions. Lastly, new results of contacting p- and n-type $\text{Mg}_2\text{Si}_{0.8}\text{Sn}_{0.2}$ with Ni will also be introduced and compared with calculations.

Hybrid-DFT calculations of the defect formation energies of Ni with Mg_2Si and Mg_2Sn

Li-doped and Bi-doped Mg_2Si and Mg_2Sn systems are studied in this section, with the considered chemical potentials for the formation energy calculations are, here too, Mg-rich and Mg-poor

environment. However, unlike the case of Cu, in this case, we consider a particular impurity phase-related chemical potential, in addition to the basic Mg chemical potential. In fact, the first calculations of the Ni defect formation energies done under Ni-rich environment resulted in negative formation energy values (< -1.5 eV) for all cases, which indicates that we are under the wrong reference chemical potential (*vis-à-vis* the experiment). Therefore, considering further Ni-related phases is necessary to approach the correct atomic chemical potential and obtain more realistic values of the formation energies, as both are directly related. In fact, when the obtained formation energies are clearly unphysical, usually tuning the chemical potential is the method to follow to obtain more realistic values [144, 175]. Moreover, in our case, the Ni chemical potential was changed, while the Mg-rich/Mg-poor conditions were maintained to allow comparisons of the defect formation energies in the case of Ni with other elements. Such approximations enhance error probability in the calculations, however, they are acceptable for the purpose of our study.

Comparatively, when Cu defect formation energies were calculated without considering particular phases, realistic numbers were obtained, that also matched well with the experimental data, which backs up the claim that further calculations involving Cu-related phases are not necessary. As Cu-related phases were observed in the reaction layer between Cu and $\text{Mg}_2(\text{Si},\text{Sn})$, considering further Cu-related phases would be necessary to extract a more correct chemical potential. Nevertheless, the provided hybrid-DFT data under just a Cu-rich chemical potential were good and further phase consideration is not expected to drastically change the results.

When selecting the Ni-related phases that need to be considered during the calculations, NiSi_2 and Ni_3Si were considered for the Mg_2Si system, while Ni_3Sn was considered for the Mg_2Sn system. These phases were chosen based on the Materials Project database. The selection between NiSi_2 and Ni_3Si for Mg_2Si was done based on a previous works reporting the phases formed after joining Mg_2Si with Ni [5, 68]. In this literature, the phase $\text{Ni}_{31}\text{Si}_{12}$ was detected (experimentally), which is chemically closer to the Ni_3Si phase than the NiSi_2 phase. In the following discussion, the Ni_3Si phase will be used as a reference for the chemical potential, however, $\text{Ni}_{31}\text{Si}_{12}$ should also be checked in a further work.

Figure 6.13 shows the defect formation energies of Li-doped and Bi-doped Mg_2Si and Mg_2Sn , under Mg-rich and Mg-poor environment, and the calculations with respect to the Ni_3Si and Ni_3Sn phase chemical potentials, respectively for Mg_2Si and Mg_2Sn . Here too, for simplicity, the curves of the formation energies are only shown in a Fermi level range restricted around the valence band maxima for p-type samples, and a Fermi level range around the conduction band minima for n-type samples. Also, only defects with formation energies below 1.5 eV for Mg_2Si and 1 eV for Mg_2Sn are considered as they are the most stable and most probable to play a role in determining the general charge carrier concentration of the system. The reason behind looking at a larger formation energy window (up to 1.5 eV) for Mg_2Si is just for visibility, to clearly see the most stable Ni-related defect in this case, and to have it in the picture with the other relevant defects.

Starting with the Li-doped Mg_2Si , as represented in Figure 6.13 a, it is clear that the only Ni-related defect, which is Ni interstitials (I_{Ni}), has a much higher formation energy in the whole presented range of Fermi level compared to other point defects, namely I_{Li} , Li_{Mg} , and I_{Mg} . Therefore, it is clear that Ni is not expected to have any significant influence on the charge carrier concentration n of Li-doped Mg_2Si . As for the Bi-doped Mg_2Si , starting from the Mg-poor chemical potential environment presented in Figure 6.13 b, the most stable Ni defect is Ni_{Si} . However, like I_{Ni} in the Li-doped case, Ni_{Si} has a much higher formation energy, which also directly translates to no significant contribution to the charge carriers, even though it is an acceptor defect with a charge $2-$ at CBM and inside the conduction band. A similar situation is observed in Bi-doped Mg_2Si under Mg-rich conditions (Figure 6.13 c), where Ni_{Si} has a much higher formation energy. Therefore, it can be concluded here that, employing the Ni_3Si -rich chemical potential, Ni is not expected to have any influence on Li and Bi-doped Mg_2Si systems, independently on the Mg chemical potential environment.

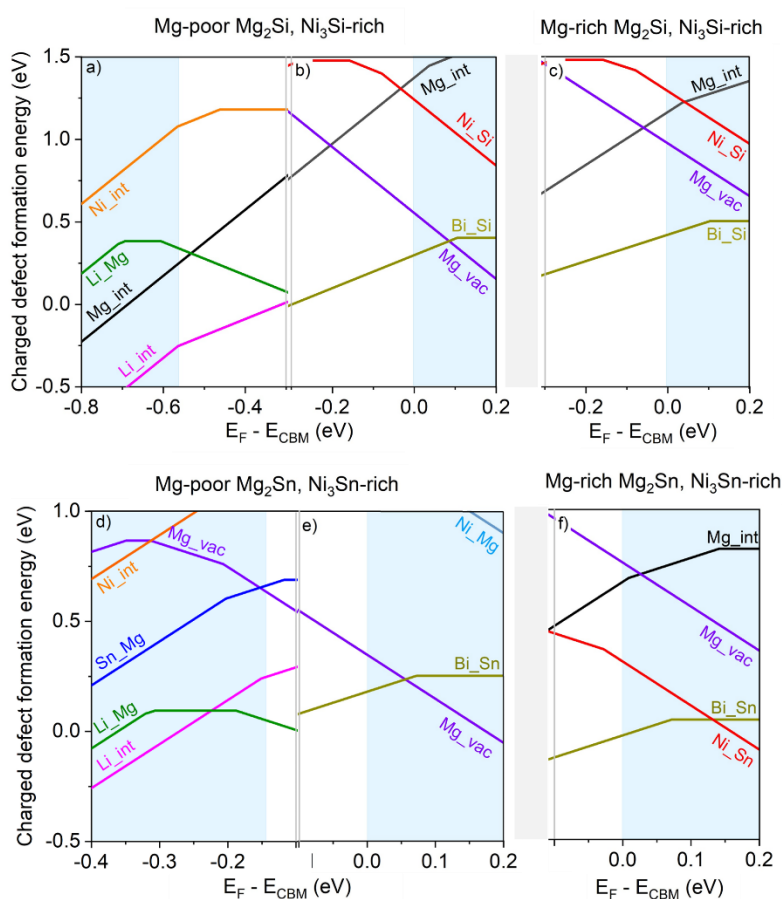


Figure 6.13: Charged defect formation energies of Ni in: a) Li-doped and b) Bi-doped Mg_2Si under Mg-poor conditions c) Bi-doped Mg_2Si under Mg-rich conditions, d) Li-doped and e) Bi-doped Mg_2Sn under Mg-poor conditions f) Bi-doped Mg_2Sn under Mg-rich conditions. For simplicity, the Li-doped Mg_2Si and Mg_2Sn are only represented in the Fermi level region around VBM while the Bi-doped samples are represented in the Fermi level region around CBM. The labeling X_Y of the defects (where X and Y are chemical elements) on the figure correspond to the X_Y labeling in the text. X_{int} and X_{vac} correspond respectively to I_X and V_X .

For the Li-doped Mg₂Sn system (Figure 6.13 d), similar to the Mg₂Si case, I_{Ni} is the most stable Ni-related defect; however, its formation energy is too high to be crucial to the carrier concentration. For Bi-doped Mg₂Sn, the most stable defects are Ni_{Mg} and Ni_{Sn} under Mg-poor (Figure 6.13 e) and Mg-rich conditions (Figure 6.13 f), respectively. The formation energy of Ni_{Mg} is too high to influence n , but Ni_{Sn} has a low formation energy, and is the defect with the lowest formation energy among all Ni-related defects in both Mg₂Si and Mg₂Sn, independently of the dopant and the chemical potential. Under Mg-rich, Ni_{Sn} is an acceptor defect of charge 1⁻ for E_F between -0.1 and -0.03 eV, then a charge 2⁻ from $E_F = -0.03$ eV towards inside the conduction band. At CBM, $E_{\text{form}}(\text{Ni}_{\text{Sn}}) = 0.31$ eV and $E_{\text{form}}(\text{Bi}_{\text{Sn}}) = 0.027$ eV while at $E_F = 0.05$ eV, $E_{\text{form}}(\text{Ni}_{\text{Sn}}) = 0.21$ eV and $E_{\text{form}}(\text{Bi}_{\text{Sn}}) = 0.023$ eV. Approximating the ratio of the defect densities $n(D^q)$ as shown through the equation below

$$\frac{n(\text{Ni}_{\text{Sn}})}{n(\text{Bi}_{\text{Sn}})} \sim \frac{\exp\left(-\frac{E_{\text{form}}(\text{Ni}_{\text{Sn}})}{k_B T}\right)}{\exp\left(-\frac{E_{\text{form}}(\text{Bi}_{\text{Sn}})}{k_B T}\right)},$$

we would have at CBM $\frac{n(\text{Ni}_{\text{Sn}})}{n(\text{Bi}_{\text{Sn}})} \sim \frac{2.5 \times 10^{-2}}{1.38} = 0.018$, and $\frac{n(\text{Ni}_{\text{Sn}})}{n(\text{Bi}_{\text{Sn}})} \sim \frac{8.3 \times 10^{-2}}{0.76} = 0.11$ at $E_F = 0.05$ eV.

From these numbers, Ni_{Sn} is expected to have a much lower density than Bi_{Sn}.

Therefore, even though Ni_{Sn} has a lower formation energy for Bi-doped Mg₂Sn under Mg-rich and Ni₃Sn-rich conditions, it is still not low enough to cause relevant changes in the charge carrier concentration of the system.

As a conclusion to this section, it can be stated that, based on the presented hybrid-DFT calculations of the formation energies of defects in Li-doped and Bi-doped Mg₂Si and Mg₂Sn, considering both Mg-rich and Mg-poor conditions, and limiting the phase chemical potential to Ni₃Si and Ni₃Sn for the two materials systems respectively, Ni defects are not expected to cause any significant changes in the charge carrier concentrations established by Li and Bi, in all cases. From this perspective, Ni could be seen as a potential neutral contacting electrode for n- and p-type Mg₂(Si,Sn) TE materials, that would cause no changes in the optimized TE properties. Technologically, for the purpose of contacting Mg₂(Si,Sn), Ni would then be a suitable additive to create new alloys with adapted CTE.

Comparison with experimental data

To compare the previously presented DFT calculations with experimental results, references [4, 5, 68] are used for a direct comparison with n-type Mg₂Si, and for n- and p-type Mg₂Sn using the Sn rich solid solution composition Mg₂Si_{0.3}Sn_{0.7}. In [5, 176], de Boer *et al.* reported the joining results of Ni with n-Mg₂Si, as well as thermal stability tests of the contact. No influence of the Ni contacts was observed neither after contacting, not after annealing at 823 K for 7 days. As we detect no change of S

experimentally, and as the hybrid-DFT calculations predict no change in carrier concentration under both Mg chemical potential conditions, we have a match between both methods.

As for the $\text{Mg}_2\text{Si}_{0.3}\text{Sn}_{0.7}$ contacting results reported by Pham *et al.* [4], no influence on the TE properties was reported for the n-type samples joined with Ni at 873 K, which matches our hybrid-DFT predictions. However, a change of the Seebeck profile for p-type samples joined at 973 K was recorded. In fact, a linear increase in the Seebeck value from one side of the sample to the other was observed, starting from 90 $\mu\text{V}/\text{K}$ on the right-hand side (which is the initial S value of the TE material before joining), going all the way up to 150 $\mu\text{V}/\text{K}$ on the left-hand side for the sample joined at 973 K. On the other hand, the p-type sample joined at 873 K showed only a slight variation of the Seebeck coefficient which ranged between 90 and 100 $\mu\text{V}/\text{K}$ across the whole sample. Such change in the TE properties is different from the observed gradients with Ag, for example; therefore, the cause is expected to be different from a diffusion of the electrode material. In the corresponding work, such differences were not fully understood, yet, a potential explanation related with the joining conditions was provided: the joining at 973 K was done on powder, so the sintering of the TE material and the contacting with the electrode were done in one step, while the joining at 873 K was done on pre-sintered $\text{Mg}_2\text{Si}_{0.3}\text{Sn}_{0.7}$ pellets. Such sintering conditions would influence the stability (phase purity) of the TE material, as the sintering step serves not only for powder compaction, but also to complete the reaction between the precursors and obtain a phase pure material [1]. As no reproduction of these results was attempted, this data needs to be carefully considered. Also, in this work, no reproduction was attempted to understand said observations because it does not fall within the scope of the current study. However, if we only consider the contacting results obtained at 873 K as the TE material was actually optimized before the joining step and because our own contacting experiments were also done on sintered pellets, we would have a match between the defect formation energy calculations and the experiments, were no visible influence would occur between p-type Mg_2Sn and Ni.

Further experiments utilizing Si-rich compositions of the $\text{Mg}_2(\text{Si},\text{Sn})$ solid solutions were conducted by our colleague Radhika Deshpande where n- and p-type $\text{Mg}_2\text{Si}_{0.8}\text{Sn}_{0.2}$ were contacted with Ni, under my supervision, and analysis of the data was done together. These results are presented in this section. For the purpose of the study, p-type $\text{Mg}_{1.97}\text{Li}_{0.03}\text{Si}_{0.8}\text{Sn}_{0.2}$ and n-type $\text{Mg}_{2.06}\text{Si}_{0.8}\text{Sn}_{0.17}\text{Bi}_{0.03}$ were synthesized and pressed into pellets following the methods reported in [3] and [1], then joined with Ni at 973 K under direct current sintering for a holding time of 10 mins and a temperature increase rate of 1 K/s.

Seebeck scans of the sintered p- and n-type pellets were done using a Potential & Seebeck Microprobe as explained in Chapter 2.4.2, and the recorded data is presented in Figure 6.14 a and b. From these scans, the Seebeck values of the samples are $\sim 345 \mu\text{V}/\text{K}$ for the p-type sample and $\sim -55 \mu\text{V}/\text{K}$ for n-type.

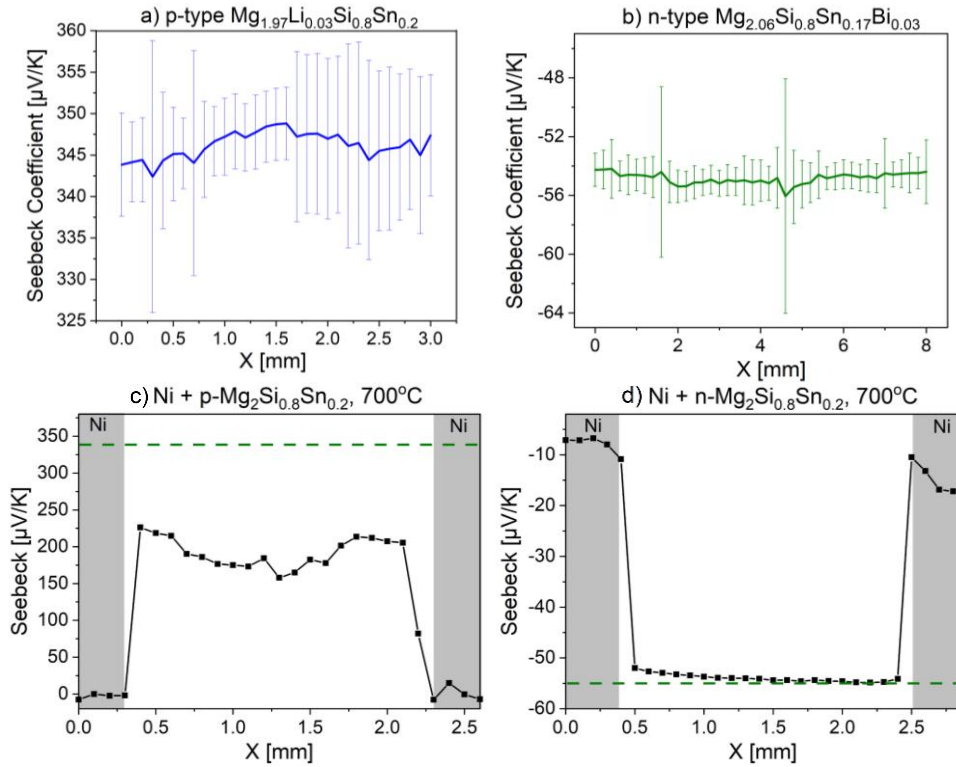


Figure 6.14: Average Seebeck profile line scan (with error bars) on the surfaces of as-sintered a) p-type $\text{Mg}_{1.97}\text{Li}_{0.03}\text{Si}_{0.8}\text{Sn}_{0.2}$, b) n-type $\text{Mg}_{2.06}\text{Si}_{0.8}\text{Sn}_{0.17}\text{Bi}_{0.03}$, and representative Seebeck profile lines of c) p-type $\text{Mg}_{1.97}\text{Li}_{0.03}\text{Si}_{0.8}\text{Sn}_{0.2}$ contacted with Ni and d) n-type $\text{Mg}_{2.06}\text{Si}_{0.8}\text{Sn}_{0.17}\text{Bi}_{0.03}$ contacted with Ni. The green dashed lines on c) and d) indicate the Seebeck coefficient values of the TE material before contacting.

Contacting results of both pellets with Ni are presented in Figure 6.14 c and d, for p- and n-type samples respectively. From a first observation on both figures, it can be concluded that no change occurred to the n-type sample after joining, while the p-type sample has a very different Seebeck profile. In fact, after contacting, the S value changed across the whole sample thickness (~ 2 mm) from 335 to ~ 200 $\mu\text{V/K}$. This indicates a certain increase in the charge carrier concentration. Furthermore, the change in Seebeck looks like a gradient: the edges of the profile line close to the contacting interfaces have a higher Seebeck value (225 $\mu\text{V/K}$ on left-hand side, 200 $\mu\text{V/K}$ on right-hand side), and, as the line goes further inside the TE material, S decreases until it reaches a minimum value of 150 $\mu\text{V/K}$ almost at the center of the sample. Unlike the gradients of Seebeck observed when contacting $\text{Mg}_2(\text{Si},\text{Sn})$ with Ag reported in Chapter 5, the value of S does not go back to the initial value of the TE material after a certain diffusion length on both sides of the sample. In this case, the intermediate value is even smaller than the values at the edges, indicating an even stronger change in the charge carrier concentration. The reason behind such behavior, whether the results are due to Ni diffusion or not, is not fully clear. The observed change could be related with the Ni contacting, though highly unlikely as the change of the TE properties is actually enhanced in the middle of the TE material further away from the electrode. It could also be related to the high joining temperature, which is close to the material's sintering (973 K and 1023 K respectively). Such elevated joining temperature could influence the material's properties that were

optimized during sintering, hence the observed discrepancies before and after contacting. Further comparative experiments with and without Ni need to be conducted to have a full image.

Comparing these experimental results with the hybrid-DFT results presented above, only the n-type sample case presents a match between both methods: no influence of the Ni defects on the carrier concentration was predicted by DFT, no change in S was recorded experimentally. These results join what was concluded above when comparing with literature on Ni-joined Mg_2Si and $\text{Mg}_2\text{Si}_{0.3}\text{Sn}_{0.7}$ [4, 5, 68, 149]. However, when comparing the formation energy calculation results with the experiments in the p-type sample, a disagreement is clearly observed, as the Seebeck profile changes quite drastically after joining. Such disagreement was also observed and discussed above between calculations and experiments in the case of p-type $\text{Mg}_2\text{Si}_{0.3}\text{Sn}_{0.7}$, but in this case, the unexpected behavior was attributed to the fact that the joining with Ni was conducted on powder instead of a pre-sintered pellet. Another potential explanation could be that some Si or Sn from the $\text{Mg}_2(\text{Si},\text{Sn})$ powder would react easier with the Ni electrode material, resulting in a final non-optimized TE material with a different Seebeck profile. When the experiments were repeated on a pellet and joined at 873 K, no change of TE properties was observed then. Following this reasoning, the unexpected behavior of p-type $\text{Mg}_2\text{Si}_{0.8}\text{Sn}_{0.2}$ could also be related to the unstable p-type conduction (poor dopability) in the Si-rich composition range of the $\text{Mg}_2\text{Si}_{1-x}\text{Sn}_x$ solid solutions, as reported previously in [36, 177]. This instability would also be enhanced by the high-temperature joining step.

From a DFT perspective, this instability can be explained by the fact that, even though the band gap of the $\text{Mg}_2\text{Si}_{0.8}\text{Sn}_{0.2}$ composition is smaller than that of the Mg_2Si composition, the Fermi level is still pinned deep inside the band gap and far from the valence band. In fact, as shown in Figure 6.15, when the most stable native defects of Mg_2Si are considered, namely V_{Mg} and I_{Mg} shown in dashed lines in the figure, both defect lines pin the Fermi level at ~ 0.2 eV (marked with the grey circle), which is much closer to the conduction band than the valence band. This should not come as a surprise as several literature reported a stable n-type conduction of Mg_2Si [41, 178-180]. Furthermore, Figure 6.15 shows Li-doped Mg_2Si , still with a Fermi level pinned far from the valence band (marked with the brown circle), even though it is moved closer towards it.

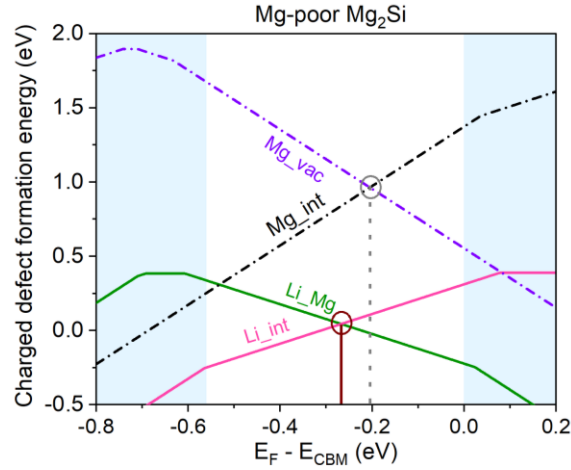


Figure 6.15: Most stable native defects (in dashed lines) and Li (dopant)-related defects (in full lines) in Mg-poor Mg_2Si , showing the pinning of the Fermi level inside the band gap. The labeling X_Y of the defects (where X and Y are chemical elements) on the figure correspond to the X_Y labeling in the text. X_{int} and X_{vac} correspond respectively to I_X and V_X .

These reasons can explain the starting low carrier concentration of the $\text{Mg}_2\text{Si}_{0.8}\text{Sn}_{0.2}$ composition that would also be hard to maintain after the contacting step. Even though Ni defects are not expected to change the carrier concentration of the system, the formation of stable defects such as V_{Mg} that could have increased in density (which we can call $\Delta\rho(V_{\text{Mg}})$) after the joining step, would have a visible influence on n . Comparatively, a more stable $\text{Mg}_2\text{Si}_{1-x}\text{Sn}_x$ n-type composition with a larger n such as $\text{Mg}_2\text{Si}_{0.3}\text{Sn}_{0.7}$ would not feel the effect of the same $\Delta\rho(V_{\text{Mg}})$ as strongly. Nevertheless, here too, a control experiment where the sample would be subjected to the same joining conditions but without the Ni layer would give a better overview and allow more conclusive experiments.

6.2.3 Summary and Conclusions

In the previous sections, an inclusive perspective on contacting results involving experimental data and hybrid-DFT calculation data was introduced, where a discussion of the results obtained from both methods for specific study cases was presented, then compared to establish either agreement or lack thereof. Through this comparison, the importance of DFT in general and defect formation energies in particular in the contacting procedure of TE materials was tested, using the examples of Cu and Ni as contacting electrodes for the $\text{Mg}_2(\text{Si},\text{Sn})$ system.

Good agreements were obtained in the case of Cu contacted with n- and p-type $\text{Mg}_2(\text{Si},\text{Sn})$ materials and Ni contacted with n-type $\text{Mg}_2(\text{Si},\text{Sn})$ under *direct resistive heating* conditions. A summary of all the studied cases as well as the match or mismatch results are provided in Table 6-3. In this table, different TE materials with different contacting electrodes are presented, and their joining condition (sintering

current) is also introduced, where *DRH* stands for *direct resistive heating* and *IRH* stands for *indirect resistive heating* (both conditions are explained in Chapter 2.2). The references for the experimental results are provided, and the answer to whether experiments and calculation match or not is color coded: green is used for a match, yellow is used for a conditional match, and red is used for a mismatch. The conditional match cases are further explained below.

Table 6-3: Summary of the match or mismatch between experimental and hybrid-DFT calculations results for the different studied cases.

Studied case	Experimental Reference	Match?
n-Mg ₂ Si _{0.3} Sn _{0.7} + Cu (<i>DRH</i>)	Chapter 4	Yes
p-Mg ₂ Si _{0.3} Sn _{0.7} + Cu (<i>DRH</i>)		Yes
n-Mg ₂ Si _{0.3} Sn _{0.7} + Cu (<i>DRH</i>) annealed		Yes
p-Mg ₂ Si _{0.3} Sn _{0.7} + Cu (<i>DRH</i>) annealed		Yes
n-Mg ₂ Si _{0.3} Sn _{0.7} + Cu (<i>IRH</i>)	Chapter 5	Yes
p-Mg ₂ Si _{0.3} Sn _{0.7} + Cu (<i>IRH</i>)		Yes
n-Mg ₂ Si + Ni (<i>DRH</i>)	[5]	yes
n-Mg ₂ Si + Ni (<i>DRH</i>) annealed	[68]	Yes
n-Mg ₂ Si _{0.3} Sn _{0.7} + Ni (<i>DRH</i>)	[4]	Yes
p-Mg ₂ Si _{0.3} Sn _{0.7} + Ni (<i>DRH</i>)		Yes
n-Mg ₂ Si _{0.8} Sn _{0.2} + Ni (<i>DRH</i>)	Chapter 6.2.2	Yes
p-Mg ₂ Si _{0.8} Sn _{0.2} + Ni (<i>DRH</i>)		Unclear

From Table 6-3, it can be concluded that most of the studied cases present a good match between calculation and experiment study methods. In fact, out of the twelve different presented cases, three cases present a conditional match (in yellow), and only one case is unclear (in red). The last case is p-Mg₂Si_{0.8}Sn_{0.2} contacted with Ni under *direct resistive heating* where the implication of Ni is not believed to be the main reason behind the change in TE properties, and the case was related, for now, to the instability of the p-type conduction in the Si-rich ($\geq 80\%$) compositions of the Mg₂(Si,Sn) solid solution range [36].

The conditional match cases are the n-type Mg₂Si_{0.3}Sn_{0.7} joined with Cu under both *direct* and *indirect resistive heating conditions*, and p-type Mg₂Si_{0.3}Sn_{0.7} + Ni under *direct resistive heating*. The first cases of Cu joined with n-type are conditional because there is a match between experiments and calculations only when the sample is assumed to be under an Mg-poor environment, which is not completely sure. Under Mg-rich conditions, the outcomes of both methods don't match. As for the p-type sample with Ni, a match was only obtained for the sample joined at 873 K, when the joining experiment was done on pre-pressed pellets. When the joining was done at 973 K on TE material powder, the results of the joining did not match the calculation predictions. In this case, the mismatch was assigned to the non-optimized properties of the TE material powder that would have been obtained when first pressing the powder into a pellet.

Based on these studies, hybrid-DFT calculations could predict the behavior between TE materials and their potential contacting electrodes in a strong majority of the considered cases with a good match when we only consider the good matches, and for about 90% when we include the conditional matches. Such results indicate that, in general, hybrid-DFT calculations could be utilized and should be considered in the contacting process of TE materials, and that, based on the predicted defect formation energies, electrode pre-selection could be achieved. Evidently, these calculations cannot replace experimental verifications, but they can be used as good guidelines to direct the experimental process towards potentially successful electrodes.

6.2.4 Limitations of the calculations as an electrode selection tool

Even though DFT and hybrid-DFT calculations provide good results and have successfully been used for decades to describe material properties, in many cases, the results should be considered carefully. In fact, behind each calculation method are a set of assumptions that inevitably dismiss certain physical parameters, which would lead, in our particular case for example, to shifted values of the total energy of the studied system, or the actual band gap. Even though hybrid-DFT calculations manage to give better approximations than conventional DFT, they are still not perfectly precise [111]. Another major issue with DFT calculations is the chemical potentials, both electronic (E_F in Equation 2.11) and phase related (μ_j in the same equation). In fact, generally, knowing the exact experimental electrochemical potential E_F is not straightforward. Certain approximations can be provided by a single parabolic band model for example, using carrier concentrations approximated from the experimental Seebeck values [36], but they remain approximations. Here, it is also necessary to mention the effect of temperature, as calculations are usually done for 0 K, while the actual experiments are done at much higher temperatures. As defect formation energies can be dependent on temperature [181-183], the actual numbers for the formation energies are expected to be different in the real experimental cases compared to what DFT provides, however these differences are usually very small, which maintains the reliability of the method. Moreover, defect density estimation using formation energy calculations is usually done under equilibrium conditions; however, equilibrium cannot be guaranteed in the comparative experimental situation. In fact, in case of joining experiments, the diffusion between the electrode and the TE material will basically be limited to the set experimental holding time (which is 10 min in our case), and whether equilibrium was reached or not after this time cannot be ensured.

Another limitation to keep in mind is the fact that, in our calculations, isolated point defects were considered, meaning that defects were regarded as independent entities. However, in real scenarios, charged defects can interact among each other, resulting in either repulsive or attractive electrostatic forces which would influence defect stability and therefore change the overall picture. An example to this would be the work of Han *et al.* where they studied the interplay between the defects in Ag-doped

Mg₂Si, but they took into consideration the interaction between the defects [184]. Some of their results showed that a simple substitution of Mg by Ag (Ag_{Mg}) in the perfect supercell induces a p-type conduction; however, taking into consideration other defects next to it such as I_{Mg}, gives an n-type conduction.

In our particular study cases, most of the comparisons between calculations and experiments were done using binary calculations and solid solution experimental compositions. Though the interpolation from the results of the binaries to intermediate compositions was successfully established using Ag as an electrode in Chapter 5, there is no guarantee that it can work as well for other electrode materials. If the comparison between both methods matches, then the interpolation can be established; however, if the results between binary calculations and ternary experimental results don't match, the reason behind the mismatch cannot be stated for sure, and the interpolation logic fails. Nevertheless, the interpolation of the data gives in general a reliable trend, and saves the high effort for solid solution DFT-calculations. In fact, running such calculations for solid solutions is very tedious and time-consuming, as it is already complicated to find a fitting reference supercell as a starting point, as the number of configurations (in our case Si/Sn substitution configurations) is very high.

Finally, it is also important to keep in mind that, for simplicity, DFT calculations are usually done for single metallic elements (as potential electrodes), while combined element electrodes such as alloys are not easily computed. The issue here is that a large fraction of the considered metallic elements will fail as electrodes when experimentally tested due to various reasons such as temperature range incompatibility, CTE mismatch etc. but therefore will be used as alloys instead. The interaction of the electrode's extrinsic defects with the TE material in such real cases might be different from what is seen for single elements, therefore, the DFT predictions won't be able to properly describe the overall defect formation energy picture. Additionally, DFT calculations won't properly work for all metallic materials, especially those with strong spin polarization (i.e. the ferromagnetics Fe, Co and Ni). In fact, the hybrid-DFT calculations done for our study cases do not include spin polarization; however, such simplification can fail for elements such as Fe and Cr. For these elements, much more configurations would need to be taken into consideration when calculating the defect formation energies, and finding the stable configuration would cost much more computational time.

Despite these limitations, the hybrid-DFT method is still a good method to employ in defect formation energy calculations. Some cases might take longer to compute than others due to specific limitations (chemical potential, spin polarization...); nevertheless, hybrid-DFT calculations usually provide successful description of the general trend of the material studied. In the particular case of contacting of TE materials, hybrid-DFT can be utilized as a first tool to pre-screen potential electrodes, which will add another criteria on the list of requirements for contacting solutions and makes the selection procedure more refined.

Chapter 7

7. Conclusions and Outlook

The main topic of this work is to find contacting solutions for $\text{Mg}_2(\text{Si},\text{Sn})$ -based thermoelectric materials. So far and to the best of our knowledge, in thermoelectricity, most of the research has focused on developing the TE materials and improving their efficiency, while not as much was done and reported on contacting, despite its necessity. In fact, a comparison in Web of Science of the total number of works published between 2001 and the first quarter of 2021 about thermoelectric materials and thermoelectric contacts gives a search result of more than 40000 publications for the former, and only about 7000 publications for the latter. However, contacting is actually a crucial step in developing thermoelectric generators (TEGs), as it is the step that take single separate TE legs into the desired arrangement of legs on which TEGs are based and that determine the generator's power output.

Finding the right contacting solution for TE materials is not straightforward, as there are no clear guidelines to follow when selecting the proper electrode. What is known so far is that the selected electrode needs to be a metallic material in order to allow an undisturbed flow of the electric current in the TEG, and that it needs to result in a stable joining with the TE materials, as well as a low electrical contact resistance [185]. These starting parameters imply various criteria such as: (i) a stable mechanical adhesion between the metal and the semiconductor after joining, (ii) a physical stability (adhesion) through the thermal cycles that TEGs are subjected to, (iii) no cracks between both materials and inside the TE leg even after thermal cycling – which requires comparable coefficients of thermal expansions (CTE) from both materials, (iv) chemical stability, which includes a controllable diffusion and reaction between the TE material and the metallic electrode, as well as a stable reaction layer through thermal cycling, (v) newly formed phases in the reaction layer that do not add resistance and hinder the current flow, and further requirements.

As can be seen from the mentioned list, most of the selection criteria actually need experimental testing, apart from the CTE compatibility which is based on a screening of tabulated values. This means that, each time an electrode with comparable CTE is found, tests need to be processed in order to conclude on the success or failure of said electrode with the selected TE material.

In the process of developing contacting solutions for $\text{Mg}_2(\text{Si},\text{Sn})$ thermoelectric materials, this list of requirements was followed as a starting point to this work. Efficient n- and p-type $\text{Mg}_2\text{Si}_{1-x}\text{Sn}_x$ compositions were already reported in [2] and [3] respectively, and the final solid solutions used were Bi-doped and Li-doped $\text{Mg}_2\text{Si}_{0.3}\text{Sn}_{0.7}$. Contacting evaluations started with using Cu and $\text{Ni}_{45}\text{Cu}_{55}$ as potential electrodes, as these two electrodes have comparable CTE to the selected $\text{Mg}_2(\text{Si},\text{Sn})$ composition. The results of these experiments showed that, despite the fact that these electrodes fulfill

most of the mentioned requirements, they both failed regarding chemical stability. In fact, both electrode materials diffused rapidly inside the TE material and result in thick and inhomogeneous reaction layers. The samples contacted with Ni₄₅Cu₅₅ also showed some cracks inside the TE material, caused by the difference in CTE due to the Ni content [4].

In an attempt to understand the diffusion mechanism of Cu inside the TE material, a study based on controlling the sintering current (explained in Chapter 2.2) during the joining experiments is reported. The purpose of this study was to investigate the potential influence of the sintering current on the diffusion and contacting results. In the particular case of Cu, joining results were the same in both cases of (i) *direct resistive heating*, where the sintering current was allowed to flow freely through the samples and (ii) *indirect resistive heating*, where a layer of BN was added inside the graphite die in an attempt to block the sintering current from crossing the samples. This allowed to conclude that Cu diffusion is mainly thermally activated.

Another interesting unexpected behavior was observed after Cu and Ni₄₅Cu₅₅ joining experiments: the Seebeck coefficient of the contacted n-type samples changed from $-110 \mu\text{V/K}$ to $-170 \mu\text{V/K}$, while no such behavior was recorded for the p-type samples. As such results were also reported with Ag as an electrode in a previous work by Pham *et al.* [4], it became clear that such behavior is not a singular occurrence, and that there is a clear influence of the electrode materials on the properties of the TE material in the considered cases. In order to further understand these observations, joining experiments using Ag as electrodes to the binaries Mg₂Si and Mg₂Sn were processed and the results are provided in Chapter 5. This study utilized a combined analysis based on experimental testing as well as hybrid-DFT calculations [111] of the formation energies of charged point defects in the studied materials. The obtained results confirmed the effect of the Ag electrode on the binaries, and showed that defect formation energy calculations succeeded in explaining the experimental observations. Therefore, this study allowed to establish two major points in contacting research: (1) the importance of considering charged defects of the contacted TE material (both of the electrode-induced defects and the intrinsic defects of the TE material) while selecting contacting electrodes, and (2) hybrid-DFT calculations as a method to predict the interaction between an electrode and a TE material of interest based on the stability of their defects.

Including these findings, we could add one more criterion to the list of requirements to improve and facilitate the joining electrode selection process. This list contains:

- Type of material (metal, conductive, stable, ...)
- Matching with TE material (CTE: higher CTE of the electrode is probably better, adhesion...)
- Expected interactions between electrode and TE material (phase diagrams...)

- Interplay between the TE material's intrinsic defects and the electrode-related defects (no compensation of the optimized TE material's charge carrier concentration caused by the electrode defects).

In this conclusion chapter and based on the studies done in this work, a few suggestions are proposed, which can be used as starting point for future work in the process of developing contacting solutions for $Mg_2(Si,Sn)$ materials in particular, and potentially for contacting TE materials in general.

7.1 Suggestions for Cu contacting on $Mg_2(Si,Sn)$

As mentioned above, Cu is in principle an attractive electrode for $Mg_2(Si,Sn)$. In fact, due to its very close CTE to that of the TE material, good adhesion was observed after contacting, and it remained stable after thermal treatment. No cracks were observed, and a very low electrical contact resistance was reported, even after annealing. The major shortcoming of this electrode is its fast diffusion and reaction that not only changed the TE properties of the n-type samples, but also resulted in very thick new phases that replaced the initial optimized TE material. Even though the consequences of the diffusion seem drastic, they can be avoided by adding a diffusion barrier between the TE material and the electrode.

Several studies were already reported on diffusion barriers for Cu such as the works of Ivanov [186], Wang [187], Liu *et al.* [188], Reid *et al.* [189], Oku *et al.* [190], etc. In these works, several compositions based on transition metals were tested in an attempt to block Cu from diffusion into Si; however, the most reported results stated failure based on crystallization of the diffusion barrier, which leads to an inevitable grain boundary diffusion of Cu. Therefore, these works established that in order for the diffusion barriers to succeed, they have to be sputtered as amorphous and remain amorphous after adding the Cu layer and through thermal stability testing. Among the successful reported barriers are $W_{64}B_{20}N_{16}$ and $W_{37}Si_{12}N_{48}$ reported in [189], that successfully managed to block Cu diffusion up to 800 °C for 30 mins. Cr also worked as a diffusion barrier for Cu in Si, but only up to 400 °C, as $CrSi_2$ forms starting from $T = 450$ °C and consumes the intended barrier layer [191]. Sputtered Ta-W-N was also reported as a potentially successful barrier for Cu diffusion in Si, but this barrier failed at 800 °C after Cu diffused inside Si and formed Cu_3Si [188]. Nevertheless, 800 °C would be enough in our application case, where our working temperatures are around 450 °C.

Based on these literatures, among others, several compositions could be considered as a diffusion barrier for Cu. However, it is important to keep in mind that the TE materials we work with here are $Mg_2(Si,Sn)$ solid solutions, with a higher Sn content. Therefore, it is important to keep in mind the well-known affinity between Sn and Cu [192] compared to Cu and Si [193] as the Cu-Sn system has a much lower temperature, therefore kinetics of reactions are expected to be faster compared to Cu-Si. This which

could make the diffusion barriers reported above fail when used with the solid solutions. Nevertheless, some compositions might be worth testing with the solid solutions. Another material has been recently tested as a Cu diffusion barrier for the solid solution in the recently published in the work of Jayachandran *et al.* [194] where they used SS304 foil –stainless-steel containing a minimum of 18% Cr and 88% Ni– as a diffusion barrier between Cu and Bi-doped $\text{Mg}_2\text{Si}_{0.4}\text{Sn}_{0.6}$. Their results showed a significant decrease in the reaction layer thickness ($< 30 \mu\text{m}$) after incorporating the SS304 foil in the joining process, compared to a much thicker reaction layer (up to $300 \mu\text{m}$) during the joining without the diffusion barrier. The chemical stability was also maintained after annealing at $500 \text{ }^\circ\text{C}$ for 15 days.

Another matter to keep in mind is the coefficient of thermal expansion of the sputtered materials. Cr might have worked well up to $400 \text{ }^\circ\text{C}$ between Cu and Si, however its CTE ($6.2 \times 10^{-6} \text{ K}^{-1}$) is quite far from the CTE of the $\text{Mg}_2\text{Si}_{0.3}\text{Sn}_{0.7}$ composition ($17.5 \times 10^{-6} \text{ K}^{-1}$), which enhances the chances of cracking at the interface region between the barrier and the TE material and could lead to a failure of the contacts. These CTE numbers (excluding that of $\text{Mg}_2\text{Si}_{0.3}\text{Sn}_{0.7}$), as well as all the data presented in the following discussion, were taken from [195].

Other experimental techniques could be considered in adding a diffusion barrier layer between Cu and $\text{Mg}_2\text{Si}_{0.3}\text{Sn}_{0.7}$. Even though sputtering seems to be the most commonly used technique, adding a diffusion barrier layer as a thin foil or as powder material could also be considered. In the first case, foils of similar melting temperatures as that of Cu ($\sim 1080 \text{ }^\circ\text{C}$) should be considered, so that the joining temperature (which is usually around half of the melting temperature) works for both materials and allows their adhesion as well as the adhesion of the diffusion barrier to the TE material. Thin foils of bronze or brass could be considered here as they both melt around 900 to $1000 \text{ }^\circ\text{C}$. Bronze with 12 to 15 % Sn content could be a starting point for experimental testing as it also has a CTE of $\sim 18.5 \times 10^{-6} \text{ K}^{-1}$, which is similar to both that of Cu and that of $\text{Mg}_2\text{Si}_{0.3}\text{Sn}_{0.7}$. SEM/EDX investigations of the Cu joined samples in Chapter 3 showed that the reaction layers showed several potential phases based on Cu-Sn-Mg compositions. Adding a layer of CuSn in between could maybe block the Cu from diffusing as the intermediate layer already has Cu that is bound with Sn. Au could also be an option as it is stable and with a similar melting temperature, however it would be a costly solution.

Another suggestion in the Cu contacting procedure could be to process a treatment to the foil and the TE material where both contact surfaces would be grinded and then polished to mirror-like surfaces. Such procedure is not straightforward, and would not be very convenient in technological applications; however, it would potentially give different joining results as the contact surfaces would then be much more homogeneous. The polishing would guarantee a scratch-free surface with optimized parallelism, which would potentially influence the wetting and adhesion between both used materials and result in a different interface. Electrochemical polishing and electric etching might also be a suitable method to clean the foil surface before contacting. Such study might give further scientific insight concerning the

reactions between Cu and the $\text{Mg}_2(\text{Si},\text{Sn})$ system, in particular in the observed local variations in the thickness of the reaction layers.

7.2 Suggestions for the *indirect resistive heating* method

In this work, results of different joining conditions are reported to investigate the influence of the sintering current on the joining process. In fact, Cu and $\text{Ni}_{45}\text{Cu}_{55}$ electrodes were contacted on n- and p-type $\text{Mg}_2\text{Si}_{1-x}\text{Sn}_x$ samples, once under *direct resistive heating* conditions (where the heating of the sample occurs through a direct Joule heating effect of the sample itself) and once under *indirect resistive heating* conditions (where the heating of the sample occurs through a Joule heating effect of the graphite die around the sample). The difference between both conditions mainly resides in the path followed by the sintering current inside the DSP apparatus, whereas all other joining conditions (temperature, time, pressure, heat increase rate) were maintained. Practically, the indirect resistive joining conditions were established through adding an extra layer of boron nitride on the inner base faces of the graphite punches, then using the coated punches to hold the sample inside the graphite die during contacting. As such, the direct vertical path through the sample would be blocked, and the current would be forced to follow the parallel path through the graphite surrounding (punch, die, punch).

The issue with this technique is that, even though the added resistive layer blocked the direct vertical path through the sample, it doesn't guarantee that the current lines will not go from the graphite die towards the sample again. Even though the portion of the current following this path is minor compared to the portion of the current density that simply goes through the graphite die, it is still existing. Therefore, any potential effect of the sintering current on the electrode, the TE material and their joining experiment would not be completely avoided. As much as the assumption of *indirect resistive heating* would stand following the method used in this work, it does not guarantee a total absence of the current through the sample and a completely *indirect* heating.

In order to achieve that, the current lines have to also be blocked from accessing the electrode from the sides (the contact surfaces between the sample and the inner walls of the die). Here too, a resistive layer would be necessary to fully insulate the sample from all current lines. For this, using a boron nitride solution on the inner walls of the die would not work, because as the solution dries, the powder would be scratched off the walls as the TE material, electrode and punches would be inserted. Instead, boron nitride foil would be much cleaner and much easier to keep intact, therefore guaranteeing a better insulation. The boron nitride foil could also be used for the insulation on top and bottom of the sample instead of coating the punches with the solution. By doing so, no breaking and no movement of dried powder would occur, therefore allowing a better and more homogeneous insulation. Using the foil would

also guarantee a similar thickness of the insulating layer, and would make reproducibility and comparability between experiments more reliable.

7.3 Suggestions for the contacting of $Mg_2(Si,Sn)$

As observed from previous literature and through this work, n- and p-type $Mg_2Si_{1-x}Sn_x$ materials displayed different behaviors after contacting with the same electrodes, namely Ag [4], Cu and $Ni_{45}Cu_{55}$. In the case of p-type materials, all mentioned electrodes showed a stable mechanical adhesion and a very low electrical contact resistance. In the cases of Cu and $Ni_{45}Cu_{55}$, diffusion and reaction resulted in thick reaction layers and newly formed phases; nevertheless, they did not affect the TE properties of the optimized material. In these particular cases, if successful diffusion barriers are found, both electrodes can be implemented in technological application with p-type $Mg_2(Si,Sn)$.

The issue remains mainly with n-type materials. We have strong charge carrier compensation that leads to a change in the TE properties. In the particular case of Ag, the resulting electrical contact resistance numbers were also very high ($\sim 180 \mu\Omega \text{ cm}^2$ for samples joined at $600 \text{ }^\circ\text{C}$, and $\sim 400 \mu\Omega \text{ cm}^2$ for samples joined at $450 \text{ }^\circ\text{C}$). To avoid issues related to charge compensation, preliminary calculations of charged defects formation energies of potential electrode materials in the Mg_2Si and the Mg_2Sn binary system could be processed. In our case, we worked with hybrid-DFT calculations and successfully established the reliability of the method in predicting the interactions between an electrode material and the $Mg_2(Si,Sn)$ system. Based on the obtained results, a selection of the electrodes that would not result into a compensation of the carriers could be achieved, and would narrow down the pool of tests. As the TE material of interest is rich in Sn (70%), the behavior of a certain electrode with the Mg_2Sn system would be a reference for the expected behavior of the solid solution. However, having results of both ends of the solid solution spectrums would help guarantee a better result for the compositions in between. Another option would be to run defect calculations for solid solutions, but these are more complex, and would cost more in time and money.

At first, choosing the same electrode for both n- and p-type materials was adopted in order to facilitate experimental testing. In fact, as the TE materials used in this work only differed by their dopants, the same behavior when contacted with a certain electrode was expected. The interactions on the defect level was not in focus compared to chemical diffusion and contact resistances. However, after the studies established during this work, the importance of the defects came strongly into play, and a suggestion to avoid charge carrier compensation is to use different electrodes for n- and p-type samples. As mentioned above, Ag could already be used for p-type, once its thermal stability is tested and confirmed. For n-type, hybrid-DFT calculations could suggest new potential electrodes.

7.4 Expanding the hybrid-DFT calculation to further electrodes: Ti as an example

In Chapters 5 and 6.2, hybrid-DFT calculations of defect formation energies proved to be a good pre-selection tool for contacting electrodes, by investigating the potential interplay between the TE material and the electrode based on their most stable charged point defects. In fact, the observed experimental results with Ag, Cu, Ni were successfully explained through hybrid-DFT calculations.

In this section, we expand the use of this method to another electrode material, namely Ti, and preliminary results of the formation energies of the defects of Ti in Li- and Bi-doped Mg_2Si and Mg_2Sn are provided in Figure 7.1.

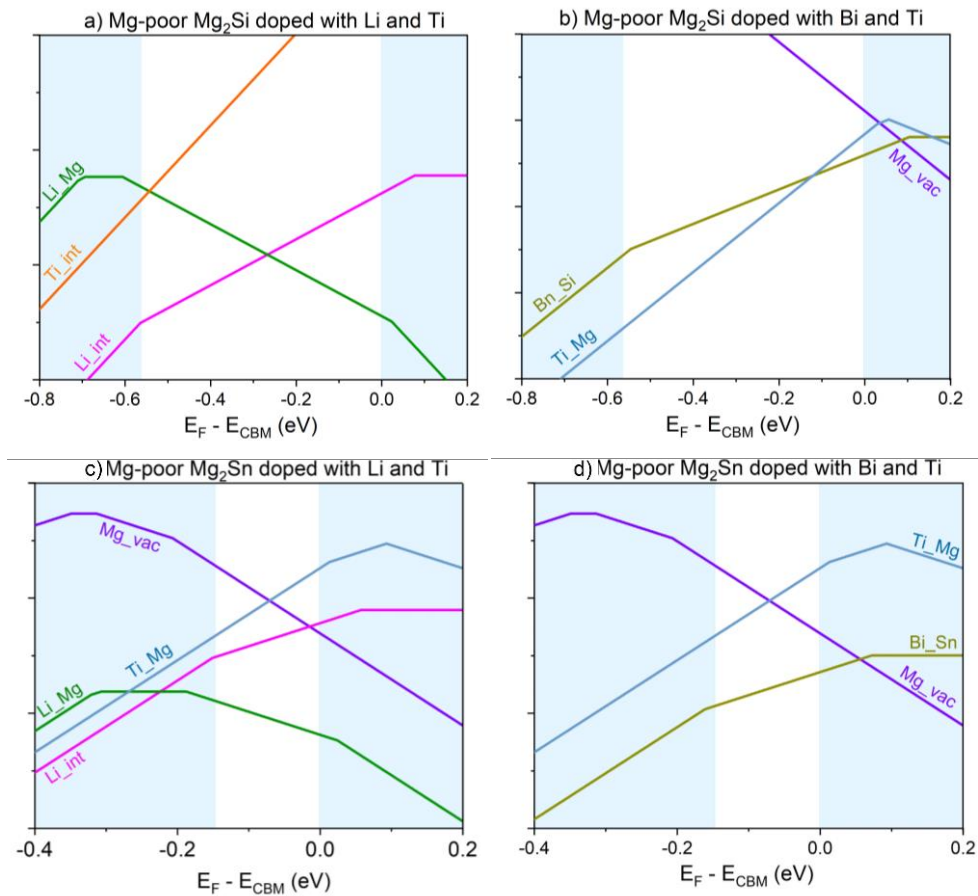


Figure 7.1: Schematics of charged defect formation energies for Ti defects in: a) Li-doped and b) Bi-doped Mg_2Si , c) Li-doped and d) Bi-doped Mg_2Sn , all under Mg-poor conditions. The labeling X_Y of the defects (where X and Y are chemical elements) on the figure correspond to the X_Y labeling in the text. X_{int} and X_{vac} correspond respectively to I_X and V_X .

Figure 7.1 shows the most stable defects in the systems of interest. The most stable Ti-related defect in Bi-doped Mg_2Si and Li- and Bi-doped Mg_2Sn is Ti_{Mg} , which is an electron donor defect of charge $q = 2+$ in the Fermi energy window ranging from $E_{\text{F}} \sim -0.4$ to $E_{\text{F}} \sim -0.05$ eV. As for Li-doped Mg_2Si , the most stable Ti-related defect is I_{Ti} which is also a donor defect of charge $q = 2+$. In all cases, and in the Fermi energy windows of interest (in the vicinity of VBM for p-type, and in the vicinity of CBM for n-type), these Ti defects have higher formation energies than the main dopant defects which are Li_{Mg} for the p-type conduction and $\text{Bi}_{\text{Si/Sn}}$ for the n-type conduction. Such calculation results translate to no significant influence on the charge carrier concentrations of the studied systems to be expected. In the particular case of Bi-doped Mg_2Si , the formation energy of Ti_{Mg} is comparable to that of Bi_{Si} in the vicinity of CBM, which would result in similar defect densities, and thus a significant effect of the carrier concentration and TE properties of the system. However, as Ti_{Mg} is an electron donor defect, the effect won't be observed as charge compensation as seen with Ag or Cu electrodes. In fact, Ti_{Mg} will add electrons to the carrier concentration, and would eventually result in higher n-type doping.

Based on these predictions, Ti could be tested experimentally on n- and p-type compositions of the $\text{Mg}_2\text{Si}_{1-x}\text{Sn}_x$ solid solution, as it has potential to be a successful candidate. Moreover, experimental tests would help in providing another comparative case to verify the match between experiments and predictions from hybrid-DFT calculations are put together.

Bibliography

Below are the references used in Chapters 1 (Introduction), 2 (Methods), 6 (Discussion) and 7 (Conclusions and Outlook).

- [1] A. Sankhla, A. Patil, H. Kamila, M. Yasseri, N. Farahi, E. Mueller, J. de Boor, Mechanical alloying of optimized $Mg_2(Si,Sn)$ solid solutions: Understanding phase evolution and tuning synthesis parameters for thermoelectric applications, *ACS Appl. Energy Mater.* 1(2) (2018) 531-542.
- [2] N. Farahi, C. Stiewe, D.N. Truong, J. de Boor, E. Müller, High efficiency $Mg_2(Si,Sn)$ -based thermoelectric materials: scale-up synthesis, functional homogeneity, and thermal stability, *RSC Adv.* 9(40) (2019) 23021-23028.
- [3] H. Kamila, M. Yasseri, N. Pham, N. Farahi, E. Müller, J. de Boor, Synthesis of p-type $Mg_2Si_{1-x}Sn_x$ with $x= 0-1$ and optimization of the synthesis parameters, *Mater.Today: Proc.* 8 (2019) 546-555.
- [4] N.H. Pham, N. Farahi, H. Kamila, A. Sankhla, S. Ayachi, E. Müller, J. de Boor, Ni and Ag electrodes for magnesium silicide based thermoelectric generators, *Mater. Today Energy* 11 (2019) 97-105.
- [5] J. de Boor, C. Gloanec, H. Kolb, R. Sottong, P. Ziolkowski, E. Müller, Fabrication and characterization of nickel contacts for magnesium silicide based thermoelectric generators, *J. Alloys Compd.* 632 (2015) 348-353.
- [6] J. He, T.M. Tritt, Advances in thermoelectric materials research: Looking back and moving forward, *Science* 357(6358) (2017) eaak9997.
- [7] T.M. Tritt, Thermoelectric phenomena, materials, and applications, *Annu. Rev. Mater. Res.* 41 (2011) 433-448.
- [8] D.D. Pollock, Thermoelectricity: theory, thermometry, tool, ASTM International (1985).
- [9] I. Terasaki, Comprehensive semiconductor science and technology, (2011) 326.
- [10] G.W. Sutton, Direct energy conversion, (1966).
- [11] M. Lundstrom, A. Shakouri, Introduction to thermoelectricity, (2019).
- [12] V. Drebuschak, The peltier effect, *J. Therm. Anal. Calorim.* 91(1) (2008) 311.
- [13] E.J. Sandoz-Rosado, S.J. Weinstein, R.J. Stevens, On the Thomson effect in thermoelectric power devices, *Int. J. Therm. Sci.* 66 (2013) 1-7.
- [14] H. Lee, The Thomson effect and the ideal equation on thermoelectric coolers, *Energy* 56 (2013) 61-69.
- [15] H. Lee, Thermoelectrics: design and materials, Wiley (2016).
- [16] F.J. DiSalvo, Thermoelectric cooling and power generation, *Science* 285(5428) (1999) 703-706.
- [17] H.S. Kim, W. Liu, Z. Ren, The bridge between the materials and devices of thermoelectric power generators, *Energy & Environ. Sci.* 10(1) (2017) 69-85.
- [18] W. Liu, Q. Jie, H.S. Kim, Z. Ren, Current progress and future challenges in thermoelectric power generation: From materials to devices, *Acta Mater.* 87 (2015) 357-376.
- [19] R. Chasmar, R. Stratton, The thermoelectric figure of merit and its relation to thermoelectric generators, *Int. J. Electron.* 7(1) (1959) 52-72.
- [20] B. Sherman, R.R. Heikes, R.W. Ure Jr, *J. Appl. Phys.*, Calculation of efficiency of thermoelectric devices, 31(1) (1960) 1-16.
- [21] S. Priya, D.J. Inman, Energy harvesting technologies, Springer (2009).
- [22] D.K. Aswal, R. Basu, A. Singh, Key issues in development of thermoelectric power generators: High figure-of-merit materials and their highly conducting interfaces with metallic interconnects, *Energy Convers. Manage.* 114 (2016) 50-67.
- [23] D. Ebling, K. Bartholomé, M. Bartel, M. Jäggle, Module geometry and contact resistance of thermoelectric generators analyzed by multiphysics simulation, *J. Electron. Mater.* 39(9) (2010) 1376-1380.
- [24] K. Zabrocki, C. Goupil, H. Ouerdane, Y. Apertet, W. Seifert, E. Müller, Continuum theory of TE elements, continuum theory and modeling of thermoelectric elements, Wiley (2016), 75-156.

- [25] P. Zhu, Y. Imai, Y. Isoda, Y. Shinohara, X. Jia, G. Zou, Enhanced thermoelectric properties of PbTe alloyed with Sb₂Te₃, *J. Phys.: Condens. Matter* 17(46) (2005) 7319.
- [26] J. Martin, L. Wang, L. Chen, G. Nolas, Enhanced Seebeck coefficient through energy-barrier scattering in PbTe nanocomposites, *Phys. Rev. B Condens. Matter* 79(11) (2009) 115311.
- [27] S. Wang, Z. Yang, Y. Sun, Y. Xiao, L.D. Zhao, Synergistically optimizing charge and phonon transport properties in n-type PbTe via introducing ternary compound AgSb(Se,Te)₂, *J. Alloys Compd.* 815 (2020) 152463
- [28] J. Li, Z. Lu, S. Li, F. Liu, W. Ao, Y. Li, High thermoelectric properties of PbTe–Sm₂Se₃ composites, *Scr. Mater.* 112 (2016) 144-147.
- [29] G. Rogl, K. Yubuta, V. Romaka, H. Michor, E. Schafner, A. Grytsiv, E. Bauer, P. Rogl, High-ZT half-Heusler thermoelectrics, Ti_{0.5}Zr_{0.5}NiSn and Ti_{0.5}Zr_{0.5}NiSn_{0.98}Sb_{0.02}: Physical properties at low temperatures, *Acta Mater.* 166 (2019) 466-483.
- [30] R. He, H. Zhu, J. Sun, J. Mao, H. Reith, S. Chen, G. Schierning, K. Nielsch, Z. Ren, Improved thermoelectric performance of n-type half-Heusler MCo_{1-x}Ni_xSb (M= Hf, Zr), *Mater. Today Phys.* 1 (2017) 24-30.
- [31] Y. Xing, R. Liu, J. Liao, Q. Zhang, X. Xia, C. Wang, H. Huang, J. Chu, M. Gu, T. Zhu, High-efficiency half-Heusler thermoelectric modules enabled by self-propagating synthesis and topologic structure optimization, *Energy & Environ. Sci.* 12(11) (2019) 3390-3399.
- [32] Y. Lei, W. Gao, R. Zheng, Y. Li, R. Wan, W. Chen, L. Ma, H. Zhou, P.K. Chu, Rapid synthesis, microstructure, and thermoelectric properties of skutterudites, *J. Alloys and Compd.* 806 (2019) 537-542.
- [33] G. Rogl, P. Rogl, Skutterudites, A most promising group of thermoelectric materials, *Curr. Opin. Green and Sustain.* 4 (2017) 50-57.
- [34] G. Rogl, P. Rogl, Skutterudites: Progress and challenges, novel thermoelectric materials and device design concepts, Springer (2019), 177-201.
- [35] J. Tani, H. Kido, First-principles and experimental studies of impurity doping into Mg₂Si, *Intermetallics* 16(3) (2008) 418-423.
- [36] H. Kamila, P. Sahu, A. Sankhla, M. Yasserli, H.N. Pham, T. Dasgupta, E. Mueller, J. de Boor, Analyzing transport properties of p-type Mg₂Si–Mg₂Sn solid solutions: Optimization of thermoelectric performance and insight into the electronic band structure, *J. Mater. Chem. A* 7(3) (2019) 1045-1054.
- [37] M. Yasserli, A. Sankhla, H. Kamila, R. Orenstein, D.N. Truong, N. Farahi, J. de Boor, E. Mueller, Solid solution formation in Mg₂(Si, Sn) and shape of the miscibility gap, *Acta Mater.* 185 (2020) 80-88.
- [38] Z. Du, T. Zhu, X. Zhao, Enhanced thermoelectric properties of Mg₂Si_{0.58}Sn_{0.42} compounds by Bi doping, *Mater. Lett.* 66(1) (2012) 76-78.
- [39] M.I. Fedorov, V.K. Zaitsev, G.N. Isachenko, High effective thermoelectrics based on the Mg₂Si–Mg₂Sn solid solution, *Solid State Phenom.* 170 (2011) 286-292.
- [40] W. Liu, H.S. Kim, S. Chen, Q. Jie, B. Lv, M. Yao, Z. Ren, C.P. Opeil, S. Wilson, C.W. Chu, n-type thermoelectric material Mg₂Sn_{0.75}Ge_{0.25} for high power generation, *PNAS* 112(11) (2015) 3269-3274.
- [41] X. Liu, L. Xi, W. Qiu, J. Yang, T. Zhu, X. Zhao, W. Zhang, Significant roles of intrinsic point defects in Mg₂X (X= Si, Ge, Sn) thermoelectric materials, *Adv. Electron. Mater.* 2(2) (2016) 1500284.
- [42] D.M. Rowe, CRC handbook of thermoelectrics, CRC Press (2018).
- [43] A.A. Luo, Recent magnesium alloy development for automotive powertrain applications, *Mater. Sci. Forum* 419, (2003) 57-66.
- [44] R. Santos, S.A. Yamini, S.X. Dou, Recent progress in magnesium-based thermoelectric materials, *J. Mater. Chem. A* 6(8) (2018) 3328-3341.
- [45] V. Zaitsev, M. Fedorov, E. Gurieva, I. Eremin, P. Konstantinov, A.Y. Samunin, M. Vedernikov, Highly effective Mg₂Si_{1-x}Sn_x thermoelectrics, *Phys. Rev. B* 74(4) (2006) 045207.
- [46] H.S. Kim, K. Kikuchi, T. Itoh, T. Iida, M. Taya, Design of segmented thermoelectric generator based on cost-effective and light-weight thermoelectric alloys, *Mater. Sci. Eng. B* 185 (2014) 45-52.
- [47] T. Zhu, Y. Liu, C. Fu, J.P. Heremans, J.G. Snyder, X. Zhao, Compromise and synergy in high-efficiency thermoelectric materials, *Adv. Mater.* 29(14) (2017) 1605884.
- [48] M. Ioannou, G. Polymeris, E. Hatzikraniotis, K. Paraskevopoulos, T. Kyratsi, Effect of Bi-doping and Mg-excess on the thermoelectric properties of Mg₂Si materials, *J. Phys. Chem. Solids* 75(8) (2014) 984-991.

- [49] A. Khan, N. Vlachos, T. Kyratsi, High thermoelectric figure of merit of $\text{Mg}_2\text{Si}_{0.55}\text{Sn}_{0.4}\text{Ge}_{0.05}$ materials doped with Bi and Sb, *Scr. Mater.* 69(8) (2013) 606-609.
- [50] H. Gao, T. Zhu, X. Liu, L. Chen, X. Zhao, Flux synthesis and thermoelectric properties of eco-friendly Sb doped $\text{Mg}_2\text{Si}_{0.5}\text{Sn}_{0.5}$ solid solutions for energy harvesting, *J. Mater. Chem.* 21(16) (2011) 5933-5937.
- [51] Y. Sadia, Y. Gelbstein, Silicon-rich higher manganese silicides for thermoelectric applications, *J. Electron. Mater.* 41(6) (2012) 1504-1508.
- [52] P. Norouzzadeh, Z. Zamanipour, J.S. Krasinski, D. Vashaee, The effect of nanostructuring on thermoelectric transport properties of p-type higher manganese silicide $\text{MnSi}_{1.73}$, *J. Appl. Phys.* 112(12) (2012) 124308.
- [53] G. Skomedal, L. Holmgren, H. Middleton, I. Eremin, G. Isachenko, M. Jaegle, K. Tarantik, N. Vlachos, M. Manoli, T. Kyratsi, Design, assembly and characterization of silicide-based thermoelectric modules, *Energy Convers. Manage.* 110 (2016) 13-21.
- [54] Y. Gelbstein, J. Tunbridge, R. Dixon, M.J. Reece, H. Ning, R. Gilchrist, R. Summers, I. Agote, M.A. Lagos, K. Simpson, Physical, mechanical, and structural properties of highly efficient nanostructured n-and p-silicides for practical thermoelectric applications, *J. Electron. Mater.* 43(6) (2014) 1703-1711.
- [55] M. Søndergaard, M. Christensen, K.A. Borup, H. Yin, B.B. Iversen, Thermoelectric properties of the entire composition range in $\text{Mg}_2\text{Si}_{0.9925-x}\text{Sn}_x\text{Sb}_{0.0075}$, *J. Electron. Mater.* 42(7) (2013) 1417-1421.
- [56] I. Engström, B. Lönnberg, Thermal expansion studies of the group IV-VII transition-metal disilicides, *J. Appl. Phys.* 63(9) (1988) 4476-4484.
- [57] P. Zwolenski, J. Tobola, S. Kaprzyk, A theoretical search for efficient dopants in Mg_2X (X= Si, Ge, Sn) thermoelectric materials, *J. Electron. Mater.* 40(5) (2011) 889-897.
- [58] J. de Boor, T. Dasgupta, U. Saparamadu, E. Müller, Z. Ren, Recent progress in p-type thermoelectric magnesium silicide based solid solutions, *Mater. Today Energy* 4 (2017) 105-121.
- [59] J. de Boor, U. Saparamadu, J. Mao, K. Dahal, E. Müller, Z. Ren, Thermoelectric performance of Li doped, p-type $\text{Mg}_2(\text{Ge}, \text{Sn})$ and comparison with $\text{Mg}_2(\text{Si}, \text{Sn})$, *Acta Mater.* 120 (2016) 273-280.
- [60] U. Saparamadu, J. De Boor, J. Mao, S. Song, F. Tian, W. Liu, Q. Zhang, Z. Ren, Comparative studies on thermoelectric properties of p-type $\text{Mg}_2\text{Sn}_{0.75}\text{Ge}_{0.25}$ doped with lithium, sodium, and gallium, *Acta Mater* 141 (2017) 154-162.
- [61] S. Kasap, Hall effect in semiconductors, *Electron. Booklet* 1(1) (2001).
- [62] C. Chien, The Hall effect and its applications, Springer Science & Business (2013).
- [63] G.J. Snyder, E.S. Toberer, Complex thermoelectric materials, materials for sustainable energy: A collection of peer-reviewed research and review articles from Nature Publishing Group, World Scientific (2011) 101-110.
- [64] A.Y. Samunin, V. Zaitsev, P. Konstantinov, M. Fedorov, G. Isachenko, A. Burkov, S. Novikov, E. Gurieva, Thermoelectric properties of hot-pressed materials based on $\text{Mg}_2\text{Si}_n\text{Sn}_{1-n}$, *J. Electron. Mater.* 42(7) (2013) 1676-1679.
- [65] J. Chen, W. Xue, S. Li, G. Zhang, G. Cai, H. Zhao, Enhanced thermoelectric properties in n-type $\text{Mg}_2\text{Si}_{0.4-x}\text{Sn}_{0.6}\text{Sb}_x$ synthesized by alkaline earth metal reduction, *RSC Adv.* 9(7) (2019) 4008-4014.
- [66] Q. Zhang, L. Cheng, W. Liu, Y. Zheng, X. Su, H. Chi, H. Liu, Y. Yan, X. Tang, C. Uher, Low effective mass and carrier concentration optimization for high performance p-type $\text{Mg}_{2(1-x)}\text{Li}_{2x}\text{Si}_{0.3}\text{Sn}_{0.7}$ solid solutions, *Phys. Chem.Chem. Phys.* 16(43) (2014) 23576-23583.
- [67] D. Ebling, M. Jaegle, M. Bartel, A. Jacquot, H. Böttner, Multiphysics simulation of thermoelectric systems for comparison with experimental device performance, *J. Electron. Mater.* 38(7) (2009) 1456-1461.
- [68] J. de Boor, D. Droste, C. Schneider, J. Janek, E. Mueller, Thermal stability of magnesium silicide/nickel contacts, *J. Electron. Mater.* 45(10) (2016) 5313-5320.
- [69] J. Tani, H. Kido, Thermoelectric properties of Bi-doped Mg_2Si semiconductors, *Physica B: Condens. Matter* 364(1-4) (2005) 218-224.
- [70] A. Ferrario, S. Battiston, S. Boldrini, T. Sakamoto, E. Miorin, A. Famengo, A. Miozzo, S. Fiameni, T. Iida, M. Fabrizio, Mechanical and electrical characterization of low-resistivity contact materials for Mg_2Si , *Mater. Today: Proc.* 2(2) (2015) 573-582.
- [71] B. Zhang, T. Zheng, Q. Wang, Y. Zhu, H.N. Alshareef, M.J. Kim, B.E. Gnade, Compounds, Contact resistance and stability study for Au, Ti, Hf and Ni contacts on thin-film Mg_2Si , *J. Alloys Compd.* 699 (2017) 1134-1139.

- [72] L. Cai, P. Li, P. Wang, Q. Luo, P. Zhai, Q. Zhang, Duration of thermal stability and mechanical properties of Mg₂Si/Cu thermoelectric joints, *J. Electron. Mater.* 47(5) (2018) 2591-2599.
- [73] J. Crofton, L. Porter, J. Williams, The physics of ohmic contacts to SiC, *Phys. Status Solidi B* 202(1) (1997) 581-603.
- [74] A. Piotrowska, A. Guivarc'h, G. Pelous, Ohmic contacts to III–V compound semiconductors: A review of fabrication techniques, *Solid-State Electron.* 26(3) (1983) 179-197.
- [75] T. Blank, Y.A Gol'Dberg, Mechanisms of current flow in metal-semiconductor ohmic contacts, *Semiconductors* 41(11) (2007) 1263-1292.
- [76] A. Baca, F. Ren, J. Zolper, R. Briggs, S.J. Pearton, A survey of ohmic contacts to III-V compound semiconductors, *Thin Solid Films* 308 (1997) 599-606.
- [77] B. Schwartz, Ohmic contacts to semiconductors, Electronics Division, Electrochemical Society (1969).
- [78] Y. Chen, Y. Li, J. Wu, W. Duan, General criterion to distinguish between Schottky and ohmic contacts at the metal/two-dimensional semiconductor interface, *Nanoscale* 9(5) (2017) 2068-2073.
- [79] B.M. Wilamowski, Schottky diodes with high breakdown voltages, *Solid-State Electron.* 26(5) (1983) 491-493.
- [80] W. Schottky, Discrepancies in Ohm's laws in semiconductors, *Phys. Z* 41 (1940) 570-573.
- [81] C.Y. Chang, Y.K. Fang, S.M. Sze, Specific contact resistance of metal-semiconductor barriers, *Solid-State Electron.* 14(7) (1971) 541-550.
- [82] S.S. Cohen, G.S. Gildenblat, Metal–semiconductor contacts and devices, Academic Press (2014).
- [83] S. Timsit, Electrical contact resistance: properties of stationary interfaces, Electrical Contacts, 44th IEEE Holm Conference on Electrical Contacts Proc, IEEE (1998), 1-19.
- [84] H.J. Queisser, E.E. Haller, Defects in semiconductors: some fatal, some vital, *Science* 281(5379) (1998) 945-950.
- [85] S. Ögüt, K.M. Rabe, Band gap and stability in the ternary intermetallic compounds NiSnM (M= Ti, Zr, Hf): A first-principles study, *Phys. Rev. B* 51(16) (1995) 10443.
- [86] L. Hu, T. Zhu, X. Liu, X. Zhao, Point defect engineering of high-performance Bismuth-Telluride-based thermoelectric materials, *Adv. Funct. Mater.* 24(33) (2014) 5211-5218.
- [87] Y. Qiu, L. Xi, X. Shi, P. Qiu, W. Zhang, L. Chen, J.R. Salvador, J.Y. Cho, J. Yang, Y. Chien, Charge-compensated compound defects in Ga-containing thermoelectric skutterudites, *Adv. Funct. Mater.* 23(25) (2013) 3194-3203.
- [88] G. Jiang, J. He, T. Zhu, C. Fu, X. Liu, L. Hu, X. Zhao, High performance Mg₂(Si,Sn) solid solutions: A point defect chemistry approach to enhancing thermoelectric properties, *Adv. Funct. Mater.* 24(24) (2014) 3776-3781.
- [89] P. Jund, R. Viennois, C. Colinet, G. Hug, M. Fèvre, J.C. Tedenac, Lattice stability and formation energies of intrinsic defects in Mg₂Si and Mg₂Ge via first principles simulations, *J. Phys.: Cond. Matter* 25(3) (2012) 035403.
- [90] A. Berche, P. Jund, Thermoelectric power factor of pure and doped ZnSb via DFT based defect calculations, *PCCP* 21(41) (2019) 23056-23064.
- [91] A. Kato, T. Yagi, N. Fukusako, First-principles studies of intrinsic point defects in magnesium silicide, *J. Phys.: Cond. Matter* 21(20) (2009) 205801.
- [92] S.W. You, I.H. Kim, S.M. Choi, W.S. Seo, Thermoelectric properties of Bi-doped Mg₂Si_{1-x}Sn_x prepared by mechanical alloying, *J. Korean Phys. Soc.* 63(11) (2013) 2153-2157.
- [93] N. Farahi, S. Prabhudev, G.A. Botton, J.R. Salvador, H. Kleinke, Nano- and microstructure engineering: An effective method for creating high efficiency magnesium silicide based thermoelectrics, *ACS Appl. Mater. & Interfaces* 8(50) (2016) 34431-34437.
- [94] E.G. Araújo, R.M.L. Neto, M.F. Pillis, F. Filho, High energy ball mill processing, *Mater. Sci. Forum* (2003) 128-133.
- [95] S. Banerjee, P. Mukhopadhyay, Phase transformations: examples from titanium and zirconium alloys, Elsevier (2010).
- [96] S. Ayachi, G. Castillo Hernandez, N.H. Pham, N. Farahi, E. Müller, J. de Boor, Developing contacting solutions for Mg₂Si_{1-x}Sn_x-Based thermoelectric generators: Cu and Ni₄₅Cu₅₅ as potential contacting electrodes, *ACS Appl. Mater. Interfaces* 11(43) (2019) 40769-40780.
- [97] G. Castillo-Hernandez, M. Yasserli, B. Klobes, S. Ayachi, E. Müller, J. de Boor, Room and high temperature mechanical properties of Mg₂Si, Mg₂Sn and their solid solutions, *J. Alloys Compd.* 845 (2020) 156205.

- [98] R.M. German, Sintering with external pressure, sintering: from empirical observations to scientific principles, Elsevier (2014) 305-354.
- [99] H. Atkinson, S. Davies, Fundamental aspects of hot isostatic pressing: An overview, *Metall. Mater. Trans. A* 31(12) (2000) 2981-3000.
- [100] J. Torralba, Improvement of mechanical and physical properties in powder metallurgy, Elsevier (2014).
- [101] L.F. Francis, Powder Processes, Materias Processing, Academic Press (2016) 343-414.
- [102] V. Solozhenko, A. Lazarenko, J.P. Petitet, A. Kanaev, Bandgap energy of graphite-like hexagonal boron nitride, *J. Phys. Chem. Solids* 62(7) (2001) 1331-1334.
- [103] K. Akhtar, S.A. Khan, S.B. Khan, A.M. Asiri, Scanning electron microscopy: Principle and applications in nanomaterials characterization, Handbook of Materials Characterization, Springer (2018) 113-145.
- [104] D.E. Newbury, N.W. Ritchie, Is scanning electron microscopy/energy dispersive X-ray spectrometry (SEM/EDS) quantitative?, *Scanning* 35(3) (2013) 141-168.
- [105] D. Platzek, G. Karpinski, C. Stiewe, P. Ziolkowski, C. Drasar, E. Muller, Potential-Seebeck-microprobe (PSM): measuring the spatial resolution of the Seebeck coefficient and the electric potential, *ICT 2005 Proceedings*, IEEE, (2005) 13-16.
- [106] P. Ziolkowski, M. Wambach, A. Ludwig, E. Mueller, Application of high-throughput Seebeck microprobe measurements on thermoelectric half-heusler thin film combinatorial material libraries, *ACS Comb. Sci.* 20(1) (2018) 1-18.
- [107] P. Ziolkowski, G. Karpinski, T. Dasgupta, E. Mueller, Probing thermopower on the microscale, *Phys. Status Solidi A* 210(1) (2013) 89-105.
- [108] K.N. Chen, A. Fan, C. Tan, R. Reif, Contact resistance measurement of bonded copper interconnects for three-dimensional integration technology, *IEEE Electron Device Lett.* 25(1) (2004) 10-12.
- [109] S. Nakamura, Y. Mori, K. Takarabe, Analysis of the microstructure of Mg₂Si thermoelectric devices, *J. Electron Mater.* 43(6) (2014) 2174-2178.
- [110] Y. Thimont, Q. Lognoné, C. Goupil, F. Gascoin, E. Guilmeau, Design of apparatus for Ni/Mg₂Si and Ni/MnSi_{1.75} contact resistance determination for thermoelectric legs, *J. Electron Mater.* 43(6) (2014) 2023-2028.
- [111] B. Ryu, S. Park, E.A. Choi, J. de Boor, P. Ziolkowski, J. Chung, S.D. Park, Hybrid-functional and quasi-particle calculations of band structures of Mg₂Si, Mg₂Ge, and Mg₂Sn, *J. Korean Phys. Soc.* 75(2) (2019) 144-152.
- [112] K. Burke, The ABC of DFT, Department of Chemistry, University of California Irvine (2007).
- [113] K. Burke, Perspective on density functional theory, *J. Chem. Phys.* 136(15) (2012) 150901.
- [114] E. Runge, E. Gross, Density-functional theory for time-dependent systems, *Phys. Rev. Lett.* 52(12) (1984) 997.
- [115] P. Hohenberg, W. Kohn, Inhomogeneous electron gas, *Phys. Rev.* 136(3B) (1964) B864.
- [116] P. Geerlings, F. De Proft, W. Langenaeker, Conceptual density functional theory, *Chem. Rev.* 103(5) (2003) 1793-1874.
- [117] G.A Hagedorn, A time dependent Born-Oppenheimer approximation, *Commun. Math. Phys.* 77(1) (1980) 1-19.
- [118] J.M. Combes, P. Duclos, R. Seiler, The Born-Oppenheimer approximation, Rigorous atomic and molecular physics, Springer (1981) 185-213.
- [119] H. Essén, The physics of the Born–Oppenheimer approximation, *Int. J. Quantum Chem.* 12(4) (1977) 721-735..
- [120] H. Feldmeier, Fermionic molecular dynamics, *Nucl. Phys. A* 515(1) (1990) 147-172.
- [121] D.M. Ceperley, Fermion nodes, *J. Stat. Phys.* 63(5) (1991) 1237-1267.
- [122] J.C. Slater, A simplification of the Hartree-Fock method, *Phys. Rev.* 81(3) (1951) 385.
- [123] J.G. Valatin, Generalized Hartree-Fock method, *Phys. Rev.* 122(4) (1961) 1012.
- [124] P. Lykos, G. Pratt, Discussion on the Hartree-Fock approximation, *Rev. Mod. Phys.* 35(3) (1963) 496.
- [125] W. Kohn, L.J. Sham, Self-consistent equations including exchange and correlation effects, *Phys. Rev.* 140(4A) (1965) A1133.
- [126] V. Karasiev, T. Sjöstrom, J. Dufty, S. Trickey, Local density approximation exchange-correlation free-energy functional, *APS* (2014) A1. 009.

- [127] M. Lewin, E.H. Lieb, R. Seiringer, The local density approximation in density functional theory, *Pure Appl. Anal.* 2(1) (2019) 35-73.
- [128] P. Misra, Physics of condensed matter, Academic Press (2011).
- [129] C. Hsing, M. Chou, T.K. Lee, Exchange-correlation energy in molecules: A variational quantum Monte Carlo study, *Phys. Rev. A* 74(3) (2006) 032507.
- [130] R.Q. Hood, M. Chou, A. Williamson, G. Rajagopal, R. Needs, W. Foulkes, Quantum monte carlo investigation of exchange and correlation in silicon, *Phys. Rev. Lett.* 78(17) (1997) 3350.
- [131] J.P. Perdew, K. Burke, M. Ernzerhof, Generalized gradient approximation made simple, *Phys. Rev. Lett.* 77(18) (1996) 3865.
- [132] J.P. Perdew, K. Burke, Y. Wang, Generalized gradient approximation for the exchange-correlation hole of a many-electron system, *Phys. Rev. B* 54(23) (1996) 16533.
- [133] Y. Zhang, W. Yang, Comment on “Generalized gradient approximation made simple”, *Phys. Rev. Lett.* 80(4) (1998) 890.
- [134] R.Q. Hood, P. Kent, F.A. Reboredo, Diffusion quantum Monte Carlo study of the equation of state and point defects in aluminum, *Phys. Rev. B* 85(13) (2012) 134109.
- [135] B. Huang, H. Lee, Defect and impurity properties of hexagonal boron nitride: A first-principles calculation, *Phys. Rev. B* 86(24) (2012) 245406.
- [136] M. Ernzerhof, G.E. Scuseria, Assessment of the Perdew–Burke–Ernzerhof exchange-correlation functional, *J. Chem. Phys.* 110(11) (1999) 5029-5036.
- [137] X. Xu, W.A. Goddard III, The extended Perdew-Burke-Ernzerhof functional with improved accuracy for thermodynamic and electronic properties of molecular systems, *J. Chem. Phys.* 121(9) (2004) 4068-4082.
- [138] M. Giantomassi, M. Stankovski, R. Shaltaf, M. Grüning, F. Bruneval, P. Rinke, G.M. Rignanese, Electronic properties of interfaces and defects from many-body perturbation theory: Recent developments and applications, *Phys. Status Solidi B* 248(2) (2011) 275-289.
- [139] M. Grüning, A. Marini, A. Rubio, Density functionals from many-body perturbation theory: The band gap for semiconductors and insulators, *J. Chem. Phys.* 124(15) (2006) 154108.
- [140] B. Ryu, E.A. Choi, S. Park, J. Chung, J. de Boer, P. Ziolkowski, E. Müller, S.D. Park, Native point defects and low p-doping efficiency in $\text{Mg}_2(\text{Si},\text{Sn})$ solid solutions: A hybrid-density functional study, *J. Alloys Compd.* 853 (2021) 157145.
- [141] S. Zhang, J.E. Northrup, Chemical potential dependence of defect formation energies in GaAs: Application to Ga self-diffusion, *Phys. Rev. Lett.* 67(17) (1991) 2339.
- [142] B. Ryu, M.W. Oh, J.K. Lee, J.E. Lee, S.J. Joo, B.S. Kim, B.K. Min, H.W. Lee, S.D. Park, Defects responsible for abnormal n-type conductivity in Ag-excess doped PbTe thermoelectrics, *J. Appl. Phys.* 118(1) (2015) 015705.
- [143] C.G. Van de Walle, J. Neugebauer, First-principles calculations for defects and impurities: Applications to III-nitrides, *J. Appl. Phys.* 95(8) (2004) 3851-3879.
- [144] C. Freysoldt, B. Lange, J. Neugebauer, Q. Yan, J.L. Lyons, A. Janotti, C.G. Van de Walle, Electron and chemical reservoir corrections for point-defect formation energies, *Phys. Rev. B* 93(16) (2016) 165206.
- [145] S. Ayachi, G.C. Hernandez, E. Müller, J. de Boer, Contacting Cu electrodes to $\text{Mg}_2\text{Si}_{0.3}\text{Sn}_{0.7}$: Direct vs. indirect resistive heating, *Semiconductors* 53(13) (2019) 1825-1830.
- [146] S. Ayachi, R. Deshpande, P. Ponnusamy, S. Park, J. Chung, S. Park, B. Ryu, E. Müller, J. de Boer, On the relevance of point defects for the selection of contacting electrodes: Ag as an example for $\text{Mg}_2(\text{Si}, \text{Sn})$ -based thermoelectric generators, *Mater. Today Phys.* (2020) 100309.
- [147] J. Chu, J. Huang, R. Liu, J. Liao, X. Xia, Q. Zhang, C. Wang, M. Gu, S. Bai, X. Shi, L. Chen, Electrode interface optimization advances conversion efficiency and stability of thermoelectric devices, *Nat. Commun.* 11(1) (2020) 1-8.
- [148] W.D. Liu, Z.G. Chen, J. Zou, Eco-Friendly Higher Manganese Silicide Thermoelectric Materials: Progress and Future Challenges, *Adv. Energy Mater.* 8(19) (2018) 1800056.
- [149] N.H. Pham, N. Farahi, H. Kamila, A. Sankhla, S. Ayachi, E. Müller, J. de Boer, Ni and Ag electrodes for magnesium silicide based thermoelectric generators, *Mater. Today Energy* 11 (2019) 97-105.
- [150] J. Camut, N.H. Pham, D.Y.N. Truong, G. Castillo-Hernandez, N. Farahi, M. Yasseri, E. Mueller, J. de Boer, Aluminum as promising electrode for $\text{Mg}_2(\text{Si},\text{Sn})$ -based thermoelectric devices, *Mater. Today Energy* (2021) 100718.

- [151] M. Yasseri, D. Schüpfer, M. Weinhold, L. Chen, H. Kamila, E. Mueller, J. de Boor, P.J. Klar, Comparing Raman mapping and electron microscopy for characterizing compositional gradients in thermoelectric materials, *Scr. Mater.* 179 (2020) 61-64.
- [152] H. Kamila, G. Goyal, A. Sankhla, P. Ponnusamy, E. Mueller, T. Dasgupta, J. de Boor, Systematic analysis of the interplay between synthesis route, microstructure, and thermoelectric performance in p-type $\text{Mg}_2\text{Si}_{0.2}\text{Sn}_{0.8}$, *Mater. Today Phys.* 9 (2019) 100133.
- [153] S. Kochawattana, A. Stevenson, S.-H. Lee, M. Ramirez, V. Gopalan, J. Dumm, V.K. Castillo, G.J. Quarles, G.L. Messing, Sintering and grain growth in SiO_2 doped Nd:YAG, *J. Eur. Ceram. Soc.* 28(7) (2008) 1527-1534.
- [154] B. Stawarczyk, M. Özcan, L. Hallmann, A. Ender, A. Mehl, C.H.F. Hämmerlet, The effect of zirconia sintering temperature on flexural strength, grain size, and contrast ratio, *Clin. Oral Investig.* 17(1) (2013) 269-274.
- [155] A. Kozlov, J. Gröbner, R. Schmid-Fetzer, compounds, Phase formation in Mg–Sn–Si and Mg–Sn–Si–Ca alloys, *J. Alloys Compd.* 509(7) (2011) 3326-3337.
- [156] M. Yasseri, N. Farahi, K. Kelm, E. Mueller, J. de Boor, Rapid determination of local composition in quasi-binary, inhomogeneous material systems from backscattered electron image contrast, *Materialia* (2018).
- [157] N. Bochvar, E. Lysova, L. Rokhlin, Cu-Mg-Si (Copper-Magnesium-Silicon), Light Metal Systems. Part 4, Springer Materials (2006).
- [158] L. Rokhlin, E. Lysova, Cu-Mg-Sn (Copper-Magnesium-Tin), Light Metal Systems. Part 4, Springer Materials (2006).
- [159] S. Tumminello, S. Ayachi, S.G. Fries, J. de Boor, E. Müller, Applications of thermodynamic calculations to practical TEG design: $\text{Mg}_2(\text{Si}_{0.3}\text{Sn}_{0.7})/\text{Cu}$ interconnections, *J. Mater. Chem. A* (2021) Advance Article.
- [160] N.K. Karri, C. Mo, Structural reliability evaluation of thermoelectric generator modules: Influence of end conditions, leg geometry, metallization, and processing temperatures, *J. Electron. Mater.* 47(10) (2018) 6101-6120.
- [161] S. Zhao, G.M. Stocks, Y. Zhang, Defect energetics of concentrated solid-solution alloys from ab initio calculations: $\text{Ni}_{0.5}\text{Co}_{0.5}$, $\text{Ni}_{0.5}\text{Fe}_{0.5}$, $\text{Ni}_{0.8}\text{Fe}_{0.2}$ and $\text{Ni}_{0.8}\text{Cr}_{0.2}$, *PCCP* 18(34) (2016) 24043-24056.
- [162] C. Lea, C. Molinari, Magnesium diffusion, surface segregation and oxidation in Al-Mg alloys, *J. Mater. Sci.* 19(7) (1984) 2336-2352.
- [163] S.W. Kim, D.H. Kim, B.D. You, J.W. Han, M.S. Kim, Evaporation behavior of magnesium under reduced pressure, *Mater. Sci. Forum* (2003) 238-243.
- [164] E.G. Seebauer, M.C. Kratzer, Diffusion, fundamentals of defect ionization and transport, charged semiconductor defects: Structure, thermodynamics and diffusion (2009) 5-37.
- [165] P.M. Fahey, P. Griffin, J.D. Plummer, Point defects and dopant diffusion in silicon, *Rev. Mod. Phys.* 61(2) (1989) 289.
- [166] J. Buckeridge, Equilibrium point defect and charge carrier concentrations in a material determined through calculation of the self-consistent Fermi energy, *Comput. Phys. Commun.* 244 (2019) 329-342.
- [167] W. Walukiewicz, Defect formation and diffusion in heavily doped semiconductors, *Phys. Rev. B* 50(8) (1994) 5221.
- [168] J. Jang, B. Ryu, S.J. Joo, B.-S. Kim, B.K. Min, H.W. Lee, S.D. Park, H.S. Lee, J.E. Lee, Antimony-induced heterogeneous microstructure of $\text{Mg}_2\text{Si}_{0.6}\text{Sn}_{0.4}$ thermoelectric materials and their thermoelectric properties, *J. Alloys Compd.* 739 (2018) 129-138.
- [169] A. Sankhla, H. Kamila, K. Kelm, E. Mueller, J. de Boor, Analyzing thermoelectric transport in n-type $\text{Mg}_2\text{Si}_{0.4}\text{Sn}_{0.6}$ and correlation with microstructural effects: An insight on the role of Mg, *Acta Mater.* 199 (2020) 85-95.
- [170] J. Bourgeois, J. Tobola, B. Wiendlocha, L. Chaput, P. Zwolenski, D. Berthebaud, F. Gascoin, Q. Recour, H. Scherrer, Study of electron, phonon and crystal stability versus thermoelectric properties in Mg_2X (X= Si, Sn) compounds and their alloys, *Funct. Mater. Lett.* 6(05) (2013) 1340005.
- [171] A. Sizov, H. Reardon, B.B. Iversen, P. Erhart, A.E.C. Palmqvist, Influence of phase separation and spinodal decomposition on microstructure of $\text{Mg}_2\text{Si}_{1-x}\text{Sn}_x$ Alloys, *Cryst. Growth Des.* 19(9) (2019) 4927-4933.
- [172] G. Skomedal, N.R. Kristiansen, M. Engvoll, H. Middleton, Methods for enhancing the thermal durability of high-temperature thermoelectric materials, *J. Electron. Mater.* 43(6) (2014) 1946-1951.

- [173] G.K. Goyal, T. Dasgupta, Effect of magnesium content and processing conditions on phase formation and stability in $\text{Mg}_{2+\delta}\text{Si}_{0.3}\text{Sn}_{0.7}$, *J. Electron. Mater.* 47(3) (2018) 2066-2072.
- [174] K. Yin, Q. Zhang, Y. Zheng, X. Su, X. Tang, C. Uher, Thermal stability of $\text{Mg}_2\text{Si}_{0.3}\text{Sn}_{0.7}$ under different heat treatment conditions, *J. Mater. Chem. C* 3(40) (2015) 10381-10387.
- [175] S. Zhang, J.E. Northrup, Chemical potential dependence of defect formation energies in GaAs: Application to Ga self-diffusion, *Phys. Rev. Lett.* 67(17) (1991) 2339.
- [176] J. de Boor, U. Saparamadu, J. Mao, K. Dahal, E. Müller, Z. Ren, Thermoelectric performance of Li doped, p-type $\text{Mg}_2(\text{Ge},\text{Sn})$ and comparison with $\text{Mg}_2(\text{Si},\text{Sn})$, *Acta Mater.* 120 (2016) 273-280.
- [177] H. Ihou-Mouko, C. Mercier, J. Tobola, G. Pont, H. Scherrer, Thermoelectric properties and electronic structure of p-type Mg_2Si and $\text{Mg}_2\text{Si}_{0.6}\text{Ge}_{0.4}$ compounds doped with Ga, *J. Alloys Compd.* 509(23) (2011) 6503-6508.
- [178] N. Hirayama, T. Iida, S. Morioka, M. Sakamoto, K. Nishio, Y. Kogo, Y. Takanashi, N. Hamada, First-principles investigation of structural, electronic, and thermoelectric properties of n- and p-type Mg_2Si , *J. Mater. Res.* 30(17) (2015) 2564-2577.
- [179] J. Tani, H. Kido, First-principles and experimental studies of impurity doping into Mg_2Si , *Intermetallics* 16(3) (2008) 418-423.
- [180] J.Y. Jung, I.H. Kim, Synthesis and thermoelectric properties of n-Type Mg_2Si , *Electron. Mater. Lett.* 6(4) (2010) 187-191.
- [181] W. Brown, W. Augustyniak, Energy, orientation, and temperature dependence of defect formation in electron irradiation of n-Type Germanium, *J. Appl. Phys.* 30(8) (1959) 1300-1309.
- [182] F. Gao, D. Bacon, L. Howe, C.B. So, Temperature-dependence of defect creation and clustering by displacement cascades in α -zirconium, *J. Nucl. Mater.* 294(3) (2001) 288-298.
- [183] C.H. Lin, T.A. Merz, D.R. Douff, J. Joh, J.A. del Alamo, U.K. Mishra, L.J. Brillson, Strain and temperature dependence of defect formation at AlGaN/GaN high-electron-mobility transistors on a nanometer scale, *IEEE Trans. Electron Devices* 59(10) (2012) 2667-2674.
- [184] X. Han, G. Shao, Interplay between Ag and interstitial Mg on the p-type characteristics of Ag-doped Mg_2Si : challenges for high hole conductivity, *J. Mater. Chem. C* 3(3) (2015) 530-537.
- [185] D.M. Rowe, Conversion efficiency and figure-of-Merit, CRC Handbook of Thermoelectrics, CRC press (1995) 31-37.
- [186] E. Ivanov, Evaluation of tantalum silicide sputtering target materials for amorphous Ta-Si-N diffusion barrier for Cu metallization, *Thin Solid Films* 332(1-2) (1998) 325-328.
- [187] S.Q. Wang, Barriers against copper diffusion into silicon and drift through silicon dioxide, *MRS Bulletin* 19(8) (1994) 30-40.
- [188] Y. Liu, S. Song, D. Mao, H. Ling, M. Li, Diffusion barrier performance of reactively sputtered Ta-W-N between Cu and Si, *Microelectron. Eng.* 75(3) (2004) 309-315.
- [189] J. Reid, R. Liu, P.M. Smith, R. Ruiz, M.A. Nicolet, WBN diffusion barriers for Si/Cu metallizations, *Thin Solid Films* 262(1-2) (1995) 218-223.
- [190] T. Oku, E. Kawakami, M. Uekubo, K. Takahiro, S. Yamaguchi, M. Murakami, Diffusion barrier property of TaN between Si and Cu, *Appl. Surf. Sci.* 99(4) (1996) 265-272.
- [191] Y. Ezer, J. Härkönen, V. Sokolov, J. Saarihahti, J. Kaitila, P. Kuivalainen, Diffusion barrier performance of thin Cr films in the Cu/Cr/Si structure, *Mater. Res. Bull.* 33(9) (1998) 1331-1337.
- [192] N. Saunders, A. Miodownik, The Cu-Sn (copper-tin) system, *Bull. Alloy Phase Diag.* 11(3) (1990) 278-287.
- [193] R. Olesinski, G. Abbaschian, The Cu-Si (Copper-Silicon) system, *Bull. Alloy Phase Diag.* 7(2) (1986) 170-178.
- [194] B. Jayachandran, B. Prasanth, R. Gopalan, T. Dasgupta, D. Sivaprahasam, Thermally stable, low resistance $\text{Mg}_2\text{Si}_{0.4}\text{Sn}_{0.6}/\text{Cu}$ thermoelectric contacts using SS304 interlayer by one step sintering, *Mater. Res. Bull.* 136 (2021) 111147.
- [195] D.R. Lide, Handbook of Chemistry and Physics, CRC Press (1974).

Appendix

In this section, a further discussion of the results obtained using the $\text{Ni}_{45}\text{Cu}_{55}$ electrode is presented. The first section A.1 includes more details about the effect of the sintering current discussion that was presented in Chapter 6.1.1, where a first comparison between the *direct resistive heating (DRH)* and the *indirect resistive heating (IRH)* methods using $\text{Ni}_{45}\text{Cu}_{55}$ was provided. The second section A.2 presents an attempt to investigate hybrid-DFT calculation results of combined Ni and Cu defects in Bi-doped and Li-doped Mg_2Si and Mg_2Sn . Using these results, a comparison with the experimental contacting results with $\text{Ni}_{45}\text{Cu}_{55}$ is attempted in order to evaluate the viability of combining defects from single elements to approximate the behavior of the alloy defects.

These studies are presented in the Appendix because they are not fully understood yet, thus, preliminary and not completely conclusive. Therefore, they are to be taken with consideration of their limitations, and as first attempts that could guide and motivate future research.

A.1 Effect of the sintering current on the contacting results of $\text{Ni}_{45}\text{Cu}_{55}$

A.1.1 Microstructure and SEM investigations

Different reaction layer thicknesses

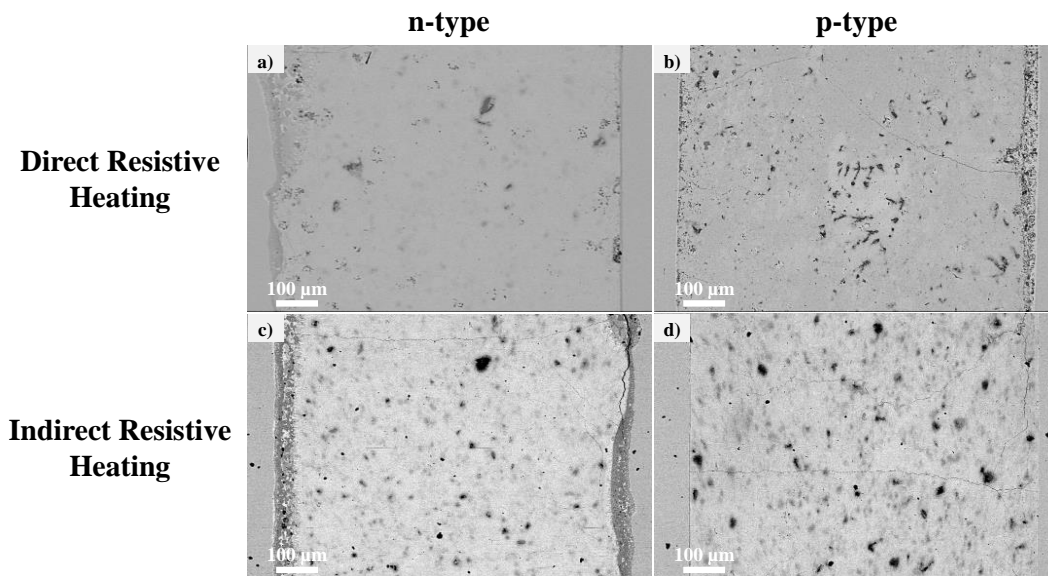


Figure A.1: SEM images of $\text{Ni}_{45}\text{Cu}_{55}$ -contacted n- and p-type $\text{Mg}_2\text{Si}_{0.3}\text{Sn}_{0.7}$ a) and b) under direct resistive heating respectively, and c) and d) under indirect resistive heating, respectively. The same figure is presented as Figure 6.9 in Chapter 6.1.1.

As already mentioned in Chapter 6.1.1, and as can be seen from Figure A.1, the reaction layers resulting from the *direct* and the *indirect resistive heating* methods are different. Moreover, the thickness of the layers also differs between the n- and p-type samples.

In Chapter 3, it was reported that the n- and p-type samples joined with Ni₄₅Cu₅₅ under *DRH* conditions showed a difference in the thickness of the reaction layers on both sides of each sample: the thick layer had a thickness between 150 and 200 μm, while the thin layer was only ~ 20 μm. Nevertheless, EDX investigations showed similar compositions and microstructure. The difference in thickness was explained by the direct current that runs through the samples from bottom to top (technical current direction), as explained in Chapter 2.2, and could favor the electromigration of Ni and Cu cations in a certain direction. As such, the thick reaction layer would be the layer on the bottom side of the sample. On the top sample side, Ni would also act as a diffusion barrier to Cu [196-198], when the movement of the Cu atoms occurs in the opposite direction to the current, which could explain the thin reaction layers. In fact, as Ni diffuses inside the TE material, it reacts with the matrix Si, forming Ni-Si which is known to be good diffusion barriers for Cu, (among other metallic silicides), so it would block Cu from diffusing further in the material.

However, under *IRH* conditions, the thickness of the reaction layers is similar on both sides. From this perspective, it can be concluded that the electromigration of Ni is not as intensified, and its different effects depending on whether the diffusion occurs along the technical current direction or against it are not as prominent. Nevertheless, the discrepancy can be seen in the thickness of these interfaces when comparing the n- and p-type samples (*indirect* current conditions), where the reaction layers on both sides of the p-type sample have a thickness ~ 15 μm, while those on both sides of the n-type sample have a thickness ~ 100 μm.

Following these results, one can potentially establish that the behavior of the p-type sample under *indirect* current conditions follows the explanation presented above as being Ni forming Ni-Si and acting as a diffusion barrier to Cu. This would fit with the explanation provided for the thin reaction layer side in the samples joined under *direct* current conditions. However, the behavior of the n-type sample contradicts the hypothesis proposed above, as the thick reaction layer that was observed on the bottom side of the *directly* joined samples is seen here on both sides. Potential explanations to this behavior could be:

- Ni is quite effectively transported by current, and the electromigration is potentially relevant for Ni₄₅Cu₅₅, which explains the different thicknesses for the *DRH* Ni₄₅Cu₅₅ sample. On the other hand, when the sample was joined under *indirect* current conditions, Ni behaved the same for both reaction layers and just followed a temperature-induced diffusion. As Cu was already shown to diffuse the same way independently of the current conditions (Chapter 4), we would be here seeing a temperature-induced diffusion of both elements, not strongly affected by the

sintering current. Therefore, we would have a similar reaction layer on both sides, which is the case for both p and n-type. However, why the layer thicknesses for n- and p-type are so different for *IRH* (Did the potentially formed Ni-Si not act as a diffusion barrier to Cu for the n-type sample like it did for the p-type sample?) remains unclear.

- In this particular sample case, a probable error could have occurred during the joining process, which caused different and unexpected results. In fact, unlike the joining under *indirect* resistive heating current, the joining of n- and p-type under *direct* resistive heating current was repeated, and the results were successfully reproduced. So, the observation of different reaction layer thicknesses is not a one-time occurrence. From this perspective, the explanation related to the electromigration and Ni-Si formation could hold, and the results observed with the p-type sample joined under *indirect* resistive heating would be more reliable than those of the n-type. A repetition of the *indirect* joining experiments would be necessary here to potentially cross out preparation errors.

Similar interface microstructure

In this section, we provide SEM/EDX analysis of the reaction layer of the *indirectly* joined samples. As the n-type sample is the one that showed thick reaction layers, it is used here for this study. A composition mapping is presented in Figure A.2.

In this figure, a multilayered structure is observed, similar to the *directly* joined sample as reported in Chapter 3. The layer marked 1 contains the Ni-Si square-shaped precipitates surrounded by an Mg-Cu-Sn matrix. The layer 2 is almost completely depleted of Sn, and containing a mixture of 2 phases, all with atomic percentages of Mg, Si, Cu and Ni higher than 20%. Layer 3 seems to be composed of a Cu-Ni-Si structure in an Mg₂Sn-rich matrix, and finally, layer 4 contains Cu, Mg and Sn and can possibly be the γ (Cu_{1.55}MgSn_{0.45}) phase.

Therefore, despite the difference in thicknesses, the potential phases and the different layers composition the interface are similar under both current conditions. From this perspective, and assuming that no major issue occurred with our *indirectly* joined n-type sample, the phase formation here would be mainly due to a temperature-induced diffusion, and reaction of the electrode material with the TE material.

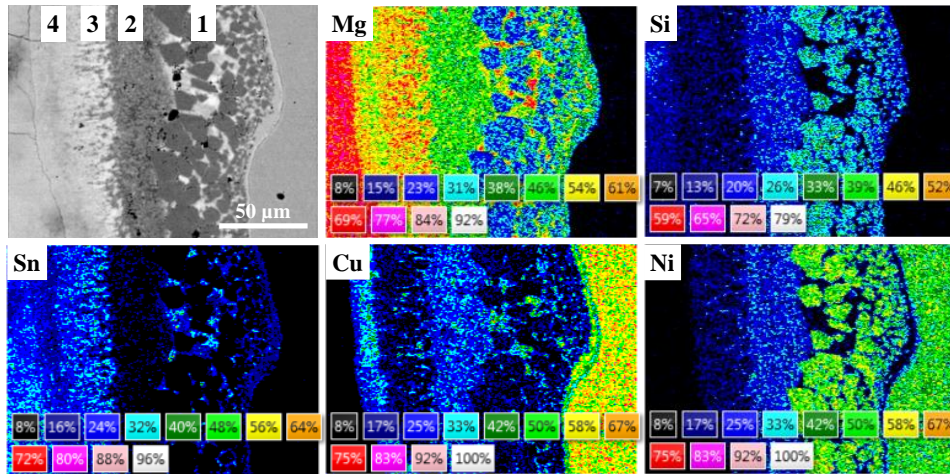


Figure A.2: Atomic percentage composition mapping of the interface layer between $\text{Ni}_{45}\text{Cu}_{55}$ and n-type $\text{Mg}_2\text{Si}_{0.3}\text{Sn}_{0.7}$ joined under indirect resistive heating conditions.

On the cracking behavior

The n- and p-type samples *indirectly* joined with $\text{Ni}_{45}\text{Cu}_{55}$ contain several cracks growing in different directions, that are also more prominent than in the *directly* joined counterparts. As explained in Chapter 6.1.2, the cracks that occur inside the $\text{Mg}_2(\text{Si},\text{Sn})$ material system can be divided into three groups: (i) cracks inside the TE material, (ii) cracks inside the reaction layer and (iii) filled cracks.

In the studied case, we are looking into the first group, which is cracks inside the TE material. When such cracks are observed in a contacted sample, it is not possible to identify if they occurred during the sintering step, or during the joining step. In both cases, the material is subjected to static and thermomechanical stresses, and, to the best of our knowledge, no thorough analysis of stresses under sintering has been reported yet. Some of these cracks would be related to the CTE mismatch between the electrode and the TE material, but it is not always straightforward to differentiate them from the cracks that occurred during pellet sintering. Some of these cracks could have occurred during the joining step, but they were electrode-independent, meaning they occurred in the beginning of the joining step when the pressure was first applied.

For the purpose of this analysis, these cracks can be divided according to their direction of growth: perpendicular to the interface and parallel to the interface.

The cracks that are perpendicular to the interface would be due to the compressive stresses from the punches pressing on the sample system. These cracks would happen during the event of the application of the pressing force on the sample and/or during the heating step, during both the first sintering as well as the contacting step.

As the main difference between the *DRH* and the *IRH* procedures resides in the heating method, one could assume that the difference in the cracking behavior is also related to the heating step. In fact, in *DRH*, the center of the sample would be at a higher temperature than the edges of the sample, due to the direct current running through it and the potential heat transfer from the sample to the graphite die around it, which could result in cracks. On the other hand, in *IRH*, the edges of the sample would be at a higher temperature than its center, and the effect of the temperature gradient could also be seen as cracking in the material.

However, in the case of our used TE materials, compressive stresses are not expected to have a strong effect as the material has a high compressive strength. In the case of the n-type $\text{Mg}_2\text{Si}_{1-x}\text{Sn}_x$ ($x = 0.4 \sim 0.6$) compositions, for example, values of compressive strengths > 400 MPa were reported, compared to only a tensile strength of ~ 70 MPa [199]. This indicates that most of the cracks that are observed in the *DRH* and the *IRH* samples would then be from tensile stresses, that would occur when the core temperature of a system is higher than its surface temperature [200]. Nevertheless, if observed, cracks of compressive origin would be then related to local defects in the structure of the material, which would facilitate cracks appearance and growth under the effect of compressive stresses.

The cracks parallel to the interface would be cracks that grow during the cooling step under the effect of tensile stresses (along the *Z* axis, which is the direction of pressing and perpendicular to the sample surface). Such stresses expand the material following a direction parallel to the interface in the *XY* plane (parallel to the surface of the material), causing cracks to grow in that direction. However, as polycrystalline $\text{Mg}_2(\text{Si},\text{Sn})$ behaves as an isotropic material with no definite preferred direction for the tensile stresses to cause crack growth [160], such cracks would grow in different directions, all the while remaining in a 2D array. Sometimes, impurities like pores and secondary phases can divert the growth direction, and the cracks would then grow in 3D. Even though the cooling step is similar in both *DRH* and *IRH* processes, the nature of the $\text{Mg}_2(\text{Si},\text{Sn})$ system and its response to tensile stresses could explain the observed crack behavior of the studied samples. Thus, in this case, the fact that more cracks were observed in the *IRH* sample can be related to the ceramic nature of the TE material more than the contacting procedure. Furthermore, more cracks could have already occurred during the sintering of the TE pellets used later for the *IRH* joining, compared to the pellets used for *DRH* joining.

One way to check this would be to investigate the sintered sample for cracking before joining. However, this would, in most cases, include destruction of the sample (as the cracks need to be observed on the cross section), and would complicate the joining step, by increasing the probability of failure due to a concentration of stresses produced by an inconvenient sample shape.

A.1.2 Favorable current paths

In this section, a trial to look into the possible current paths in the *direct* and *indirect resistive heating* methods is provided, in an attempt to better understand the obtained results.

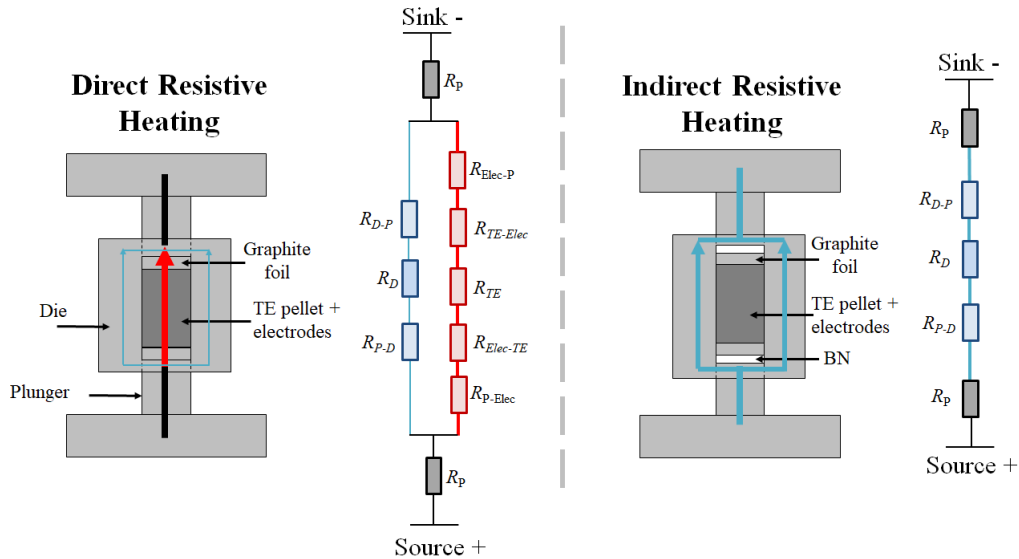


Figure A.3: Schematic figure representing the equivalent circuits/current paths in both *direct* and *indirect resistive heating* processes. The main path in both situations is shown in bulk lines (in red for the *DRH*, and in blue for *IRH*). The resistances R_p , R_D , R_{Elec} and R_{TE} correspond to the bulk resistances of the plungers, the die, the electrode and the TE material respectively. The electrodes being metallic, their resistances were disregarded in these circuits. Contact resistances are labeled R_{X-Y} where X and Y respectively correspond to the two materials below and above the contact surface.

In Figure A.3, the favorable current paths in the (die + sample) system is shown for both *DRH* and *IRH* conditions. In case of *DRH*, there are two possible paths for the current to follow, as there is not fully insulating layer added in the system, and they are shown in red and blue lines. The path shown in red is the main path as, during contacting, the plungers, TE material and electrode are subjected to a pressing force (~ 20 MPa). Such force would favor good contact between the different material interfaces, which minimizes the electrical contact resistance between the single components. Comparatively, the contact interface between the plunger and the die is not subjected to any pressing forces; therefore, the contact between these two components is expected to be worse than that of the plunger with the electrode.

To better visualize this, Figure A.4 taken from [201] shows the influence of an applied pressure on the current distribution in a Spark Plasma Sintering (SPS) graphite setup. The difference between the two cases resides in the tightness (f) between the graphite die and the plungers: in case a, the setting is looser ($f1$), while in case b, it is tighter ($f2$). The zoomed-in portions on top of each setting show schematically the quality of the contact surface between the die and the plunger, as well as the current distribution. It is clear that, in case b, where $f2 < f1$, the contact is much better with less discontinuities, and the current

density is higher. In these experiments, several pressures were tested ranging from 5 to 80 MPa, and it was shown that the different applied pressures significantly influenced electric and thermal fields, including Joule heating.

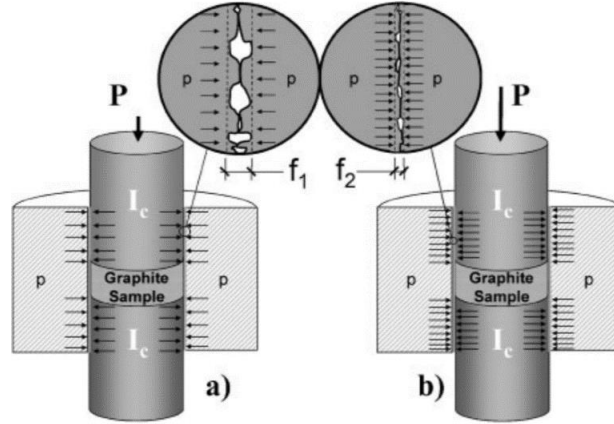


Figure A.4: Two different SPS configurations showing the influence of the tightness as induced by an applied pressure P , on the current distribution along the different components of the setup. Taken from [201].

Extrapolating this study to our current work, we know that the shown in red lines in the *DRH* setting is subjected to pressing forces; therefore, it is the tighter path compared to the path shown in blue lines (at the crossing surface points from the punch to the die). Even though our studied case comprises several materials with different resistances and contact resistances, it is still possible to conclude that the red path is the path with the largest current distribution, and therefore, the sample heating does in fact occur majorly due to a Joule heating of the sample itself.

Concerning the *IRH* setup, the addition of the BN layer majorly blocks the red path, and only the blue path is remaining. In fact, BN is a typical isolating material with an electrical resistivity $\sim 2.3 \times 10^{10} \Omega \text{ cm}$ at 480°C [202]. As our DSP setup is a three-phase system providing a total connection voltage of $3 \times 400 \text{ V}$, and its maximum thermal power P_{max} is 205 kW/A, we can approximate the used current during the contacting process as the output file gives a percentage of the used power each time. If we assume that the total voltage is divided equally among the three phases, so $V_{\text{phase}} = 400 \text{ V}$, we can approximate the used current I_{used} during the *DRH* and *IRH* experiments as follow

$$I_{\text{used}} = \frac{P_{\text{used}}}{\sqrt{3} \times 400}$$

Where P_{used} is the used power during the joining. In the case of *DRH* joining, $P_{\text{used}} = 3\% P_{\text{max}} = 6150 \text{ W}$ and in the case of *IRH*, $P_{\text{used}} = 2\% P_{\text{max}} = 4100 \text{ W}$, which correspond to $I_{\text{used}} (\text{DRH}) = 8.8 \text{ A}$ and $I_{\text{used}} (\text{IRH}) = 6 \text{ A}$. Here too, we can see how the total resistance in the main path of the *direct resistive heating*

(red path) process is smaller than the total resistance in the main path of the *indirect resistive heating* process (blue path).

In the main manuscript, we define our *DRH* process as being the path followed vertically by the current, and we dismiss the current lines that flow from the plunger to the die because the vertically stacked components are subjected to a pressing force that allows better contact surfaces and helps minimize the electrical contact resistances. Using the current numbers obtained above, we can approximate the potential electrical contact resistances r_c for both paths: r_c (plunger -> electrode) for the vertical path (in *DRH*) and r_c (plunger -> die) for the parallel path (in *IRH*). For a better visibility, the geometries of the parts in play and the paths are schematically shown in Figure A.5.

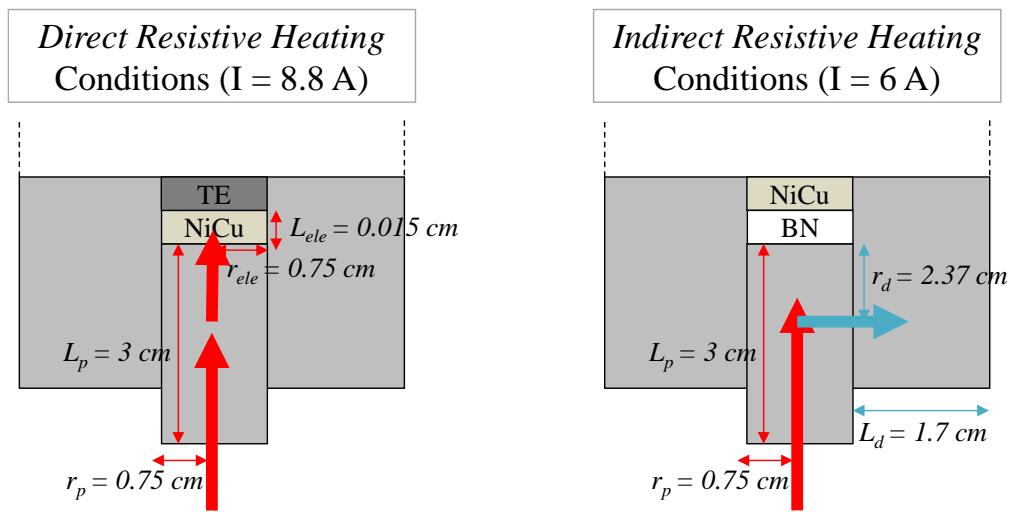


Figure A.5: Schematic of the two current paths in both processes (red and blue). Numbers of the lengths L and the radii r of the components in play (plunger, $\text{Ni}_{45}\text{Cu}_{55}$ electrode and die) are marked with p, ele and d respectively in subscript.

In these calculations, the numbers used for the electrical resistivity of the materials (graphite and $\text{Ni}_{45}\text{Cu}_{55}$) were taken from [202]. The resistance R for each part is calculated using $R = \frac{\rho \times L}{A}$, where ρ is the resistivity and L the length as shown in Figure A.5, and A the surface crossed by the current. As these surfaces are cylindrical, $A = \pi \times r^2$, r are the radii shown in the same Figure A.5. The voltage across each segment (plunger, electrode, die) is then calculated and the corresponding specific electrical contact resistances r_c are calculated as $r_c = \frac{V_1 - V_2}{j}$, where V_1 and V_2 are the voltages across the components of interest and j is the current density crossing the contact surface. In the case of the vertical path (in red), r_c (p_ele) between the plunger and the electrode is calculated using the current value I_{used} (*DRH*), while for the case of the parallel path (in blue), r_c (p_die) between the plunger and the die is calculated using the current value of I_{used} (*IRH*). All the numbers are provided in Table A-1.

Table A-1: Table summarizing the numbers for the geometries (length L , surface A), the electrical resistivities ρ (taken from [202]) and resistance R , the voltage drops V along the segments of interest from the circuit, as well as the current densities j and the specific electrical resistances r_c in both *DRH* and *IRH* processes. The r_c were calculated using the current values I_{used} (*DRH*) and I_{used} (*IRH*) for the $r_c(p_ele)$ and $r_c(p_die)$, respectively.

	L (cm)	A (cm ²)	ρ ($\mu\Omega$ cm)	R ($\mu\Omega$)	V (μ V)	<i>DRH</i> Process / $I = 8.8$ A		<i>IRH</i> Process / $I = 6$ A	
						$j(p_ele)$ (A cm ⁻²)	$r_c(p_ele)$ ($\mu\Omega$ cm ²)	$j(p_die)$ (A cm ⁻²)	$r_c(p_die)$ ($\mu\Omega$ cm ²)
Plunger	3	1.76	910	1545	9270	4.97	13591	0.34	25713
Electrode	0.015	1.76	49.87	0.42	3.72				
Die	1.7	17.64	910	87.66	526				

From the table, it is clear that the contact resistance between the plunger and the electrode is almost half of that between the plunger and the die. Therefore, as $r_c(p_die)$ would be the same for the *IRH* and the *DRH* processes, and based on the used approximations and calculations, it is possible to assume that the *direct resistive heating* process occurs in fact mainly through a Joule heating of the sample itself as most of the current density does travel vertically.

A.2 Hybrid-DFT calculations for the combined defect case of Ni₄₅Cu₅₅

In this section, we discuss the case of n- and p-type Mg₂Si_{0.3}Sn_{0.7} contacted with Ni₄₅Cu₅₅. Experimentally, this case was reported in Chapter 3 and Chapter 6.1.1 using the composition Mg₂Si_{0.3}Sn_{0.7}. Following Chapter 3, when the samples were joined under *direct resistive heating*, the results showed a change in the TE properties for n-type samples and none for p-type sample, similar to what was reported for Cu. However, the results reported in Chapter 5 where the samples were joined under *indirect resistive heating*, no change in the TE properties was recorded, neither for the n-type nor for the p-type samples.

Trying to look at this case from a defect formation energy perspective, we tried to look at the defects of Cu and Ni (as reported in Chapter 6.2.1 and Chapter 6.2.2) simultaneously and compare their formation energies with the formation energies of the dopants and the native lattice defects. No calculations were done using combined defects yet; however, a first investigation of this study can be established through assuming defect stability as calculated in the single cases of Cu and Ni. For simplicity and to keep the study focused, we only look into the defect formation energies of Mg₂Sn as our experimental samples are all rich in Mg₂Sn (70%). We also just look at the Mg-poor chemical potential conditions because the p-type samples are in any case synthesized deficient in Mg, and the n-type can be assumed to be Mg

deficient as Mg losses can occur and cannot be completely refuted. Lastly, the selected Ni defects are the ones obtained for the calculations done considering the Ni₃Sn phase. Results of the hybrid-DFT calculations are given in Figure A.6, where only the defects with formation energies below 1.5 eV are represented. Also, only the most stable defect related to Cu and Ni are shown.

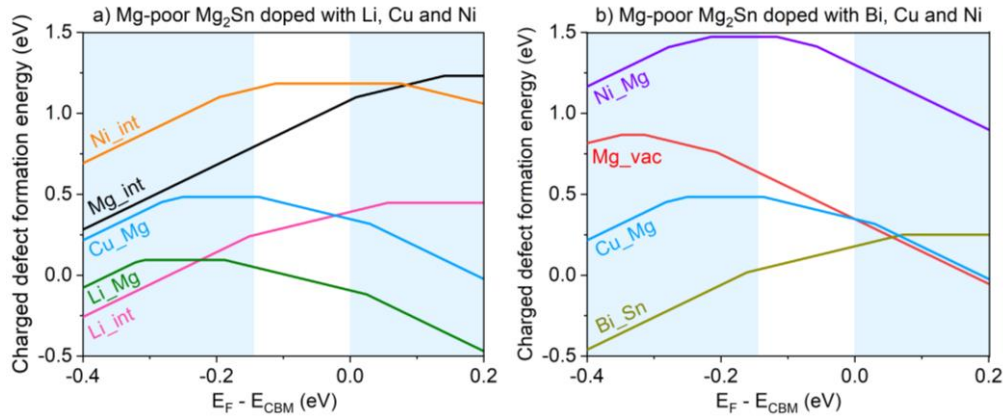


Figure A.6: Charged defect formation energies of Cu and Ni in Mg-poor a) Li-doped and b) Bi-doped Mg₂Sn with the most stable Cu and Ni related defects.

Figure A.6 a presents the defect formation energy results for Mg₂Sn doped with Li, Cu and Ni. Looking in the vicinity of the valence band maxima, the most stable defects are clearly I_{Li} and Li_{Mg}, which determine the p-type conduction of the material and the charge carrier concentration n . The following most stable defect is Cu_{Mg}, which was already reported in Chapter 6.2.1 as being a neutral defect, and therefore would have no influence on n . I_{Ni} is the most stable Ni-related defect, and even though it is a donor defect of charge 1+ around VBM, its formation energy is too high (> 1.1 eV) to have a relevant influence on n . The same goes for I_{Mg}, which is a donor defect with charge 2+ but has a high formation energy. Therefore, from this comparison, it can be deduced that the combined presence of Cu and Ni won't have any influence on the charge carrier concentration of the sample and the p-type conduction established by the Li defects. This matches what was reported in Chapter 3 and Chapter 6.1.1 for p-type Mg₂Si_{0.3}Sn_{0.7} joined with Ni₄₅Cu₅₅ under both used sintering current conditions (*direct resistive* and *indirect resistive heating*, respectively).

Figure A.6 b represented the defect formation energies of Mg₂Sn doped with Bi, Cu and Ni. Around CBM, the most stable Ni-defect (Ni_{Mg}) has a much higher formation energy compared to the three other stable defects, namely Bi_{Sn}, Cu_{Mg} and V_{Mg}. Therefore, it can be concluded up to here that Ni won't significantly contribute to the system's carrier concentration during a simultaneous presence of Ni and Cu. Cu, on the other hand, would play a considerable role in changing n through the Cu_{Mg} defect and its interplay with the Bi_{Sn} and V_{Mg} defects, as described in more details in Chapter 6.2.1. Such results match

the experimental results reported in Chapter 3, and also make sense because, experimentally, the Seebeck value recorded on n-type samples joined with both Cu and Ni₄₅Cu₅₅ electrodes was the same (–160 μV/K), which signifies that both electrodes have the same charge compensation effect. The Hybrid-DFT calculations join this statement as they also show that in case of both Ni and Cu, only the Cu effect would be considerable and would have a visible effect on the TE properties of the samples.

However, these calculation results do not match what was reported in Chapter 6.1.1 when n-type Mg₂Si_{0.3}Sn_{0.7} was joined with Ni₄₅Cu₅₅ under *indirect resistive heating*, as the Seebeck value after joining was reported as unchanged. This disagreement in the comparison can come from the various assumptions which the comparison is based on. In fact, the provided calculation results are done under specific chemical potential conditions: Mg-poor, Cu-rich for the Cu defects, Ni₃Sn-rich for the Ni defects. The actual atomic chemical potential of the n-type sample joined with Ni₄₅Cu₅₅ is unknown, it is strongly plausible that the comparison failed because the chemical potential used during the calculations is different from the experimental one, which leads to different defect formation energies, and therefore a different conclusion. Another potential explanation could be the implication of the current in the transport of the electrode ions (electromigration), which is not considered in DFT calculations, and therefore, different results can also be expected.

References of the Appendix:

- [196] B. Liu, L. Yang, X. Li, K. Wang, Z. Guo, J. Chen, M. Li, D. Zhao, Q. Zhao, X. Zhang, Ultrathin amorphous Ni–Ti film as diffusion barrier for Cu interconnection, *Appl. Surf. Sci.* 257(7) (2011) 2920-2922.
- [197] A. Kale, E. Beese, T. Saenz, E. Warren, W. Nemeth, D. Young, A. Marshall, K. Florent, S.K. Kurinec, S. Agarwal, Study of nickel silicide as a copper diffusion barrier in monocrystalline silicon solar cells, *IEEE 44th PVSC*, (2017) 1-4.
- [198] S.K. Min, D.H. Kim, S.H. Lee, Nickel silicide for Ni/Cu contact mono-silicon solar cells, *Electron. Mater. Lett.* 9(4) (2013) 433-435.
- [199] Y. Gelbstein, J. Tunbridge, R. Dixon, M.J. Reece, H. Ning, R. Gilchrist, R. Summers, I. Agote, M.A. Lagos, K. Simpson, C. Rouaud, P. Feulner, D. Rivera, R. Torrecillas, M. Husband, J. Crossley, I. Robinson, Physical, mechanical, and structural properties of highly efficient nanostructured n-and p-silicides for practical thermoelectric applications, *J. Electron. Mater.* 43(6) (2014) 1703-1711.
- [200] W.D. Kingery, Factors affecting thermal stress resistance of ceramic materials, *J. Am. Ceram. Soc.* 38(1) (1955) 3-15.
- [201] S. Grasso, Y. Sakka, G. Maizza, Pressure effects on temperature distribution during spark plasma sintering with graphite sample, *Mater. Trans.* 50(8) (2009) 2111-2114.
- [202] J.F. Shackelford, Y.H. Han, S. Kim, S.H. Kwon, CRC Materials science and engineering handbook, CRC press (2016)

Co-Authorship Statement

In this manuscript, three papers are utilized as the main chapters (Chapters 3, 4 and 5). These papers were published in peer-reviewed journals with accordance to the corresponding journals' regulations.

Information about the co-authors of the papers, as well as the task distribution are provided in the tables below (one table per paper).

- Paper 1:** “*Developing Contacting Solutions for Mg₂Si_{1-x}Sn_x-based Thermoelectric Generators: Cu and Ni₄₅Cu₅₅ as Potential Contacting Electrodes*”, ACS Applied Materials & Interfaces, 11, 43, 40769, 2019.

Co-author & title	Address	Task
Sahar Ayachi, M.Sc.	German Aerospace Center, Institute of Materials Research, Dept. of Thermoelectric Materials & Systems, Cologne, 51147, Germany	- First author - Methodology - Analysis - Writing - Review & editing - Experimental investigation
Gustavo Castillo Hernandez, M.Sc.	German Aerospace Center, Institute of Materials Research, Dept. of Thermoelectric Materials & Systems, Cologne, 51147, Germany	- Discussion - Review & editing
Ngan H. Pham, PhD.	German Aerospace Center, Institute of Materials Research, Dept. of Thermoelectric Materials & Systems, Cologne, 51147, Germany	- Supervision of experimental work - Review & editing
N. Farahi, PhD.	German Aerospace Center, Institute of Materials Research, Dept. of Thermoelectric Materials & Systems, Cologne, 51147, Germany	- Supervision of experimental work - Review & editing
Eckhard Müller, Prof.	German Aerospace Center, Institute of Materials Research, Dept. of Thermoelectric Materials & Systems, Cologne, 51147, Germany JLU Giessen, Institute of Inorganic and Analytical Chemistry, Giessen, 35390 Germany	- Writing - Review & editing - Supervision
Johannes de Boor, Jun.- Prof.	German Aerospace Center, Institute of Materials Research, Dept. of Thermoelectric Materials & Systems, Cologne, 51147, Germany Duisburg-Essen University, Faculty of Engineering, Institute of Technology for Nanostructures (NST), Duisburg, 47057, Germany	- Conceptualization - Methodology - Writing - Review & editing - Supervision

2. **Paper 2:** “*Contacting Cu Electrodes to Mg₂Si_{0.3}Sn_{0.7}: Direct vs Indirect Resistive Heating*”, Semiconductors, 53, 13, 1825, 2019.

Co-author & title	Address	Task
Sahar Ayachi, M.Sc.	German Aerospace Center, Institute of Materials Research, Dept. of Thermoelectric Materials & Systems, Cologne, 51147, Germany	- First author - Methodology - Analysis - Writing - Review & editing - Experimental investigation
Gustavo Castillo Hernandez, M.Sc.	German Aerospace Center, Institute of Materials Research, Dept. of Thermoelectric Materials & Systems, Cologne, 51147, Germany	- Discussion - Review & editing
Eckhard Müller, Prof.	German Aerospace Center, Institute of Materials Research, Dept. of Thermoelectric Materials & Systems, Cologne, 51147, Germany JLU Giessen, Institute of Inorganic and Analytical Chemistry, Giessen, 35390 Germany	- Writing - Review & editing - Supervision
Johannes de Boor, Jun.- Prof.	German Aerospace Center, Institute of Materials Research, Dept. of Thermoelectric Materials & Systems, Cologne, 51147, Germany Duisburg-Essen University, Faculty of Engineering, Institute of Technology for Nanostructures (NST), Duisburg, 47057, Germany	- Conceptualization - Methodology - Writing - Review & editing - Supervision

3. **Paper 3:** “*On the Relevance of Point Defects for the Selection of Contacting Electrodes: Ag as an example for Mg₂(Si,Sn)-based Thermoelectric Generators*”, Materials Today Physics, 16, 100309, 2021.

Co-author & title	Address	Task
Sahar Ayachi, M.Sc.	German Aerospace Center, Institute of Materials Research, Dept. of Thermoelectric Materials & Systems, Cologne, 51147, Germany	- First author - Methodology - Analysis - Writing - Review & editing - Experimental investigation
Radhika Deshpande, M.Sc.	German Aerospace Center, Institute of Materials Research, Dept. of Thermoelectric Materials & Systems, Cologne, 51147, Germany	- Experimental investigation
Prasanna Ponnusamy, M.Sc.	German Aerospace Center, Institute of Materials Research, Dept. of Thermoelectric Materials & Systems, Cologne, 51147, Germany	- Software/calculations - Review & editing

Sungjin Park, PhD.	Korea Electrotechnology Research Institute (KERI), Energy Conversion Research Center, Electrical Materials Research Division, Changwon, 51543, Korea	<ul style="list-style-type: none"> - Theoretical investigation - Analysis - Review & editing
Jaywan Chung, PhD.	Korea Electrotechnology Research Institute (KERI), Energy Conversion Research Center, Electrical Materials Research Division, Changwon, 51543, Korea	<ul style="list-style-type: none"> - Software/calculations
Sudong Park, PhD.	Korea Electrotechnology Research Institute (KERI), Energy Conversion Research Center, Electrical Materials Research Division, Changwon, 51543, Korea	<ul style="list-style-type: none"> - Software/calculations - Writing - Review & editing - Supervision - Funding acquisition
Byungki Ryu, PhD.	Korea Electrotechnology Research Institute (KERI), Energy Conversion Research Center, Electrical Materials Research Division, Changwon, 51543, Korea	<ul style="list-style-type: none"> - Conceptualization - Methodology - Software/calculations - Theoretical investigation - Analysis - Writing - Review & editing - Project administration - Funding acquisition
Eckhard Müller, Prof.	<p>German Aerospace Center, Institute of Materials Research, Dept. of Thermoelectric Materials & Systems, Cologne, 51147, Germany</p> <p>JLU Giessen, Institute of Inorganic and Analytical Chemistry, Giessen, 35390 Germany</p>	<ul style="list-style-type: none"> - Writing - Review & editing - Supervision
Johannes de Boor, Jun.- Prof.	<p>German Aerospace Center, Institute of Materials Research, Dept. of Thermoelectric Materials & Systems, Cologne, 51147, Germany</p> <p>Duisburg-Essen German Aerospace Center, Institute of Materials Research, Dept. of Thermoelectric Materials & Systems, Cologne, 51147, Germany</p>	<ul style="list-style-type: none"> - Conceptualization - Methodology - Writing - Review & editing - Supervision - Project administration

DuEPublico

Duisburg-Essen Publications online

UNIVERSITÄT
DUISBURG
ESSEN

Offen im Denken

ub | universitäts
bibliothek

Diese Dissertation wird via DuEPublico, dem Dokumenten- und Publikationsserver der Universität Duisburg-Essen, zur Verfügung gestellt und liegt auch als Print-Version vor.

DOI: 10.17185/duepublico/74786

URN: urn:nbn:de:hbz:464-20210916-104524-7



Dieses Werk kann unter einer Creative Commons Namensnennung - Nicht kommerziell - Keine Bearbeitungen 4.0 Lizenz (CC BY-NC-ND 4.0) genutzt werden.